# Elastic Properties of Metals and Minerals Under Shock Compression

Thesis by

Thomas S. Duffy

In Partial Fulfillment of the Requirements

for the Degree of

Doctor of Philosophy

California Institute of Technology

Pasadena, California

1992

(Submitted January 29, 1992)

# Acknowledgements

The thesis could never have completed without the assistance of a great many people. I would particularly like to thank my advisor, Tom Ahrens, for his guidance, friendship, support and for providing an environment that made this research possible. I also had the opportunity to collaborate with Don Anderson and I'm also grateful to Don for his continuing interest in my work. I benefited from many other faculty members as well. Dave Harkrider was a great academic advisor, Rob Clayton provided a first-class computer system, and Don Helmberger threw me a lot of passes. Dave Stevenson, Ed Stolper, and Geoff Blake provided many helpful comments.

Working in the shock wave lab was a very enjoyable and enriching experience. The technical staff of the laboratory, Mike Long, Papo Gelle, and Alberto DeVora, provide a very professional and congenial working environment. In addition, I would like to thank all the colleagues who I had the opportunity to work with over the years: Toshimori Sekine, Bill Anderson, Toshiko Takata, Alan Rubin, David Potter, Tan Hua, Jim Tyburczy, Greg Miller, Linda Rowan, Wenbo Yang, Kathleen Gallagher, Doug Schmidt, and Bob Svendsen.

The preparation of sample surfaces for my experiments could be quite tedious. I therefore want to particularly thank all those who helped me with these tasks: Andy

Campbell, Kathleen Gallagher, Toshiko Takata, Scott Scarborough, Steve Wilensky, and Alberto DeVora. I also acknowledge the assistance I received from the Seismo Lab technical staff and machine shop, especially Bill Barber, Dick Wickes, Gunthar Haehn, Bart Pelsue, and Wayne Miller. Vic Nenow was particularly generous in allowing us to borrow equipment for long periods of time and helped solve many electronics problems. Sue Yamada was helpful in countless ways.

I am grateful for valuable technical advice received from Lynn Barker, O. B. Crump, Jr., and Colin Selleck of Sandia National Laboratory and from Willard Hemsing at Los Alamos. Sally Rigden of Australian National University performed some important ultrasonic measurements and her cheerful help was greatly appreciated.

There are many people who made my stay at Caltech more enjoyable and whose friendship I value greatly. I particularly would like to mention Joann Yoshimura, Luciana Astiz, Scott King, Allison Bent, Yu-Shen Zhang, Lian-She Zhao, Lorraine Hwang, Brad Woods, Richard Stead, Shingo Watada, Helen Qian, Dave Wald, Ed Garnero, Andrea Donnellan, Doug Dreger, Bruce Worden, Cathy Smither, Linda Rowan, Hong Kie Thio, and Huw Davies. Playing basketball provided a much-needed escape from graduate student life and I'll miss the games and my friends from the courts. Ernie and Kathy Khirallah provided friendship as well as some fine tennis matches.

Throughout my stay at Caltech, and for my whole life, I have been fortunate to have a large and wonderful family. My sister Mary's annual winter-time visits were great fun. I'd like to thank Helen, Ann, and Jeff Walls and Sara McGuire for always being so cute. The Molina-Durango Family, both the southern California and

Chicago branches, always welcomed me with open arms. I thank my mother, my late father, Cele, and my brothers and sisters for all they have done for me. Finally, I thank my wife, Luz Stella Cristina Cecilia Durango Molina, for *todo*.

## Abstract

Thomas S. Duffy, Ph.D.

California Institute of Technology 1992

Comparison of laboratory elasticity data with seismic measurements of the Earth provides a means to understand the deep interior. The effect of pressure and temperature on elastic properties must be well understood for meaningful comparisons. In this work, elastic wave velocities have been measured under shock compression to 80 GPa in an Fe-Cr-Ni alloy, to 27 GPa in polycrystalline MgO, and to 81 GPa in molybdenum preheated to 1400°C. These measurements were made by recording particle velocity histories at a sample surface using the method of velocity interferometry. In addition to elastic properties, these experiments provide information on the constitutive and equation of state (EOS) properties of the sample as well as the unloading adiabats.

Compressional and bulk wave velocities in Fe-Cr-Ni alloy are consistent with third-order finite strain theory and ultrasonic data. Thermal effects on the wave velocities are less than 2% at 80 GPa. Second pressure derivatives of velocity were constrained along the Hugoniot to be: $(\partial^2 C_L/\partial P^2)_H$ = -0.16 (0.06) GPa$^{-1}$ and $(\partial^2 K_S/\partial P^2)_H$ = -0.17 (0.08) GPa$^{-1}$. The measured wave profiles can be successfully

reproduced by numerical simulations utilizing elastic-plastic theory modified by a Bauschinger effect and stress relaxation. Material strength was found to increase by a factor of at least 5 up to 80 GPa and to be 2-3% of the total stress.

Compressional and bulk velocities in Fe-Cr-Ni define linear velocity-density trends and can be modeled by averaging properties of Fe, Cr, and Ni. The effect of alloying ~4 wt.% Ni with Fe would change both $V_P$ and $V_B$ by less than 1% under core conditions. Compressional velocities in Fe-Ni are compatible with inner core values when corrected for thermal effects. Shear velocities in Fe, determined from a combination of $V_P$ and $V_B$ data, are ~3.6 km/s at P=150-200 GPa. Low values are most likely caused by a weak pressure dependence of the rigidity and imply that partial melting is not required in the inner core.

Wave profile and EOS measurements in polycrystalline MgO define its EOS: $U_S = 6.77(0.08) + 1.27(0.04)u_p$. Compressional sound velocities to 27 GPa yield the longitudinal modulus and its pressure derivative: $C_{Lo} = K_{oS} + 4/3G = 335 \pm 1$ GPa and $C'_{Lo} = 7.4 \pm 0.2$, which are in good agreement with ultrasonic determinations. The unloading wave profiles can be modeled using a modified elastic-plastic constitutive response originally developed for metals. Thermal expansivities in MgO have been determined to be $12 \pm 4 \times 10^{-6}$ $K^{-1}$ at P=174-200 GPa and T=3100-3600 K from shock temperature and EOS data. These results imply that the lower mantle is enriched in Si and/or Fe relative to the upper mantle.

Wave profiles in molybdenum at 1400°C are the first wave profile determinations at significantly high initial temperature. The EOS determined from these measurements agrees well with previous data. The compressive yield strength of Mo is

0.79-0.94 GPa at 1400°C, and the HEL stress is 1.5-1.7 GPa. The temperature coefficient of compressional velocity, $(\partial V_P/\partial T)_P$, is found to vary from -0.35(0.13) m/s/K at 12 GPa to -0.18(0.14) m/s/K at 81 GPa and compares with an ambient pressure value of -0.26 m/s/K. It is inferred that $(\partial V_P/\partial T)_P$ decreases with pressure, and data for Mo are shown to be consistent with trends defined by other metals.

# Table of Contents

# List of Tables

# List of Figures

# Chapter 1

# Elastic and Constitutive Properties of an Fe-Cr-Ni alloy shock compressed to 80 GPa

## 1.1 Introduction

The elastic properties of Fe and Fe alloys at high pressure are important for understanding the seismic properties of the Earth's core. While the Earth's core is known to be dominantly iron on the basis of density data and cosmochemical arguments, a number of possible alloying elements have been proposed. Measurement of elastic wave velocities in iron alloys offers a means to place constraints on the nature and amount of such components. Comparing laboratory data to Earth's core conditions requires large and uncertain extrapolations in pressure and temperature. It is therefore important to delineate the separate pressure and temperature variation of wave velocities.

In this study, elastic wave velocities will be reported in an Fe-Cr-Ni alloy (type 304 stainless steel) that has been shock compressed to 80 GPa. Elastic properties were

determined from interface particle velocity histories measured using velocity interferometry. In addition to information on elasticity, detailed wave profile measurements provide information on constitutive properties such as the yield stress, the stress change upon unloading, and the importance of the Bauschinger effect and stress relaxation. These properties provide insights into the details of the shock-compression process, which are important in attempting to relate shock data to static data or geophysical measurements of the Earth's interior.

Fe-Cr-Ni alloy (304 steel), which is important for both engineering and geological applications, has been the subject of a number of shock-compression studies. The Hugoniot equation of state (EOS) has been determined to 190 GPa [*McQueen et al.,* 1970], and shock temperatures have been determined between 138 and 271 GPa [*Bass et al.,* 1990]. Because of its engineering importance, extensive microstructural investigations have been carried out on shock-recovered 304 steel [e.g., *Murr,* 1988]. Plane uniaxial strain at moderate shock pressures (20-120 GPa) and short pulse durations ($\sim$0.5 $\mu$s) has been shown to induce a martensitic $\gamma$-$\alpha'$ transformation with up to 8 vol. % martensite being identified in TEM observations [*Murr,* 1981].

## 1.2 Experimental Technique

### 1.2.1 Samples

The Fe-Cr-Ni alloy used in this study was type 304 stainless steel. The chemical composition of the steel was determined by electron microprobe analysis and is listed in Table 1.1 together with the compositions reported in shock wave EOS and temperature experiments on this material. In all cases, the compositions are within the AISI standard ranges for this material.

Samples were machined into 32-mm diameter disks from commercial steel rods. The end faces were lapped flat and parallel to better than 0.01 mm. Bulk and crystal densities were measured by weighing the samples in air and toluene under controlled

| Element | This Study | *McQueen et al.* [1970] | *Bass et al.* [1990] |
|---|---|---|---|
| Fe | 69.7 | 68 | 69.3 |
| Cr | 19.3 | 19 | 19.4 |
| Ni | 8.2 | 10 | 9.1 |
| Mn | 1.3 | 2 | - |
| Si | 0.4 | 1 | 0.7 |
| Total | 98.9 | 100 | 98.5 |

Table 1.1: Chemical composition of stainless steel samples in this and other shock studies. Values are in weight percentages.

temperature conditions. The average crystal density was 7.88 $\pm$ 0.01 g/cm$^3$, in good agreement with the x-ray density of 7.89 g/cm$^3$ for this material. The average bulk density was 7.87 $\pm$ 0.01 g/cm$^3$, indicating minimal porosity.

The rear surface of each specimen was prepared in one of two ways, depending on the particular experiment to be performed. A number of specularly reflecting steel targets were prepared by polishing with successively finer grits of alumina powder. For the remaining targets, diffuse reflecting surfaces were produced by lapping the rear of the sample with 5 $\mu$ alumina powder. More details regarding the sample preparation process are provided in Appendix A.

The longitudinal sound velocity was measured ultrasonically and found to be 5.75 $\pm$ 0.03 km/s. This agrees well with the value of 5.76 $\pm$ 0.02 km/s reported by *Ledbetter et al.* [1980]. Type 304 stainless steel has been the subject of a number of ultrasonic sound velocity studies which have included measurement of the temperature [*Ledbetter et al.,* 1975] and pressure [*Gerlich and Hart,* 1984] dependences of the aggregate elastic moduli.

### 1.2.2 Experiments

#### Dynamic Loading System

The Fe-Cr-Ni alloy specimens were shock-loaded using a 40-mm bore propellant gun. The experimental apparatus for achieving one-dimensional planar shock loading has been described in detail elsewhere [*Ahrens et al.,* 1971; *Ahrens,* 1987]. A brief summary is included here. Projectiles are ~100 g and consist of a lexan sabot with a variable thickness, 32-mm diameter flyer plate mounted as a facing. The flyer plate is usually backed by ~3-mm thick layer of 40 lb/ft$^3$ polyurethane foam. The flyer-plate materials used in this study were polymethyl methacrylate (PMMA), 304 stainless steel, and tantalum. The equation of state properties of the flyers, as well as those of other materials used in these experiments, are listed in Table 1.2. Variable amounts of nitroglycerine-nitrocellulose propellant are used to accelerate the projectile down the 24.5 ft. length of the gun barrel into an evacuated chamber containing the target assembly. Impact velocities between 0.9-2.5 km/s are achievable in this manner. Projectile velocity is determined to ~1-2% precision using both double-exposure flash x-ray photography and time-interval counters triggered by laser-beam interrupts.

#### Interferometry

The primary diagnostic technique used in this study was velocity interferometry, which gives a time-resolved picture of the motion of a diffusely or specularly reflecting sample surface. Two types of interferometers were used in the present work: the specular velocity interferometer (SVI) [*Barker,* 1968] and the velocity interferometer system for any reflector (VISAR) [*Barker and Hollenbach,* 1972]. Both interferometers work on the same principle: motion of the target surface induces a Doppler shift in reflected laser light, which creates interference fringes in a modified Michelson interferometer. The interference fringes record the velocity history of the reflecting surface.

| Material | $\rho_o$ (bulk) ($g/cm^3$) | $c_o$ (km/s) | s | $\gamma_o$ | $\nu_o$ | $Y_o$ (GPa) | Refs. |
|---|---|---|---|---|---|---|---|
| 304 Steel | 7.87 | 4.58 | 1.49 | 2.2 | 0.29 | 0.2 | a,b |
| | 0.02 | 0.01 | 0.01 | | | | |
| PMMA | 1.18 | 2.58 | 1.53 | 1.0 | - | - | c |
| | 0.01 | 0.02 | 0.01 | | | | |
| Al6061 | 2.683 | 5.349 | 1.338 | 2.1 | 0.34 | 0.2 | c |
| | 0.003 | 0.056 | 0.020 | | | | |
| Al2024 | 2.784 | 5.33 | 1.34 | 2.0 | - | - | c |
| | 0.005 | 0.05 | 0.02 | | | | |
| Ta | 16.65 | 3.293 | 1.307 | 1.6 | 0.34 | 0.8 | d |
| | 0.03 | 0.005 | 0.025 | | | | |
| LiF | 2.64 | 5.15 | 1.35 | 1.6 | 0.22 | 0.2 | c |
| | 0.02 | 0.03 | 0.01 | | | | |
| $Al_2O_3$ | 3.985 | 11.19 | 1.00 | 1.3 | - | - | e |
| | 0.005 | 0.01 | 0.05 | | | | |
| Lexan | 1.193 | 2.421 | 1.32 | - | - | - | c |
| | 0.01 | 0.033 | 0.11 | | | | |
| Polyurethane | 0.64 | 0.87 | 2.03 | - | - | - | f |
| Foam | 0.01 | - | - | | | | |

Table 1.2: Equation of state standards for Fe-Cr-Ni alloy experiments. Numbers below each value represent one standard deviation uncertainties. $\rho_o$ is the density, $c_o$ and $s$ are shock wave EOS constants, $\gamma_o$ is the Grüneisen parameter, $\nu_o$ is Poisson's ratio, and $Y_o$ is the yield strength. References: a, this study; b, *McQueen et al.* [1970]; c, *Marsh* [1980]; d, *Mitchell and Nellis* [1981a]; e, *Barker and Hollenbach* [1970]; f, *Grady and Furnish* [1988].

Figure 1.1: Schematic of specular velocity interferometer (SVI) used in some of the present experiments. The designation M refers to mirrors, L to lenses, BS to beam splitters (10-mm cube with broadband dielectric coating), F to neutral density filters (0.001-0.1% transmission), and PMT to photomultiplier tubes (Burle 7764).

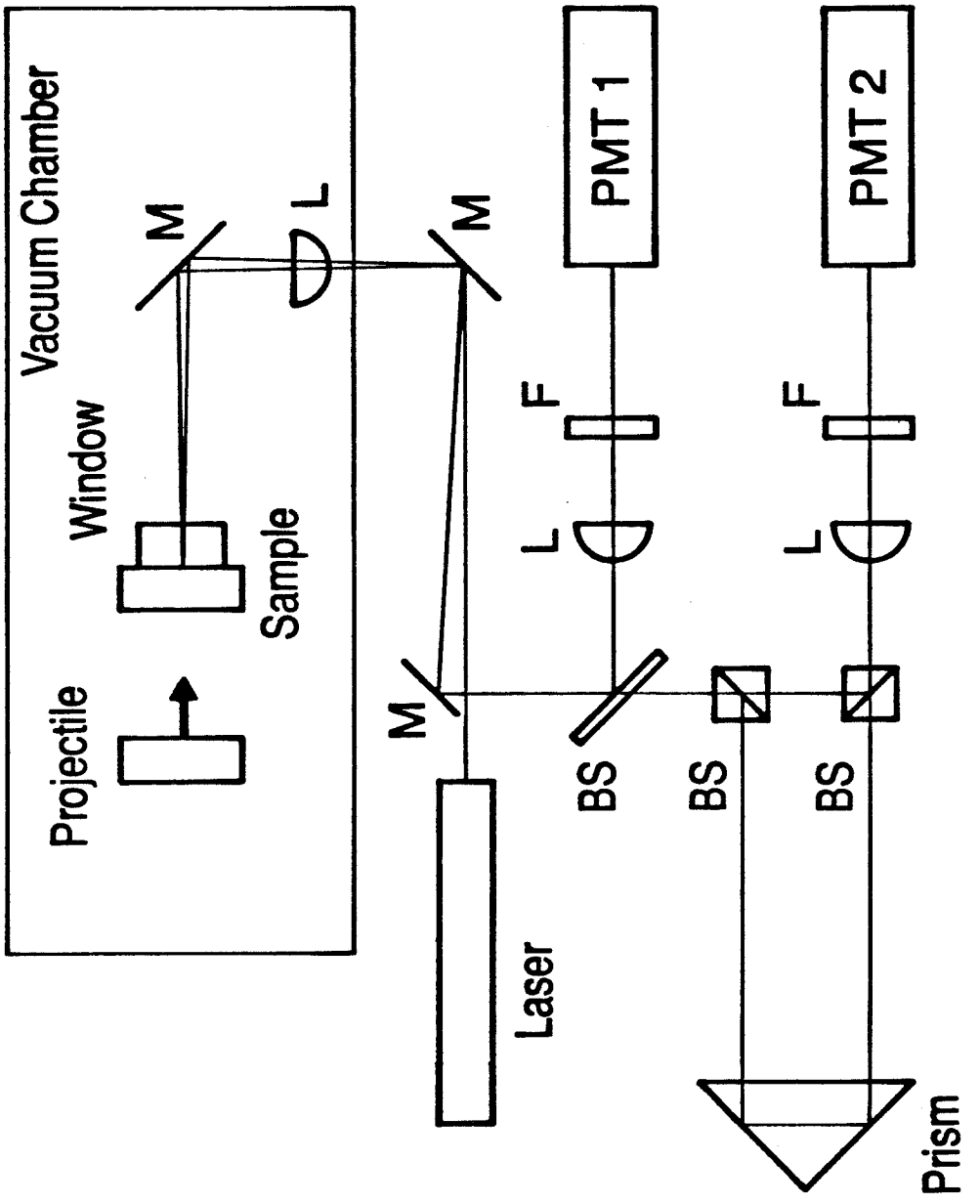
Vacuum Chamber
Window
Sample
Projectile
M
L
M
M
L
F
PMT 1
L
F
PMT 2
BS
BS
BS
Laser
Prism

The interferometer setup for the SVI is shown in Figure 1.1. Light from a 1.5 mW He-Ne laser (Spectra-Physics 117a) is focused onto a specularly reflecting sample surface. The returned light is separated from the incident light, and a portion of it is routed to a photomultiplier tube (pmt) (Burle 7764), which monitors the overall beam intensity. The remaining light strikes a second beam splitter, which directs a portion of it around a delay leg by means of a 60-mm right-angle prism (Rolyn Optics Co.). The light is recombined at a third beam splitter and directed to a second photomultiplier tube. The signals are recorded using analog oscilloscopes (Tektronix 485) and transient digitizers (Lecroy 8081). Interference is produced at the third beam splitter by combining two coherent beams that have been reflected at different times from the target surface. Changes in reflector velocity cause changes in the Doppler shifts of the recombined beams that create time-varying light-intensity fluctuations at the pmt, which are recorded as interference fringes. The primary limitation of this device is the requirement that the sample retain a mirror finish after passage of the shock wave. In the present study, SVI experiments were limited to pressures below 12 GPa.

Although more complex to construct, the VISAR is a more generally useful interferometer. A schematic of the VISAR setup is shown in Figure 1.2. In this device, a small time delay (1-2 ns) is introduced in one leg of the interferometer by means of fused silica cylinders, but the mirrors are positioned such that the distance along both paths appears to be the same from the point of view of the detector. This allows interference fringes to be formed with a diffuse (spatially incoherent) source. Light from a 3 Watt $Ar^+$ laser (Lexel 5000-3) is focused onto the target surface (Figure 1.2). The returned light is recollimated before passing through beam-shaping and polarization optics. The light is then split, delayed, and recombined at the beam splitter, generating interference fringes that are recorded using photomultipliers and digital oscilloscopes. The VISAR we have constructed is similar to that originally

described by *Barker and Hollenbach* [1972] except that it incorporates the push-pull modification and data reduction scheme of *Hemsing* [1979]. More details on interferometers for shock wave profile measurements are contained in Appendix A.

For both the VISAR and the SVI, the relationship between surface velocity and the number of interference fringes can be expressed as [*Barker,* 1968; *Barker and Hollenbach,* 1972]:

$$u(t - \tau/2) = kF(t), \tag{1.1}$$

where $u$ is the surface velocity, $t$ is time, $\tau$ is the variable delay time of the interferometer, $k$ is the fringe constant in velocity per fringe, and $F$ is number of fringes recorded. For the VISAR, the fringe constant $k$ is given by:

$$k = \frac{\lambda}{2\tau w_c e_c}, \tag{1.2}$$

where $\lambda$ is the laser wavelength, $\tau$ is the delay time of the interferometer which depends on the length of etalon material and its refractive index, $w_c$ is a correction term that accounts for the stress-induced change of refractive index in the shock-compressed window material, and $e_c$ is a correction term that accounts for dispersion in the fused silica etalons. The fringe constant, and hence the surface velocity, is constrained to within 1% when the uncertainties in Equation 1.2 are taken into account. The time resolution of our VISAR is estimated to be 2-3 ns.

### Target Assembly

Two types of target assemblies were used in the present experiments. These are illustrated in Figures 1.3 and 1.4. In the forward-impact geometry (Figure 1.3), the Fe-Cr-Ni alloy is placed in the target position and impacted with a polyurethane foam-backed flyer plate of PMMA, 304 steel, or tantalum. An array of 4-6 electrical shorting pins are used to trigger the recording instrumentation and to measure the tilt between the flyer and target at impact, which was typically a few milliradians. A transparent window of either Z-cut sapphire (Adolf Meller Co.) or lithium fluoride

Figure 1.2: Schematic diagram of VISAR setup. The VISAR was constructed on an optical table placed next to the tank of the 40-mm gun. The abbreviations are the same as for Figure 1. PBS refers to polarizing cube beam splitters, S refers to a quartz wedge polarization scrambler, P represents a Glan-Thompson polarizing prism, PZT is a piezoelectric translator attached to a mirror that is mounted in a precision angular-orientation device, and F is a a narrow bandwidth (1 nm) laser-line interference filter.

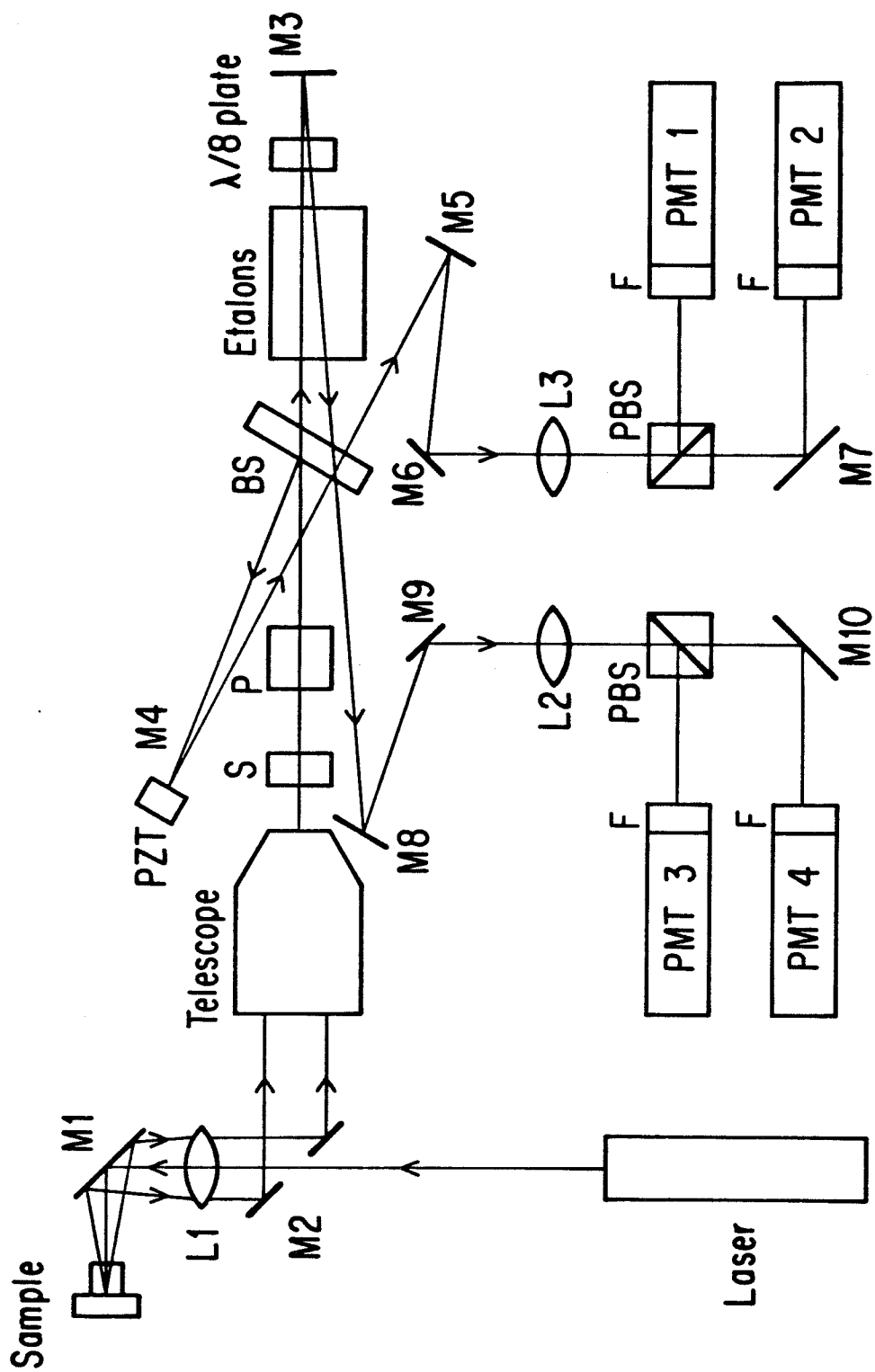
Sample
M1
L1
M2
Telescope
PZT
M4
S
P
M8
M9
L2
PBS
M10
F
PMT 3
F
PMT 4
Laser
BS
M6
L3
PBS
M7
F
PMT 1
F
PMT 2
Etalons
λ/8 plate
M3
M5

(LiF) (Solon Technologies, Inc.) is affixed to the rear surface of the target, using a $\sim$10 $\mu$ epoxy layer.

The purpose of the window is to attempt to match the impedance of the sample in order to obtain a wave profile as close as possible to that propagating through the interior of the sample. Sapphire provides an excellent impedance match to 304 stainless steel but was not used above 12 GPa because its yielding properties prevent its use as an interferometer window at higher stresses [*Barker and Hollenbach,* 1970]. LiF, which has been calibrated for use as a VISAR window to 115 GPa [*Wise and Chhabildas,* 1986], was used for the majority of the present experiments, although its impedance differs from steel by more than a factor of 2.

The main features of a forward-impact VISAR experiment are shown in the Lagrangian distance time diagram of Figure 1.5. Impact at zero time generates shock waves propagating into the flyer and sample, which, depending on stress level and material properties, could be preceded by an elastic precursor whose effects are neglected for the moment. Upon arriving at the interface between the flyer and its low-density foam backing, the shock wave reflects as a rarefaction fan [*Zel'dovich and Razier,* 1967], partially unloading the material from its high-pressure state. The rarefaction fan is shown as a set of characteristics representing initial elastic, plastic, and final unloading. When the flyer and sample are different materials, the characteristics will be bent when encountering the change in material properties at the flyer-sample interface. The shock traveling through the sample reaches the sample-window interface at time $t_1$ and is recorded by the VISAR. Because of the mechanical impedance mismatch at this interface, a rarefaction fan is generated, which propagates back into the sample, interacts with the oncoming rarefaction, and perturbs the unloading waveform observed at the sample-window interface beginning at time $t_2$.

The effect of this wave interaction is eliminated in the reverse-impact geometry illustrated in Figure 1.4. In this case, the material under study is mounted in the

Figure 1.3: Forward-impact arrangement for VISAR and SVI experiments. The experiments are carried out in an evacuated (100-mm Hg) chamber beyond the gun muzzle. The flyer plate is backed by a layer of rigid, low-density polyurethane foam. Electrical switches (pins) are placed around the periphery of the sample to provide tilt diagnostics and to trigger the oscilloscopes.

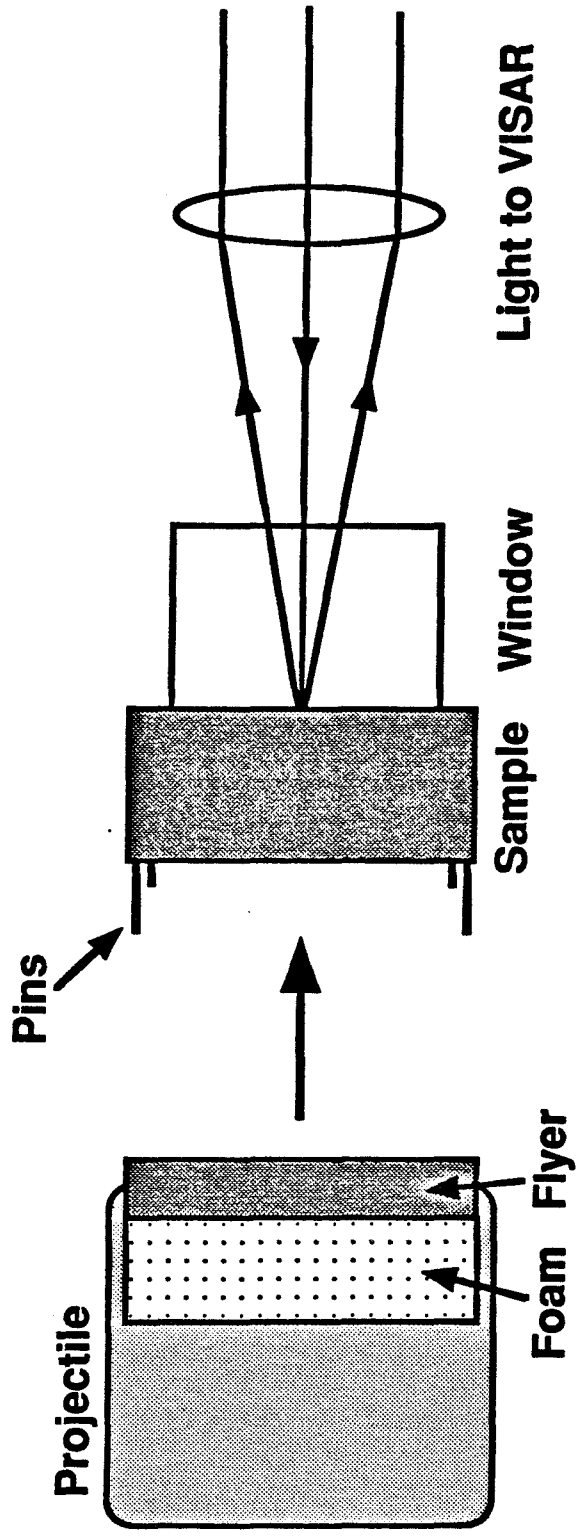
Light to VISAR
Window
Sample
Pins
Flyer
Foam
Projectile

Figure 1.4: Reverse-impact arrangement for VISAR experiments. See preceding figure for details.

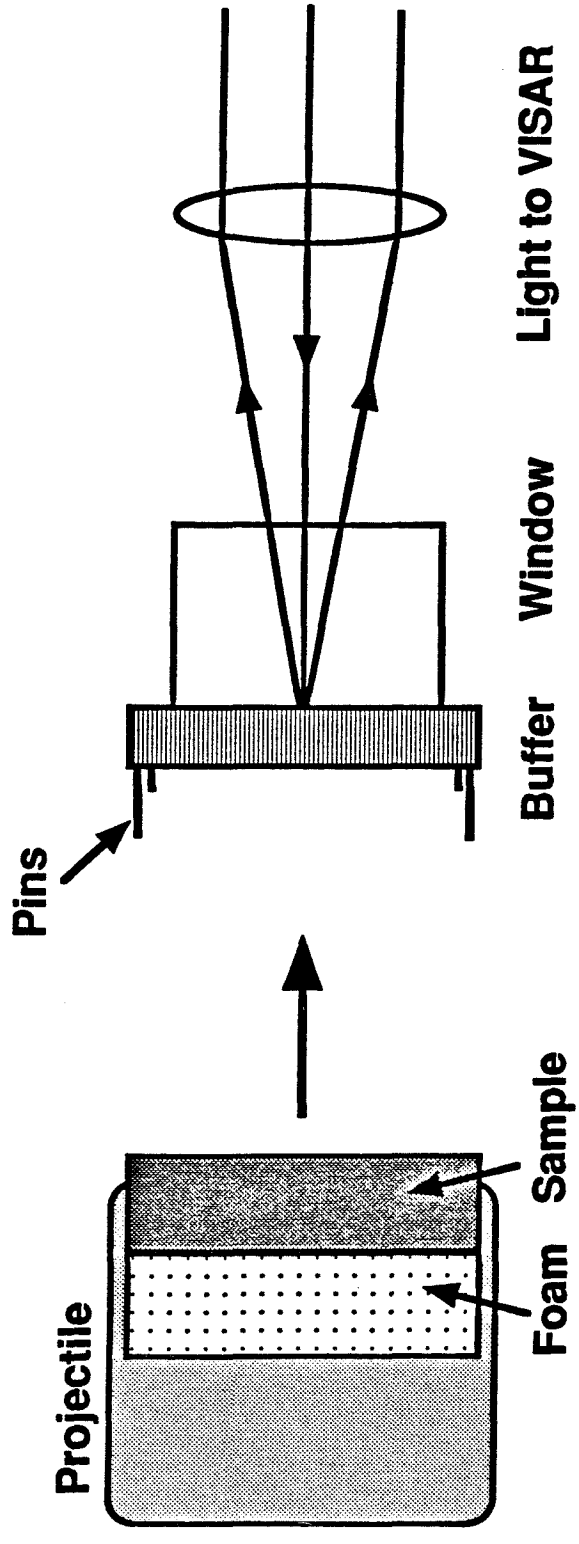
Light to VISAR
Window
Buffer
Pins
Sample
Foam
Projectile

Figure 1.5: Representative Lagrangian x-t diagram for forward-impact experiments (shot 809). $U_{Ss}$ and $U_{Sf}$ are the shock wave velocities in the sample and flyer, respectively. $V_{PLs}$ and $V_{PLf}$ are the Lagrangian velocities of initial release in the sample and flyer, respectively. $V_L^*$ is the sound speed in the interaction region ($h_2$) defined by the intersection of the forward and backward leading characteristics. $t_1$ is the arrival time of the plastic wave at the interface monitored by the VISAR. $t_2$ marks the onset of the unloading history at the interface.

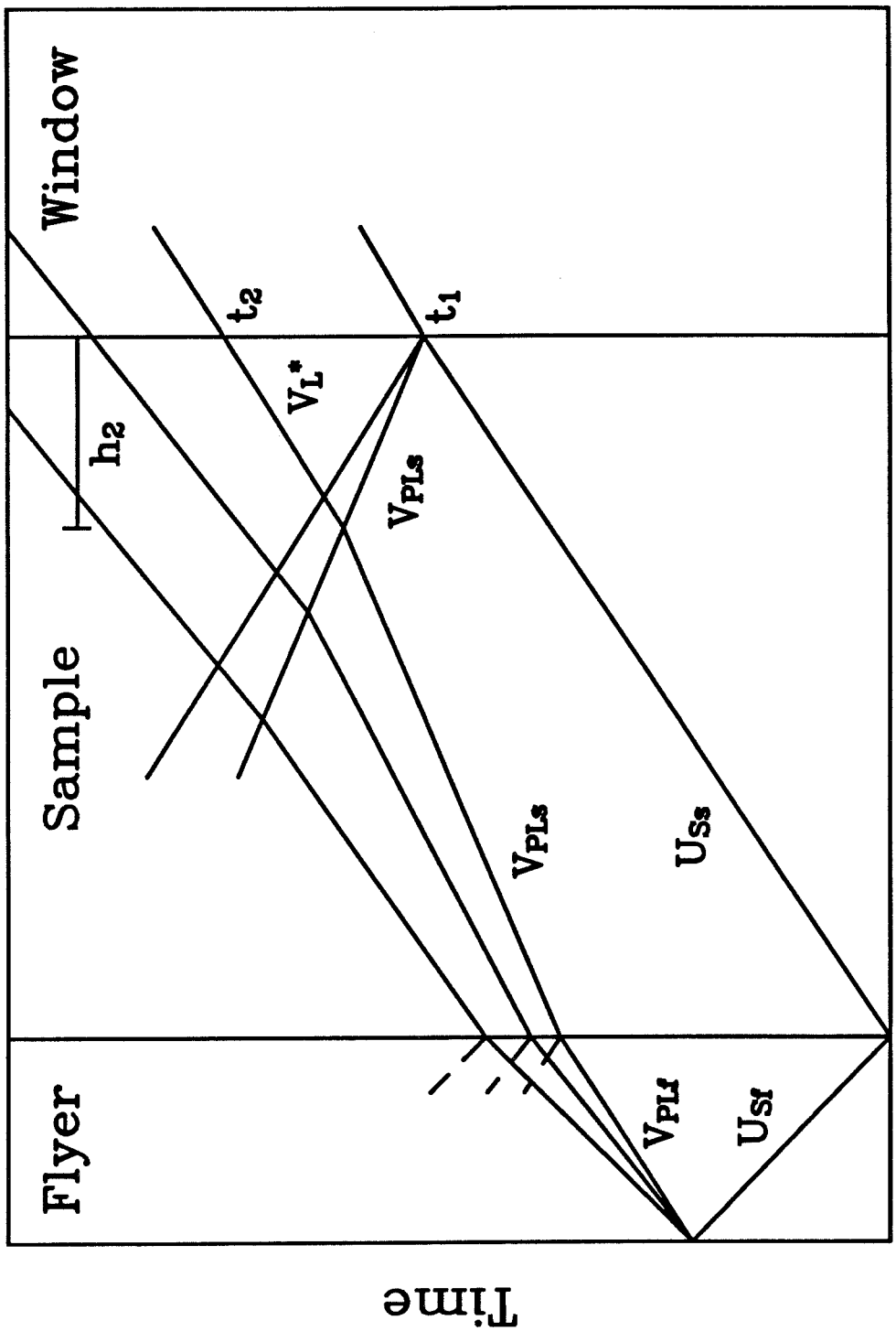
Time
Distance
Flyer
Sample
Window
$t_2$
$t_1$
$V_L^*$
$h_2$
$V_{PLs}$
$V_{PLs}$
$U_{Ss}$
$V_{PLf}$
$U_{Sf}$

projectile and used to impact a thin (1-2 mm) aluminum buffer with an LiF window epoxied to it. Again, shorting pins are used for triggering and tilt diagnostics and the buffer-window interface velocity history is monitored with the VISAR. The advantage of this technique can be seen with reference to Figure 1.6. Impact at t=0 produces compressive waves in both the buffer and sample. The arrival of the shock at the buffer-window interface produces only a small perturbation, as the impedances of aluminum and LiF differ by only about 5%. A weak rarefaction is propagated back through the buffer, which returns to the interface as a weak reshock at time $t_2$. The compressive-wave structure in the sample reflects off the sample-foam interface and a rarefaction fan propagates back through the sample and buffer as shown, with the first arrival reaching the interface at $t_3$. The distortion of the waveform is minimal in this geometry, making it a very desirable arrangement. However, the maximum pressure attainable is limited by the impedance of the aluminum buffer. In addition, no direct information on the compressive-wave structure in the sample is obtained in this method. The unloading history must also be corrected for the effect of the aluminum buffer.

In both experimental geometries, sample dimensions are chosen to maintain uniaxial strain conditions through the unloading of the specimen. The window thickness is chosen so that the shock arrives at the window free surface after the entire unloading history has been recorded. The experimental conditions for the forward-geometry SVI experiments and both the forward- and reverse-impact VISAR experiments are listed in Tables 1.3, 1.4, and 1.5.

## 1.3 Results

Interface particle velocity histories for the forward-impact VISAR experiments are presented in Figure 1.7 and for the reverse-impact experiments in Figure 1.8. The results of experiments 804 and 802 have been scaled by factors of 1.12 and 1.07,

Figure 1.6: Representative Lagrangian x-t diagram for reverse-impact experiments (shot 858). The subscript b refers to the buffer, and the subscript s refers to the sample. $V_{P0}$ is the elastic precursor velocity in the sample, which is taken to be equal to the zero-presure compressional sound velocity. $t_1$ is the arrival time of the plastic wave at the interface monitored by the VISAR. At $t_2$, a weak reverberation in the buffer is detected. $t_3$ marks the onset of the unloading history at the interface. Other symbols are the same as in the preceding Figure.

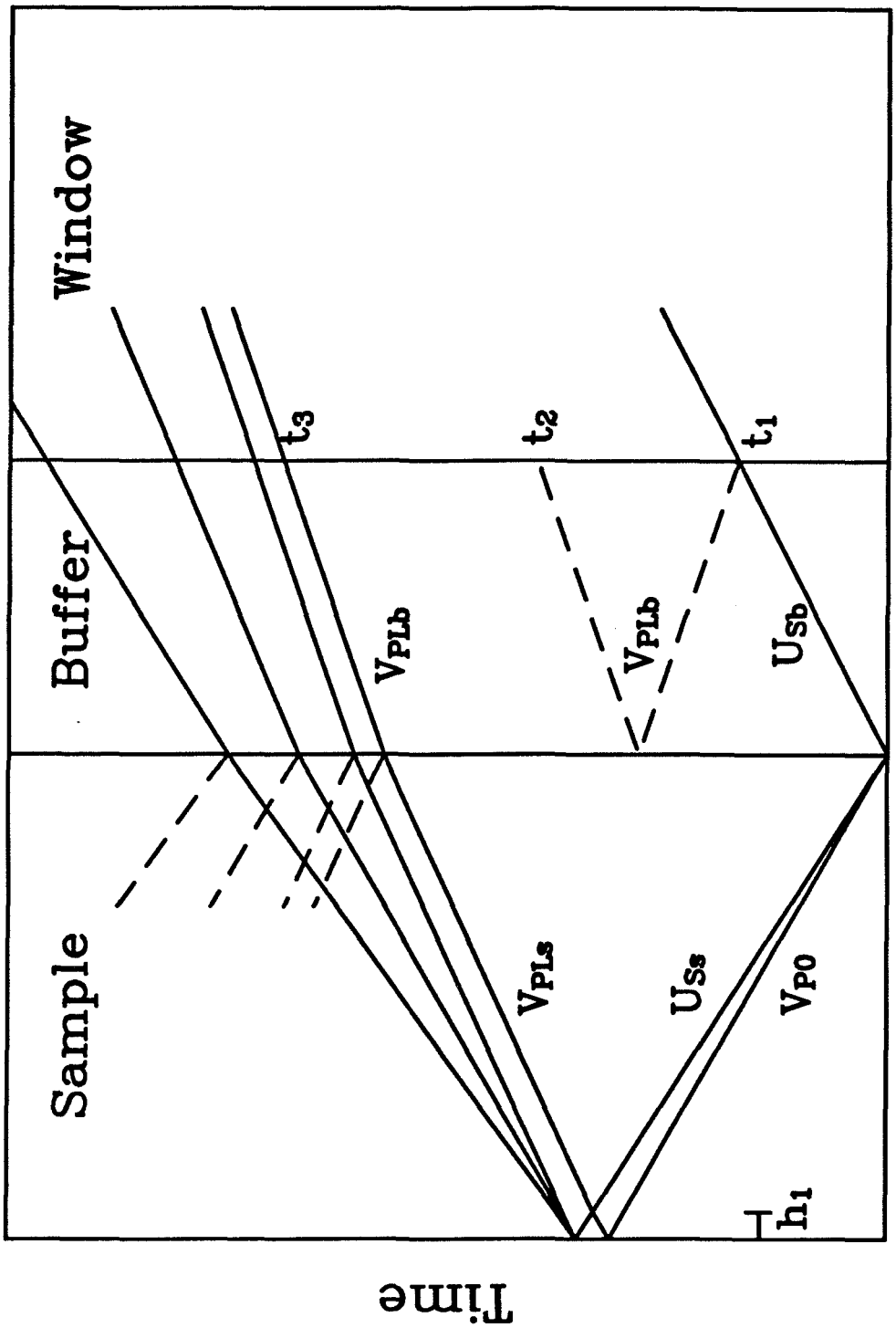
Window
Buffer
Sample
$t_3$
$t_2$
$t_1$
$V_{PLb}$
$V_{PLb}$
$U_{Sb}$
$V_{PLs}$
$U_{Ss}$
$V_{P0}$
$h_1$
Time
Distance

| Shot | Flyer material | Flyer thickness (mm) | Sample $\rho_o$ (g/cm$^3$) | Sample thickness (mm) | Window material | $u_{fp}$ (km/s) |
|---|---|---|---|---|---|---|
| 746 | PMMA | 0.993 | 7.857 | 2.004 | Sapphire | 1.62 |
| | | 0.002 | 0.016 | 0.004 | | 0.02 |
| 747 | PMMA | 0.983 | 7.838 | 2.075 | Sapphire | 1.37 |
| | | 0.006 | 0.012 | 0.003 | | 0.01 |
| 749 | PMMA | 1.575 | 7.857 | 6.429 | Sapphire | 1.79 |
| | | 0.006 | 0.008 | 0.004 | | 0.01 |
| 771 | PMMA | 2.159 | 7.820 | 6.300 | LiF | 2.15 |
| | | 0.003 | 0.009 | 0.004 | | 0.03 |

Table 1.3: Initial conditions for Fe-Cr-Ni specular velocity interferometer (SVI) experiments. $\rho_o$ is the initial density and $u_{fp}$ is the impact velocity. The numbers below each value are one standard deviation uncertainties.

| Shot | Flyer | | | Sample | | Window | | |
|---|---|---|---|---|---|---|---|---|
| | material | $\rho_o$ | thickness | $\rho_o$ | thickness | $\rho_o$ | thickness | $u_{fp}$ |
| | | ($g/cm^3$) | (mm) | ($g/cm^3$) | (mm) | ($g/cm^3$) | (mm) | (km/s) |
| 802 | ss304 | 7.875 | 2.613 | 7.878 | 6.299 | 2.63 | 7.953 | 1.15 |
| | | 0.012 | 0.005 | 0.006 | 0.004 | 0.01 | 0.002 | 0.02 |
| 804 | ss304 | 7.88 | 2.548 | 7.847 | 6.352 | 2.63 | 7.945 | 1.94 |
| | | 0.02 | 0.004 | 0.011 | 0.009 | 0.01 | 0.005 | 0.12 |
| 809 | Ta | 16.47 | 1.858 | 7.835 | 6.375 | 2.632 | 7.950 | 2.00 |
| | | 0.04 | 0.005 | 0.012 | 0.001 | 0.001 | 0.002 | 0.04 |
| 812 | Ta | 16.61 | 1.892 | 7.827 | 6.359 | 2.626 | 7.827 | 2.46 |
| | | 0.02 | 0.001 | 0.023 | 0.002 | 0.001 | 0.002 | 0.04 |
| 813 | ss304 | 7.882 | 2.027 | 7.867 | 6.415 | 2.625 | 7.831 | 1.19 |
| | | 0.02 | 0.004 | 0.006 | 0.002 | 0.005 | 0.001 | 0.02 |
| 847 | Ta | 16.57 | 1.891 | 7.891 | 6.335 | 2.630 | 8.128 | 2.45 |
| | | 0.03 | 0.003 | 0.006 | 0.003 | 0.002 | 0.007 | 0.03 |
| 862 | Ta | 16.55 | 2.275 | 7.893 | 6.326 | 2.632 | 8.150 | 2.52 |
| | | 0.03 | 0.003 | 0.006 | 0.004 | 0.002 | 0.004 | 0.04 |

Table 1.4: Initial conditions for Fe-Cr-Ni forward-impact VISAR experiments. The numbers below each line are one standard deviation uncertainties.

| Shot | Sample | | Buffer | | | Window | | $u_{fp}$ |
|---|---|---|---|---|---|---|---|---|
| | $\rho_o$ | thickness | material | $\rho_o$ | thickness | $\rho_o$ | thickness | |
| | ($g/cm^3$) | (mm) | | ($g/cm^3$) | (mm) | ($g/cm^3$) | (mm) | (km/s) |
| 820 | 7.887 | 3.192 | Al2024 | 2.720 | 0.809 | 2.625 | 11.930 | 1.95 |
| | 0.012 | 0.005 | | 0.020 | 0.002 | 0.010 | 0.002 | 0.03 |
| 849 | 7.855 | 3.189 | Al6061 | 2.682 | 1.970 | 2.631 | 12.118 | 2.31 |
| | 0.004 | 0.002 | | 0.004 | 0.001 | 0.002 | 0.004 | 0.04 |
| 858 | 7.871 | 3.192 | Al6061 | 2.681 | 1.938 | 2.630 | 12.121 | 1.29 |
| | 0.011 | 0.004 | | 0.004 | 0.003 | 0.002 | 0.004 | 0.02 |

Table 1.5: Initial conditions for reverse impact VISAR experiments.

respectively, to account for non-normal incidence of the laser beam for these two experiments and to bring them into accord with the impedance-match results discussed below.

The forward-impact experiments are characterized by a sharp shock arrival, followed by a flat-topped plateau region, and by broad, relatively featureless unloading. The shape of the wave profile changes little with increasing stress. The scalloping observed in the wave profile for experiment 812 is an artifact of data reduction that is due to severe changes in sample reflectivity for this experiment. The reverse-impact experiments show a slight dip in particle velocity in the plateau region because of the arrival of the reverberation through the aluminum buffer (time $t_2$ in Figure 1.6). The initial unloading point is more distinct in the reverse-impact experiments.

The measured impact velocity, together with EOS data (Table 1.2), can be used to determine the Hugoniot state through impedance matching [*Ahrens,* 1987]. By requiring the pressure to be continuous across the impact interface, the particle

Figure 1.7: Steel-LiF interface wave profiles for forward-impact experiments. Shot numbers are listed to the left of each wave profile. Dashed lines show the particle velocity expected on the basis of impedance-matching calculations. The vertical lines show the point of initial unloading. The times are arbitrary.

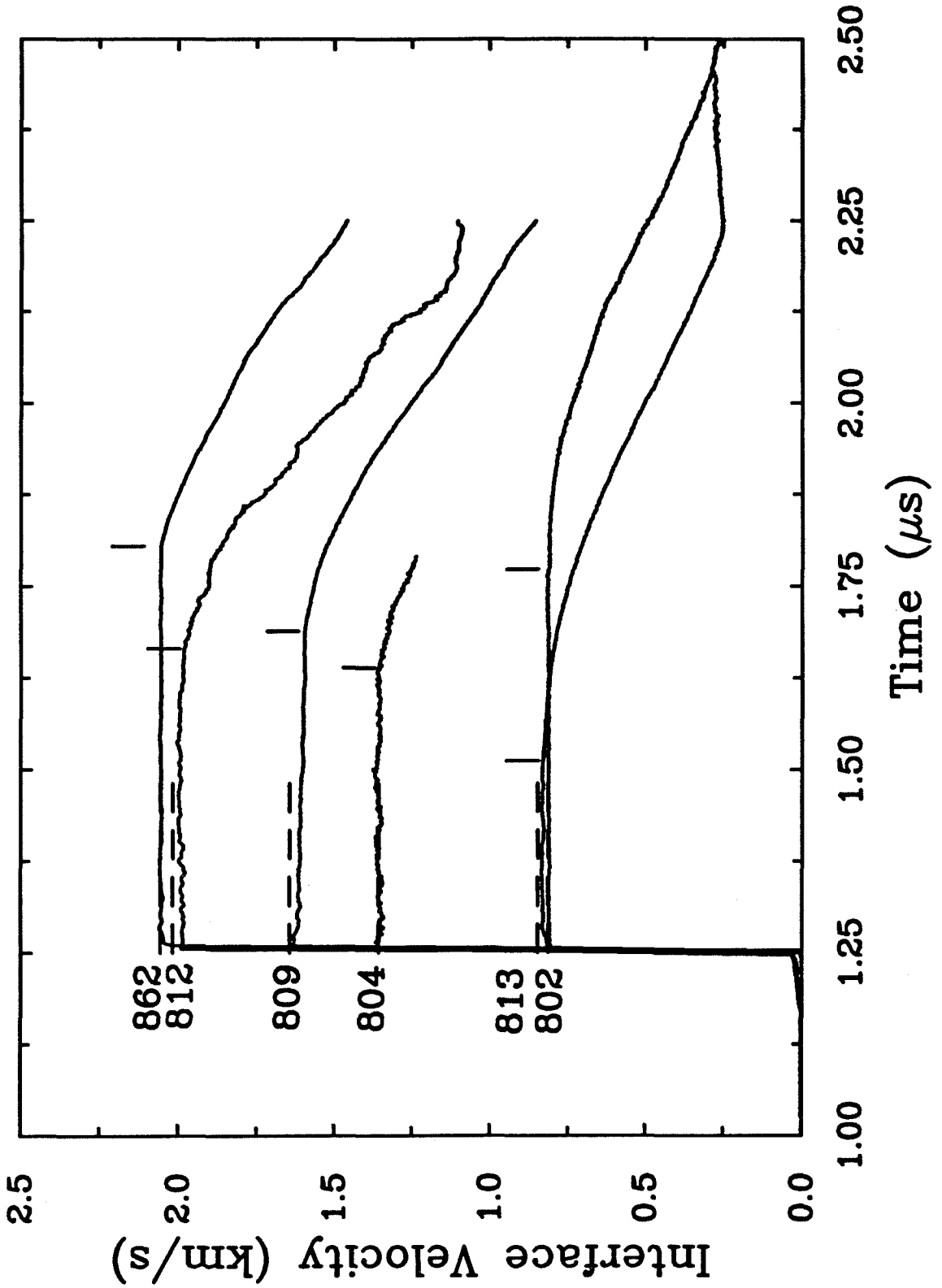
Interface Velocity (km/s)
2.5
2.0
1.5
1.0
0.5
0.0
1.00
1.25
1.50
1.75
2.00
2.25
2.50
Time (μs)
862
812
809
804
813
802

Figure 1.8: Aluminum-LiF interface wave profiles for reverse-impact experiments. Shot numbers are listed to the left of each wave profile. Dashed lines show the particle velocity expected on the basis of impedance-matching calculations. The vertical lines show the point of initial unloading. The times are arbitrary.

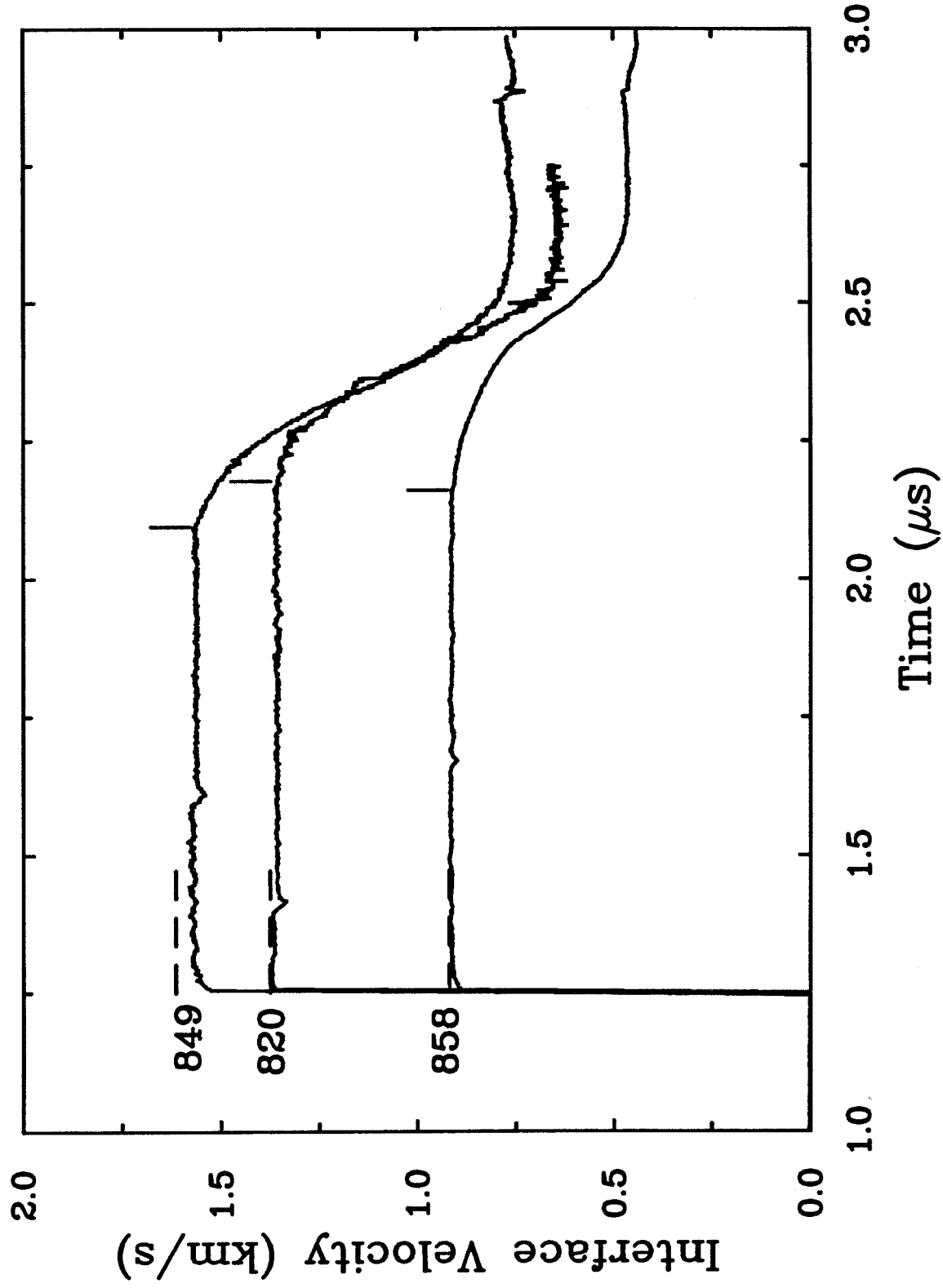
Interface Velocity (km/s)
2.0
1.5
1.0
0.5
0.0
1.0
1.5
2.0
2.5
3.0
Time (μs)
849
820
858

velocity, $u_p$, is constrained by the known pressure-particle velocity relations in the flyer and target. The shock velocity, $U_S$, is then determined from the material law:

$$U_S = c_o + su_p \tag{1.3}$$

In the case of reflection from a higher- or lower-impedance boundary, the release isentrope is approximated by using the Hugoniot itself, and the free-surface approximation is made [*Walsh et al.*, 1957]. The resulting Hugoniot states for the samples are listed in Tables 1.6 and 1.7 together with the calculated and measured particle velocities at the sample-window interface. In most cases, the calculated particle velocities agree with the VISAR measurements within their ~2% uncertainties. The measured particle velocities lie systematicly below the impedance-match calculations, however.

Unloading wave velocities were determined from the initial unloading points shown in Figures 1.7 and 1.8, using the analysis outlined below. For the SVI experiments, the initial unloading point was measured directly from the interferometer records, and the wave profiles were not analyzed in detail. For VISAR experiments 804 and 847, only the initial portions of the unloading history were recovered because of recording failures. These give well-defined initial unloading velocities but little additional information on the unloading characteristics.

For experiments using the reverse geometry, the following expression for the initial Lagrangian unloading velocity, $V_{PLs}$, can be obtained with reference to Figure 1.6.

$$V_{PLs} = \frac{x_s - h_1}{\Delta t + x_b/U_{Sb} - (x_s + h_1)/V_{Pos} - x_b/V_{PLb}}, \tag{1.4}$$

where $x_s$ and $x_b$ are the sample and buffer thicknesses, $U_{Sb}$ and $V_{PLb}$ are the shock and unloading wave velocities in the buffer, $\Delta t = t_3 - t_1$ is the time between the shock arrival at the reflector and the initial arrival of the unloading wave, $h_1$ is the thickness of the interaction region between the precursor and shock at the rear of

| Shot | Sample | | | | Sample/Window | |
|---|---|---|---|---|---|---|
| | $u_p$ (km/s) | $U_s$ (km/s) | $\rho$ (g/cm$^3$) | $P$ (GPa) | $u_{pc}$ (km/s) | $u_{pm}$ (km/s) |
| 746 | 0.209 | 4.891 | 8.208 | 8.1 | 0.192 | - |
| | 0.005 | 0.011 | 0.019 | 0.2 | 0.006 | |
| 747 | 0.170 | 4.834 | 8.119 | 6.5 | 0.156 | - |
| | 0.003 | 0.011 | 0.013 | 0.1 | 0.004 | |
| 749 | 0.239 | 4.936 | 8.257 | 9.3 | 0.221 | - |
| | 0.004 | 0.012 | 0.011 | 0.1 | 0.005 | |
| 771 | 0.288 | 5.010 | 8.298 | 11.3 | 0.412 | - |
| | 0.012 | 0.021 | 0.024 | 0.5 | 0.022 | |
| 802 | 0.575 | 5.437 | 8.810 | 24.6 | 0.814 | 0.758 |
| | 0.008 | 0.016 | 0.013 | 0.4 | 0.011 | |
| 804 | 0.970 | 6.025 | 9.385 | 46.0 | 1.357 | 1.220 |
| | 0.060 | 0.090 | 0.086 | 3.6 | 0.082 | |
| 809 | 1.183 | 6.342 | 9.630 | 58.7 | 1.644 | 1.611 |
| | 0.024 | 0.038 | 0.035 | 1.5 | 0.032 | |
| 812 | 1.458 | 6.753 | 9.983 | 77.1 | 2.017 | 1.991 |
| | 0.022 | 0.037 | 0.041 | 1.6 | 0.030 | |
| 813 | 0.597 | 5.470 | 8.831 | 25.7 | 0.847 | 0.831 |
| | 0.008 | 0.016 | 0.013 | 0.4 | 0.010 | |
| 847 | 1.447 | 6.736 | 10.050 | 76.9 | 2.005 | - |
| | 0.015 | 0.027 | 0.022 | 1.1 | 0.020 | |
| 862 | 1.485 | 6.793 | 10.102 | 79.6 | 2.056 | 2.054 |
| | 0.021 | 0.035 | 0.030 | 1.6 | 0.029 | |

Table 1.6: Forward-impact impedance-match solutions for Fe-Cr-Ni alloy.

| Shot | Sample | | | | Buffer | | | Buffer/Window | |
|---|---|---|---|---|---|---|---|---|---|
| | $u_p$ (km/s) | $U_s$ (km/s) | $P$ (GPa) | $\rho$ (g/cm$^3$) | $u_p$ (km/s) | $U_s$ (km/s) | $\rho$ (g/cm$^3$) | $u_{pc}$ (km/s) | $u_{pm}$ (km/s) |
| 820 | 0.604 | 5.477 | 26.1 | 8.863 | 1.344 | 7.132 | 3.519 | 1.376 | 1.370 |
| | 0.010 | 0.039 | 0.6 | 0.021 | 0.021 | 0.026 | 0.026 | 0.022 | |
| 849 | 0.718 | 5.649 | 31.8 | 8.998 | 1.558 | 7.474 | 3.406 | 1.615 | 1.570 |
| | 0.013 | 0.024 | 0.8 | 0.020 | 0.018 | 0.069 | 0.015 | 0.027 | |
| 858 | 0.390 | 5.160 | 15.8 | 8.514 | 0.900 | 6.554 | 3.108 | 0.919 | 0.914 |
| | 0.006 | 0.015 | 0.3 | 0.015 | 0.013 | 0.058 | 0.009 | 0.013 | |

Table 1.7: Reverse-impact impedance-match solutions. $u_{pc}$ is the calculated interface particle velocity, and $u_{pm}$ is the measured interface particle velocity.

the sample:

$$h_1 = x_s \left( \frac{V_{Pos} - U_{Ss}}{V_{Pos} + U_{Ss}} \right), \tag{1.5}$$

where $h_1 = 0$ if $U_{Ss} > V_{Pos}$. The elastic precursor velocity was taken to be 5.76 $\pm$ 0.02 km/s from the results of ultrasonic compressional velocity measurements [*Ledbetter et al.,* 1980]. The shock velocities in the flyer and sample are determined from impedance matching (Tables 1.6 and 1.7). The unloading velocity in the buffer is obtained from the reverberation arrival time:

$$V_{PLb} = \frac{2x_b}{t_2 - t_1}, \tag{1.6}$$

which makes use of the experimental observation that release waves and reshocks in aluminum travel with the same velocity [*Lipkin and Asay,* 1977]. In addition, the slight change in stress state (~3%) caused by the reverberation is neglected, and it is assumed that the material can support passage of multiple elastic waves. Elastic wave velocities in aluminum are fully discussed in the next chapter. Lagrangian and

| Shot | $\Delta t$ ($\mu$s) | $h_1$ (mm) | $V_{PLb}$ (km/s) | $V_{PLs}$ (km/s) | $V_{Ps}$ (km/s) |
|---|---|---|---|---|---|
| 820 | 0.927 | 0.083 | 11.08 | 7.78 | 6.92 |
| | 0.009 | 0.013 | - | 0.20 | 0.18 |
| 849 | 0.848 | 0.034 | 11.32 | 8.32 | 7.26 |
| | 0.004 | 0.009 | - | 0.14 | 0.12 |
| 858 | 0.910 | 0.178 | 9.62 | 7.17 | 6.63 |
| | 0.004 | 0.007 | - | 0.12 | 0.11 |

Table 1.8: Initial Lagrangian and Eulerian unloading wave velocities in Fe-Cr-Ni from reverse-impact experiments and the parameters used in obtaining them. A nominal $\pm 1.5\%$ uncertainty has been assumed for the buffer velocity.

Eulerian wave velocities are related through:

$$V_{PL} = \frac{\rho}{\rho_o} V_P, \tag{1.7}$$

The parameters used to solve Equation 1.4 and the resulting Lagrangian and Eulerian velocities are listed in Table 1.8. Layer thicknesses are listed in Table 1.5, and shock velocities and densities are listed in Table 1.7.

Interpretation of the forward-impact experiments is complicated by the wave interaction that occurs in the sample interior. In this case (Figure 1.5), the velocity is expressed as:

$$V_{PLs} = \frac{a - h_1 - h_2}{t_2 - h_2/V_L^* - \left(x_f + h_1\right)/U_{1f} - b}, \tag{1.8}$$

where $x_f$ is the flyer thickness, $U_{1f}$ is the velocity of the initial loading wave (shock or precursor) in the flyer, and $h_1$, is given by

$$h_1 = x_f \left( \frac{V_{0f} - U_{Sf}}{V_{0f} + U_{Sf}} \right), \tag{1.9}$$

and $h_1 = 0$ if $U_{Sf} \geq V_{0f}$. For symmetric impact (flyer material = sample material), a $= x_f + x_s$ and b = 0. For a non-symmetric impact, a $= x_s$ and b $= (x_f - h_1)/V_{PLf}$, where $V_{PLf}$ is the Lagrangian unloading velocity in the flyer. The arrival time $t_2$ is given by either

$$t_2 = \Delta t_{SR} + \frac{x_s}{U_{Ss}} \tag{1.10}$$

or

$$t_2 = \Delta t_{PR} + \frac{x_s}{V_{Pos}}, \tag{1.11}$$

where $\Delta t_{SR}$ is the time difference between the shock and release arrivals and $\Delta t_{PR}$ is the time difference between the elastic precursor and release arrivals.

The interaction region $h_2$ is defined by the point where the forward-traveling and backward-traveling rarefactions intersect:

$$h_2 = \frac{V_{PLs}}{2}\left[x_f\left(\frac{1}{V_{PLf}} + \frac{1}{U_{1f}}\right) + x_s\left(\frac{1}{V_{PLs}} - \frac{1}{U_{Ss}}\right) + h_1\left(\frac{1}{U_{1f}} - \frac{1}{V_{PLf}}\right)\right]. \tag{1.12}$$

The average velocity in the interaction region, $V_L^*$, was taken to be the bulk Lagrangian velocity at the interaction-region pressure. The bulk velocity is appropriate because of the large pressure change in the interaction region and the low yield strength of 304 steel. Estimates of the bulk wave velocity were obtained from Hugoniot slope calculations described below and agree with measured bulk velocities discussed below.

Equations 1.8 and 1.12 form a coupled set that are solved in an iterative manner. The parameters used in the solution together with the Eulerian and Lagrangian unloading velocities are listed in Table 1.9. The interaction region, $h_2$, typically extends about 1/4 of the distance into the sample for these experiments. Neglect of the interaction region would produce about a 5% decrease in the measured velocity on average. For the flyer plates, compressional unloading velocities were estimated by extrapolating trends based on available data for Ta [*Brown and Shaner,* 1984; *Asay et al.,* 1986] and PMMA [*Barker and Hollenbach,* 1970; *Schuler and Nunziato,*

1974] together with ambient-pressure ultrasonic data. For Ta, the following relationship between Eulerian unloading velocity (in km/s) and shock pressure (in GPa) was used [*Duffy and Ahrens,* 1992a]:

$$V_P = 1.4298 - 0.0263 \ln P + 0.0205 \ln^2 P. \tag{1.13}$$

In the case of PMMA, a quadratic relation between Lagrangian unloading velocity and the particle velocity was used:

$$V_{PL} = 2.86 + 4.04 u_p + 0.42 u_p^2. \tag{1.14}$$

Velocities obtained using the two types of experimental geometries are in good agreement, suggesting that our corrections for the interaction region are adequate. Velocities obtained using the SVI and the VISAR are also consistent with each other.

## 1.4 Discussion

### 1.4.1 Sound Velocities

For an elastic-plastic solid, the initial unloading velocity corresponds to the compressional sound velocity [*Zel'dovich and Razier,* 1967], while for a liquid it corresponds to the bulk velocity. The initial velocities we have measured lie significantly above expected bulk velocities, consistent with the expectation that Fe-Cr-Ni remains solid over the pressure range investigated. The measured Hugoniot compressional and bulk velocities are shown as a function of pressure in Figure 1.9 and listed in Table 1.10. Bulk wave velocities were obtained from detailed analysis of the unloading profiles discussed in Section 1.4.2. The measured velocities are also compared with third-order finite-strain extrapolations of ultrasonic data in the figure. The compressional and bulk velocities are in very good agreement with ultrasonic extrapolations throughout the pressure range of this study. The Hugoniot states become increasingly hotter than those along the isotherm. Temperature calculations indicate that

Table 1.9: Initial Lagrangian and Eulerian unloading wave velocities in Fe-Cr-Ni from forward-impact experiments and the parameters used in obtaining them. A nominal 0.1 km/s uncertainty has been assumed for the interaction-region velocity, $V_L^*$, and a 1% uncertainty has been assumed for the unloading wave velocities in Ta and PMMA.

| Shot | $t_2$ ($\mu$s) | $h_1$ (mm) | $h_2$ (mm) | $V_{PLf}$ (km/s) | $V_L^*$ (km/s) | $V_{PLs}$ (km/s) | $V_{Ps}$ (km/s) |
|---|---|---|---|---|---|---|---|
| 746 | 0.618 | - | - | 9.51 | - | 6.57 | 6.29 |
| | 0.015 | | | | | 0.31 | 0.30 |
| 747 | 0.660 | - | - | 8.48 | - | 6.44 | 6.22 |
| | 0.014 | | | | | 0.29 | 0.28 |
| 749 | 1.416 | - | - | 10.28 | - | 6.80 | 6.47 |
| | 0.015 | | | | | 0.10 | 0.10 |
| 771 | 1.524 | - | - | 11.53 | 5.1 | 6.77 | 6.38 |
| | 0.015 | | | | | 0.12 | 0.12 |
| 802 | 1.691 | 0.078 | 1.717 | - | 5.5 | 7.80 | 6.98 |
| | 0.006 | 0.006 | 0.008 | | | 0.09 | 0.08 |
| 804 | 1.448 | - | 1.486 | - | 6.3 | 9.54 | 7.85 |
| | 0.017 | | 0.081 | | | 0.30 | 0.26 |
| 809 | 1.437 | - | 1.730 | 6.49 | 6.7 | 9.95 | 8.10 |
| | 0.008 | | 0.037 | | | 0.25 | 0.20 |
| 812 | 1.350 | - | 1.792 | 7.11 | 7.3 | 10.81 | 8.35 |
| | 0.008 | | 0.037 | | | 0.28 | 0.23 |
| 813 | 1.459 | 0.054 | 0.943 | - | 5.6 | 8.02 | 7.13 |
| | 0.006 | 0.005 | 0.029 | | | 0.08 | 0.07 |
| 847 | 1.354 | - | 1.778 | 7.02 | 7.2 | 10.65 | 8.36 |
| | 0.006 | | 0.040 | | | 0.22 | 0.17 |
| 862 | 1.489 | - | 2.471 | 7.11 | 7.3 | 11.33 | 8.86 |
| | 0.005 | | 0.038 | | | 0.27 | 0.21 |

the Hugoniot temperature at 80 GPa is 854°C [*McQueen et al.*, 1970]. To estimate the thermal effect on sound velocities we have followed the method outlined in *Duffy and Ahrens* [1992a]. The temperature coefficients of compressional and bulk velocity are given by:

$$\left(\frac{\partial V_P}{\partial T}\right)_P = \frac{V_P}{2}\left((\partial C_L/\partial T)_P/C_L + \alpha\right), \tag{1.15}$$

$$\left(\frac{\partial V_B}{\partial T}\right)_P = \frac{V_B}{2}\left((\partial K_S/\partial T)_P/K_S + \alpha\right), \tag{1.16}$$

where $T$ is the temperature, $C_L = K_S + 4G/3$ is the longitudinal modulus, $K_S$ is the bulk modulus, $G$ is the shear modulus, and $\alpha$ is the thermal expansivity. We assume that the temperature coefficients of the elastic moduli as well as the product $\alpha K_s$ are constant with pressure. *Duffy and Ahrens* [1992a] have shown that these assumptions provide an upper bound to the inferred thermal effects along the Hugoniot for Al, Cu, Ta, and $Mg_2SiO_4$. They also describe the pressure variation of $(\partial V_P/\partial T)_P$ in Mo as discussed in Chapter 4. The temperature coefficient of the elastic moduli for 304 steel were taken from *Ledbetter et al.* [1975]. From Eqns. (1.15) and (1.16) we find that $(\partial V_P/\partial T)_P$ increases from -7 x $10^{-4}$ km/s/K at ambient pressure to -3.5 x $10^{-4}$ km/s/K at 80 GPa, while $(\partial V_B/\partial T)_P$ increases from -2.64 x $10^{-4}$ to -1.21 x $10^{-4}$ km/s/K over the same pressure range. The resultant thermal corrections to the 300 K velocities are shown in the figure. The measured Hugoniot velocities lie above the calculated values, suggesting that thermal effects may be smaller than those inferred here.

There are several other potential reasons as to why the Hugoniot velocities show little difference from the 300 K isotherm trends. First, errors in the ultrasonic pressure derivatives or higher-order pressure effects may be biasing the extrapolated isotherm velocities. Second, as discussed above, specimens of shock-recovered 304 steel show complex deformation histories with a martensitic $\gamma$-$\alpha'$ transformation occurring along twins. The amount of martensite formed depends strongly on sam-

| Shot | Pressure (GPa) | $V_P$ (km/s) | $V_B$ (km/s) | $\rho\gamma$ (g/cm$^3$) | $\nu$ |
|---|---|---|---|---|---|
| 747 | 6.5 | 6.22 (0.28) | - | - | 0.30 (0.04) |
| 746 | 8.0 | 6.29 (0.30) | - | - | 0.30 (0.04) |
| 749 | 9.3 | 6.47 (0.10) | - | - | 0.29 (0.01) |
| 771 | 11.3 | 6.50 (0.13) | - | - | 0.30 (0.02) |
| 858 | 15.8 | 6.63 (0.11) | - | - | 0.31 (0.01) |
| 802 | 24.6 | 6.98 (0.08) | 5.79 (0.17) | -15 (33) | 0.33 (0.01) |
| 813 | 25.7 | 7.13 (0.07) | 5.66 (0.17) | 14 (31) | 0.31 (0.01) |
| 820 | 26.1 | 6.92 (0.18) | - | - | 0.34 (0.02) |
| 849 | 31.8 | 7.27 (0.12) | - | - | 0.32 (0.02) |
| 804 | 46.0 | 7.85 (0.26) | - | - | 0.31 (0.03) |
| 809 | 58.7 | 8.10 (0.20) | 6.52 (0.20) | 16 (12) | 0.32 (0.02) |
| 847 | 76.9 | 8.36 (0.17) | - | - | 0.35 (0.02) |
| 812 | 77.1 | 8.35 (0.23) | 6.93 (0.35) | 16 (14) | 0.35 (0.03) |
| 862 | 79.6 | 8.86 (0.21) | 6.89 (0.21) | 22 (8) | 0.30 (0.02) |

Table 1.10: Measured sound velocities in Fe-Cr-Ni alloy under Hugoniot conditions. Poisson's ratio was calculated using bulk velocities from Eqn. 1.17 and $\rho\gamma$ =17.

Figure 1.9: Compressional ($V_P$) and bulk ($V_B$) wave velocities determined from experiments on Fe-Cr-Ni alloy. Experimental uncertainties are 1-3%. Also shown are bulk and compressional velocities estimated from the Hugoniot, using the assumptions that $\rho\gamma$ and Poisson's ratio are constant (dashed lines). The solid curves are third-order finite-strain extrapolations of 1 GPa ultrasonic data [*Gerlich and Hart,* 1984]. The dotted curves have been corrected for thermal differences between the Hugoniot and the isotherm, using the method outlined in the text. The numbers in parentheses near the top are estimated shock temperatures in K at 20 GPa intervals [*McQueen et al.,* 1970].

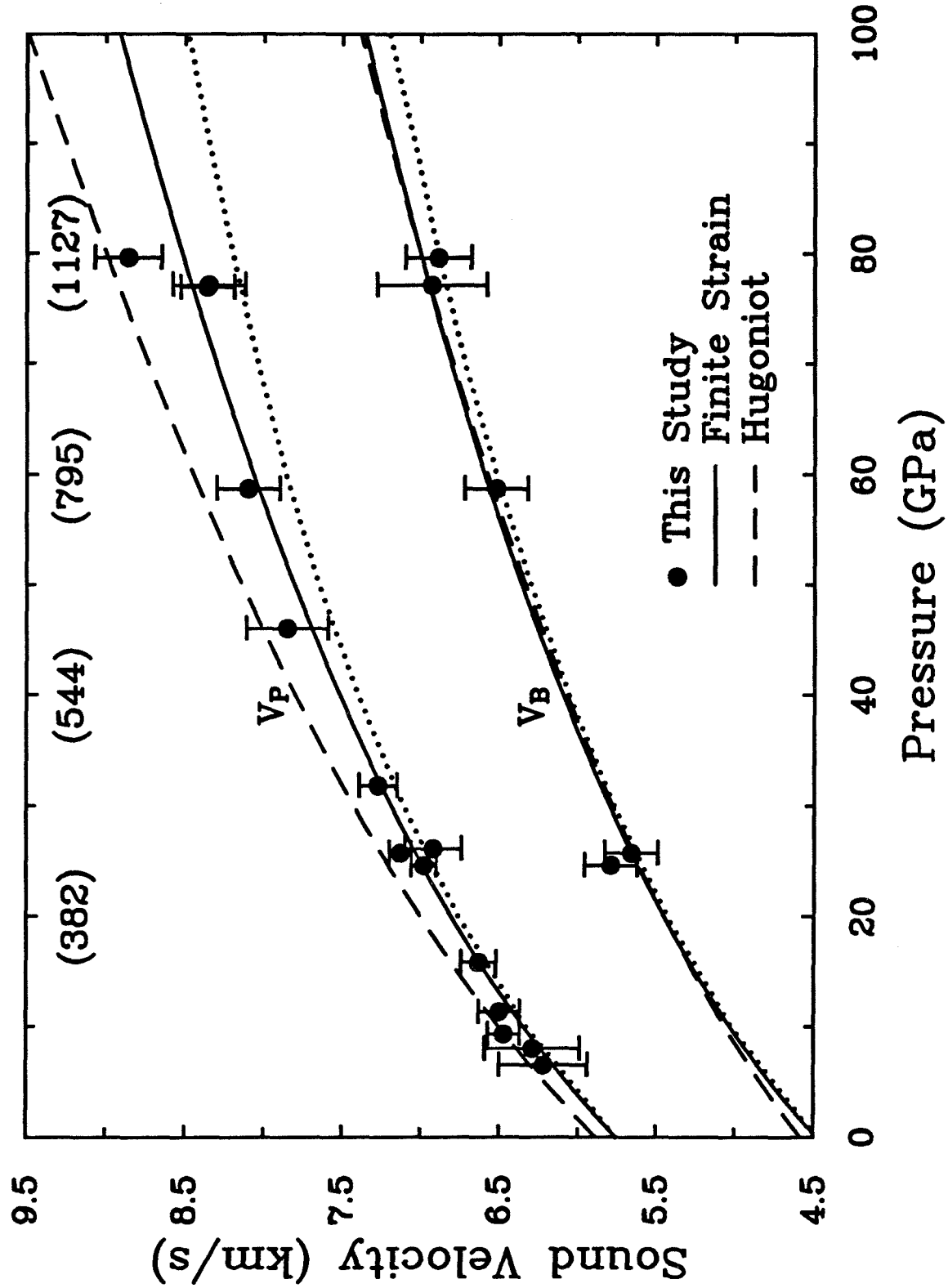
Sound Velocity (km/s)
9.5
8.5
7.5
6.5
5.5
4.5
0
20
40
60
80
100
Pressure (GPa)
(382)
(544)
(795)
(1127)
$V_P$
$V_B$
This Study
Finite Strain
Hugoniot

ple history, strain, and pulse duration. For short pulse durations (<2 $\mu$s), maximum amounts of martensite are less than 10 vol.%. The martensite fraction increases with shock pressure, reaching a maximum around 30-60 GPa and thereafter decreases because of shock-heating effects. Hardness and twin volume also reach maxima at similar pressures. While martensite production produces no clear effects on the equation of state, it could be responsible for slightly elevated sound velocities. The discrepancy between Hugoniot measurements and the thermally corrected isotherm is greatest between 45-60 GPa, where martensite fraction is at a maximum.

Finally, an incorrect value for velocity in the interaction region or an incorrect velocity for the ancillary materials (buffer or flyer) could produce a systematic error in the measured velocities for steel. However, the general agreement obtained using different experimental geometries argues against this possibility.

The hydrodynamic sound velocity along the Hugoniot can be obtained by relating the initial slope of the release adiabat to the Hugoniot through the Mie-Grüneisen Equation [*McQueen et al.*, 1967]. This can be expressed as:

$$V_B = \sqrt{\frac{K_S}{\rho}} = \left\{ \left(\frac{\partial P}{\partial \rho}\right)_H \left[1 - \left(\frac{1}{\rho_o} - \frac{1}{\rho}\right)\frac{\rho\gamma}{2}\right] + \frac{P_H \gamma}{2\rho} \right\}^{\frac{1}{2}}, \qquad (1.17)$$

where $V_B$ is the bulk sound, $(\partial P/\partial \rho)_H$ is the local Hugoniot slope, $P_H$ is the Hugoniot pressure, and $\gamma$ is the Grüneisen constant. Bulk sound velocities calculated in this manner for 304 steel are shown in Figure 1.9, where the assumption has been made that $\gamma\rho$ is constant. The measured bulk sound velocities are consistent with the calculated Hugoniot trends. Also shown in the figure is the compressional velocity calculated by making the additional assumption that Poisson's ratio is a constant function of pressure. That this assumption overpredicts the trend of the data implies that Poisson's ratio is an increasing function of compression. The variation of Poisson's ratio along the Hugoniot to 80 GPa is given by (Table 1.10):

$$\nu = 0.29(0.01) + 8(2) \text{ x } 10^{-4} P \qquad (1.18)$$

Measured bulk sound velocities can, in conjunction with the equation of state, be used to solve Equation 1.17 for the product $\rho\gamma$. The results of this calculation are given in Table 1.10. The uncertainties are quite large, particularly at low pressure, and illustrate that a substantial range of Grüneisen parameters can fit the present data. For comparison, $\rho_o\gamma_o = 17$ at ambient pressure for 304 steel [*McQueen et al.*, 1970].

In order to extract elastic coefficients from the data of Figure 1.9, we adopt the normalized representation of the finite-strain equations as originally applied to compression data [*Birch, 1978*]. The fourth-order finite-strain equation for $V_P$ can be written in terms of Eulerian strain, f, and a normalized elastic modulus, $M_L$, as [*Duffy and Ahrens,* 1992b]:

$$M_L = a_{L0} + a_{L1}f + a_{L2}f^2, \tag{1.19}$$

$$M_K = a_{K0} + a_{K1}f + a_{K2}f^2, \tag{1.20}$$

where

$$f = \frac{1}{2}\left[\left(\frac{\rho}{\rho_o}\right)^{2/3} - 1\right] \tag{1.21}$$

and

$$M_L = \frac{\rho V_P^2}{(1+2f)^{5/2}}, \tag{1.22}$$

$$M_K = \frac{\rho V_B^2}{(1+2f)^{5/2}}, \tag{1.23}$$

and the coefficients are:

$$a_{L0} = C_{Lo} \tag{1.24}$$

$$a_{L1} = 3K_{oS}C'_{Lo} - 5C_{Lo} \tag{1.25}$$

$$a_{L2} = \frac{9}{2}\left[K_{oS}^2\left(C''_{Lo} + (K'_{oS} - 4)\frac{C'_{Lo}}{K_{oS}}\right) + \frac{35C_{Lo}}{9}\right] \tag{1.26}$$

$$a_{K0} = K_{oS} \tag{1.27}$$

$$a_{K1} = 3K_{oS}K'_{oS} - 5K_{oS} \tag{1.28}$$

$$a_{K2} = \frac{9}{2}\left[K_{oS}^2\left(K_{oS}'' + (K_{oS}' - 4)\frac{K_{oS}'}{K_{oS}}\right) + \frac{35K_{oS}}{9}\right], \tag{1.29}$$

where $C_{Lo}$ is the longitudinal modulus, $K_{os}$ is the adiabatic bulk modulus, and $G_o$ is the shear modulus. The subscript $o$ represents ambient-pressure quantities and single and double primes represent first and second pressure derivatives, respectively. In Figure 1.10, the Hugoniot data for steel 304 are plotted in the $M_L$-f representation. A weighted, quadratic least-squares fit to the Hugoniot data and the ambient-pressure elastic moduli yield the elastic coefficients along the Hugoniot (Table 1.11). The first pressure derivatives along the Hugoniot are comparable to 1 GPa ultrasonic data over the 5-80 GPa pressure interval. In addition, we are able to resolve second pressure derivatives for this material (Table 1.11). In order to assess thermal effects, constant-pressure thermal corrections were made using the pressure-dependent values of $\alpha$, $(\partial V_P/\partial T)_P$, and $(\partial V_B/\partial T)_P$ dciscussed previously. The corrected values are indicated in the figure. Corrections tend to parallel the trend of the uncorrected data, so the elastic properties for the thermally corrected data differ only slightly.

### 1.4.2 Constitutive Model

As seen in Figure 1.7, the elastic precursor was recorded in two experiments (802 and 813). The precursor manifests itself not as a sharp jump, but as a ramp increase in velocity with a distinct shoulder. The magnitude of the Hugoniot elastic limit (HEL) was determined from the measured particle velocity of the elastic wave at the shoulder, using:

$$\sigma_{HEL} = \frac{(Z_s + Z_w)\, u_{pm}}{2}, \tag{1.30}$$

where $\sigma_{HEL}$ is the elastic limit stress, $u_{pm}$ is the measured interface particle velocity, and $Z_s$ and $Z_w$ are the impedances of the sample and window given by the product of density and elastic sound velocity. The measured particle velocities were 0.011 $\pm$ 0.05 km/s, and the corresponding HEL stress was 0.35 $\pm$ 0.12 GPa. The yield stress

| Modulus | Hugoniot | Ultrasonics |
|---|---|---|
| $C_{Lo}$ (GPa) | 262 (2) | 261.3 |
| $K_o$ (GPa) | 158 (1) | 158.2 |
| $G_o$ (GPa) | 78 (2) | 77.4 |
| $C'_{Lo}$ | 7.9 (0.5) | 7.90 |
| $K'_o$ | 6.4 (1.0) | 5.57 |
| $G'_o$ | 1.1 (0.8) | 1.75 |
| $C''_{Lo}$ ($GPa^{-1}$) | -0.16 (0.06) | - |
| $K''_o$ ($GPa^{-1}$) | -0.17 (0.08) | - |
| $G''_o$ ($GPa^{-1}$) | 0.0 (0.08) | - |

Table 1.11: Comparison of elastic properties of Fe-Cr-Ni alloy under Hugoniot conditions (5-80 GPa) with ultrasonic measurements (0-1 GPa). Numbers in parentheses are one standard deviation uncertainties. The ultrasonic data is from *Gerlich and Hart* [1984].

Figure 1.10: Normalized longitudinal ($M_L$) and bulk ($M_K$) moduli along the Hugoniot as a function of Eulerian strain, f. Error bars represent Hugoniot data points. Values corrected to a 300 K isotherm at constant pressure are shown as solid circles. Solid squares are ambient-pressure values from ultrasonic measurements. The curves are fourth-order fits to the combined Hugoniot data and ambient-pressure ultrasonic data.

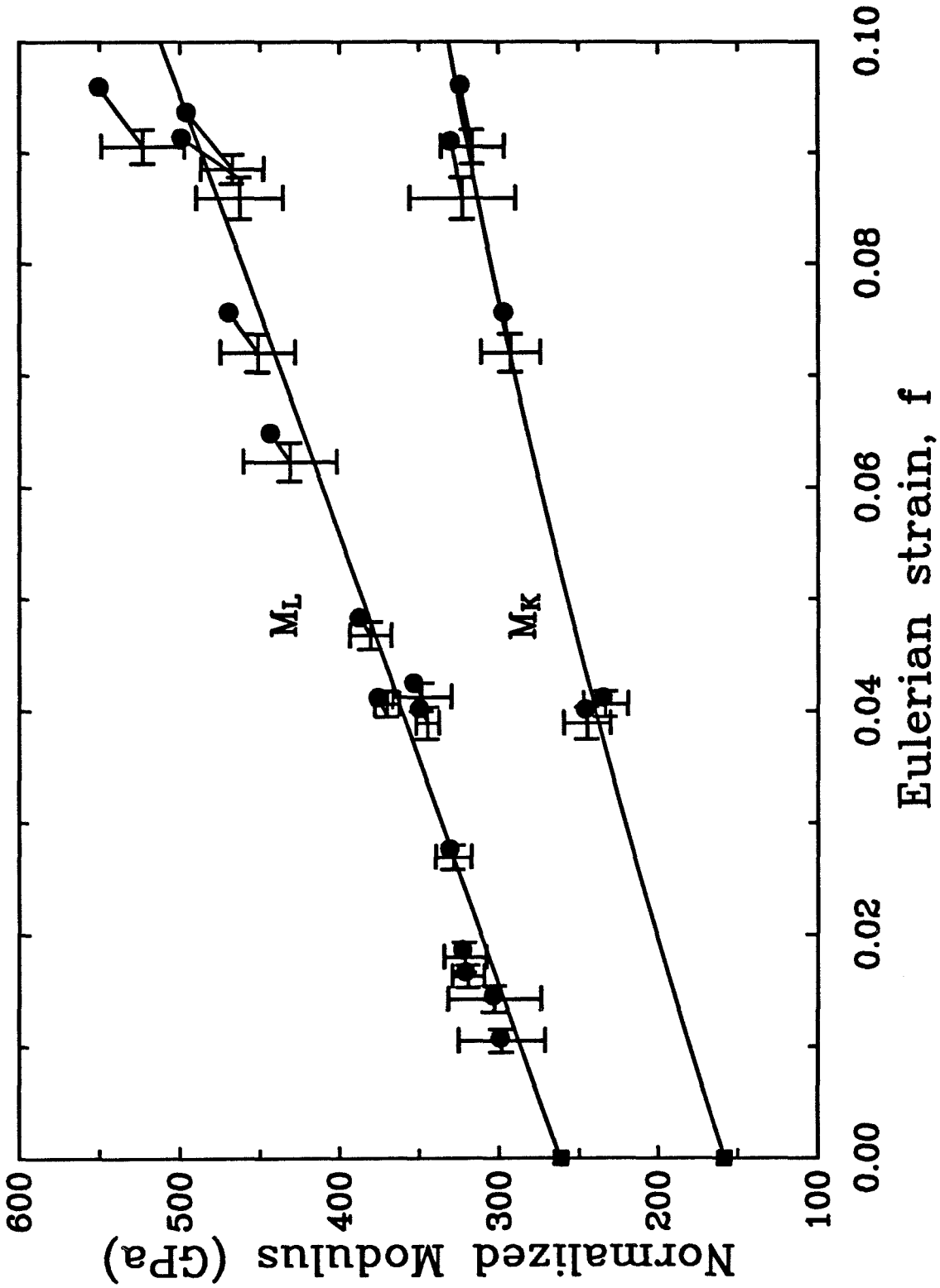
Normalized Modulus (GPa)
600
500
400
300
200
100
0.00
0.02
0.04
0.06
0.08
0.10
Eulerian strain, f
$M_L$
$M_K$

$Y_o$ can be obtained from:

$$Y_o = \frac{(1-2\nu)}{(1-\nu)}\sigma_{HEL}, \tag{1.31}$$

where $\nu$ is Poisson's ratio. The value of $Y_o$ obtained from these experiments is 0.21 $\pm$ 0.07 GPa, which is consistent with values of 0.2 and 0.34 GPa reported previously using other techniques [*Jones and Graham,* 1971; *Morris,* 1982].

The velocity of the elastic precursor was calculated to be 5.72 $\pm$ 0.1 km/s and 5.76 $\pm$ 0.1 km/s for the two experiments. This was determined by using the measured time difference between the precursor shoulder and the shock arrival, together with the shock velocity determined from the impedance-match solution. This is in excellent agreement with the ultrasonic value of 5.76 $\pm$ 0.03 km/s discussed above.

In order to better understand the measured wave profiles, numerical simulations were carried out using the one-dimensional Lagrangian finite difference wavecode WONDY [*Kipp and Lawrence,* 1982]. This wavecode solves equations for conservation of mass, momentum, and energy together with a constitutive law. Relevant geometric- and material-property data are input for each material layer in a particular experiment. A full description of the code including the governing equations for the constitutive laws is given in Chapter 3.

The simplest material law for solids that retain their strength is the elastic-perfectly plastic (EPP) model. In this model, the material behaves elastically until it yields at a stress of $2/3Y_o$ after which it flows irreversibly, maintaining a constant offset from the hydrostat. Upon unloading, the material again behaves elastically until it reaches a stress of $2/3Y_o$ below the Hugoniot, after which further decompression is plastic and also parallels the hydrostat.

Wavecode simulations of the experimental particle velocity histories were first performed by treating each material layer as EPP except for the foam layer for which the foam model of [*Grady and Furnish* 1988] was used. The material parameters required are the density, Hugoniot EOS parameters, Grüneisen constant, Poisson's ratio, and

the yield stress (Table 1.2). Figure 1.11 compares a representative measured particle velocity history with a simulation using the EPP model. The difference in peak velocity level is within the combined uncertainties of the flyer plate velocity and the VISAR measurement. The experimental data show significant deviations from the EPP model. Specifically, no sharp transition from elastic to plastic behavior is evident, but there is rather a gradual transition. This type of deviation is seen in wave profile data for other metals such as aluminum [*Lawrence and Asay,* 1979; *Steinberg et al.,* 1980] and can be attributed to the Bauschinger effect.

In an attempt to obtain a better description of the high-strain-rate dynamic response of 304 steel, we broadened our constitutive model to include the possibility for both a Bauschinger effect and strain rate dependent stress relaxation. The Bauschinger effect, or anisotropic strain hardening, is a consequence of the micromechanics of the deformation process and can be described as a hysteresis in the stress-strain curve. The yield stress upon loading and unloading differs and the clear distinction between elastic and plastic behavior is blurred by this effect. The Bauschinger effect is implemented into the code using a multi-element kinematic model which requires a set of normalized weighting factors, $a_i$ and a set of elemental yield stresses $Y_i$ [*Hermann,* 1974]. A more complete description of this effect, including a representative stress-strain diagram, is included in Chapter 3.

The possibility for strain-rate dependent stress relaxation was also included in the model. In this phenomenon, the deviatoric stresses temporarily exceed their equilibrium value and relax back to steady state at a rate controlled by a time constant. The viscoplastic response is incorporated into the wavecode using a Maxwellian relaxation function, $g$, of the form:

$$g = \frac{\sigma' - \sigma'_{eq}}{G\tau}, \tag{1.32}$$

where $\sigma'$ is the stress deviator, $\sigma'_{eq}$ is the equilibrium stress deviator, $G$ is the shear modulus, and $\tau$ is the effective material relaxation time. The bulk modulus is com-

Figure 1.11: Comparison of measured wave profile (shot 813) with a wavecode simulation that assumes an elastic-perfectly plastic rheology. The circles show the experimental data, and the solid lines are the numerical simulations. The times are arbitrary.

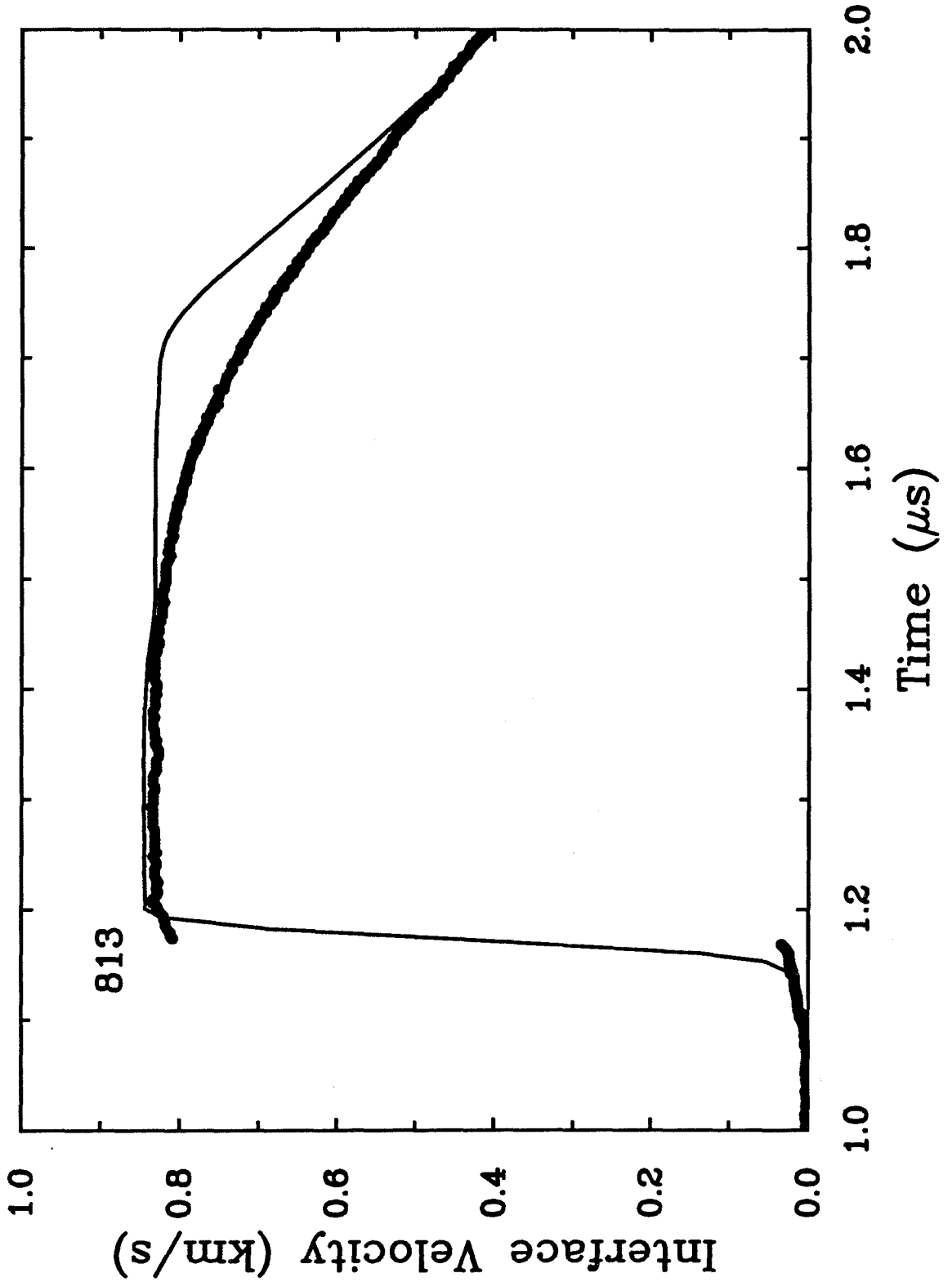
Interface Velocity (km/s)
1.0
0.8
0.6
0.4
0.2
0.0
1.0
1.2
1.4
1.6
1.8
2.0
Time (μs)
813

puted from the isentropic derivative of pressure with density. The shear modulus, in turn, is calculated using $K_S$ and a user-supplied value of Poisson's ratio. The stress deviators, together with the pressure, determine the axial stress, $\sigma$:

$$\sigma = P + \sigma', \tag{1.33}$$

where the pressure is determined using the Hugoniot EOS and the Mie-Gruneisen equation. The complete constitutive equation is described in Chapter 3 as well as in *Kipp and Lawrence* [1982].

The measured wave profiles were fit in an iterative fashion by adjusting the parameters of the Bauschinger model and the relaxation time constant. The LiF windows were treated as elastic-perfectly plastic throughout the calculations as were the Ta flyer plates. Lexan was treated as a hydrodynamic (strengthless) solid for those experiments in which it was used as a backing. In simulating the reverse-impact experiments, the material response of aluminum 6061 is important. Deviations for EPP behavior are well documented in aluminum [*Herrmann,* 1974; *Steinberg et al.,* 1980; *Asay and Chhabildas,* 1981; *Asay,* 1985]. The model used here was taken from *Lawrence and Asay* [1979] and incorporates anisotropic strain hardening in addition to the parameters of Table 1.2.

The model arrived at for describing the dynamic response of 304 steel is compared to wave-profile measurements for selected forward- and reverse-impact experments in Figures 1.12 and 1.13. Significant improvements over the EPP model were achieved by incorporation of both the Bauschinger effect and strain-rate dependent stress relaxation. Inclusion of stress relaxation improved the fit to the data at late times in the unloading history. A time constant of 15 ns was found to give the best fit to the unloading profiles. The incorporation of stress relaxation broadens the shock front to a much greater extent than was experimentally observed for the forward-impact experiments. Viscoplastic response, therefore, is an important feature of the unloading, not the loading, behavior of Fe-Cr-Ni. The broadening of the shock front

| $a_i$ | $Y_i$ (GPa) |
|---|---|
| 0.4 | 0.20 |
| 0.2 | 0.35 |
| 0.1 | 0.50 |
| 0.1 | 0.65 |
| 0.2 | 1.25 |

Table 1.12: Parameters of Bauschinger model for Fe-Cr-Ni alloy.

is also partially caused by the inclusion of artificial viscosity terms, widening the shock front over several zones for computational stability. The Bauschinger effect is responsible for smoothing the transition from elastic to plastic unloading. The Bauschinger model parameters are listed in Table 1.12.

It should be mentioned that the model derived here is based solely on the present shock data, and therefore its validity outside the range of the current experiments is uncertain. We have found that it is possible to represent the response over this range of conditions with a single, simple model whose main features are consistent with the observed behavior of many other metals [*Steinberg et al.*, 1980].

Release adiabats were calculated for the forward-impact experiments using a centered, simple-wave analysis [*Grady*, 1977]. The initial unloading point was first identified and connected to the Hugoniot state, using the EOS of the sample and window. The stress state at the sample-window interface was calculated from the non-linear stress-particle velocity relationship for the window (Table 1.2):

$$\sigma_w = \rho_o c_o u_w + \rho_o s u_w^2, \tag{1.34}$$

where $\sigma_w$ and $u_w$ are the stress and particle velocity at the interface. The La-

Figure 1.12: Comparison of measured wave profiles with wavecode simulations for several forward-impact experiments. The circles show the experimental data, and the solid lines are numerical simulations. The length of the experimental data records is determined by the arrival time of edge effects or of the shock front at the window free surface. Shot numbers are listed above each profile. The times are arbitrary.

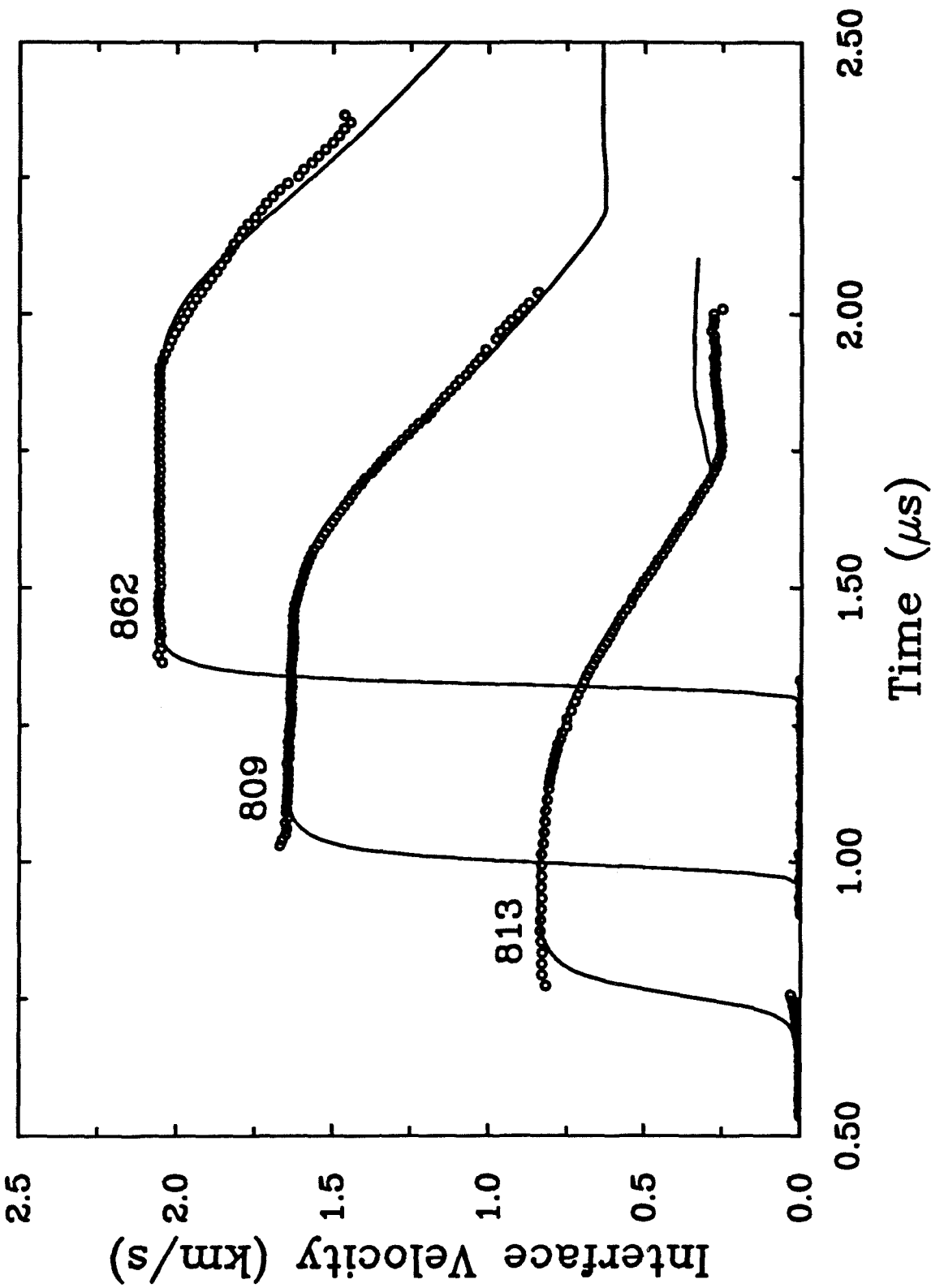
Interface Velocity (km/s)
2.5
2.0
1.5
1.0
0.5
0.0
0.50
1.00
1.50
2.00
2.50
Time (μs)
862
809
813

Figure 1.13: Comparison of measured wave profiles with wavecode simulations for several reverse-impact experiments. The circles show experimental data, and the solid lines are numerical simulations. The length of the experimental data records is determined by the arrival time of edge effects or of the shock front at the window free surface. Shot numbers are listed above each profile. The times are arbitrary.

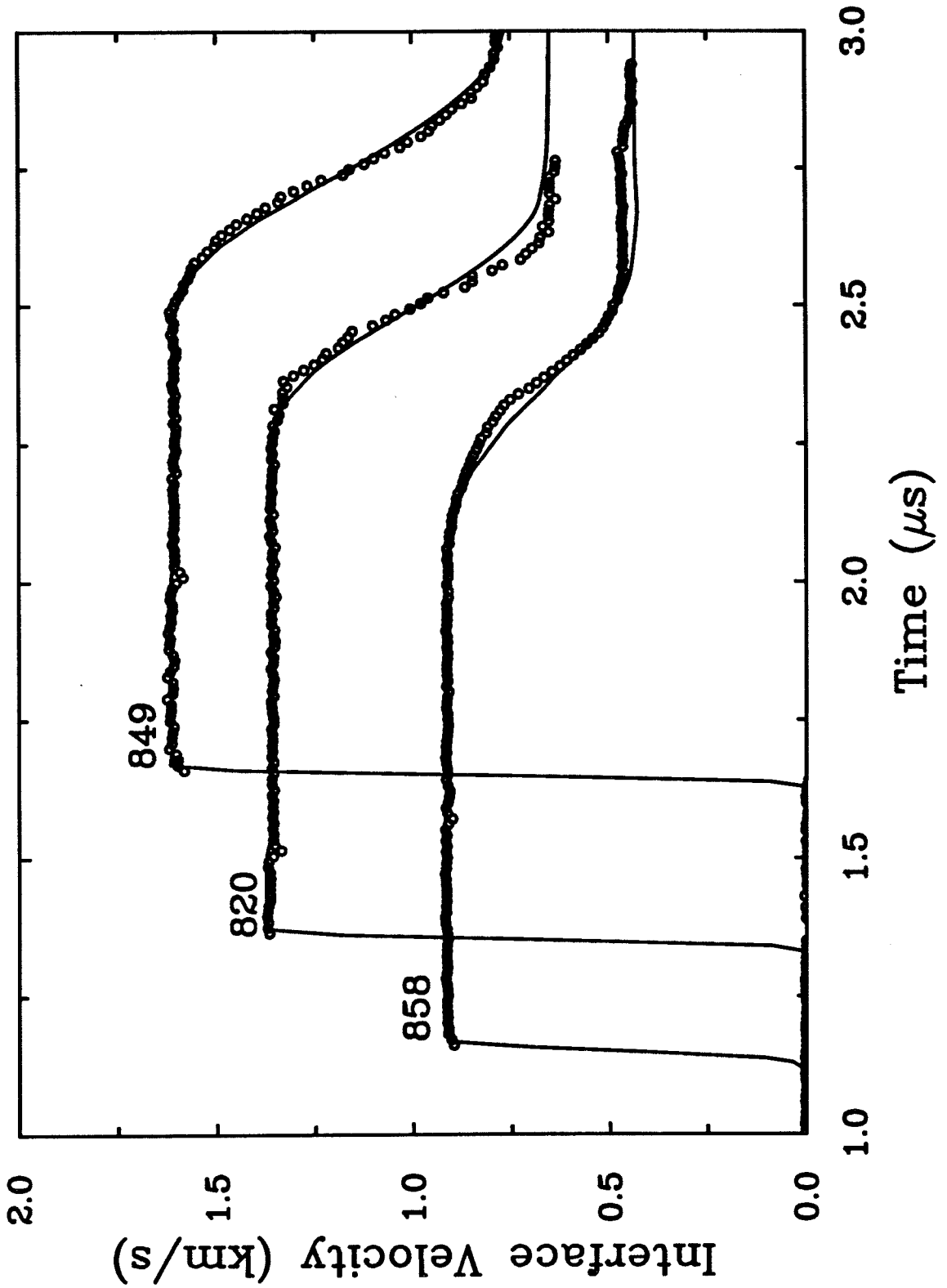
Interface Velocity (km/s)
Time (μs)
849
820
858
0.0
0.5
1.0
1.5
2.0
1.0
1.5
2.0
2.5
3.0

grangian wave speed as a function of particle velocity, c(u), was then estimated from release wave arrival times and the travel time of the shock (symmetric impact) or the travel time of the shock and release (non-symmetric impact) through the flyer. An approximate correction was made for the effect of wave interactions near the window, based on the explicit analysis of the preceding section. The wave profiles were then corrected from interface to in-material conditions using the incremental expressions [*Asay et al.*, 1980]:

$$du_s = \frac{1}{2}\left(du_w + d\sigma_w/\rho_o c(u_s)\right), \tag{1.35}$$

$$d\sigma_s = \frac{1}{2}\left(d\sigma_w + \rho_o c(u_s) du_w\right), \tag{1.36}$$

where $\sigma_s$ and $u_s$ are the in-material stress and particle velocity, respectively. Once the in-material properties are in hand, the conservation equations can be applied:

$$d\sigma_s = \rho_o c(u_s) du_s \tag{1.37}$$

$$d\eta = du_s/c(u_s), \tag{1.38}$$

to determine the stress-strain paths. Here the strain, $\eta$ is defined as:

$$\eta = 1 - \rho_o/\rho. \tag{1.39}$$

A plot of Lagrangian wave speed, $c(u_s)$, versus strain is shown in Figure 1.14. A gradual transition from elastic to plastic unloading behavior is evident. This again reflects the continual transition from elastic to plastic deformation of the Bauschinger model and further emphasizes the deviation of real material behavior from the elastic-perfectly plastic model. The Lagrangian bulk velocity at the Hugoniot state is estimated by extrapolating the linear plastic velocity trend to Hugoniot conditions

[*Asay and Chhabildas,* 1981]. The Eulerian bulk velocities are then obtained from Eqn. 1.7 (Table 1.10)

The calculated release adiabats are shown in Figure 1.15. Also shown are release adiabats extracted from the WONDY fits to the data. The wavecode uses the Mie-Grüneisen equation and the assumption that $\rho\gamma$ = const, where $\gamma$ is the Grüneisen constant. The release adiabats are initially steeper than the Hugoniot, reflecting the initial elastic response, but gradually become less steep. This is also illustrated in Figure 1.16 where the stress differences between the Hugoniot and the release curves are plotted against density. A positive stress difference means that the release curves lie below the Hugoniot.

According to Figures 1.15 and 1.16, the calculated release curve is less steep than the Mie-Grüneisen prediction at low densities for the higher-stress experiments. There are two possible causes for this. First, the centered, simple-wave analysis strictly applies only to rate independent materials for which wave speed is constant at a given u. The computer simulations require some rate dependence to fit the profiles at late times. Second, the higher stress experiments used Ta impactors, and the dispersion of the unloading wave through Ta has been neglected. This will lead to increasingly underestimated unloading wave speeds and hence calculation of a shallower release curve than actually occurs. In Figure 1.16 the stress difference is initially negative for the WONDY results because of the effect of deviatoric stresses. The uncertainty in the Hugoniot states determined from impedance matching was $\pm 0.4$ to $\pm 1.6$ GPa for these experiments.

Returning to Figure 1.14, the release wave speeds can be used to estimate the shear stress increase upon unloading [*Asay and Chhabildas,* 1981]. The stress state in the shocked state can be written:

$$\sigma = P + \frac{4}{3}\tau, \tag{1.40}$$

where $\tau$ is the shear stress. The shear stress at the Hugoniot state is designated

Figure 1.14: Lagrangian wave speed in Fe-Cr-Ni alloy as a function of strain determined from the centered, simple-wave analysis. The dashed lines are extrapolations of the bulk sound velocity to the Hugoniot state. The dotted curve is the Lagrangian bulk sound speed-strain relationship along the principal isentrope from extrapolation of ultrasonic data.

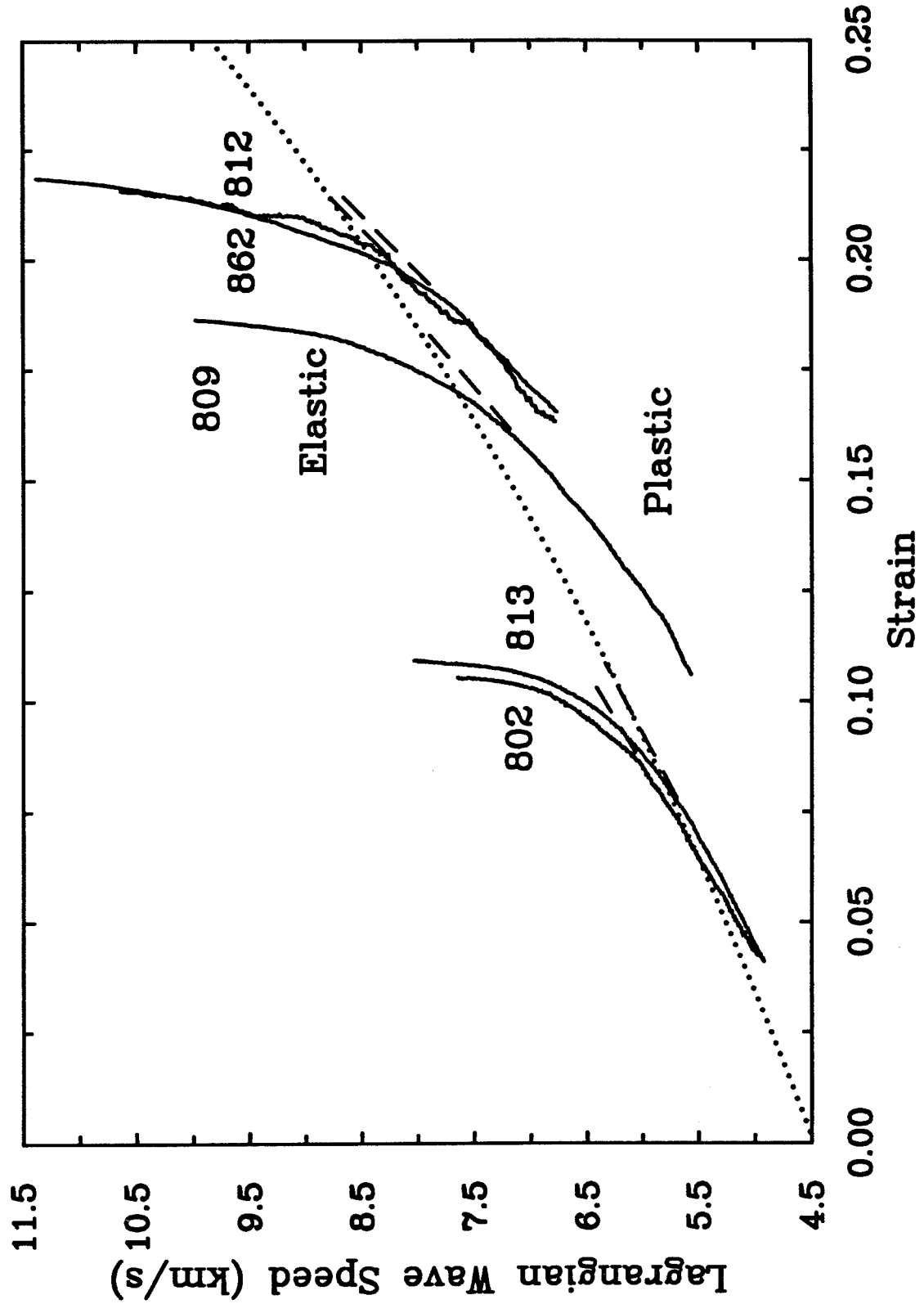
Lagrangian Wave Speed (km/s)
11.5
10.5
9.5
8.5
7.5
6.5
5.5
4.5
0.00
0.05
0.10
0.15
0.20
0.25
Strain
812
862
809
Elastic
813
802
Plastic

Figure 1.15: Release adiabats from Fe-Cr-Ni alloy at 3 different stress levels. Dotted lines are calculated from simple-wave analysis. The dashed lines are inferred from wavecode simulations using Mie-Grüneisen theory. The solid line is the principal Hugoniot.

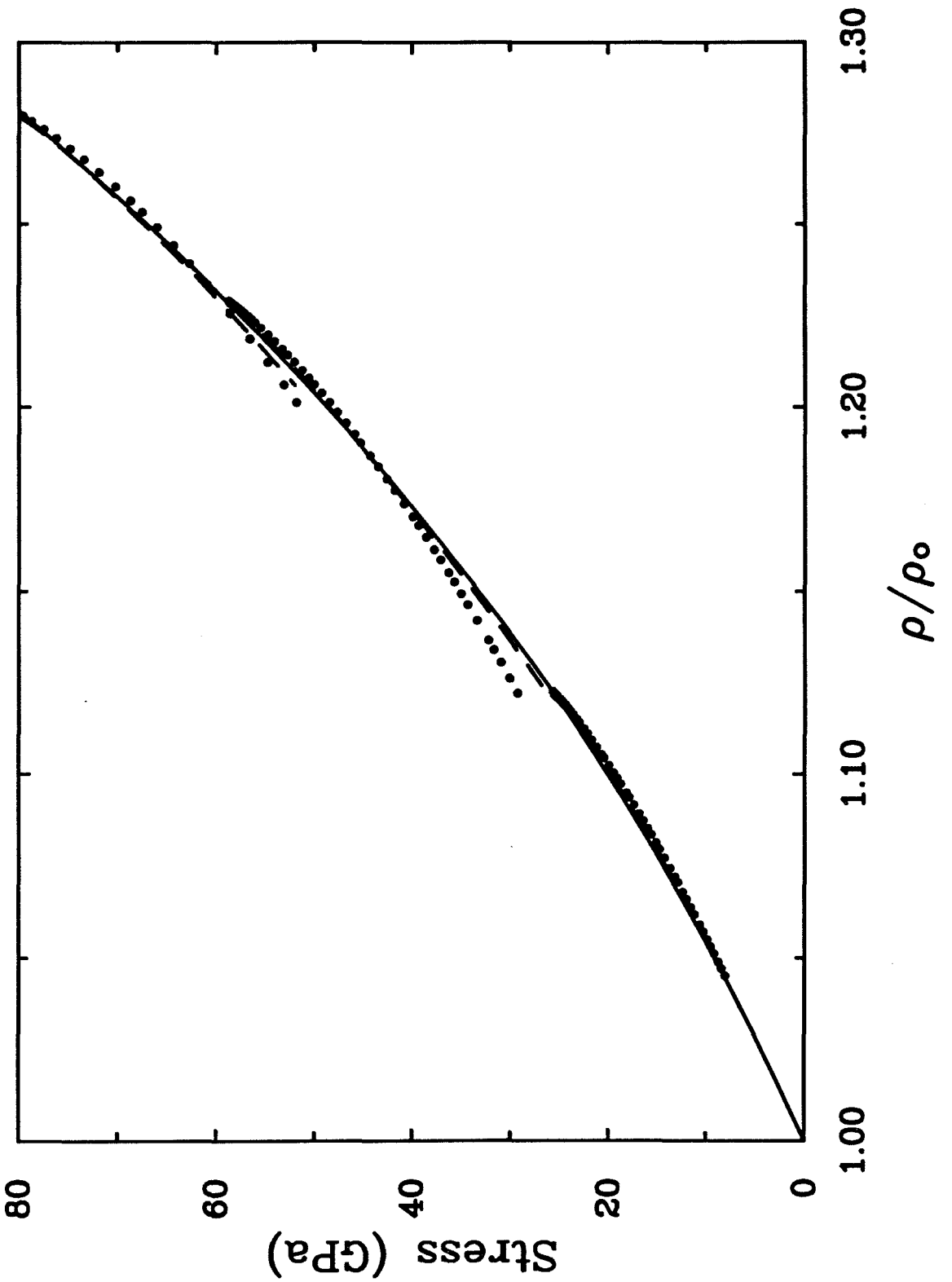
Stress (GPa)
0
20
40
60
80
1.00
1.10
1.20
1.30
ρ/ρo

Figure 1.16: Stress difference between the Hugoniot and release adiabat as a function of density. A positive stress difference indicates that the release curve lies below the Hugoniot. $\sigma_H$ is the Hugoniot stress and $\sigma_R$ is the stress along the release adiabat. The dashed curves are taken from WONDY fits to the wave profiles.

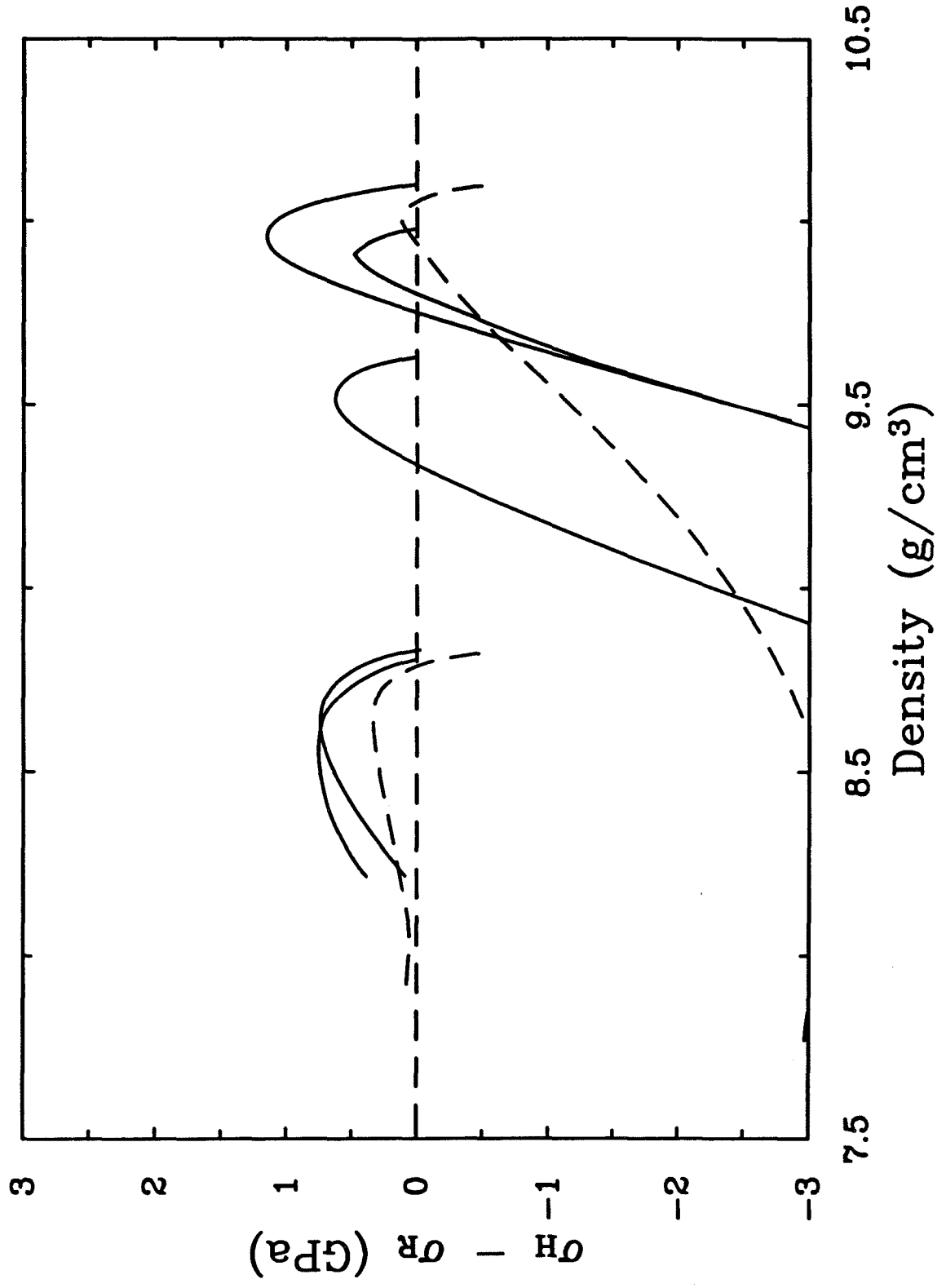
3
2
1
0
−1
−2
−3
7.5
8.5
9.5
10.5
Density (g/cm³)
σH − σR (GPa)

$\tau_o$. For an EPP solid, this is equal to the maximum shear strength $\tau_c$, which is also equal to $Y_o/2$. In real materials, $\tau_o$ can be either above or below $\tau_c$ if hardening or softening has taken place. Upon unloading, $\tau$ decreases from $\tau_o$ to a minimum value of -$\tau_c$ at the point p at which reverse yielding occurs. Differentiation of the above equation with respect to engineering strain, $\eta$, yields

$$\frac{d\sigma}{d\eta} = \frac{dP}{d\eta} + \frac{4d\tau}{3d\eta}, \tag{1.41}$$

which upon integration over strain from the Hugoniot state (state o) to the reverse yield point (state p) gives the following expression for the sum of the shear stress at the Hugoniot state and the shear strength maximum at reverse yielding:

$$\tau_o + \tau_c = \frac{3}{4}\rho_o \int_{\eta_o}^{\eta_p} \left(V_P^2 - V_B^2\right) d\eta, \tag{1.42}$$

*Asay and Chhabildas* [1981] have shown that the difference $\tau_o$ - $\tau_c$ can be obtained from reloading experiments, and hence the components $\tau_o$ and $\tau_c$ can be determined. Since no reloading experiments were performed in the present study, only the sum can be determined. $\tau_o + \tau_c$ is the shear stress change upon unloading. For the EPP model, the shear stress change is $2\tau_c$. The Lagrangian wave velocities required in the above equation were taken from the data of Figure 1.14. Point p is determined to be the strain at which the linear trend of the bulk velocities diverges from the measured wave speeds. A sharp transition from elastic to plastic loading is not evident in the present data. *Asay and Chhabildas* [1981] discuss in detail the assumptions that are necessary in applying this technique. The shear stress changes for stainless steel 304 determined using the data of Figure 1.14 are shown in Figure 1.17. The shear stress change increases in a linear fashion to 59 GPa. This implies significant variation from the elastic-perfectly plastic model for which the shear stress change is constant. The stress dependence of $\tau_o + \tau_c$ can be written as:

$$\tau_o + \tau_c = 0.149 + 0.018\sigma, \tag{1.43}$$

Figure 1.17: Shear stress change upon unloading as a function of stress. The dashed line is a least-squares fit to the data.

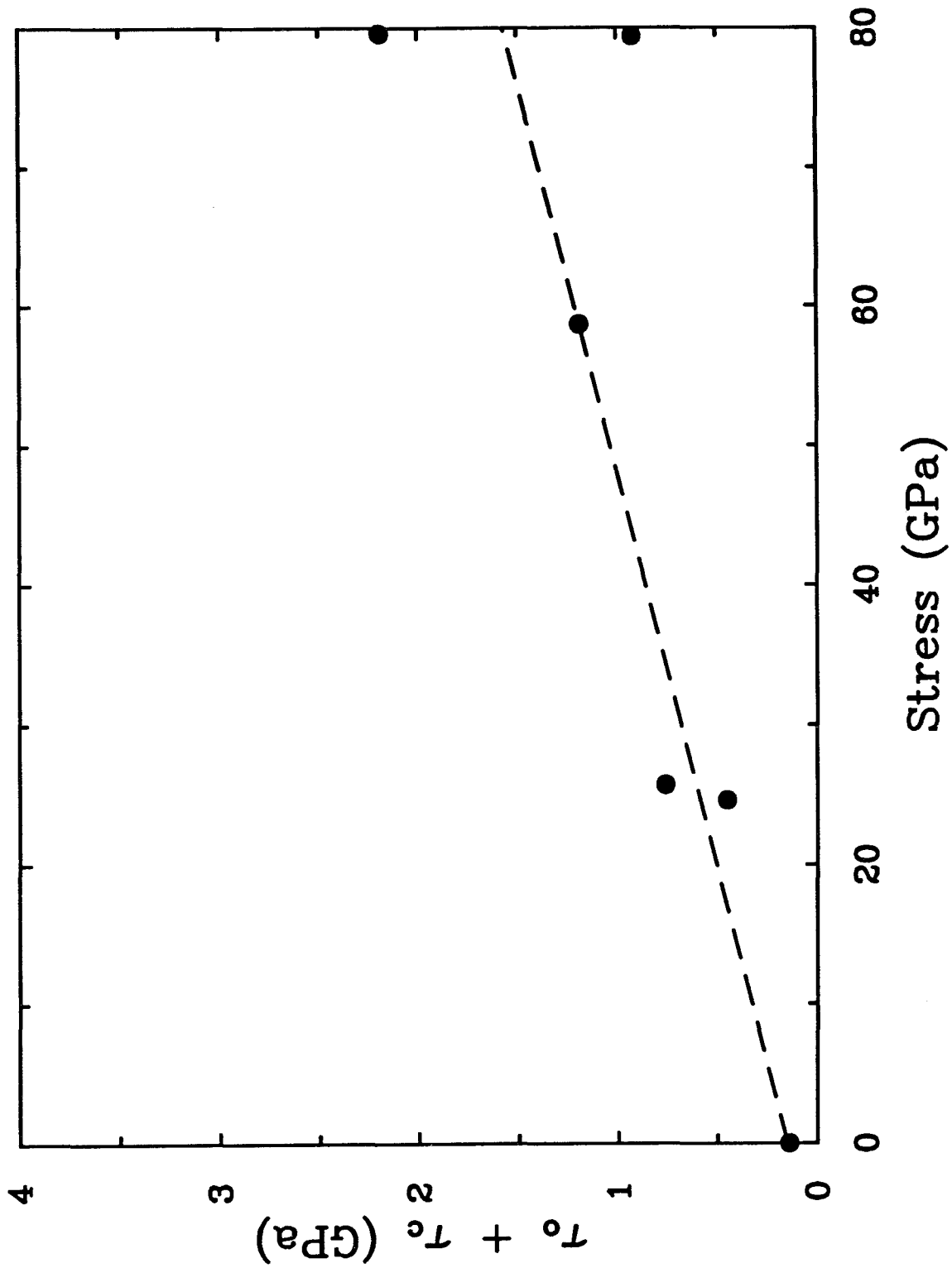
Stress (GPa)
0
20
40
60
80
$\tau_o + \tau_c$ (GPa)
0
1
2
3
4

where $\sigma$ is expressed in GPa.

The increase in $\tau_o + \tau_c$ for 304 steel is similar to that observed in copper, where the shear stress change upon unloading increases from its ambient value 0.08 GPa to 1.5 GPa at 93 GPa [*Chhabildas and Asay,* 1982]. *Asay and Kerley* [1987] summarize data that also show shear strength increases in 2024 Al, 6061 Al, pure Al, Ta, Be, and W. For the aluminum data, a maximum in shear strength followed by a gradual decline is observed to occur. This is believed to be due to the shock-induced temperature rise. No strength maximum can be unequivocally identified for 304 steel over the range of the present data. The strength determinations near 80 GPa are divergent because of the large differences in elastic sound velocity inferred from the two experiments near this pressure.

## 1.5 Summary

Shock compression of Fe-Cr-Ni alloy (304 stainless steel) has been carried out to 80 GPa. Wave profiles were measured using interferometric techniques, and these provided information on elastic wave velocities and high-strain-rate constitutive response.

Measured bulk and compressional wave velocities are similar to third-order finite-strain extrapolations of ultrasonic data. Bulk wave velocities are consistent with a constant $\rho\gamma = 17$, and compressional velocities required an increase in Poisson's ratio with compression. Thermal effects on the sound velocities are less than 2%, implying that the temperature coefficients of $V_P$ and $V_B$ decrease in magnitude by more than 50% between 0 and 80 GPa. Comparison of Hugoniot data and ultrasonic extrapolations is complicated by the formation of small fractions ($< 10$ vol.%) of $\alpha$-martensite at high pressure.

A method was developed for extracting elastic coefficients from measured Hugoniot velocities by using a normalized modulus - strain formalism. The present data

yield first pressure derivatives of compressional, bulk and shear moduli in agreement with ultrasonic determinations to 1 GPa. Second pressure derivatives along the Hugoniot were also constrained: $(\partial^2 C_L/\partial P^2)_H$ = -0.16 (0.06) $GPa^{-1}$ and $(\partial^2 K_S/\partial P^2)_H$ = -0.17 (0.08) $GPa^{-1}$. These terms cannot be resolved from current ultrasonic data, but the values that result from truncation of the finite-strain expressions at third order in strain (the last term on the RHS of equations 1.19 and 1.20 are set to zero) are $(\partial^2 C_L/\partial P^2)_S$ = -0.12 $GPa^{-1}$ and $(\partial^2 K_S/\partial P^2)_S$ = -0.08 $GPa^{-1}$.

The Hugoniot elastic limit stress for 304 steel was found to be 0.35 GPa, implying a yield stress of 0.21 GPa. Computer simulations of measured wave profiles indicate substantial deviations from elastic perfectly-plastic response. The wave profiles were successfully reproduced by a constitutive model including anisotropic strain hardening (Bauschinger effect) and strain-rate-dependent stress relaxation with an effective time constant of 15 ns.

A centered wave analysis was used to extract stress-strain histories from a subset of the experiments. Calculated release adiabats are initially steeper than the Hugoniot because of elastic response. The release adiabats show deviations from wavecode predictions that use the Mie-Grüneisen equation. The yield strength of 304 steel was found to increase by at least a factor of 5 up to 80 GPa. Material strength is a small (2-3%) but not negligible contributor to the total stress between 25 and 80 GPa.

# Chapter 2

# Elasticity of the Outer and Inner Core From Shock Wave Data

## 2.1 Introduction

Understanding the Earth's core requires detailed knowledge of the properties of iron and iron alloys at conditions of ultra-high pressure and temperature. Shock wave equation of state (EOS), temperature, and sound velocity measurements on iron and iron alloys have placed important constraints on this region of the Earth. While considerable work has focused on the properties of pure iron and possible light contaminants, the presence of other transition metals, particularly nickel, is also expected in the core on the basis of cosmochemical considerations [*Brett,* 1976]. Both shock wave equation of state and static experiments have shown that alloying iron with modest amounts of nickel increases the density of the alloy only slightly relative to pure iron [*McQueen and Marsh,* 1966; *Mao et al.,* 1990]. According to *Mao et al.* [1990], at 300 K and 330 GPa, the density of Fe alloyed with 20% Ni is about 2% greater than the density of pure iron. Static-density measurements on Fe also allow the inner core to contain some fraction of lighter material (e.g, Si, S, O, or H), up to 50% of the

amount of light material found in the outer core [*Jephcoat and Olson,* 1987]. Sound velocity measurements under Hugoniot conditions have shown that the properties of $\epsilon$-Fe are broadly consistent with seismologically determined velocities in the core [*Brown and McQueen,* 1986]. In this study, we evaluate new sound velocity data on an Fe-Cr-Ni alloy shock-compressed to 80 GPa (Chapter 1) as well as existing sound velocity data for Fe in order to draw constraints on the properties of the Earth's core from a comparison of laboratory and seismic data. In particular, we emphasize the effect of Ni on the elastic properties of Fe alloys. We also utilize new data on the effect of temperature on compressional sound velocity at high pressure (Chapter 4) to better constrain thermal effects at ultra-high pressure.

An isotropic elastic solid can be characterized by its density, $\rho$, and two elastic moduli, the bulk modulus, $K_S$, and the rigidity or shear modulus, $G$. The compressional, bulk, and elastic wave velocities are then given by:

$$\rho V_P^2 = C_L = K + 4/3G, \tag{2.1}$$

$$\rho V_B^2 = K, \tag{2.2}$$

$$\rho V_S^2 = G, \tag{2.3}$$

where $C_L$ is known as the longitudinal modulus. For a liquid, the rigidity is zero, and sound waves propagate only with the bulk velocity. The elastic properties and density of the inner and outer core are reasonably well constrained from a variety of seismic data (see *Masters and Shearer* [1990] for a recent summary). That the Earth's core is composed largely of iron has long been inferred on the basis of comparisons of seismic densities with shock wave data as well as cosmochemical and other considerations.

*Al'tshuler et al.* [1960] pioneered sound velocity measurements under shock compression using lateral relaxation and overtaking wave techniques. Currently, two techniques are commonly used to obtain sound velocities at ultra-high pressure. These are the VISAR [*Barker and Hollenbach,* 1972] and the optical-analyzer technique [*McQueen et al.,* 1982]. A discussion of the relative merits of both methods is

contained in *Duffy and Ahrens* [1992b]. Compressional sound velocities in Fe have been measured to 243 GPa and bulk velocities to 400 GPa [*Al'tshuler et al.,* 1960; *Al'tshuler et al.,* 1971; *Barker and Hollenbach,* 1974; *Brown and McQueen,* 1986; *Wang,* 1988]. In Chapter 1, compressional and bulk sound velocities in Fe-Cr-Ni alloy were reported to 80 GPa. Melting of Fe along the Hugoniot has been identified at 243 ± 2 GPa by the change in initial unloading velocity from compressional to bulk [*Brown and McQueen,* 1986]. In addition, a solid-solid phase change under Hugoniot conditions was identified on the basis of a change in compressional velocity at 200 ± 2 GPa, and this was interpreted as a transformation from $\epsilon$-iron (hcp) to $\gamma$-iron (fcc) [*Brown and McQueen,* 1986]. It has been proposed more recently that this second high-pressure phase of iron is a body-centered cubic phase ($\alpha'$) [*Ross et al.,* 1990], and we will refer to this phase as $\gamma$(?)-Fe. At 13 GPa, iron undergoes an extensively studied solid-solid phase transition from the $\alpha$-phase (bcc) to the $\epsilon$-phase [*Barker and Hollenbach,* 1974]. No phase changes were found in the Fe-Cr-Ni (fcc) alloy up to 80 GPa (Chapter 1), although small quantities (<10%) of $\alpha$-martensite (bcc) may form along twin planes at high pressure [*Murr,* 1981]. This appears to have little effect on the elastic properties of Fe-Cr-Ni.

## 2.2 Compressional Velocities in Fe and Fe Alloys and the Inner Core

We first discuss the variation of compressional velocity along the Hugoniot in Fe and Fe-Cr-Ni to assess the effect of possible alloying components, in particular, Ni, on inner core seismic properties. Hugoniot compressional sound velocities in Fe-Cr-Ni alloy are shown as a function of density in Figure 2.1. Also shown are measured Hugoniot $V_P$ values for Fe from several different studies. Compressional velocities in the Fe-Cr-Ni alloy are up to 8% faster than those in $\epsilon$-Fe over the density range investigated in the alloy. Both data sets can be fit by linear velocity-density rela-

tionships over large ranges of density. The Fe-Cr-Ni data extend to a strain of 0.22, where the strain, $\eta$, is defined as 1 - $\rho_o/\rho$. For $\epsilon$-Fe, velocities are linear in density over its entire stability range along the Hugoniot ($\eta$ = 0.08-0.34). The pressure stability field of the $\gamma$(?)-Fe phase is restricted ($\eta$ = 0.34-0.36), but these data also suggest a linear velocity-density trend. A linear relationship between sound velocity and density was first noted by *Birch* [1961] and is now known as Birch's Law. Hugoniot bulk and compressional sound velocity measurements have recently been shown to satisfy Birch's Law over large ranges in strain for a variety of solid and shock-melted metals and alkali halides [*Shaner et al,* 1988; *Boness and Brown,* 1990a; *Duffy and Ahrens,* 1992b]. Compressional velocity-density relationships for Fe and Fe-Cr-Ni from least-squares fits to the data are given by:

$$V_P = -2.87 + 1.12\rho \qquad (\mathrm{Fe - Cr - Ni}), \tag{2.4}$$

$$V_P = -2.73 + 1.04\rho \qquad (\epsilon\mathrm{-Fe}), \tag{2.5}$$

$$V_P = -0.86 + 0.86\rho \qquad (\gamma(?) - \mathrm{Fe}). \tag{2.6}$$

The alloy data define a slightly steeper slope than the $\epsilon$-Fe data, in keeping with the observation that velocity-density slopes are decreasing functions of atomic mass [*Birch,* 1961; *Shaner et al.,* 1988; *Duffy and Ahrens,* 1992b].

A simple mixing model was used to estimate velocities in Fe-Cr-Ni from its components, where we have assumed that the alloy is a solid solution of Cr and Ni in iron. Both compressional velocities and densities were computed by averaging end-member properties as a function of pressure and using atomic fractions as weights. Compressional velocities and densities in Cr and Ni at high pressure were estimated from finite-strain extrapolations of ultrasonic data [*Guinan and Steinberg,* 1974]; thus, thermal effects (and the effect of crystal structure) are neglected in the above comparison. For Cr, the P derivatives of the elastic moduli were estimated from systematic relationships [*Guinan and Steinberg,* 1974]. $K'$ was estimated to be 4.89

Figure 2.1: Compressional velocity as a function of density for Fe, Ni, Cr, and Fe-Cr-Ni. The velocities for Fe and Fe-Cr-Ni are under Hugoniot conditions, while those for Ni and Cr are extrapolated properties along a 300 K isotherm. Symbols show Hugoniot measurements for Fe-Cr-Ni and Fe. Solid lines are least-squares fits to the data and are dashed where extrapolated. Separate fits were performed for both the solid Hugoniot phases of Fe, stable above 13 GPa. The dot-dashed curve is the predicted velocity in the alloy on the basis of a weighted average of its component properties. The line with error bars labeled IC shows the range of inner core compressional velocities from PREM. Dotted lines are third-order finite-strain extrapolations of low-pressure ultrasonic data for Cr and Ni under isothermal conditions.

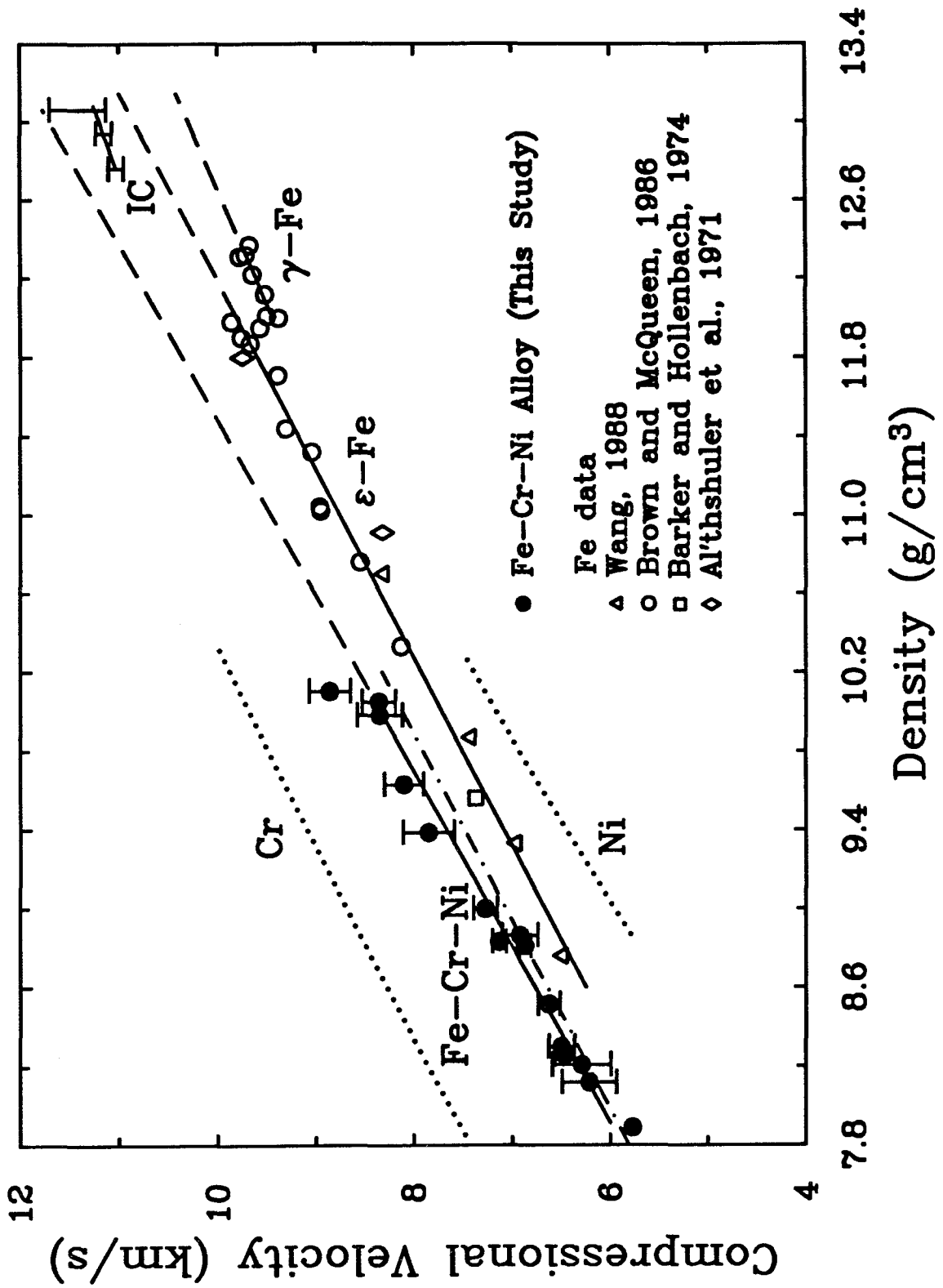
Compressional Velocity (km/s)
Density (g/cm³)
12
10
8
6
4
7.8
8.6
9.4
10.2
11.0
11.8
12.6
13.4
IC
γ–Fe
ε–Fe
Fe–Cr–Ni
Cr
Ni
Fe–Cr–Ni Alloy (This Study)
Fe data
Wang, 1988
Brown and McQueen, 1986
Barker and Hollenbach, 1974
Al'tshuler et al., 1971

from the relationship that $K' \approx 4s$ -1, where $s$ is the slope of the Hugoniot relation in shock velocity-particle velocity coordinates. The pressure derivative of the shear modulus of Cr was estimated to be 1.4, using an approximate expression relating this quantity and the acoustic Grüneisen parameter. The resultant velocity-density relationship for Fe-Cr-Ni (dot-dashed line) is shown in the Figure. The mixing model predicts the measured velocities to within 3%. The acceptable agreement, given the level of approximation, suggests that it is possible to decouple the effects of Cr and Ni on $V_P$ in the alloy. According to the Figure, Fe-Cr-Ni is up to 8% faster than $\epsilon$-Fe at a given density (up to $\sim$10.1 g/cm$^3$), largely because of high velocities in Cr. The effect of 8 wt.% Ni, on the other hand, would be to produce a slight decrease ($<$ 1% at 10.1 g/cm$^3$) in $V_P$ relative to $\epsilon$-Fe at a given density.

Extrapolation of linear velocity-density trends in Fe to inner core densities reveals that compressional velocities in $\epsilon$-Fe and $\gamma$(?)-Fe are 3% and 8% lower than inner core velocities from Earth model PREM [*Dziewonski and Anderson,* 1981]. The representative uncertainties for the inner core seismic velocities are from bounds obtained by *Stark et al.* [1986]. The core is believed to contain about 4 wt. % Ni based on cosmochemical considerations [*Brett,* 1976]. As can be seen in Figure 2.1, the effect of alloying Fe with $\sim$ 4% Ni is to produce a slight compressional velocity decrease at constant density at inner core conditions. The velocity excess in the inner core therefore cannot be explained by the presence of Ni. Other transition metals such as Cr could possibly account for the velocity difference but they are expected to be found in only very small ($<$ 0.1%, [*Brett,* 1976]) quantities in the core. The presence of 3-7 wt.% S or other light element in the inner core has been proposed on the basis of density data [*Jephcoat and Olson,* 1987]. Such a component may also be necessary to satisfy the compressional velocities in the core.

The effect of inner core temperature is assessed in Figure 2.2. This figure compares inner core compressional velocities from PREM with those in the two solid

| Material | $\rho_o$ ($g/cm^3$) | $c_o$ (km/s) | $s$ | $\gamma_o$ | Ref. |
|---|---|---|---|---|---|
| Fe-Cr-Ni | 7.87 | 4.58 | 1.49 | 2.2 | *McQueen et al.* [1970] |
| Fe | 7.85 | 3.96 | 1.58 | - | *Brown and McQueen* [1986] |
| Ni | 8.87 | 4.60 | 1.44 | 2.0 | *Marsh* [1980] |
| Cr | 7.12 | 5.17 | 1.43 | 1.2 | *McQueen et al.* [1970] |
| $FeS_2$ | 4.91 | 5.34 | 1.45 | 1.56 | *Ahrens and Jeanloz* [1987] |
| FeO | 5.5 | 3.73 | 1.59 | 1.8 | *Jeanloz and Ahrens* [1980] |

Table 2.1: Hugoniot equation of state properties for Fe, Cr, Ni and Fe alloys.

phases of iron, taking into account the effects of Ni content and temperature. Velocities in Fe and Fe-Cr-Ni at inner core pressures were calculated using the linear velocity-density trends discussed above and the known Hugoniot pressure-density relations for these materials (Table 2.1). In order to account for thermal effects, we have assumed that the temperature coefficient of compressional velocity, $(\partial V_P/\partial T)_P$, is -0.1 m/s/K. This is significantly less than the zero-pressure value of $(\partial V_P/\partial T)_P$ = -0.6 m/s/K for bcc iron [*Leese and Lord,* 1968]. Our value is based on comparison of Hugoniot $V_P$ measurements and finite-strain extrapolations of ultrasonic data at 300 K for Al, Cu, Mo, Ta, W, and $Mg_2SiO_4$, which lead to the conclusion that $(\partial V_P/\partial T)_P$ decreases strongly in magnitude with pressure [*Duffy and Ahrens,* 1992a; see also Chapter 4]. At pressures above 100 GPa, values of $(\partial V_P/\partial T)_P$ of -0.1 $\pm$ 0.1 m/s/K have been found for the materials studied to date.

The temperature of the inner core is also uncertain. A number of recent estimates of the temperature at the inner core-outer core boundary are shown in Table 2.2 and span a considerable range. We have used 6000 K and 7500 K as representing bounds

Figure 2.2: Compressional sound velocities in the inner core from Earth model PREM (dotted line) together with estimates from Hugoniot and ultrasonic sound velocity data. Dashed and dot-dashed lines show calculated compressional velocities in Fe-Ni for assumed inner core temperatures of 6000 K and 7500 K. Upper curves are for $\epsilon$-Fe containing 4 wt.% Ni, and the lower curves are for $\gamma$-Fe also containing 4 wt.% Ni. The solid curve shows extrapolated Hugoniot velocities in Fe-Cr-Ni alloy.

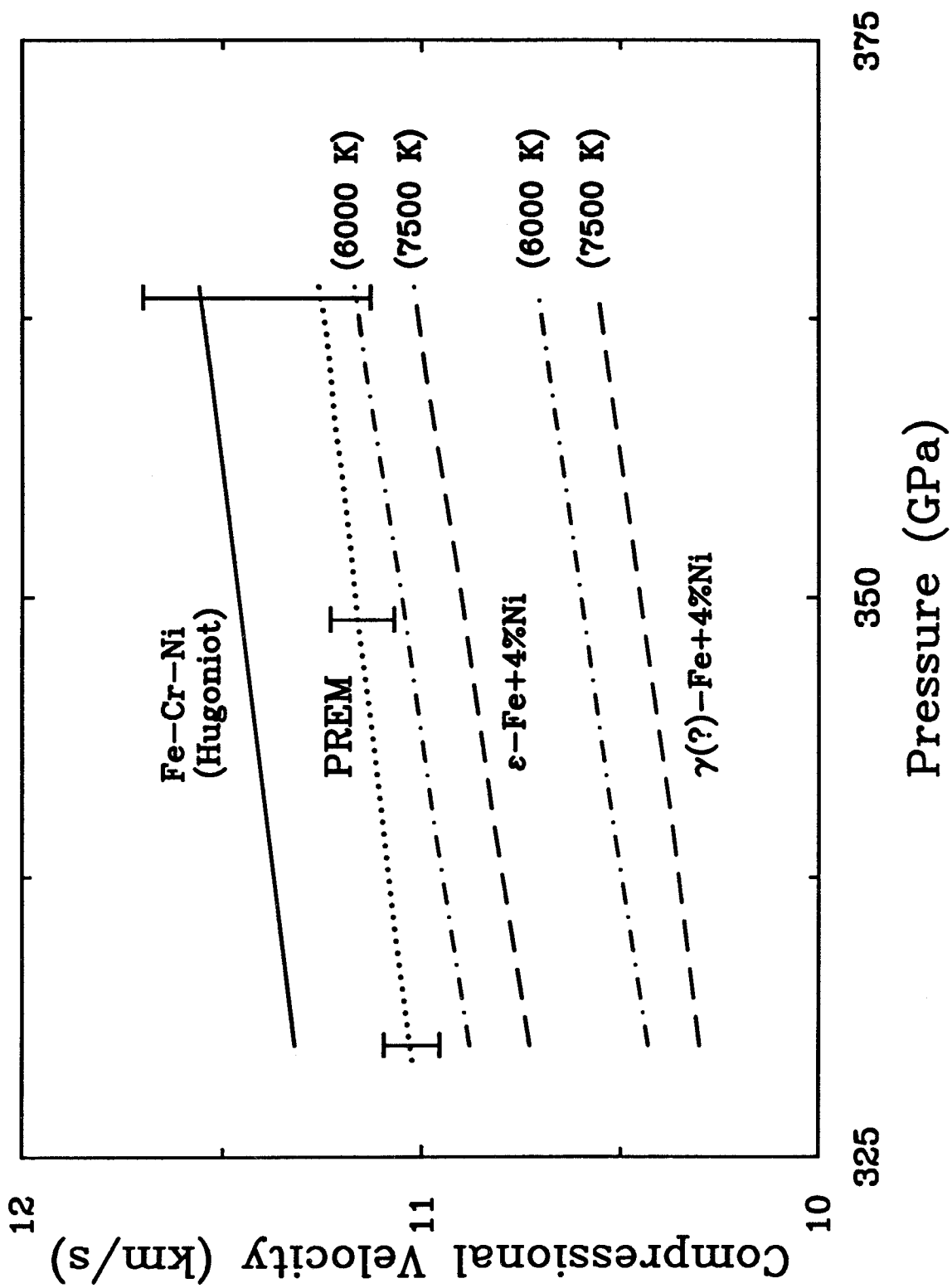
Compressional Velocity (km/s)
12
11
10
325
350
375
Pressure (GPa)
Fe–Cr–Ni
(Hugoniot)
PREM
(6000 K)
(7500 K)
ε–Fe+4%Ni
(6000 K)
(7500 K)
γ(?)–Fe+4%Ni

| Study | T (K) |
|---|---|
| *Stacey* [1977] | 4168 |
| *Brown and Shankland* [1981] | 3359 |
| *Anderson* [1986] | 6210 ± 400 |
| *Williams et al.* [1987] | 7600 ± 500 |
| *Ross et al.* [1990] | 6200 ± 500 |
| *Boness and Brown* [1990b] | 5800 ± 500 |

Table 2.2: Some recent estimates of the Earth's inner core-outer core boundary temperature.

on inner core temperatures given the latest estimates (Table 2.2). We also assume that the inner core is isothermal. Temperatures achieved along the iron Hugoniot were taken from the calculations of *Brown and McQueen* [1986] which did not include a phase-transition energy term but did include an electronic contribution to the specific heat. Velocities were corrected using the temperature difference between the Hugoniot and inner core and the velocity-temperature scaling coefficient discussed above. The resultant thermal corrections are 1 and 2.5% for the upper (7500 K) and lower (6000 K) bounds on the inner core temperature.

To account for the effect of Ni content on $V_P$, we have used our previous decomposition of the effects of Fe, Cr, and Ni on velocities in Fe-Cr-Ni. We first extrapolated Ni ultrasonic data to inner core pressures (at 300 K) and corrected the data to inner core temperatures using the $(\partial V_P/\partial T)_P$ value above. We then averaged the Fe and Ni velocities together with atomic-fraction weights. The effect of including a cosmochemically plausible 4 wt.% Ni in $\epsilon$-Fe is to produce a slight (<1%) decrease in $V_P$, while the same amount of Ni combined with $\gamma$(?)-Fe produces a slight (<1%)

increase in $V_P$. The combined effects of temperature and Ni content on $V_P$ in Fe under inner core conditions is shown in Figure 2.2. At a given pressure, the velocities in the Fe-Ni alloys are 1-2.5% greater under inner core conditions than Fe velocities under Hugoniot conditions. Thermally corrected velocities in $\gamma$(?)-Fe+4 wt.% Ni are 5.5-7% below PREM values, and those in $\epsilon$-Fe+4 wt.%Ni are 1-2.5% below PREM values. It appears that an inner core composed solely of $\epsilon$-Fe is in good agreement with seismic data, but compressional velocities in $\gamma$(?)-Fe are too low for it to be the sole component of the inner core. This conclusion was reached earlier by *Brown and McQueen* [1986] on the sole basis of Fe Hugoniot data. We have shown that this conclusion also holds when thermal effects and Ni content are taken into account. It is interesting to note that compressional velocities for both iron phases lie below seismic values. It is therefore plausible that the inner core could contain a high-velocity, low-density fraction. The lack of high-pressure compressional velocity data on phases such as FeO and FeS preclude bounds on such a fraction from being drawn at present.

## 2.3 Bulk Velocities in Fe and Fe Alloys

We now turn attention to bulk sound velocities in Fe and Fe-Cr-Ni and a comparison with seismic values in the outer and inner core. Before discussing our new data for Fe-Cr-Ni alloy, a summary of available iron data will be presented as interpretation of these data is ambiguous at present. Bulk sound velocities in Fe were first presented by *Al'tshuler et al.* [1960] at pressures between 42 and 348 GPa. Subsequently, *Brown and McQueen* [1986] reported bulk sound velocities from the Hugoniot melting point, which they determined to be at 243 $\pm$ 2 GPa, to 400 GPa. Hugoniot $V_B$ values for Fe are plotted against density in Figure 2.3. While the *Al'tshuler et al.* results represented a pioneering experimental advance, the accuracy of these measurements has been called into question [*Brown and McQueen,* 1986]. A comparison

of experimental results at similar densities (see also Figure 2.1) shows that the measurements of *Al'tshuler et al.* and *Brown and McQueen* generally differ by 1-3%. Part of this difference may be attributable to the EOS used for Fe. *Anderson* [1990] reanalyzed the *Brown and McQueen* data using a liquid-state EOS for Fe and computed sound velocities that were shifted downward by 1-2% (Figure 2.3) and are in better agreement with the results of *Al'tshuler et al.* [1960]. As a general conclusion, we find only small differences in sound velocities at similar pressures reported by *Al'tshuler et al.* [1960] and *Brown and McQueen* [1986].

As discussed in Chapter 1, thermodynamic arguments incorporating the Mie-Grüneisen equation can be used to derive a relationship between the Grüneisen parameter and the bulk sound velocity (Eqn. 1.17) which depends upon the local slope of the Hugoniot. We have used this eqn., together with EOS data for Fe, Cr, and Ni (Table 2.1), to compute Hugoniot bulk sound velocities (Fig. 2.3). In doing so, we have assumed that the product of the density and the Grüneisen parameter, $\rho\gamma$, is constant with pressure. This assumption, which is commonly used in analyses of shock data, is supported by studies of porous materials [*McQueen et al.,* 1970] and available bulk sound velocity data in metals [*Duffy and Ahrens* 1992b]. For Cr and Ni, ambient-pressure values of $\rho\gamma$ were used in the calculation (Table 2.1). For Fe, *Brown and McQueen* [1986] found a nearly constant value of $\rho\gamma = 19.7 \pm 0.7$ from their measured bulk sound velocities between 260 and 400 GPa and the EOS of iron. This value was used to compute the curve for Fe shown in the figure. *Anderson* [1990] has pointed out that *Brown and McQueen* used an EOS (Table 2.1) appropriate only for solid iron. *Anderson's* reanalysis using a liquid-state EOS implies the following $\rho$-$\gamma$ relationship for liquid Fe:

$$\gamma = 2.8 \left( \frac{\rho_o}{\rho} \right)^{1.17}, \tag{2.7}$$

where $\rho_o = 7.037$ g/cm$^3$ is the ambient-pressure density of liquid iron at its melting point.

Figure 2.3: Bulk velocity as a function of density for Fe-Cr-Ni and its components. Solid symbols are the present data for Fe-Cr-Ni through which a linear fit is drawn (solid curve). Solid curves for Cr, Fe, and Ni are from Hugoniot calculations and are discussed in detail in the text. Data for Fe are shown by open symbols. Also included (starred symbols) are *Anderson's* [1990] reinterpretation of the three highest pressure data of *Brown and McQueen* [1986]. The open box shows the estimated bulk sound velocity in $\epsilon$-Fe at ambient conditions from the static-compression data of *Mao et al.* [1990]. The vertical bar at $\rho = 12.3$ g/cm$^3$ is the Hugoniot melting boundary for Fe. The dashed curve shows a linear least-squares fit to the iron data of *Al'tshuler et al.* [1960] and *Anderson* [1990]. Outer (O.C.) and inner (I.C.) core values are from Earth model PREM. The dash-dot curve shows velocities and densities in Fe-Cr-Ni estimated from a weighted average of its components using atomic fractions as weights.

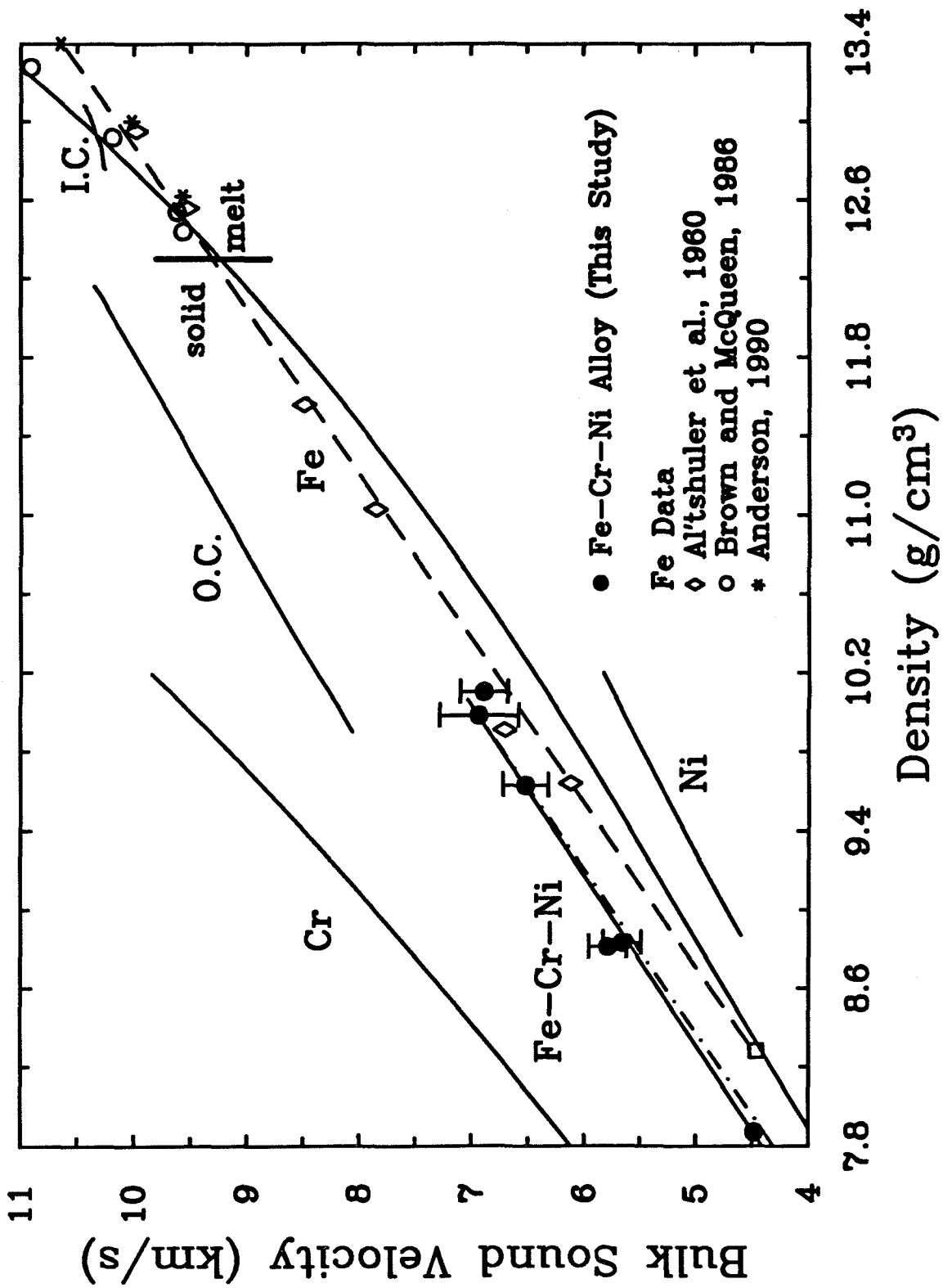
Bulk Sound Velocity (km/s)
Density (g/cm³)
11
10
9
8
7
6
5
4
7.8
8.6
9.4
10.2
11.0
11.8
12.6
13.4
I.C.
O.C.
solid
melt
Fe
Cr
Fe—Cr—Ni
Ni
● Fe—Cr—Ni Alloy (This Study)
Fe Data
◊ Al'tshuler et al., 1960
○ Brown and McQueen, 1986
* Anderson, 1990

Velocity-density relationships computed using Eqn. 1.17 and a constant $\rho\gamma$ generally show a concave upward slope but can be nearly linear over large ranges in density. There are two notable features of the calculated bulk velocities in Fe shown in the Figure. First, the velocities exhibit significant non-linearity over the density range of the outer core. The outer core, however, exhibits a linear velocity-density trend over a 23% variation in density. It may be difficult to reconcile the calculated $V_B$-$\rho$ trajectory in Fe with a homogeneous outer core. Moreover, measured values of $V_P$ and $V_B$ along the Hugoniot nearly always display linear velocity-density trends over the experimental data ranges [*Shaner et al.,* 1988; *Boness and Brown,* 1990a; *Duffy and Ahrens,* 1992b]. The second point is that calculated bulk sound velocities in Fe using this relationship are 4-10% slower than measured in the solid phase by *Al'tshuler et al.* [1960]. One difficulty may be that changes in physical properties across the melt boundary are not being properly accounted for. We further note that the data of *Al'tshuler et al.* [1960], together with *Anderson's* results (that is, incorporating both solid- and liquid-phase data) define a linear velocity-density trend throughout the experimental data range:

$$V_B = -5.45 + 1.20\rho. \tag{2.8}$$

This relationship is shown as the dashed line in Figure 2.3. In determining this result, we have included an estimate of the ambient-pressure bulk sound speed for $\epsilon$-Fe using $\rho_o = 8.30 \pm 0.01$ g/cm$^3$ and $K_o = 165 \pm 4$ GPa from room-temperature static-compression data to 300 GPa, giving $V_B$=4.46 km/s [*Mao et al.,* 1990]. The *Al'tshuler* datum at 54.2 GPa ($V_B$ = 6.70 km/s) was excluded from the fit. In summary, available bulk sound velocity data for Fe can be interpreted in one of two ways, either as a linear velocity-density relationship (Eqn. 2.8) or as a non-linear relationship for which $\rho\gamma$ = const. These two relationships predict bulk sound velocities that differ by as much as 6% in the solid-phase portion of the Fe Hugoniot.

Bulk sound velocities in Fe-Cr-Ni alloy (Chapter 1) are also shown in Figure

2.3. A weighted least-squares fit to these data yields $V_B$ = -4.64 + 1.16$\rho$. Fe-Cr-Ni data have a slightly lower slope (by 3%) than the Fe relationship discussed above (Eqn. 2.8). As was done above for $V_P$, estimated values for $V_B$ in the alloy were computed by combining densities and bulk velocities in Fe, Cr, and Ni at a given pressure, using atomic fractions as weights. For Cr and Ni, the Hugoniot-slope calculations were used to estimate the bulk velocities in these materials. For Fe, the linear velocity-density relationship described above was used. The results are shown in Figure 2.3 (dot-dashed curve) and agree well with measured values. As with compressional velocities, bulk velocities in Fe-Cr-Ni are greater than those in Fe throughout the experimental data range. The linear velocity-density relationship for Fe-Cr-Ni yields bulk velocities 6-10% greater than those for Fe up to 10.1 g/cm$^3$. We again infer that the higher velocities in Fe-Cr-Ni are a consequence of the incorporation of Cr. Addition of ~4 wt.% Ni to Fe is therefore expected to produce only a small (< 1%) decrease in $V_B$. Hugoniot velocities in Fe based on Eqn. 2.8 lie 13-25% below outer core velocities in PREM at constant density, presumably reflecting the effects of both temperature and alloying in the outer core. However, at constant pressure, Hugoniot Fe velocities are just 4% below PREM values. This is illustrated in Figure 2.4 which shows the variation of bulk sound velocities in Fe and Fe alloys as a function of pressure. By analogy with our results for $V_P$, we expect that constant-pressure thermal corrections to $V_B$ will be small (~3% or less) The temperature difference between Hugoniot and core conditions is calculated to be smaller for the outer core than for the inner core. Bulk velocities in $FeS_2$ and FeO are estimated using the EOS properties listed in Table 2.1. On the basis of current data, the effect of incorporation of both S and O will be to increase the bulk sound velocity relative to pure Fe. If these materials are incorporated into the core, they must be compensated by some material with a lower bulk sound velocity. This study has shown that the effect of Ni on $V_B$ will be very small and that therefore Ni is not likely to be a

significant compensatory material. Recent static-compression data on iron hydride of approximate composition $FeH_{0.94}$ have shown that this material is stable at 300 K to at least 62 GPa and have provided the first estimates of the elastic properties and densities for the material [*Badding et al.,* 1991]. While it is not known if FeH is stable under core conditions, it has been proposed as a potential light element on cosmochemical grounds [*Jeanloz,* 1990]. Estimated bulk velocities in FeH based on the properties derived from the static experiments are shown in Figure 2.4 as the dotted curve. Velocities in FeH at 300 K are predicted to be slightly less than those in Fe over the outer core pressure range. The incorporation of FeH into the outer core would therefore not produce a large change in bulk velocity and could partially compensate for the effects of S and O on $V_B$. In the inner core, calculated velocities in Fe are 1-4% below velocities in PREM when viewed either at constant pressure or at constant density. Both compressional and bulk velocities in Fe are therefore in reasonably good agreement with inner core values.

## 2.4 Shear Velocities and Poisson's Ratio in Fe and Fe alloys

Constraints on shear velocities in Fe and Fe alloys at high pressures and temperatures can potentially provide strong constraints on the state of the Earth's inner core. Shear velocities in the inner core appear to be anomalously low. *Masters and Shearer* [1990] have determined the shear velocity in the inner core to be 3.45 $\pm$ 0.1 km/s on the basis of free oscillation data. For comparison, the shear velocities in bcc iron and Fe-Cr-Ni at ambient conditions are 3.23 and 3.13 km/s, respectively. Normally, velocities at high pressure are significantly greater than ambient-pressure values (see Chapter 1 and Chapter 4). Possible explanations for the low values in the core include partial melting [*Loper and Fearn,* 1983], second-order pressure effects on the shear modulus [*Falzone and Stacey,* 1980], and the effect of high temperature. As a consequence of the low shear velocity, Poisson's ratio, $\nu$, is large in the inner core. In

Figure 2.4: Bulk sound velocity in Fe and Fe alloys as a function of pressure. Symbols show Hugoniot measurements. The dashed curves are calculated sound velocities for Fe and Fe alloys, based on EOS data and a constant $\rho\gamma$ . The dotted curve shows estimated 300 K velocities for $FeH_{0.94}$ based on the elastic properties and density for this material determined by the static-compression data of *Badding et al.* [1991]. Solid curves show inner (I.C.) and outer core (O.C.) values from PREM.

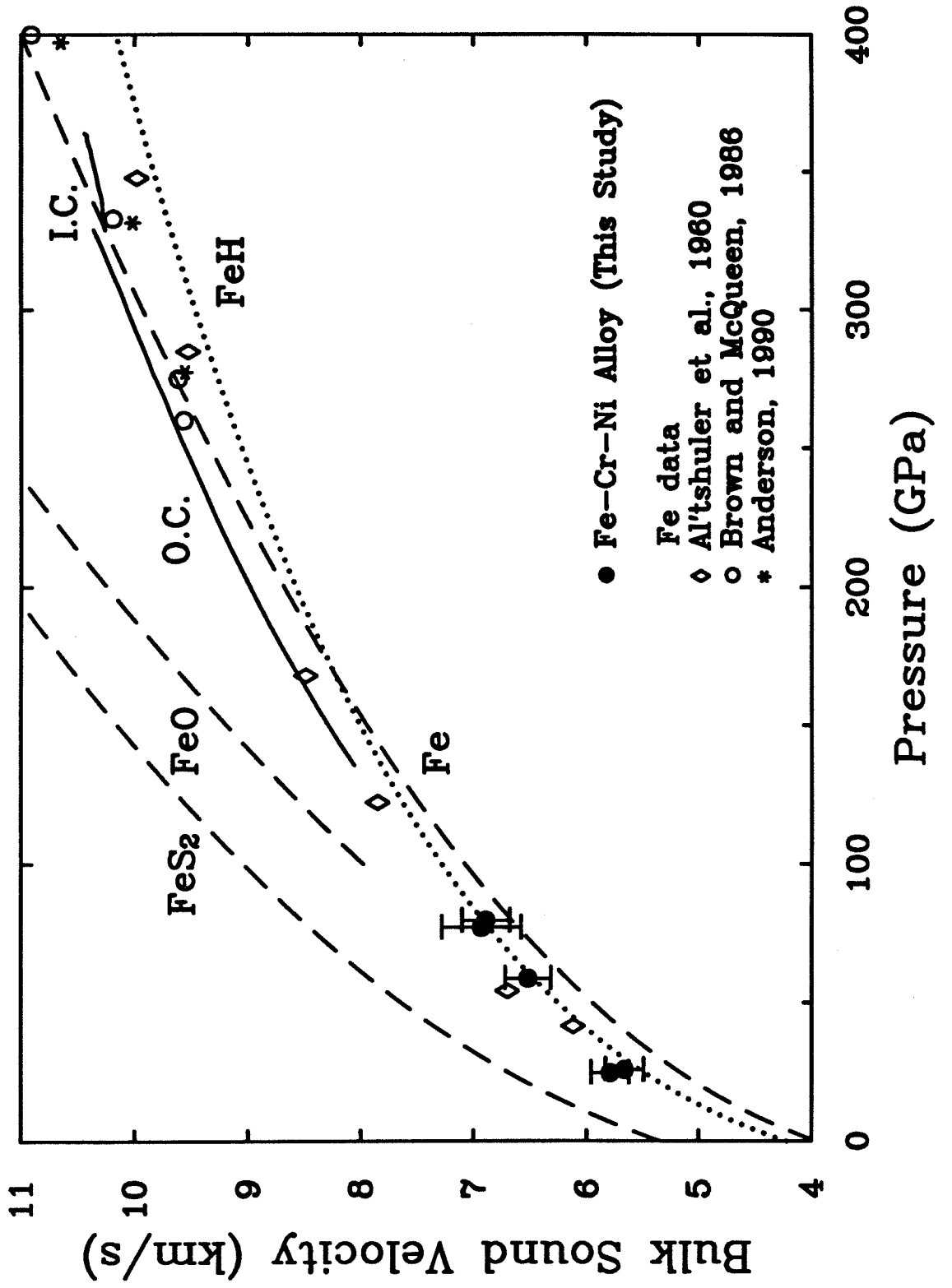
Bulk Sound Velocity (km/s)
Pressure (GPa)
11
10
9
8
7
6
5
4
0
100
200
300
400
I.C.
O.C.
FeH
Fe
FeO
FeS2
● Fe–Cr–Ni Alloy (This Study)
Fe data
◊ Al'tshuler et al., 1960
○ Brown and McQueen, 1986
* Anderson, 1990

Earth model PREM, for which the shear velocity is 3.50-3.66 km/s, Poisson's ratio is 0.44. At ambient conditions, Poisson's ratio is 0.29 for both bcc iron and Fe-Cr-Ni. For a liquid, Poisson's ratio is 0.5. Thus, $\nu$ values in the inner core are 50% greater than ambient-pressure values and are close to liquid values.

In order to provide constraints on the variation of $V_S$ with pressure and temperature, we have calculated Hugoniot shear velocities for Fe and Fe-Cr-Ni. Shear velocities cannot be directly measured under Hugoniot conditions. Instead, we have combined measured compressional velocities (Figure 2.1) with the inferred variation of the bulk velocity (Figure 2.3), using the relation:

$$V_S^2 = \frac{3}{4}\left(V_P^2 - V_B^2\right), \tag{2.9}$$

Similarly, Poisson's ratio can be calculated from $V_P$ and $V_B$:

$$\nu = \frac{3 - \left(V_P^2/V_B^2\right)}{3 + \left(V_P^2/V_B^2\right)}, \tag{2.10}$$

The variation of $V_S$ and $\nu$ along the Hugoniot for Fe and Fe-Cr-Ni are shown in Figures 2.5 and 2.6. In these figures, the bulk sound velocity has been determined from Hugoniot-slope calculations (Eqn 1.17), which utilize solid EOS data (Table 2.1) and a constant value for the product $\rho\gamma$. For Fe-Cr-Ni, the ambient-pressure value of $\rho\gamma = 17.1$ has been used [*McQueen et al.,* 1970]. High-pressure values from bulk sound velocity measurements are consistent with this, but have large (> 25%) uncertainties (Chapter 1). For Fe, the high-pressure liquid-state value of $\rho\gamma = 19.7 \pm 0.7$ has been assumed [*Brown and McQueen,* 1986].

At pressures up to 80 GPa, shear velocities and Poisson's ratios in Fe and Fe-Cr-Ni are similar, and both increase with increasing pressure. In this region, shock-heating effects are small, and the data largely reflect the pressure dependence of these quantities. For comparison, we have shown in each figure the pressure variation predicted from Eulerian third-order finite-strain extrapolation of low-pressure ultrasonic data

Figure 2.5: Calculated Hugoniot shear velocities for Fe and Fe-Cr-Ni. The solid and open symbols are obtained by combining measured compressional velocities and Hugoniot-slope calculations for $V_B$, using a constant $\rho\gamma$. The solid line shows the pressure dependence of $V_S$ from extrapolation of low-pressure isothermal ultrasonic data for Fe-Cr-Ni. The dashed curve shows the variation of $V_S$ in Fe from a combination of the linear compressional velocity-density trend and the variation of $V_B$ inferred by *Brown and McQueen* [1986]. Inner core values from free-oscillation data are shown by the box.

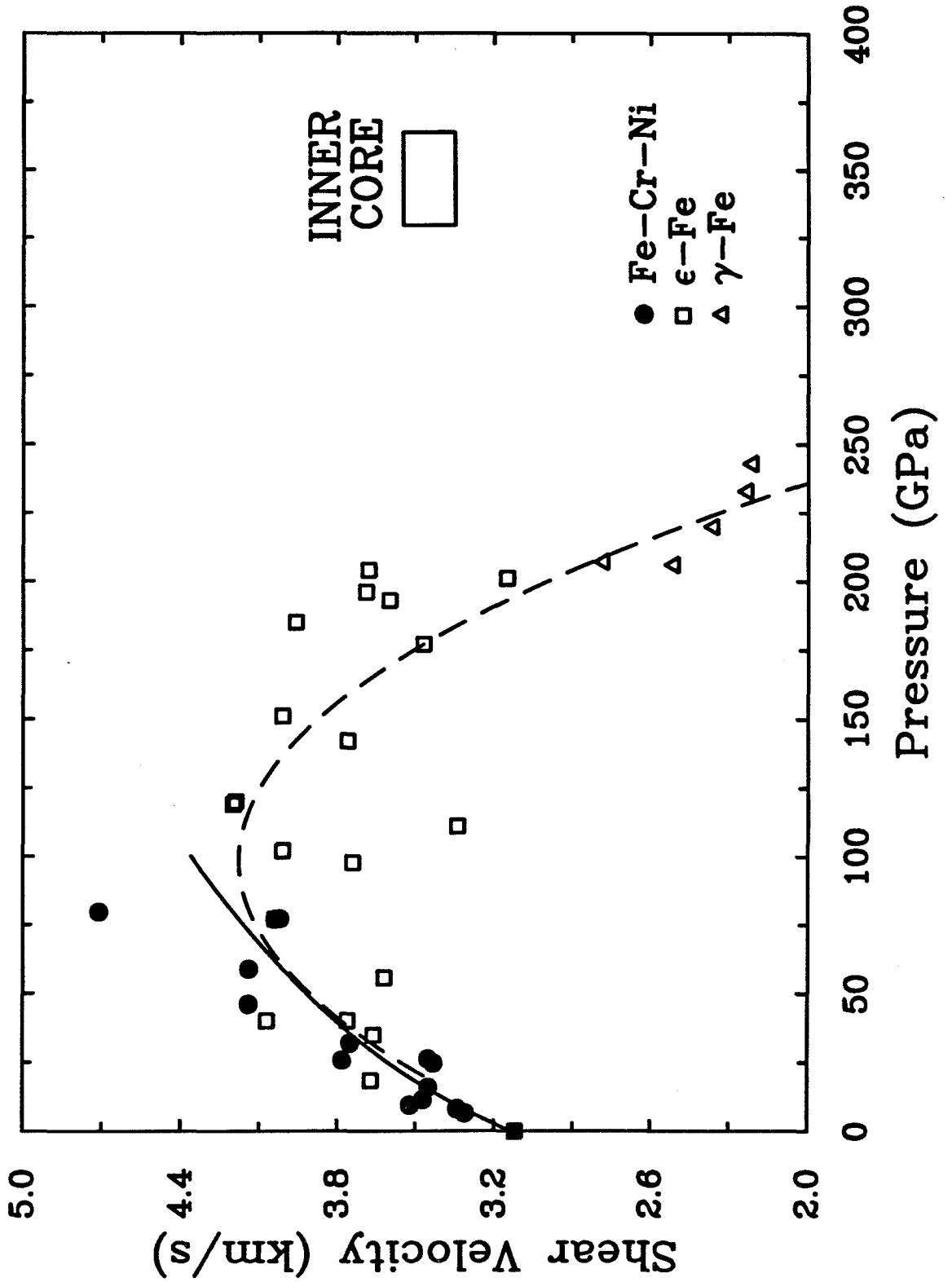
INNER
CORE
Fe–Cr–Ni
ε–Fe
γ–Fe
Shear Velocity (km/s)
5.0
4.4
3.8
3.2
2.6
2.0
Pressure (GPa)
0
50
100
150
200
250
300
350
400

Figure 2.6: Calculated Poisson's ratio along the Hugoniot for Fe and Fe-Cr-Ni from measured $V_P$ values and inferred $V_B$ trends. The bulk sound velocities are computed as described in the previous figure. The solid curve shows finite-strain extrapolation of ultrasonic data for Fe-Cr-Ni. The dotted curves are bounds on $\nu$ for Fe-Cr-Ni computed using the expressions of *Falzone and Stacey* [1980].

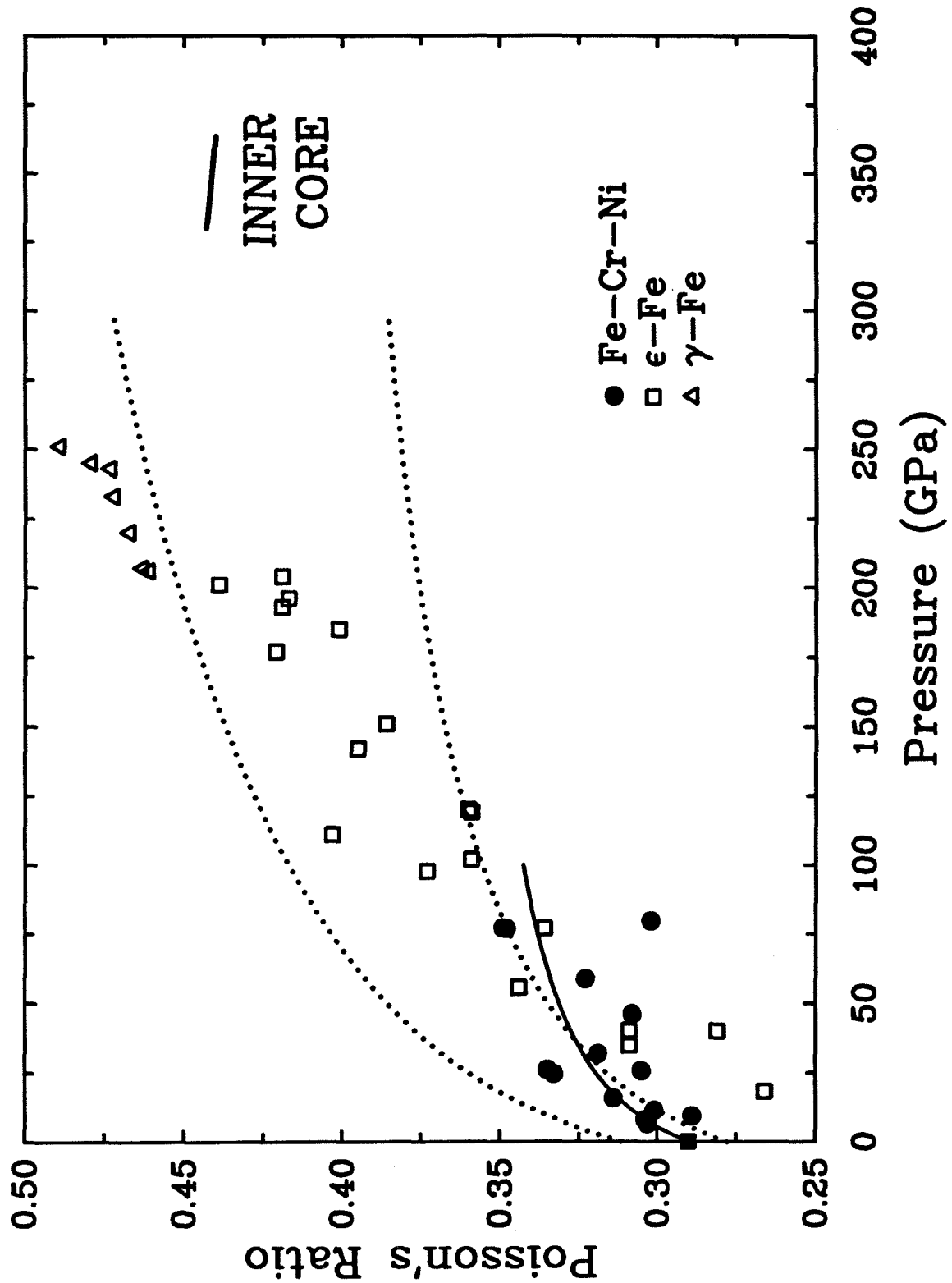
INNER
CORE
Fe–Cr–Ni
ε–Fe
γ–Fe
Poisson's Ratio
0.50
0.45
0.40
0.35
0.30
0.25
0
50
100
150
200
250
300
350
400
Pressure (GPa)

for Fe-Cr-Ni [*Gerlich and Hart,* 1984]. $V_S$ and $\nu$ for both Fe and Fe-Cr-Ni are similar to ultrasonic trends over this pressure interval. *Falzone and Stacey* [1980] proposed that higher-order pressure effects reduce the rigidity at high pressures and developed expressions for the pressure variation of the Voigt and Reuss bounds of the shear modulus for fcc metals. Application to Fe-Cr-Ni leads to the bounds on Poisson's ratio shown in Figure 2.6. Experimental data for the alloy to 80 GPa are consistent with the lower bound, which is similar to ultrasonic trends not including the second-order effects.

At higher pressures, shear velocities in Fe begin to decrease, tending towards 0 at the 243 GPa melting point. This produces a concomitant large increase in Poisson's ratio with pressure. One possible explanation for this behavior is that it reflects the effect of increasing temperature on $V_S$. It is shown in Chapter 4 that the temperature coefficient of compressional velocity, $(\partial V_P/\partial T)_P$, can be constrained at high pressure by comparing measured Hugoniot velocities with 300 K velocities calculated from extrapolation of ultrasonic data. We have performed a similar analysis to determine the value of $(\partial V_S/\partial T)_P$ required to explain the results of Figure 2.5. To accomplish this, we must know or estimate the elastic moduli and their pressure derivatives for the high-pressure phases of Fe. For $\epsilon$-Fe, the density, bulk modulus, and pressure derivative were taken from the results of 300 K static-compression experiments to 300 GPa [*Mao et al.,* 1990]. The shear modulus, $G$, and its pressure derivative, $G'$, have not been measured for this material. Since the pressure dependence of $V_S$ in Fe-Cr-Ni and Fe is similar up to ~50 GPa (Figure 2.5), we have assumed that $G$ and $G'$ are the same for these materials. Temperatures along the Hugoniot were taken from the calculations of *Brown and McQueen* [1986]. The temperature coefficient of the shear modulus is given by:

$$\left(\frac{\partial V_S}{\partial T}\right)_P \approx \frac{V_{SI} - V_{SH}}{300 - T_H}, \tag{2.11}$$

where I refers to the 300 K isotherm and H refers to the Hugoniot. Using the data

of Figure 2.5, we find $(\partial V_S/\partial T)_P$ = -0.3 ± 0.1 m/s/K for $\epsilon$-Fe between 100 and 200 GPa. Applying the same analysis to the $\gamma$(?)-Fe data above 200 GPa, we obtain $(\partial V_S/\partial T)_P$ = -0.5 ± 0.05 m/s/K. These results compare with ambient-pressure values of $(\partial V_S/\partial T)_P$ for bcc Fe and Fe-Cr-Ni of -0.3 and -0.6 m/s/K, respectively, [*Leese and Lord,* 1968; *Ledbetter et al.,* 1975]. Therefore, in order for temperature to account for the variation of $V_S$ shown in Fig. 2.5, the temperature coefficient of $V_S$ at P > 100 GPa must be comparable to ambient-pressure values for Fe and Fe alloys. In contrast, Hugoniot compressional velocities for Al, Cu, W, Ta, Mo, and $Mg_2SiO_4$ indicate that $(\partial V_P/\partial T)_P$ decreases strongly in magnitude with pressure (Chapter 4). We find that $(\partial V_P/\partial T)_P$ = -0.1 ± 0.1 m/s/K for these materials above 100 GPa. Thus, the temperature coefficient of $V_S$ required by the Fe data is inconsistent with trends for $(\partial V_P/\partial T)_P$ from a number of materials.

Shear velocities calculated using Eqn 2.9 are sensitive to the details of the inferred variation of the bulk sound velocity. Previously, it was shown that bulk velocity data for Fe could be fit with either a linear or a non-linear velocity-density trend. The above analysis for $V_S$ utilized the non-linear trend derived from the data of *Brown and McQueen* [1986]. The data of *Al'tshuler et al.* [1960] and the analysis of *Anderson* [1990] allow a linear bulk velocity-density trend to be constructed for Fe which differs from the previous relationship by $\leq$ 6%. The use of this relationship (Eqn. 2.9) produces a markedly different variation of shear velocity with pressure in Fe . This variation is shown in Figure 2.7. In this case, the shear velocities in $\epsilon$-Fe are nearly constant with pressure at $V_S$ = 3.6 ± 0.2 km/s. The shear velocities in $\gamma$(?)-Fe are lower ($V_S$ = 2.6 ± 0.1 km/s) and may decrease with pressure. The lack of variation of $V_S$ with pressure in $\epsilon$-Fe strongly contrasts with the increase in $V_S$ apparent in the Fe-Cr-Ni data up to 80 GPa.

A second possible explanation, therefore, for the low shear velocities in Fe at high pressure is a very weak pressure dependence of $G$. Many hcp metals possess

Figure 2.7: Calculated shear velocities along the Hugoniot for Fe and Fe-Cr-Ni, assuming linear velocity-density relationships for $V_P$ and $V_B$ in Fe. The solid symbols and solid curve are for Fe-Cr-Ni and are computed as described in Figure 2.5. The open symbols are calculated Fe velocities using measured compressional velocities and the linear $V_B$-$\rho$ relations of Eqn 2.8. The dashed curve shows the calculated variation of $V_S$ in Fe, using Eqns. 2.5, 2.6, and 2.8 together with the EOS for solid Fe. The dotted curves show calculated shear velocities in Fe at 300 K using various values of the pressure derivative of the shear modulus. Inner core velocities from free oscillation data are shown by the box.

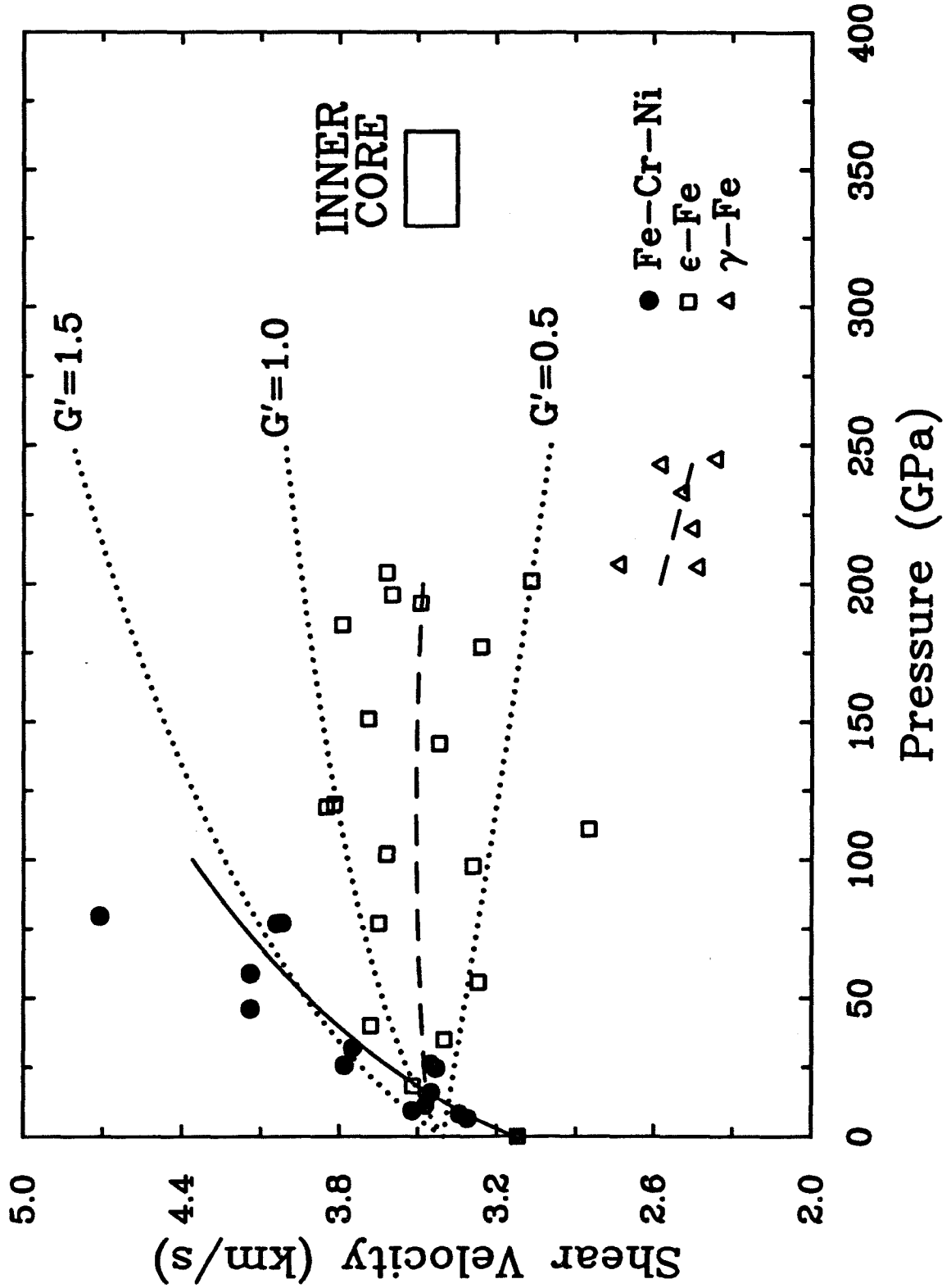
Shear Velocity (km/s)
5.0
4.4
3.8
3.2
2.6
2.0
Pressure (GPa)
0
50
100
150
200
250
300
350
400
G'=1.5
G'=1.0
G'=0.5
INNER CORE
Fe—Cr—Ni
ε—Fe
γ—Fe

low ($< 1.0$) shear modulus pressure derivatives [*Guinan and Steinberg,* 1974]. *Jeanloz and Wenk* [1988] argue that Ti is an appropriate elastic analog for $\epsilon$-Fe because in addition to having the same crystal structure, the c/a ratios and ratios of linear compressibilities at zero pressure are identical for these materials. The pressure derivative of $G$ for Ti is 0.48 [*Guinan and Steinberg,* 1974]. Assuming $V_S$ is 3.4 km/s at ambient conditions, we have computed the expected variation of $V_S$ with pressure at 300 K for different values of $G'$, and these are shown in Figure 2.7. These results show that a value of $G' \sim 1$ provides an upper bound for values of $V_S$ along the Hugoniot. The effective shear modulus pressure derivative for $\epsilon$-Fe, reflecting both the effects of pressure and temperature, is less than 1.0.

Regardless of the form chosen for $V_B$, the data for Fe suggest that shear velocities in $\epsilon$-Fe at P $>$ 100 GPa are comparable to inner core values. This could be due to a strong temperature coefficient of the shear velocity, but we feel that it is more likely due to a weak dependence of the rigidity on pressure. Shear velocities in $\gamma$(?)-Fe are $\sim$2.5 km/s and lie well below inner core values.

## 2.5 Summary

Hugoniot compressional sound velocities in Fe and Fe-Cr-Ni define linear velocity-density trends (Birch's Law) over the entire data range for these materials. Velocities in the alloy are up to 8% faster than those in Fe for densities up to 10.1 g/cm$^3$. Compressional velocities in Fe-Cr-Ni can be approximately ($\sim$3%) modeled by averaging endmember properties and using atomic fractions as weights. This analysis leads to the conclusion that it is the presence of $\sim$19% Cr that is responsible for the higher compressional velocities in the alloy.

Compressional velocities in Fe and Fe-Ni have been estimated under inner core conditions (P=329-364 GPa, T=6000-7500 K) from observed velocity-density trends, a linear mixing model that accounts for the effects of Ni, and a temperature coefficient

of velocity, $(\partial V_P/\partial T)_P$, equal to -0.1 m/s/K. At a given pressure, velocities in $\epsilon$-Fe alloyed with 4 wt.% Ni are 1-2.5% below PREM values under inner core conditions. Velocities in $\gamma$(?)-Fe alloyed with 4 wt.% Ni are 5.5-7% below PREM values. The effect of Ni is to produce a very slight ($< 1\%$) decrease in $V_P$ for $\epsilon$-Fe and an increase for $\gamma$(?)-Fe. Thermal corrections at constant pressure from Hugoniot to inner core conditions are estimated to range from 1-2.5% for upper (7500 K) and lower (6000 K) bounds on inner core temperature. These results suggest that the properties of $\epsilon$-Fe plus $\sim$4 wt.% Ni are consistent with seismic values for $V_P$ in the inner core. The properties of $\gamma$(?)-Fe lie well below inner core velocities even when the effects of alloying with Ni and thermal effects are accounted for. Our conclusions are similar to those of *Brown and McQueen* [1986] from a consideration of Fe sound velocity data. We have shown that these conclusions remain valid when the effects of Ni content and thermal corrections are taken into account. The present results cannot exclude the presence of a light, high-$V_P$ component in the inner core, but no bounds on such a component can be drawn because of the lack of high-pressure $V_P$ data for such materials.

The variation of bulk sound velocity with density in Fe is ambiguous given current shock wave data. Two possible $V_B$-$\rho$ relationships are outlined. A simple linear relationship between velocity and density ($V_B$ = -5.45 + 1.20$\rho$) is consistent with some $V_B$ data for solid and liquid Fe [*Al'tshuler et al.*, 1960; *Anderson*, 1990]. Such a relationship for $V_B$ has also been found to hold for Fe-Cr-Ni ($V_B$ = -4.64 + 1.16$\rho$) at densities between 7.9 and 10.1 g/cm$^3$. The $V_B$-$\rho$ slopes for these materials are 16-20% greater than those observed in the Earth's outer core ($V_B$ = -1.84 + 1.00$\rho$). The second possible $V_B$-$\rho$ relationship is non-linear over the outer core density range and is constrained by the liquid-iron data of *Brown and McQueen* [1986]. It is based on the thermodynamic relationship between the Grüneisen parameter and the bulk sound velocity and uses a constant $\rho\gamma = 19.7 \pm 0.7$ [*Brown and McQueen*, 1986].

These two relationships yield bulk sound velocities in Fe that differ by $\leq$ 6% at densities up to 13.4 g/cm$^3$.

Bulk sound velocities in Fe-Cr-Ni can also be modeled using a weighted average of endmember properties with atomic fractions as weights. The effect of incorporating ~4 wt.% Ni in Fe is estimated to decrease $V_B$ by less than 1%. For both the inner and outer core, Hugoniot bulk velocities in Fe are up to 4% below PREM values at a given pressure. When viewed at constant density, Fe velocities are 13-25% below outer core values but remain within 4% of inner core values. This is consistent with a nearly pure iron inner core and an outer core with a significant impurity content. At constant pressure, bulk velocities in Fe are similar to outer core values, implying that the light element in the outer core must have only a small effect on $V_B$. Calculated velocities for FeO and $FeS_2$ are significantly faster than those in Fe, while those in FeH are slightly slower than Fe velocities. This suggests that the presence of H in the outer core could at least partially compensate for increases in bulk velocity that would result from incorporation of S and O.

Constraints on shear velocities and Poisson's ratio in Fe and Fe-Cr-Ni were drawn by comparing measured compressional velocities with inferred bulk velocity trends. Shear velocities in Fe-Cr-Ni increase up to 80 GPa in a manner consistent with the extrapolation of ultrasonic data. At P = 150-200 GPa, shear velocities in $\epsilon$-Fe are ~3.6 km/s. For $\gamma$(?)-Fe, the shear velocity is ~2.5 km/s at P = 200-243 GPa. However, the variation of $V_S$ with pressure in Fe is strongly dependent on the form of the $V_B$-$\rho$ relationship. Two possible shear velocity-pressure relationships consistent with current data are outlined. The behavior of $V_S$ can be explained by either a strong temperature dependence or a weak pressure dependence of the shear modulus. The values of $(\partial V_S/\partial T)_P$ required to explain data for $\epsilon$-Fe and $\gamma$(?)-Fe are -0.3 $\pm$ 0.1 m/s/K and -0.5 $\pm$ 0.05 m/s/K, respectively. These values are considered to be implausible because they contradict compressional velocity data for a number

of materials which indicate that $(\partial V_P/\partial T)_P$ > -0.2 m/s/K for pressures exceeding 100 GPa. The second alternative is that the effective pressure derivative of $G$ along the Hugoniot is small, between 0.5 and 1.0. This is consistent with ultrasonic data for other hcp metals such as Ti. The data for Fe-Cr-Ni require a much stronger pressure dependence of $G$ ($G' \approx$ 1.5-2). Both analyses for $V_S$ lead to the conclusion that at high P (> 100 GPa) shear velocities in Fe are low (< 4.0 km/s) and Poisson's ratio values are greater than 0.35. The shear velocity of the inner core is 3.45 $\pm$ 0.1 km/s and is comparable to $\epsilon$-Fe values at P > 100 GPa. This provides further support for $\epsilon$-Fe as the stable of phase of Fe in the inner core and implies that partial melting is not required to explain the shear properties of the inner core.

# Chapter 3

# Elasticity, Equation of State, and Constitutive Behavior of Shock-Compressed Polycrystalline Magnesium Oxide

## 3.1 Introduction

Magnesium oxide (MgO) is a material of geological importance because of its potential role as a lower mantle component. Its exceptional stability from ambient conditions to pressures above 100 GPa under both dynamic and static loading also makes it an attractive and significant material for study. In this work, we have measured the equation of state (EOS), compressional wave velocities, and wave profiles on nearly fully dense polycrystalline MgO under shock wave compression. Results for ceramic MgO, or magnesia, will be compared with a variety of other data, including Hugoniot and ultrasonic data for crystalline MgO (periclase).

The comparison of shock wave data with static or ultrasonic data is important

for a number of geophysical applications. Shock wave-derived isotherms are relied upon to create pressure scales for diamond anvil and other static high-pressure experiments. Comparison of sound velocities and densities under shock conditions with those measured or extrapolated under static conditions allows the effects of pressure and temperature on these properties to be determined. There are a number of potential reasons as to why shock and ultrasonic data may not be comparable. These include shock-induced fabric, material strength, thermal heterogeneities, and thermodynamic disequilibrium [*Grady,* 1977]. To understand fully the potential role of these factors, the shock-compression process must be understood in great detail.

Compositional models of the Earth's interior rely on comparison of laboratory determinations of elastic wave velocity and density with seismic data. Shock wave measurements offer a means to assess the accuracy of sound velocities extrapolated to mantle conditions from high-precision but low-pressure ultrasonic data. In this work, we also use equation of state data and temperature measurements to infer thermal expansivities at ultra-high pressure. Knowledge of thermal expansivities at high pressure and temperature is essential to test for changes in bulk composition between the upper and lower mantle.

The equations of state of both single-crystal and porous polycrystalline MgO have been studied extensively using shock techniques. However, no data on low-porosity polycrystalline MgO have been available previously. The only existent wave profile data on this material are several profiles for single-crystal MgO between 4.8 and 11.2 GPa reported by *Grady* [1977]. It has long been recognized that the dynamic deformation of single-crystal and polycrystalline ceramics can differ greatly [*Ahrens et al.,* 1968]. Therefore, it is of interest to study the loading and release behavior of polycrystalline MgO to provide an improved basis for understanding the different response of single crystals and polycrystals to shock deformation.

Wave profile measurements have yielded extensive information on the high-strain-

rate deformation of metals, but much less information is available for ceramics. In general, single crystals exhibit at least partial loss of strength, but polycrystals retain most or all of their material strength. Most work to date has focused on high-strength ceramics that have more obvious engineering applications. We will address the question of whether the dynamic behavior of MgO, a relatively low-strength ceramic, can be described by employing concepts that have proven useful for metals. The study of ceramics is particularly relevant, as these materials are less well characterized than metals and exhibit a wide range of response to high-strain-rate deformation.

## 3.2 Experimental Method

### 3.2.1 Samples

Low-porosity polycrystalline magnesium oxide (MgO) samples were obtained commercially (Cercom Inc., Vista, CA) in the form of 1.25" diameter hot-pressed disks. The manufacturer's specifications indicated that the density was within 1% of crystal density and chemical purity was greater than 99.5%. The latter was confirmed by electron microprobe analysis which revealed a small amount of CaO ($\sim$0.3%) and the presence of no other impurities at detectable levels. Bulk densities were measured by weighing the $\sim$10 g samples in air with a sensitive microbalance to $\pm$ $10^{-4}$ g. Crystal densities were determined through the Archimedean immersion technique. The average crystal density of the samples was found via the Archimedean method to be 3.571 $\pm$ 0.004 g/cm$^3$, and the average bulk density obtained by weighing and measuring the samples was 3.562 $\pm$ 0.006 g/cm$^3$, both of which are within better than 1% of the standard x-ray density (3.584 g/cm$^3$) of this material. Examination of thin sections by optical microscopy revealed a structure of colorless, roughly equant grains with approximate dimensions of 5 $\mu$m. No porosity could be detected optically. Sample flatness variations were less than 0.01 mm.

Ultrasonic sound velocity measurements were performed on a representative sam-

ple in the direction of hot-pressing (and shock wave propagation) by Dr. Sally M. Rigden at Australian National University. Measurements between 30 and 70 MHz revealed little dispersion in velocity ($\pm$ 0.005 km/s) and a compressional wave velocity of 9.81 $\pm$ 0.02 km/s when corrected for a transducer bond thickness of 0.3 $\mu$. This is 1.1% greater than the the Voigt-Reuss-Hill (VRH) average for a single crystal of this material reported by *Jackson and Niesler* [1982].

### 3.2.2 Experiments

#### Equation of State Experiments

A series of equation of state (EOS) experiments were conducted on MgO specimens using both a propellant and a light gas gun. A 40-mm bore propellant gun was used to launch ~100-g projectiles to velocities up to 2.5 km/s. A two-stage light gas gun was used to accelerate ~20-g projectiles to 6.5 km/s. In both cases, projectiles consisted of a metallic flyer plate encased in a lexan body. Projectile velocity was measured to ~1% on the 40-mm gun and to ~0.1% on the light gas gun by recording x-ray shadowgraphs immediately prior to impact. A He-Ne laser-intervalometer system provided a redundant back-up velocity measurement for the propellant gun.

The MgO targets were mounted on driver plates of pure tantalum or aluminum 2024 and placed in an evacuated (~100 mm Hg) sample chamber. Two pairs of flat mirrors were mounted in a linear array on the rear surface of the target and driver. An inclined wedge was mounted in line in the center of the target. An expendable turning mirror directed light from a 10-kV Xenon flash lamp onto the rear of the target and reflected light was directed to a continuous writing streak camera. Shock wave velocities were measured by recording the destruction times of the mirrors by the oncoming shock front and by the change in extinction angle of the inclined wedge. Uncertainties are primarily caused by uncertainties in interpreting changes in optical density on the film and uncertainties in timing that are due to tilt.

The thermodynamic state behind the shock front was determined by application of the Rankine-Hugoniot conservation equations. Details regarding the experimental apparatus and data analysis techniques can be found in *Ahrens and Gregson* [1964]; *Jones et al.* [1966]; *Ahrens et al.* [1971]; and *Ahrens* [1987].

### Wave Profile Measurements

In addition to the equation of state experiments, a series of wave profile measurements were undertaken using shock wave velocimetry. Wave profile measurements yield a continuous record of the particle velocity at a sample interface during both the loading and unloading cycles of the experiment. The measurement technique used for recording particle velocity histories was the velocity interferometer system for any reflector (VISAR) [*Barker and Hollenbach,* 1972]. In this technique, 200-300 mW of light from an $Ar^+$ ion laser is focused onto the diffusely reflecting rear surface of the sample under test. Target motion induces a Doppler shift in the reflected laser light, which produces time-dependent light-intensity changes (interference fringes) in a wide-angle Michelson interferometer. The interference fringes are detected and recorded using four photomultiplier tubes and a pair of two-channel digital oscilloscopes. The relationship between surface velocity and the number of fringes recorded is given by [*Barker and Hollenbach,* 1972; *Barker and Schuler,* 1974]:

$$u(t - \tau/2) = kF(t), \tag{3.1}$$

where $u$ is the particle velocity, $t$ is the time, $\tau$ is the lag time of the interferometer, $k$ is the velocity-per-fringe constant, and $F(t)$ is the number of fringes recorded up to time $t$. The fringe constant $k$ can range from ~100 m/s/fringe to over 1 km/s/fringe and is controlled in part by inserting variable lengths of fused silica bars in one arm of the interferometer.

Figure 3.1 shows an example of a velocity profile and one of the fringe records from which the profile was derived. Rapid light-intensity changes associated with the

arrival of the elastic precursor and the shock front are evident as are several fringes produced during the unloading of the specimen. The shock arrival in all the present experiments produced a burst of fringes at too high a frequency to be tracked by the ~250 MHz recording system. The change in interface velocity at this point can be determined reliably from the known impact velocity, an estimate or knowledge of the EOS of the target and flyer, and the signal-intensity levels before and after the velocity jump [*Barker and Hollenbach,* 1972; *Barker,* 1988b].

The VISAR we have constructed is similar to that originally described by *Barker and Hollenbach* [1972] except that we have incorporated the push-pull modification and data reduction algorithm of *Hemsing* [1979] and the polarization-randomization scheme of *Asay and Barker* [1974]. A detailed description of VISAR construction and operation can be found in the appendix as well as in *Crump and Stanton* [1988].

Two types of impact geometries were used in the present experiments. The first type, known as the reverse-impact geometry, is illustrated in Figure 3.2. In this arrangement, the material under study is inserted in the projectile and is used to impact a thin (1-2 mm) aluminum buffer with an LiF window epoxied to it. The VISAR monitors the interface between the window and the buffer. An array of electrical shorting pins is used as part of a capacitor-discharge circuit to trigger recording instrumentation and to measure impact planarity. The sample is backed by a low-density foam layer which serves to introduce an unloading wave into the specimen. All wave profile measurements in this study were conducted on the 40-mm bore propellant gun.

A Lagrangian wave propagation diagram for the reverse-impact experiments is shown in Figure 3.3. At impact (t=0), an elastic precursor and a shock wave are propagated through the sample, and a shock is propagated through the buffer. It is assumed here that the impact stress is sufficient to overdrive the precursor in aluminum but not sufficient to overdrive the precursor in MgO. At time $t_1$, the

Figure 3.1: Velocity profile for MgO and one of the four interferograms from which the profile was derived. The lower portion of the figure shows light-intensity changes (fringes) recorded by a photomultiplier tube. Increasing light intensity produces a negative voltage. Light-intensity changes correlate with velocity changes shown in the top figure.

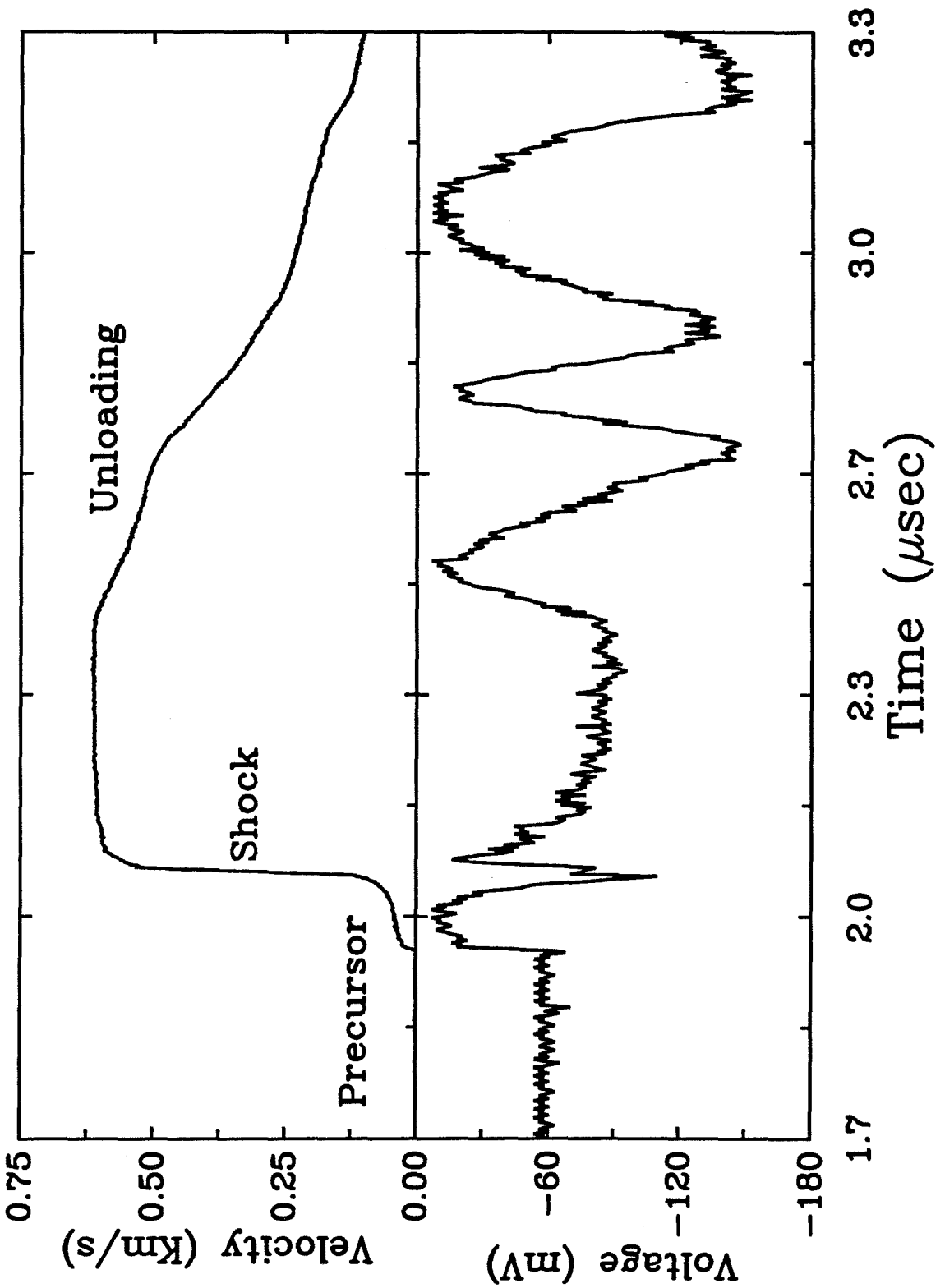
Unloading
Shock
Precursor
Velocity (Km/s)
0.75
0.50
0.25
0.00
Voltage (mV)
−60
−120
−180
1.7
2.0
2.3
2.7
3.0
3.3
Time (μsec)

Figure 3.2: Experimental set up for reverse-impact experiments on polycrystalline MgO.

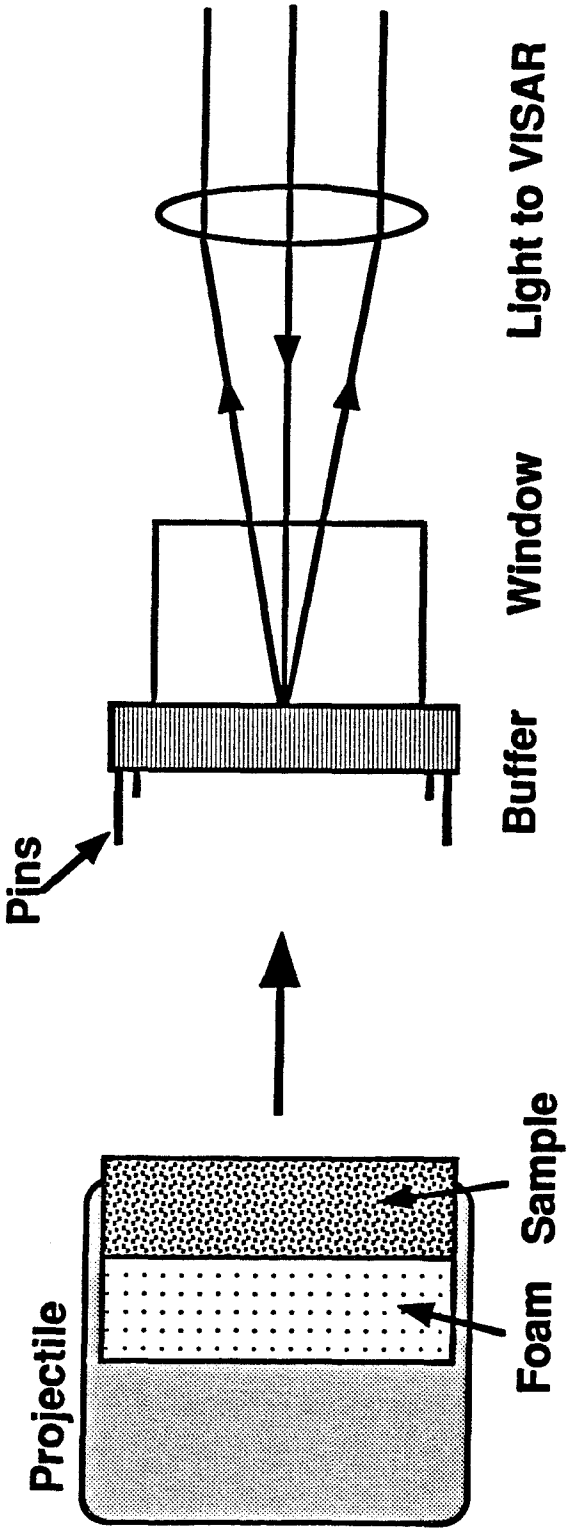
Light to VISAR
Window
Buffer
Pins
Sample
Foam
Projectile

shock reaches the buffer-window interface and is recorded by the VISAR. The slight impedance contrast between LiF and aluminum causes a weak rarefaction to propagate through the aluminum which returns to the reflecting surface at time $t_2$. The elastic precursor traveling through the sample eventually reaches the sample-foam interface, reflects from it, and interacts with the oncoming shock wave. The shock wave also reflects from the foam interface and produces a rarefaction fan which further unloads the material from the high-pressure state. The unloading of the sample is recorded as a decrease in particle velocity beginning at time $t_3$.

The reverse-impact arrangement is well suited for measuring the unloading properties of the sample and in particular, the initial unloading wave velocity. The particle velocity jump recorded at $t_1$, in conjunction with EOS information for the buffer material, provides indirect information on the EOS of the sample. A summary of the impact parameters for these experiments is given in Table 3.1.

In order to obtain more direct information on the compressive properties of the samples, a second series of experiments called forward-impact experiments were conducted. The experimental arrangement for these experiments is shown in Figure 3.4. The flyer plate impacts the sample to which a thin aluminum buffer has been epoxied. Sample-buffer and buffer-window epoxy layers were $\sim$10 mm thick in both these and the reverse experiments. For all but one of the experiments, the flyer and sample were the same material, so symmetric impact conditions applied. The VISAR again monitors the buffer-window interface. The impact parameters for these experiments are listed in Table 3.2.

A Lagrangian distance-time diagram illustrating the propagation and interaction of the waves of interest is shown in Figure 3.5. Symmetric impact causes an elastic precursor followed by a slower plastic shock to travel through both the flyer and the sample. The impedance contrast between the sample and buffer causes a partial unloading wave (dashed lines) to travel back through the sample. The precursor and

Figure 3.3: Lagrangian distance-time diagram for a representative reverse-impact experiment. $V_{P_o}$ is the elastic precursor velocity, $U_S$ is shock velocity, $V_P$ is the compressional sound velocity, $t_1$-$t_3$ correspond to wave-arrival times. $h_1$ is the distance to the point where the reflected precursor and direct shock interact. The subscript b refers to the buffer and s refers to the sample (MgO).

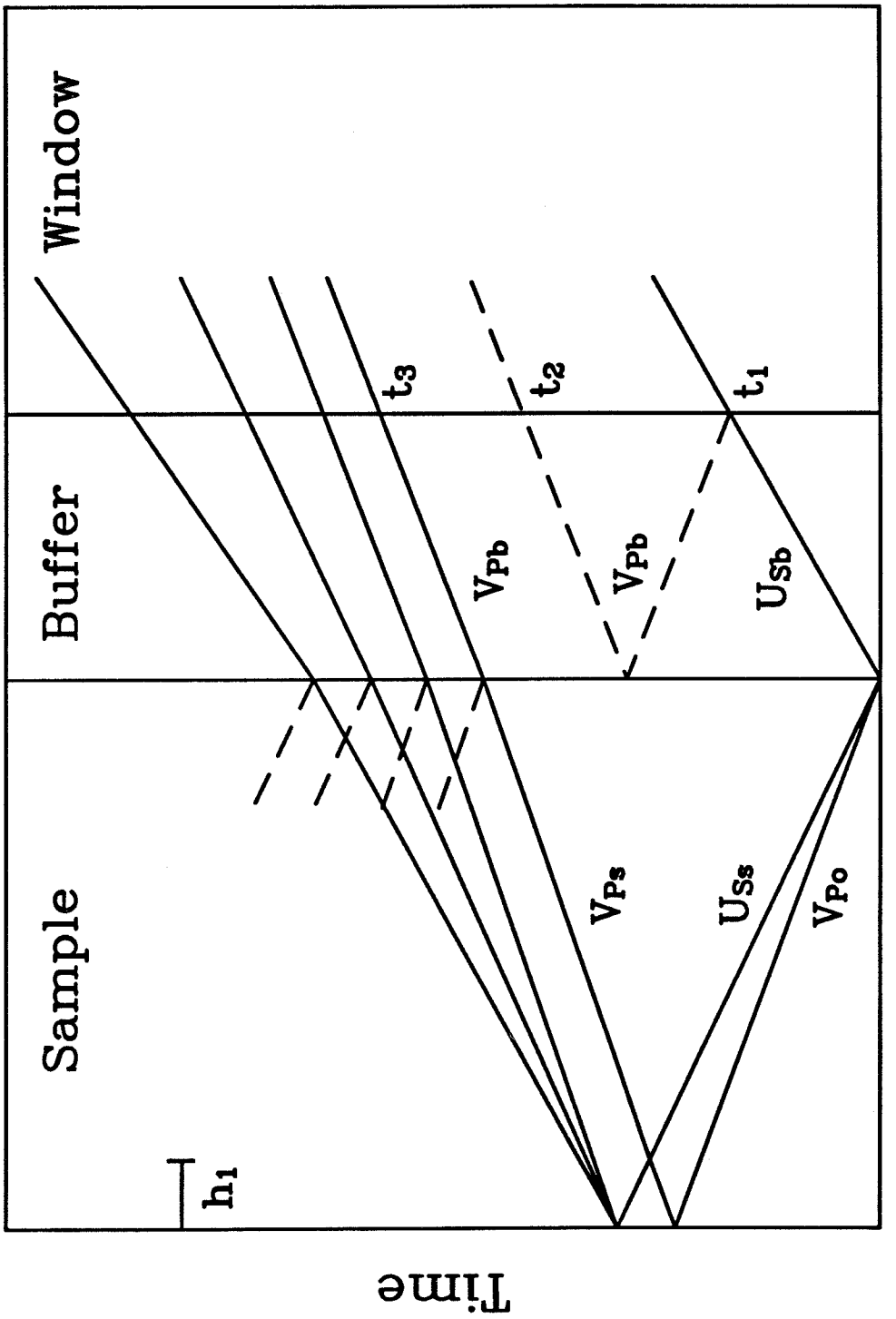
Window
Buffer
Sample
$t_3$
$t_2$
$t_1$
$V_{Pb}$
$V_{Pb}$
$U_{Sb}$
$V_{Ps}$
$U_{Ss}$
$V_{Po}$
$h_1$
Time
Distance

| Shot | Sample | | Buffer | | Window | | |
|---|---|---|---|---|---|---|---|
| | $\rho_o$ ($g/cm^3$) | thickness (mm) | $\rho_o$ ($g/cm^3$) | thickness (mm) | $\rho_o$ ($g/cm^3$) | thickness (mm) | $u_{fp}$ (km/s) |
| 844 | 3.557 | 4.026 | 2.663 | 0.976 | 2.633 | 12.128 | 2.001 |
| | 0.004 | 0.004 | 0.004 | 0.002 | 0.005 | 0.005 | 0.021 |
| 848 | 3.561 | 4.025 | 2.681 | 1.955 | 2.631 | 12.133 | 1.432 |
| | 0.002 | 0.002 | 0.004 | 0.002 | 0.001 | 0.003 | 0.010 |
| 851 | 3.569 | 3.032 | 2.681 | 1.962 | 2.630 | 12.138 | 2.366 |
| | 0.008 | 0.006 | 0.003 | 0.002 | 0.001 | 0.002 | 0.035 |
| 853 | 3.558 | 3.030 | 2.684 | 1.887 | 2.629 | 8.128 | 1.612 |
| | 0.007 | 0.002 | 0.003 | 0.002 | 0.004 | 0.003 | 0.019 |
| 854 | 3.568 | 4.018 | 2.687 | 1.880 | 2.626 | 12.142 | 1.020 |
| | 0.003 | 0.002 | 0.005 | 0.003 | 0.001 | 0.002 | 0.009 |
| 856 | 3.570 | 4.025 | 2.685 | 1.953 | 2.628 | 12.131 | 2.165 |
| | 0.004 | 0.004 | 0.006 | 0.004 | 0.001 | 0.002 | 0.020 |
| 860 | 3.573 | 6.398 | 16.614 | 2.785 | 2.634 | 12.142 | 2.445 |
| | 0.001 | 0.002 | 0.016 | 0.002 | 0.002 | 0.003 | 0.036 |

Table 3.1: Initial parameters for reverse-impact experiments. All windows are LiF and all buffers are Al 6061 except for shot 860, which used a Ta buffer.

Figure 3.4: Experimental arrangement for forward-impact experiments on polycrystalline MgO.

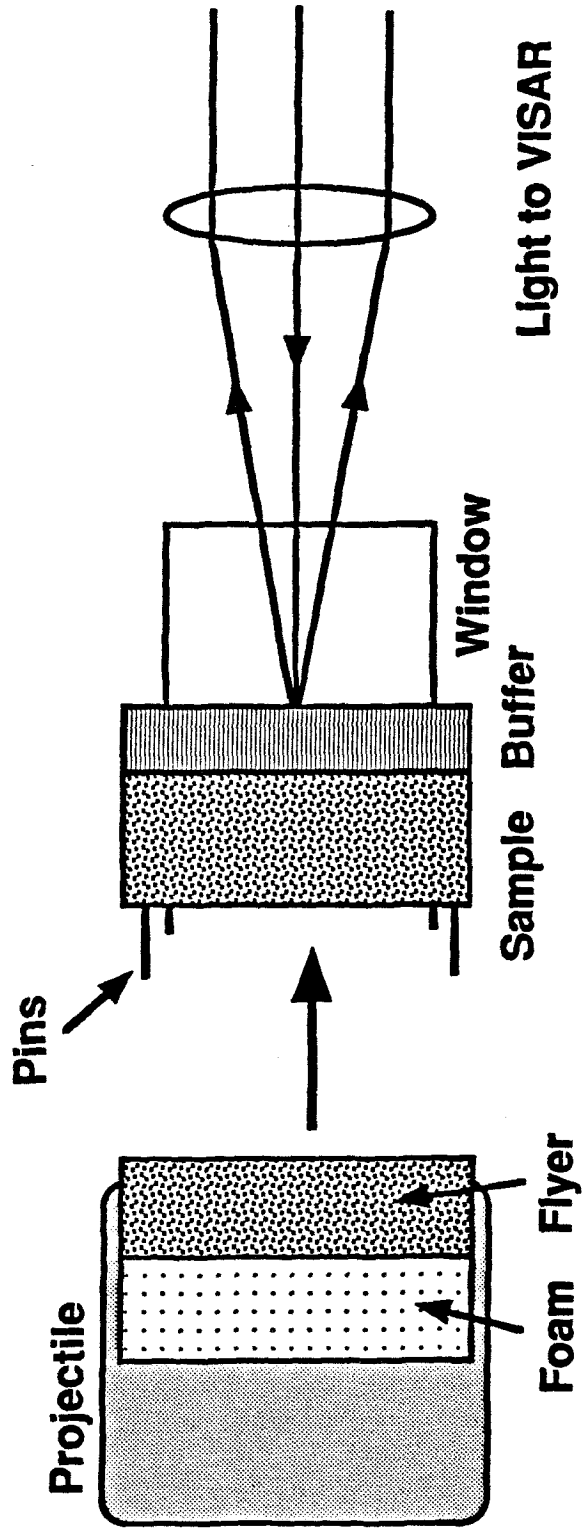
Light to VISAR
Window
Buffer
Sample
Pins
Flyer
Foam
Projectile

| Shot | Flyer | | Sample | | Buffer | | |
|---|---|---|---|---|---|---|---|
| | $\rho_o$ ($g/cm^3$) | thickness (mm) | $\rho_o$ ($g/cm^3$) | thickness (mm) | $\rho_o$ ($g/cm^3$) | thickness (mm) | $u_{fp}$ (km/s) |
| 857 | 3.563 | 3.024 | 3.561 | 4.030 | 2.683 | 1.944 | 1.520 |
| | 0.004 | 0.002 | 0.004 | 0.004 | 0.003 | 0.002 | 0.020 |
| 859 | 3.563 | 3.026 | 3.564 | 4.023 | 2.679 | 1.942 | 2.432 |
| | 0.004 | 0.003 | 0.002 | 0.002 | 0.003 | 0.002 | 0.030 |
| 861 | 3.558 | 3.030 | 3.551 | 4.025 | 2.684 | 1.980 | 1.015 |
| | 0.004 | 0.002 | 0.006 | 0.002 | 0.003 | 0.002 | 0.008 |
| 864 | 3.836 | 3.217 | 3.566 | 3.780 | 2.687 | 1.946 | 2.471 |
| | 0.012 | 0.010 | 0.005 | 0.004 | 0.004 | 0.003 | 0.032 |

Table 3.2: Initial parameters for forward-impact experiments. The flyers were all MgO except for shot 864, which had an $Al_2O_3$ flyer. The buffers were Al 6061 and the windows for these experiments were LiF (2.63 $g/cm^3$, 8 mm thick).

shock travel through the buffer and reach the buffer-window interface at times $t_1$ and $t_2$. The small (~3%) impedance contrast between the buffer and window has been neglected in this analysis. The elastic precursor in the flyer eventually reaches the back surface and reflects from it. It interacts with the oncoming shock wave at position $h_1$ and later interacts with the buffer-sample reflection at position $h_2$. It reaches the buffer-window surface at time $t_3$ and produces a decrease in particle velocity which is recorded by the VISAR. Subsequently, the unloading fan from the shock front arrives and further reduces the particle velocity. The thickness of the window free surface is chosen such that the shock front reaches the window free surface after the experimental time of interest.

The forward-impact experiments have the disadvantage that the unloading portion of the waveform is significantly affected by wave interactions generated at the sample-buffer interface. These wave interactions are eliminated in the reverse geometry which allows for a more direct determination of the unloading wave speed. The peak stress attainable in the reverse-impact experiments using an Al buffer is limited to ~27 GPa with the present propellant gun. Higher stresses were achieved by using a Ta buffer in one experiment (shot 860), but in this case the impedance contrast between the buffer and window is large and can no longer be neglected.

## 3.3 Results

The Hugoniot states determined from the equation of state experiments conducted on polycrystalline MgO are listed in Table 3.3. The measured shock and flyer plate velocities were combined with impedance-matching techniques [*Ahrens,* 1987] and the Rankine-Hugoniot conservation equations to constrain the shock velocity, particle velocity, stress, and density of the shock-compressed state. The equation of state parameters for the flyer and driver plates used in this process are listed in Table 3.4. The elastic precursor is evidently weak in amplitude and could be resolved

Figure 3.5: Lagrangian distance-time diagram for a representative forward-impact experiment. The symbols are the same as for the previous figure. In addition, $h_2$ is the thickness of the buffer-sample interaction region, and $V^*$ is the average velocity in the interaction region. The subscript f refers to flyer properties.

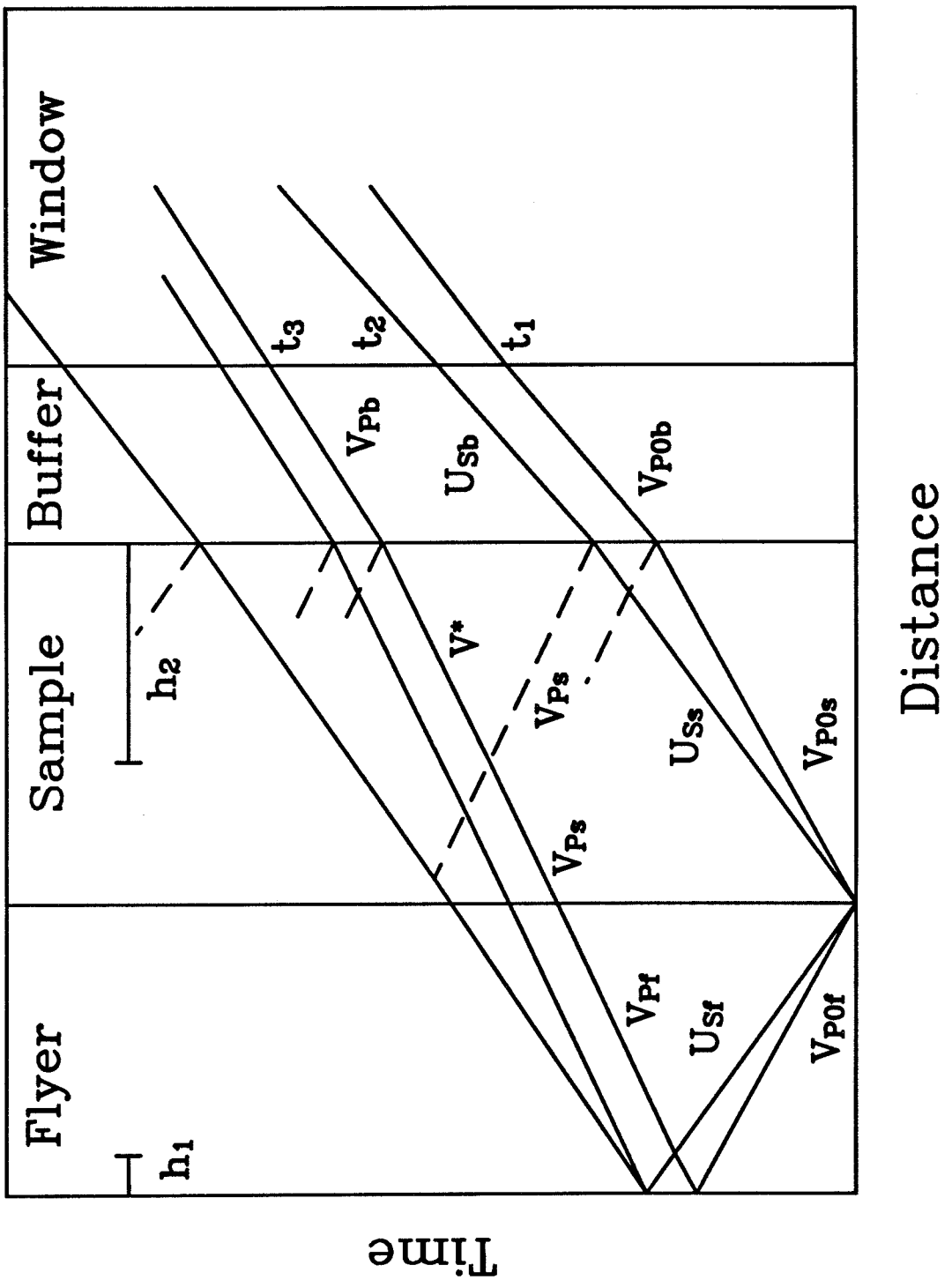
Flyer
Sample
Buffer
Window
h1
h2
t3
t2
t1
VPb
USb
VP0b
V*
VPs
VPs
USs
VP0s
VPf
USf
VP0f
Time
Distance

| Shot | Flyer/Driver | $u_{fp}$ (km/s) | $\rho_o$ (g/cm$^3$) | $u_p$ (km/s) | $U_S$ (km/s) | $\sigma$ (GPa) | $\rho$ (g/cm$^3$) | $V_{Po}$ (km/s) |
|---|---|---|---|---|---|---|---|---|
| 233 | Ta | 4.876 | 3.566 | 3.367 | 11.042 | 132.6 | 5.130 | - |
| | | (0.003) | (0.012) | (0.012) | (0.073) | (0.8) | (0.027) | |
| 840 | Ta | 1.291 | 3.552 | 0.893 | 7.96 | 25.3 | 4.001 | - |
| | | (0.011) | (0.010) | (0.008) | (0.11) | (0.3) | (0.015) | |
| 841 | Ta | 2.521 | 3.561 | 1.742 | 9.01 | 55.9 | 4.415 | - |
| | | (0.030) | (0.006) | (0.023) | (0.13) | (0.9) | (0.025) | |
| 843 | Mg/ | 1.713 | 3.566 | 0.513 | 7.53 | 13.8 | 3.827 | 9.77 |
| | Al2024 | (0.017) | (0.012) | (0.010) | (0.12) | (0.2) | (0.016) | (0.12) |

Table 3.3: Results of equation of state experiments for polycrystalline MgO. $\rho$ is the density, $u_p$ is the particle velocity, $U_S$ is the shock velocity, $\sigma$ is the stress, $V_{Po}$ is the elastic precursor velocity, and the subscript o represents ambient-pressure conditions.

only in one experiment (shot 843) from which a precursor velocity of 9.77 $\pm$ 0.12 km/s was obtained. This agrees with the ultrasonically measured ambient-pressure longitudinal sound velocity of 9.81 $\pm$ 0.02 km/s discussed previously. The results of the equation of state experiments are presented in the shock velocity-particle velocity and pressure-density planes in Figures 3.6 and Figure 3.7.

The loading and unloading wave profile measurements are shown in Figures 3.8, 3.9, and 3.10. Figure 3.8 shows the buffer-window particle velocities measured in the reverse-impact experiments using Al 6061 buffers. The arrival of the aluminum elastic precursor was recorded in the lowest-pressure experiment (shot 854). The sharp increase in particle velocity near $t = 0.8$ $\mu$sec is the arrival of the shock front ($t_1$). This is followed by a plateau region where the particle velocity is nearly con-

| Material | $\rho_o$ ($g/cm^3$) | $c_o$ (km/s) | $s$ | $\gamma_o$ | $\nu_o$ | $Y_o$ (GPa) | Refs. |
|---|---|---|---|---|---|---|---|
| MgO | 3.56 | 6.77 | 1.27 | 1.52 | 0.18 | 1.25 | a |
| | 0.01 | 0.07 | 0.04 | | | | |
| Al6061 | 2.683 | 5.349 | 1.338 | 2.10 | 0.34 | 0.3 | b |
| | 0.003 | 0.056 | 0.020 | | | | |
| Ta | 16.65 | 3.293 | 1.307 | 1.60 | 0.34 | 0.75 | c |
| | 0.03 | 0.005 | 0.025 | | | | |
| LiF | 2.64 | 5.15 | 1.35 | 1.63 | 0.22 | 0.2 | b |
| | 0.02 | 0.03 | 0.01 | | | | |
| Mg AZ31B | 1.775 | 4.52 | 1.26 | 1.43 | 0.30 | - | b |
| | 0.01 | 0.05 | 0.02 | | | | |
| $Al_2O_3$ | 3.83 | 6.91 | 1.44 | 1.27 | 0.24 | 5.8 | b |
| | 0.01 | 0.08 | 0.04 | | | | |

Table 3.4: Equation of state standards for MgO experiments. Numbers in parentheses represent one standard deviation uncertainties. $c_o$ and $s$ are Hugoniot equation of state constants, $\gamma_o$ is the Grüneisen parameter, $\nu_o$ is Poisson's ratio, and $Y_o$ is the yield strength. The references are: a, this study; b, *Marsh* [1980]; c, *Mitchell and Nellis* [1981a].

Figure 3.6: The relationship between shock velocity and particle velocity for MgO. Open symbols are data for single-crystal MgO [*Marsh,* 1980; *Vassiliou and Ahrens,* 1981]. Solid circles are data of this study for low-porosity polycrystalline MgO from equation of state experiments. The solid triangles are inferred from wave profile measurements. The solid square labeled $V_P$ shows the measured zero-pressure longitudinal sound velocity for the present samples. The solid square near the intercept of the polycrystalline Hugoniot is the bulk sound velocity from ultrasonic data. The solid curve is a least-squares fit to the polycrystalline data, and the dashed curve is a fit to the single-crystal data. Uncertainties for single-crystal MgO are not shown. For the data of this study, the uncertainties are smaller than the symbol if not shown.

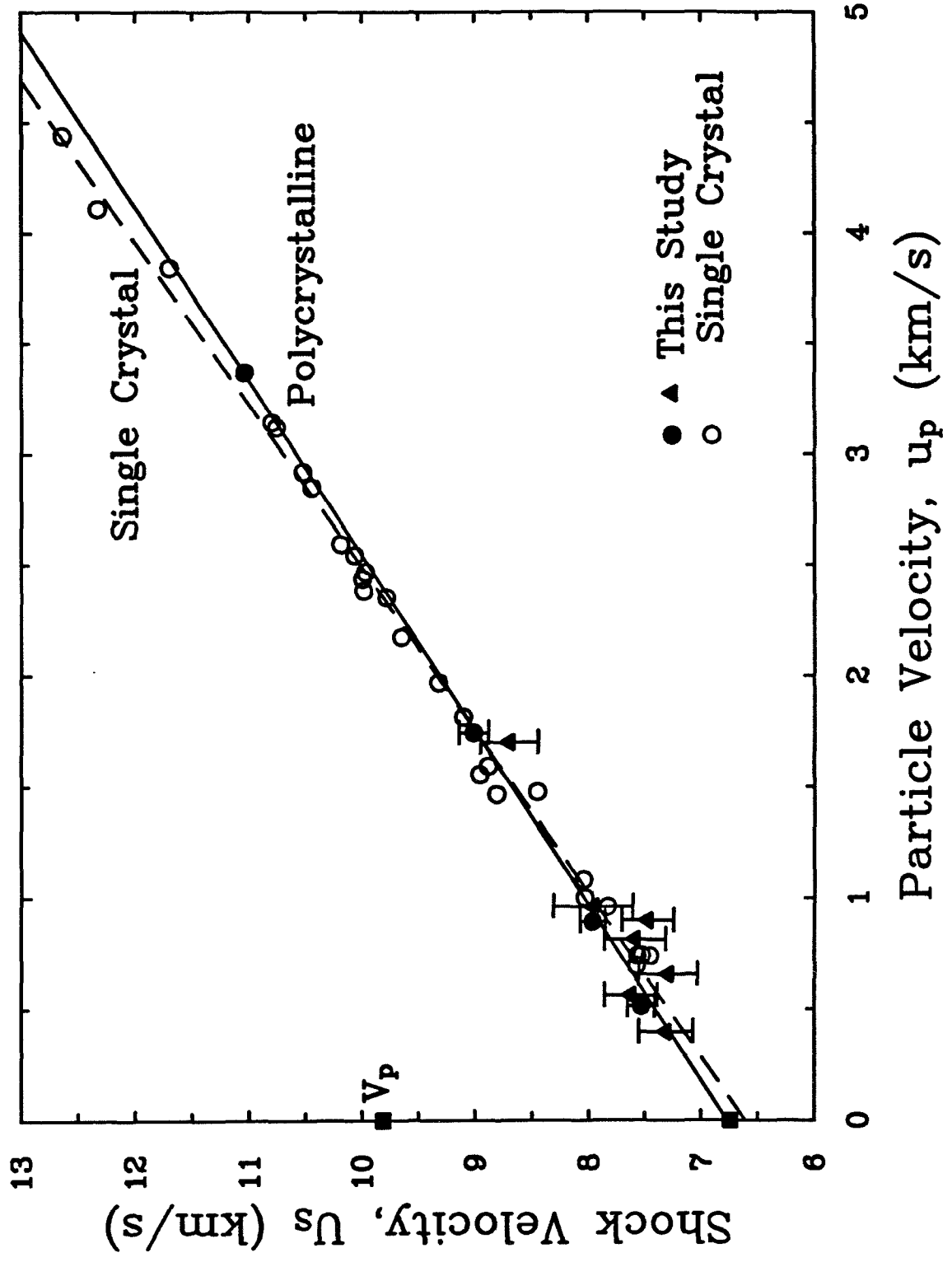
Shock Velocity, Us (km/s)
Particle Velocity, up (km/s)
Single Crystal
Polycrystalline
This Study
Single Crystal
Vp
13
12
11
10
9
8
7
6
0
1
2
3
4
5

Figure 3.7: Stress-density states achieved in shock compression of MgO. Open symbols are data for single-crystal and porous MgO [*Al'tshuler et al.,* 1965; *Marsh,* 1980; *Vassiliou and Ahrens,* 1981]. Solid circles are data of this study for low-porosity polycrystalline MgO from equation of state experiments. The highest-pressure datum of Table 3.3 is not shown in this figure (but see Figure 3.24). The solid triangles are inferred from wave profile measurements. The ambient density of MgO is shown by the solid box. The static isotherm is from *Jackson and Niesler* [1982]. Uncertainties for single-crystal and porous MgO are not shown. For the data of this study, the uncertainties are smaller than the symbol if not shown.

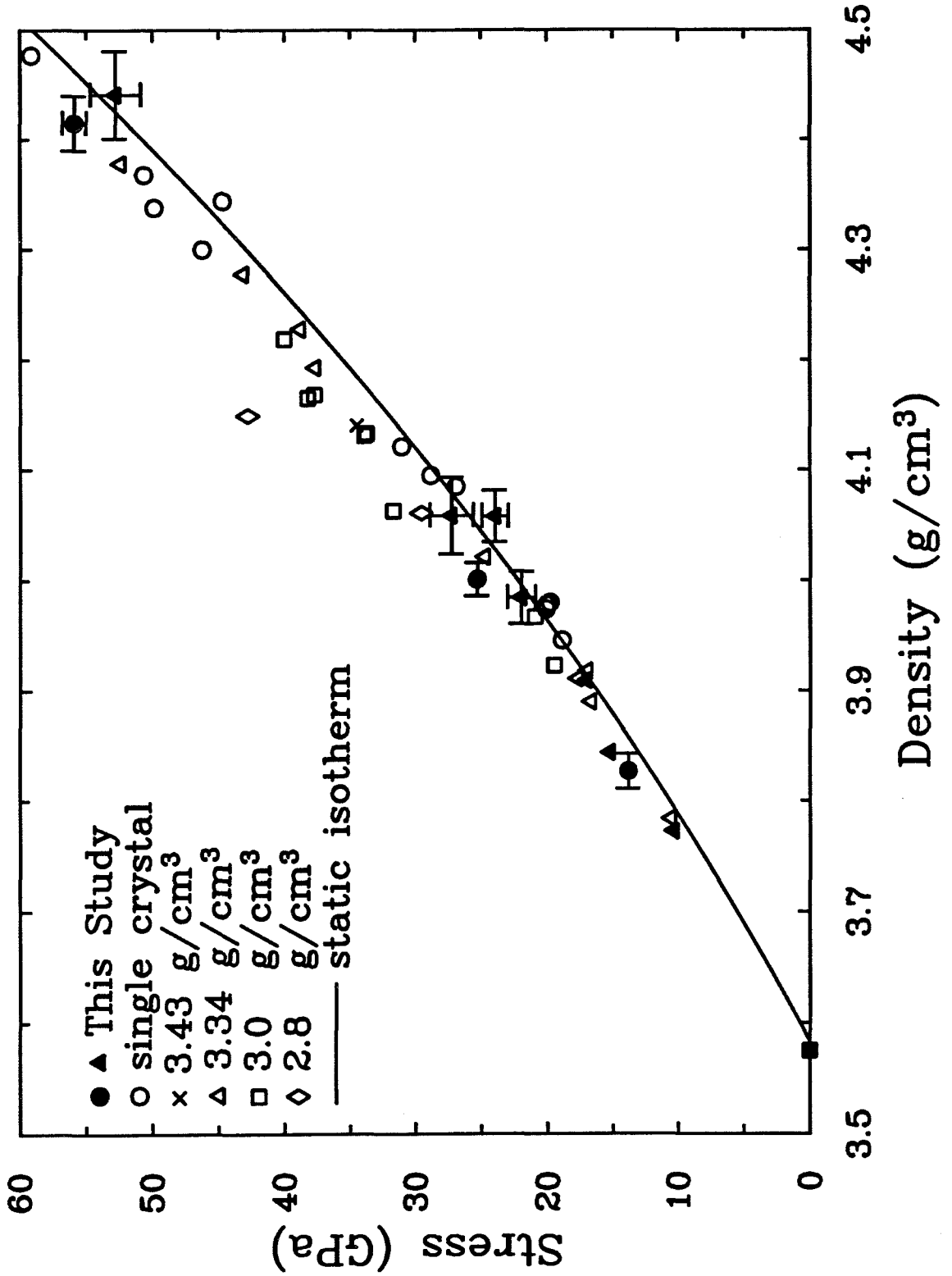
Stress (GPa)
Density (g/cm³)
0
10
20
30
40
50
60
3.5
3.7
3.9
4.1
4.3
4.5
This Study
single crystal
3.43 g/cm³
3.34 g/cm³
3.0 g/cm³
2.8 g/cm³
static isotherm

stant. Some variations in particle velocity are evident in this region, particularly for shot 851. This may reflect differential motion of grains, material reorganization, or heterogeneous faulting and has been observed previously in velocity profile measurements on ceramics [*Kipp and Grady,* 1989]. We chose to use aluminum buffers in part to smooth out such irregularities. The arrival of the unloading waves produces a decrease in particle velocity ($t_3$), which is initially steep, then becomes shallow and finally steepens again somewhat. The final particle velocity level of the experiment is dependent on the properties of the foam-backing layer of the flyer.

The results of shot 844 are not included in this figure because extraneous non-systematic light-intensity changes beginning near the time of the shock arrival obscured much of the wave profile. By masking the rear surface of the window except near the center, this problem was avoided on subsequent shots. The end of each wave profile is normally determined by the arrival of the shock front at the window free surface which results in a catastrophic loss of signal intensity. The reverse-impact experiment using the Ta buffer (shot 860) is plotted separately in Figure 3.9.

The forward-impact velocity histories show more complex structure (Figure 3.10). The initial arrival is the elastic precursor ($t_1$ in Figure 3.5) or Hugoniot elastic limit (HEL) wave. The amplitude of this wave is a measure of the largest elastic stress that can be supported by the buffer under compressive loading. This is followed by the plastic shock front ($t_2$) and the plateau region. Velocity variations in the plateau region are generally smaller for these experiments, probably because the longer propagation distance smooths out any heterogeneities. The shape of the unloading wave profile ($t_3$) is similar to the reverse experiments, but the initial release is not as sharply defined in these experiments.

In order to further constrain the EOS of polycrystalline MgO, the reverse-impact VISAR experiments were used to determine shock and particle velocity states. This was accomplished by combining the measured interface and impact velocities with

Figure 3.8: Interface particle velocity histories for reverse-impact experiments using Al 6061 buffers. Experiment (shot) numbers are listed to the left of each profile. The times $t_1$-$t_3$ correspond to those shown in the x-t diagram of Figure 3.3. Times along the x axis are arbitrary and have been shifted so that the traces are aligned.

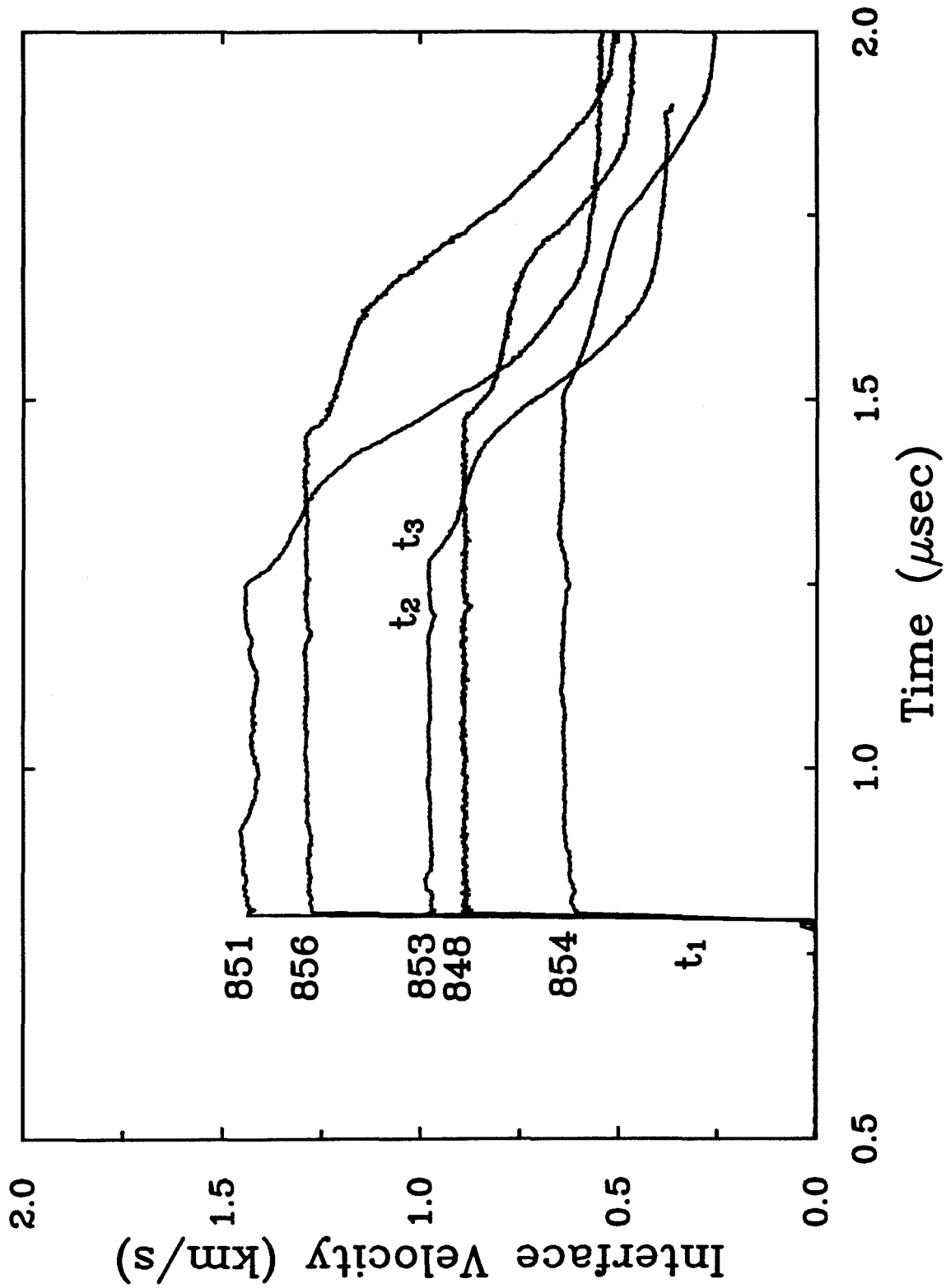
Interface Velocity (km/s)
2.0
1.5
1.0
0.5
0.0
0.5
1.0
1.5
2.0
Time (μsec)
851
856
853
848
854
t1
t2
t3

Figure 3.9: Interface particle velocity history for the reverse-impact experiment using a Ta buffer (experiment 860). The times $t_1$ and $t_3$ correspond to those shown in the x-t diagram of Figure 3.3. The time is relative to an arbitrary trigger time.

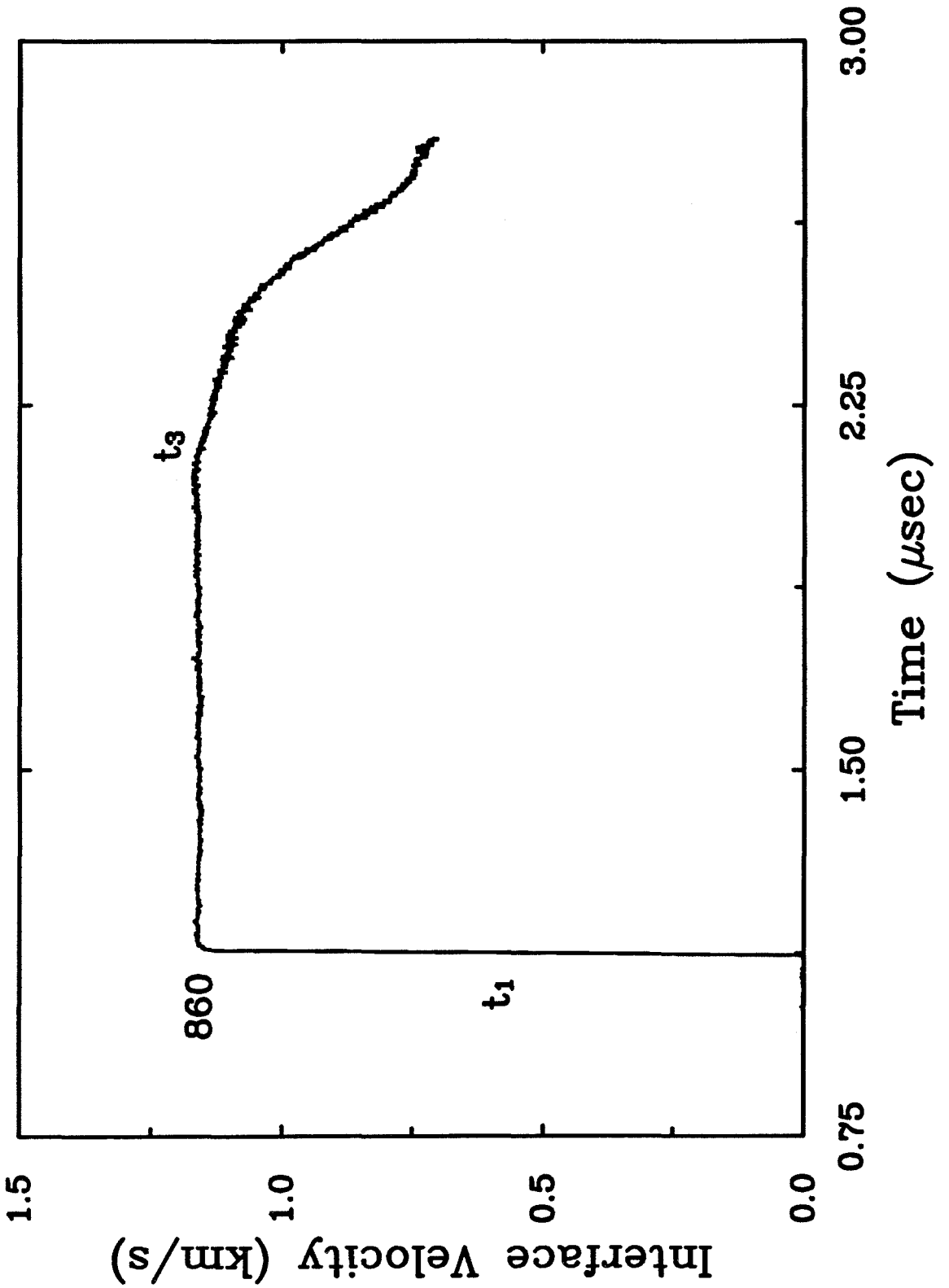
Interface Velocity (km/s)
1.5
1.0
0.5
0.0
0.75
1.50
2.25
3.00
Time (μsec)
860
t1
t3

Figure 3.10: Interface particle velocity histories for forward-impact experiments. Experiment (shot) numbers are listed to the left of each profile. The times $t_1$-$t_3$ correspond to those shown in the x-t diagram of Figure 3.5. Times along the x axis are arbitrary and have been shifted so that the traces are aligned. The elastic precursor is labeled HEL, which stands for Hugoniot elastic limit.

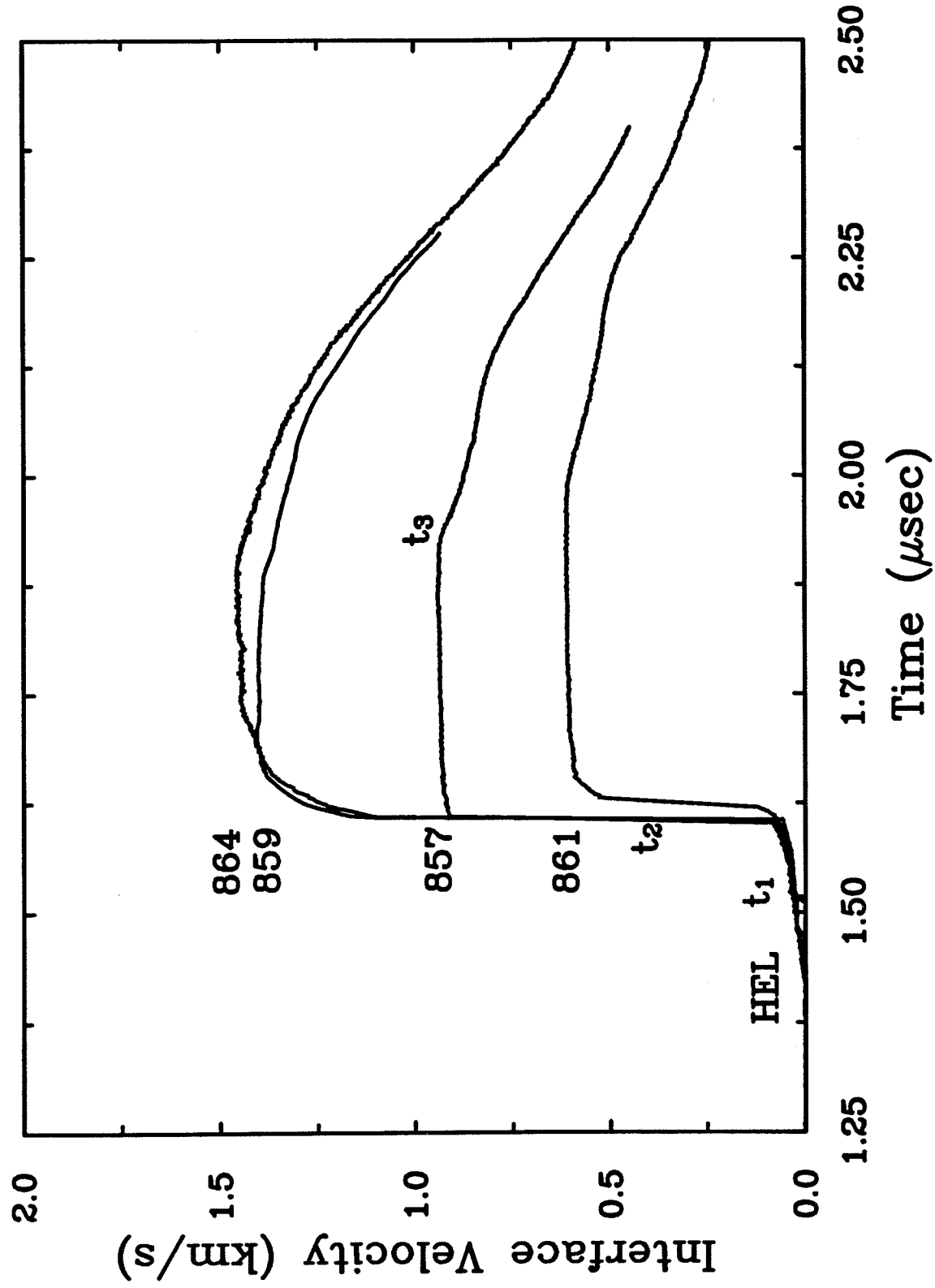
Interface Velocity (km/s)
2.0
1.5
1.0
0.5
0.0
1.25
1.50
1.75
2.00
2.25
2.50
Time (μsec)
HEL
t1
t2
t3
864
859
857
861

the known EOS of the sample and window in an impedance-matching procedure [*Grady and Furnish,* 1988]. Direct measurement of shock velocities is not possible in these VISAR experiments, as the impact time is not recorded. The shock velocity may still be recovered to ±3% by using the measured shock and interface velocities together with the EOS of the buffer and an approximation for the unloading adiabat [*Ahrens,* 1987].

Particle velocities measured by the VISAR at the buffer-window interface, $u_{pm}$, are listed in Table 3.5. The precision of ±1% is based on the uncertainty in the VISAR fringe constant (see appendix), and the standard deviation of the velocity variations in the plateau region is generally less than this. By requiring that the stresses be equal on either side of the buffer-window interface, the following equation can be written:

$$\rho_{ob}(c_{ob} + s_b(2u_{p1} - u_{pm}))(2u_{p1} - u_{pm}) = \rho_{ow}(c_{ow} + s_w u_{pm})u_{pm}. \qquad (3.2)$$

In the above equation, $u_{p1}$ is the particle velocity at the sample-buffer interface and the subscripts $b$ and $w$ refer to the buffer and window, respectively. The EOS constants, $c_o$ and $s$, and the initial densities, $\rho_o$, are listed in Table 3.4. The above equation was derived using the Rankine-Hugoniot momentum conservation expression:

$$\sigma = \rho_o U_S u_p, \qquad (3.3)$$

where $\sigma$ is the axial stress and $u_p$ is the particle velocity. The shock velocity, $U_S$, is given by the shock wave equation of state:

$$U_S = c_o + s u_p. \qquad (3.4)$$

In deriving Eqn. 3.2, the release curve of the buffer has been approximated by using the reflected Hugoniot [see *Ahrens,* 1987]. This point is illustrated in the pressure-particle velocity diagram of Figure 3.11. The measured particle velocity,

$u_{pm}$, together with the known equations of state of LiF and Al 6061 define the intersection point ($u_{p1}$) of the LiF and "reflected" Al 6061 Hugoniots. Also shown is the derived Hugoniot of MgO (Eqn. 3.6) centered at the flyer plate velocity.

Using $u_{p1}$ from Eqn. 3.2, the shock velocity in the sample, $U_{Ss}$, is determined from the continuity of stress across the sample-buffer interface:

$$\rho_{os} U_{Ss} (u_{fp} - u_{p1}) = \rho_{ob} U_{Sb} u_{p1}, \tag{3.5}$$

where the subscript $s$ refers to sample properties, and $u_{fp}$ is the flyer plate velocity.

The results of the impedance-match calculation are listed in Table 3.5 and plotted in Figures 3.6 and 3.7. Although the shock velocities are constrained to only ±3% by this method, the results are generally consistent with the higher-precision EOS experiments discussed earlier. Shock wave data for many materials can be fit with a linear relationship between shock and particle velocity (Eqn. 3.4). Fitting the VISAR and EOS measurements to such a relationship yields:

$$U_S = 6.77(0.08) + 1.27(0.04) u_p, \tag{3.6}$$

where the numbers in parentheses are one standard deviation uncertainties. A complete discussion of the equation of state of polycrystalline MgO and a comparison with single-crystal data will be deferred to the next section.

Initial unloading wave velocities were also determined from the reverse-impact experiments. For an elastic-plastic material, the initial unloading velocity is the compressional sound velocity, $V_P$, and for a fluid it is the bulk velocity, $V_B$ [*Zel'dovich and Razier,* 1967]. The method for determining the unloading velocities can be seen with reference to Figure 3.3 and is also discussed in Chapter 1. The time difference, $\Delta t$, between the unloading wave arrival, $t_3$, and the shock arrival $t_1$ is read from the wave profiles. The shock arrival time is taken to be the location of the initial jump in particle velocity, and the unloading wave arrival is the first persistent decrease in $u_p$. This time difference can be determined typically to ~3 ns and is

Figure 3.11: Stress-particle velocity diagram illustrating impedance match for reverse-impact experiments. $u_{pm}$ is the measured interface velocity, $u_{p1}$ is the particle velocity at the sample-buffer interface, $u_{fp}$ is the flyer plate velocity.

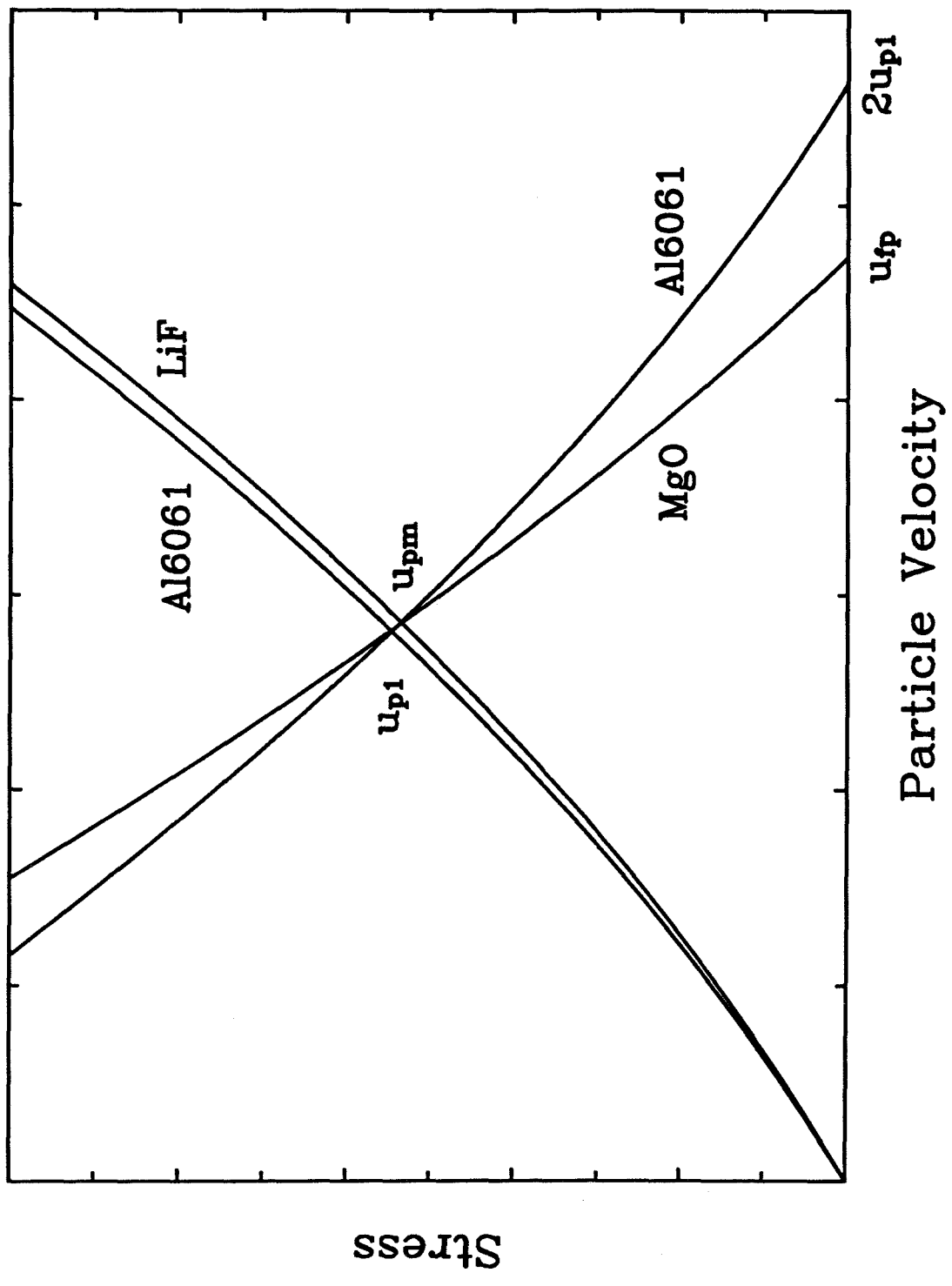
Stress
Particle Velocity
LiF
Al6061
Al6061
MgO
$u_{pm}$
$u_{p1}$
$u_{fp}$
$2u_{p1}$

| Shot | Sample | | | | Buffer | | | VISAR |
|---|---|---|---|---|---|---|---|---|
| | $u_p$ (km/s) | $U_s$ (km/s) | $\sigma$ (GPa) | $\rho$ (g/cm$^3$) | $u_p$ (km/s) | $U_s$ (km/s) | $\rho$ (g/cm$^3$) | $u_{pm}$ (km/s) |
| 844 | 0.813 | 7.58 | 21.9 | 3.984 | 1.187 | 6.93 | 3.213 | 1.206 |
| | 0.026 | 0.27 | 1.0 | 0.023 | 0.015 | 0.06 | 0.012 | 0.013 |
| 848 | 0.560 | 7.62 | 15.2 | 3.843 | 0.871 | 6.51 | 3.095 | 0.889 |
| | 0.015 | 0.24 | 0.6 | 0.013 | 0.011 | 0.06 | 0.009 | 0.009 |
| 851 | 0.959 | 7.95 | 27.2 | 4.058 | 1.406 | 7.23 | 3.328 | 1.431 |
| | 0.040 | 0.35 | 1.6 | 0.035 | 0.018 | 0.07 | 0.013 | 0.014 |
| 853 | 0.655 | 7.29 | 17.0 | 3.909 | 0.956 | 6.62 | 3.136 | 0.976 |
| | 0.023 | 0.28 | 0.9 | 0.021 | 0.012 | 0.06 | 0.009 | 0.010 |
| 854 | 0.396 | 7.30 | 10.4 | 3.772 | 0.623 | 6.18 | 2.988 | 0.638 |
| | 0.012 | 0.25 | 0.5 | 0.010 | 0.007 | 0.06 | 0.007 | 0.006 |
| 856 | 0.898 | 7.47 | 23.9 | 4.058 | 1.267 | 7.04 | 3.274 | 1.291 |
| | 0.026 | 0.24 | 1.0 | 0.025 | 0.016 | 0.07 | 0.013 | 0.013 |
| 860 | 1.699 | 8.69 | 52.8 | 4.441 | 0.745 | 4.266 | 20.13 | 1.159 |
| | 0.039 | 0.26 | 2.0 | 0.041 | 0.014 | 0.034 | 0.09 | 0.012 |

Table 3.5: Impedance-match solutions for reverse-impact experiments.

listed in Table 3.6. The Lagrangian unloading velocity is given by:

$$V_{PL} = \frac{x_s - h_1}{\Delta t + x_b/U_{Sb} - (x_s + h_1)/(V_{Po}) - x_b/V_{PLb}}, \tag{3.7}$$

where $V_{PL}$ and $V_{PLb}$ are the Lagrangian sound velocities in the sample and buffer, $x_s$ and $x_b$ are the sample and buffer thicknesses, $U_{Sb}$ is the buffer shock velocity, and $V_{Po}$ is the elastic precursor velocity. $h_1$ is defined by the point of intersection of the elastic wave reflected from the rear surface of the flyer and the oncoming shock wave:

$$h_1 = \frac{x_s(V_{Po} - U_{Ss})}{(V_{Po} + U_{Ss})}, \tag{3.8}$$

where $U_{Ss}$ is the sample shock velocity. For the precursor velocity, $V_{Po}$, we used the ultrasonically determined P-wave velocity at ambient pressure. Shock states in the buffer and sample were determined from the particle velocity at the buffer-sample interface, $u_{p1}$, obtained from the impedance match and the Hugoniot EOS relations for polycrystalline MgO (Eqn. 3.6) and Al 6061 (Table 3.4).

Compressional velocities in the buffer were determined experimentally from the time difference between the shock arrival, $t_1$, and the arrival of the reverberation through the buffer, $t_2$ (Figure 3.3) using:

$$V_{PLb} = \frac{2x_b}{t_2 - t_1}, \tag{3.9}$$

Lagrangian velocities were converted to Eulerian velocities, $V_Pb$, by multiplying by the ratio of densities, $\rho_{ob}/\rho_b$. Eulerian velocities in Al 6061 are shown in Figure 3.12. Also shown in the figure are aluminum unloading velocities determined in reverse-impact experiments using Fe-Cr-Ni flyers (Chapter 1). The results obtained in our work are consistent with the earlier data of *Asay and Chhabildas* [1981] for this material. The variation of $V_P$ with Hugoniot pressure in Al 6061 can be described by the following relationship (solid line in Figure 3.12):

$$V_P = 1.8796 + 0.0303 \ln P + 0.0177 \ln^2 P, \tag{3.10}$$

Figure 3.12: Compressional wave velocities measured in type 6061 aluminum. The data point labeled 2024 is for aluminum alloy 2024. The filled box is the zero-pressure ultrasonic velocity for Al 6061. The solid curve is a fit to all the data. The dashed curve is a third-order finite-strain extrapolation of ultrasonic data [*Thomas,* 1968] for pure Al at 300 K.

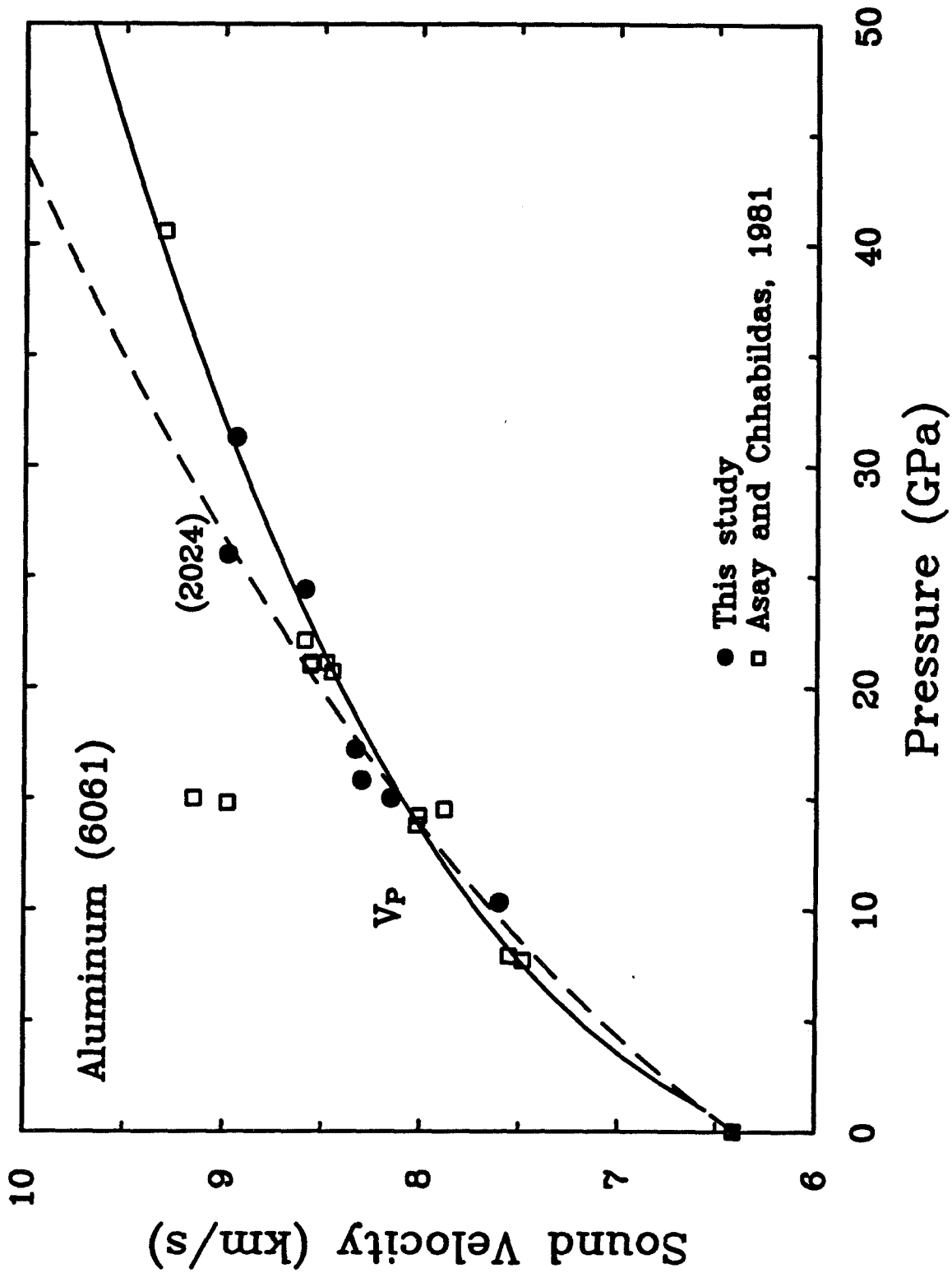
Aluminum (6061)
(2024)
$V_P$
This study
Asay and Chhabildas, 1981
Sound Velocity (km/s)
Pressure (GPa)
10
9
8
7
6
0
10
20
30
40
50

| shot | $\Delta t$ ($\mu$s) | $V_{Pb}$ (km/s) | $h_1$ (mm) | $V_{PL}$ (km/s) | $V_P$ (km/s) |
|---|---|---|---|---|---|
| 844 | 0.697 | 8.52 | 0.46 | 12.51 | 11.23 |
| | 0.008 | 0.13 | 0.02 | 0.39 | 0.35 |
| 848 | 0.677 | 8.15 | 0.53 | 11.47 | 10.61 |
| | 0.003 | 0.12 | 0.02 | 0.24 | 0.22 |
| 851 | 0.456 | 8.66 | 0.31 | 13.34 | 11.74 |
| | 0.003 | 0.13 | 0.02 | 0.35 | 0.31 |
| 853 | 0.480 | 8.33 | 0.39 | 11.90 | 10.90 |
| | 0.002 | 0.12 | 0.02 | 0.27 | 0.25 |
| 854 | 0.707 | 7.60 | 0.59 | 10.76 | 10.18 |
| | 0.003 | 0.09 | 0.02 | 0.22 | 0.21 |
| 856 | 0.654 | 8.59 | 0.44 | 12.41 | 11.04 |
| | 0.003 | 0.13 | 0.02 | 0.24 | 0.22 |

Table 3.6: Compressional wave velocities in MgO and the parameters used to obtain them.

where $V_P$ is expressed in km/s and $P$ is expressed in GPa.

The Eulerian and Lagrangian unloading velocities in MgO are listed in Table 3.6, and the Eulerian velocities are shown in Figure 3.13. The uncertainties in the velocities were determined through error propagation of the uncertainties in each of the quantities in Eqn 3.7 and are 2-3%. A nominal uncertainty of 1.5% was assigned to the buffer sound velocity. These results will be compared to ultrasonic and other shock wave data in the next section.

Figure 3.13: Compressional wave velocities in MgO. The solid symbols with error bars are for polycrystalline MgO, and the open circles are for single-crystal MgO shocked along [100]. The solid curves are the third-order finite-strain extrapolation of ultrasonic data at 300 K for $V_P$ and $V_B$. The dashed curve shows the expected effect of temperature along the Hugoniot for $V_P$. The dotted curve shows that expected variation of velocity along [100] from ultrasonic data [*Jackson and Niesler*, 1982].

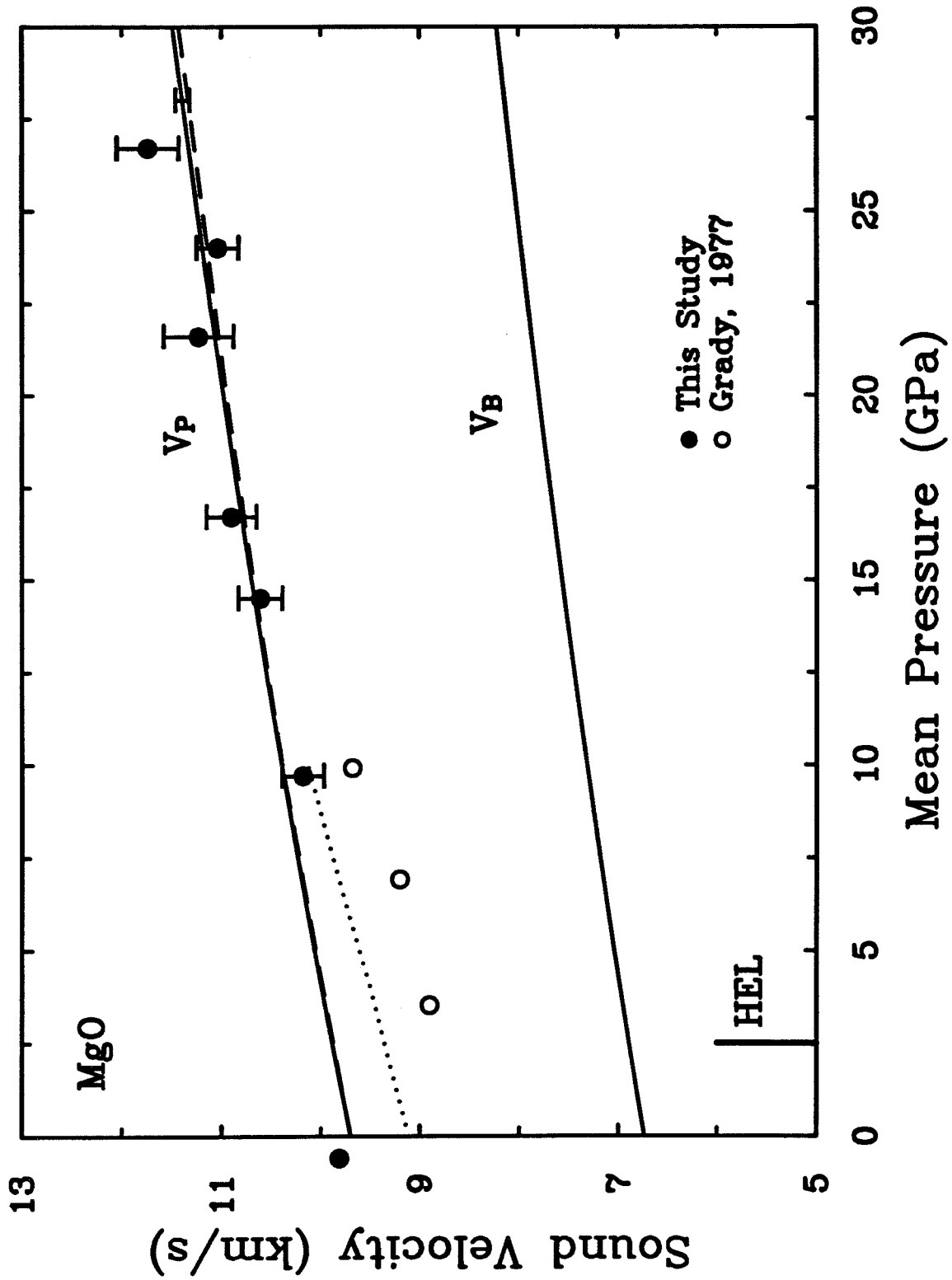
MgO
$V_P$
$V_B$
● This Study
○ Grady, 1977
HEL
Sound Velocity (km/s)
Mean Pressure (GPa)
13
11
9
7
5
0
5
10
15
20
25
30

## 3.4 Discussion

### 3.4.1 Equation of state of MgO

While single-crystal and porous polycrystalline MgO have been studied extensively using shock techniques, the present study represents the first EOS determination for low-porosity (<1%) polycrystalline MgO. The present results are generally consistent with the single-crystal data as shown in Figures 3.6 and 3.7. A least-squares fit to the single-crystal data listed in *Marsh* [1980] yields:

$$U_S = 6.61(0.05) + 1.36(0.02)u_p, \tag{3.11}$$

The intercept of the $U_S$-$u_p$ relation should correspond to the bulk sound velocity for a material undergoing no high-pressure phase change. For MgO, the bulk velocity from high-precision ultrasonic data [*Jackson and Niesler,* 1982] is 6.73 km/s, which is 1.9% above the $U_S$-$u_p$ intercept. If only data for $u_p > 1.1$ km/s is used in the fit, the single-crystal EOS then becomes:

$$U_S = 6.74(0.07) + 1.32(0.03)u_p, \tag{3.12}$$

which agrees well with the ultrasonic bulk velocity. The data at $u_p < 1.5$ km/s are sparse and rather scattered, probably because it is more difficult to make reliable measurements in the two-wave region. The data in this region may also be affected by stress relaxation in the shock front [*Grady,* 1977; *Jeanloz,* 1989a].

The EOS for polycrystalline MgO is:

$$U_S = 6.77(0.08) + 1.27(0.04)u_p$$

This is also in good agreement with the ultrasonic data and is close to the Hugoniot EOS for single-crystal MgO for $u_p > 1.1$ km/s. Stress relaxation in the single-crystal material exhibits itself in wave profile measurements as a strong decrease in

$u_p$ behind the precursor [*Grady*, 1977]. No such such effect is seen in the wave profiles for polycrystalline MgO transmitted through the Al buffer (Figure 3.10). The slope of the Hugoniot relation is related to the pressure derivative of the bulk modulus, $K'_{oS}$ through:

$$K'_{oS} = 4s - 1, \tag{3.13}$$

This relation yields $K'_{oS} = 4.1 \pm 0.2$ for polycrystalline MgO, which is in excellent agreement with the ultrasonic data (Table 3.7). In contrast, the single-crystal relation using all the data yields $K'_{oS} = 4.4 \pm 0.1$, which is greater than the ultrasonic value of $4.13 \pm 0.09$.

Although the polycrystalline results are entirely consistent with ultrasonic data, there is some evidence that the Hugoniot states are slightly stiffer than the static isotherm derived from ultrasonic data for densities below 4.0 gm/cm$^3$ (Table 3.7). This is especially true of the higher-precision streak camera measurements. The single-crystal data, in contrast, lie closer to the static isotherm. The static isotherm was constructed using parameters for *Jackson and Niesler* [1982] and the Birch-Murnaghan equation. Ultrasonic and Hugoniot data for MgO are listed in Table 3.7.

### 3.4.2 Compressional Wave Velocities

Laterally averaged seismic velocities in the Earth's mantle and core are known to better than 1% (*Lay et al.*, 1990). Comparison of these data with laboratory phase equilibria and elasticity measurements provides the most detailed constraints on the composition of the Earth's interior. There are few direct measurements of elasticity at significantly elevated pressure (> 3 GPa), however. Most such comparisons rely on extrapolation of elasticity data to both high temperature and pressure. For example, *Duffy and Anderson* [1989] used third-order finite-strain theory and ultrasonic data to constrain mineralogical models of the upper mantle. Results showed that the seismic velocity gradient in the transition region is too steep to be explained by

| Property | Value | Ref. |
|---|---|---|
| $\rho_o$ (g/cm$^3$) | 3.584 ± 0.001 | a |
| $K_{oS}$ (GPa) | 162.5 ± 0.2 | a |
| $\partial K_{oS}/\partial P$ | 4.13 ± 0.09 | a |
| $\partial K_{oS}/\partial T$ (GPa/K) | -0.016 ± 0.003 | b |
| $K_{oT}$ (GPa) | 160.1 ± 0.3 | a |
| $\partial K_{oT}/\partial P$ | 4.15 ± 0.1 | a |
| $G_o$ (GPa) | 130.8 ± 0.2 | a |
| $\partial G_o/\partial P$ | 2.5 ± 0.1 | a |
| $\partial G_o/\partial T$ (GPa/K) | -0.024 ± 0.004 | b |
| $\gamma_o$ | 1.52 ± 0.02 | b |
| $q$ | 1.0 | d |
| $c_o$ (km/s) | 6.77 ± 0.08 | c |
| $s$ | 1.27 ± 0.04 | c |

Table 3.7: Thermodynamic, elastic, and Hugoniot properties of MgO. The references are: a, *Jackson and Niesler* [1982]; b, *Sumino and Anderson* [1984]; c, this study; d, assumed.

compression of a homogeneous material and that an olivine content of 40% by volume is required to explain the seismic velocity discontinuity at 400 km. Questions have been raised about the accuracy of finite-strain extrapolations. For example, structural changes occurring at high pressure can affect elasticity and will not be reflected in the ultrasonic data.

In the case of MgO, high-precision ultrasonic measurements have been performed on single crystals to 3 GPa [*Jackson and Niesler,* 1982], which constrain the averaged elastic moduli to 0.1% and their pressure derivatives to ~4% (Table 3.7). Compressional sound velocities were calculated to 30 GPa using these data and the finite-strain equations for $V_P$ (Chapter 1). The results are shown in Figure 3.13 along with the measured Hugoniot compressional velocities between 10 and 27 GPa. The Hugoniot axial stresses were converted to mean pressures, $\bar{P}$, using:

$$\bar{P} = \sigma - \frac{4}{3}\frac{V_S^2 \sigma_{HEL}}{V_P^2} \tag{3.14}$$

where $V_S$ is the shear wave velocity and $\sigma_{HEL}$ is the Hugoniot elastic limit stress. The HEL stress for polycrystalline MgO is 1.25 ± 0.25 GPa as discussed below. The difference between the axial and mean stress is computed to be 0.6 GPa or 2-6% of the axial stress in these experiments. For single-crystal MgO [100], the HEL stress is 2.5 GPa [*Grady,* 1977], and the stress difference is 1.3 GPa.

The Hugoniot compressional velocity measurements agree with the ultrasonic extrapolations within their experimental precision (2-3%). This therefore supports the use of finite-strain theory for this material over pressures nearly a factor of 10 greater than the experimental data. The 10-27 GPa pressure range corresponds to depths between 300 and 750 km in the Earth's interior and includes the transition region.

As discussed in Chapter 1, Hugoniot measurements can be inverted to constrain elastic moduli and their pressure derivatives along the Hugoniot. In the region where thermal effects along the Hugoniot are small, these should be comparable to ultra-

sonic determinations. By combining the present Hugoniot data with the ambient-pressure compressional velocity, the following elastic parameters are obtained: $C_{Lo}$ = 335 ± 1 GPa and $C_{Lo}{\prime}$ = 7.0 ± 0.4. The ultrasonically determined parameters are: $C_{Lo}$ = 336.9 ± 0.3 GPa and $C_{Lo}{\prime}$ = 7.4 ± 0.2 This again demonstrates the consistency of the Hugoniot measurements with the ultrasonic data.

Comparison of Hugoniot data with 300 K extrapolations of ultrasonic data can be potentially biased because of thermal effects on the Hugoniot. Between 10 and 27 GPa, the continuum Hugoniot temperatures in MgO are calculated to lie between 320 and 408 K. This calculation assumes that the specific heat and the product of density and Grüneisen parameter are constant with pressure, and the calculation was carried out using the procedure described by *McQueen et al.* [1970]. By using the ambient-pressure value of the temperature coefficients of compressional velocity for MgO ($(\partial V_P/\partial T)_P$ = -0.5 m/s/K), the 300 K velocities can be adjusted to correspond to Hugoniot temperatures as shown in Figure 3.13. The thermal effect on the velocity is very small, less than 1% at the highest pressure.

Unloading wave velocities have been previously measured in other minerals, both single crystals and polycrystals. Initial velocities in polycrystalline quartz, feldspar, and calcite all propagate at wave speeds close to the estimated bulk sound velocity at stresses of 22-36 GPa in quartz, 25-46 GPa in feldspar, and ≤ 5 GPa in calcite [*Grady,* 1980]. Available data on unloading wave velocities in quartz are summarized in Figure 3.14. In the low- and high-pressure phase regimes, the initial unloading velocities are consistent with expected 300 K compressional velocities in quartz and stishovite, respectively. The 300 K velocities are based on elastic moduli and pressure derivatives in *Sumino and Anderson,* [1984]. For stishovite shock-induced from quartz, a pressure derivative of the shear modulus of 1.8 has been assumed on the basis of systematics which show that $G'$ varies inversely with the ratio of $K/G$ for many mineral groups [*Duffy and Anderson,* 1989]. In the mixed-phase regime, the

velocities are intermediate and suggest a largely bulk response [*Grady*, 1980].

For polycrystalline $Al_2O_3$, initial unloading velocities at stresses near 9 GPa ($\bar{P}$ $\sim$ 5 GPa) were reported by *Munson and Lawrence* [1979]. These velocities are 1-3% above finite-strain extrapolations of ultrasonic data for this material *Sumino and Anderson* [1984]. *Bless and Ahrens* [1976] reported sound velocities in alumina between 20-40 GPa that are intermediate between the compressional and bulk sound velocities of the finite-strain extrapolations. *Barker and Hollenbach* [1970] found that the unloading wave speed in single-crystal $Al_2O_3$ (Z-cut) at a stress of 11.7 GPa ($\bar{P}$ = 5.8 GPa) was consistent with ultrasonic extrapolations at this pressure. These data are shown in Figure 3.15. Velocities in the elastic region are consistent with ultrasonic data to within $\sim$2%. Beyond the Hugoniot elastic limit, the initial response is quasi-elastic but approaches the ultrasonic compressional velocity with increasing stress.

*Grady* [1977] reported three VISAR wave profile measurements on single-crystal MgO shocked along [100] between 4.8 and 11.2 GPa ($\bar{P}$ = 3.5 - 9.9 GPa). The initial unloading velocities are 4-6% below the extrapolated sound velocity in this direction at high pressure. Single-crystal MgO is believed to collapse to the hydrostat upon shock compression above the HEL. The unloading wave velocities indicate that material strength has recovered nearly completely in the $\sim$500 ns time interval between shock and release arrivals.

This summary illustrates the wide variety of initial unloading behavior that can be exhibited by minerals. Initial unloading velocities at similar stresses in metals, for which the elastic-plastic model is well established, are generally consistent with ultrasonic compressional velocities [*Duffy and Ahrens*, 1992a]. The above mineral data cover a range of deformation regimes. Data both above and below the HEL are reported as are data for both single crystals and polycrystals. A model of heterogeneous deformation such as that of *Grady* [1980] can at least qualitatively explain the

Figure 3.14: Initial unloading wave velocities in $SiO_2$ from Hugoniot data on single crystals, polycrystals, and fused silica. The solid and dashed curves are estimated 300 K compressional velocities in stishovite and quartz, based on ultrasonic data. Boundaries for the low- (LPP), mixed-, and high- (HPP) pressure phases are indicated at the bottom of the figure. Hugoniot pressures have not been converted to mean pressures.

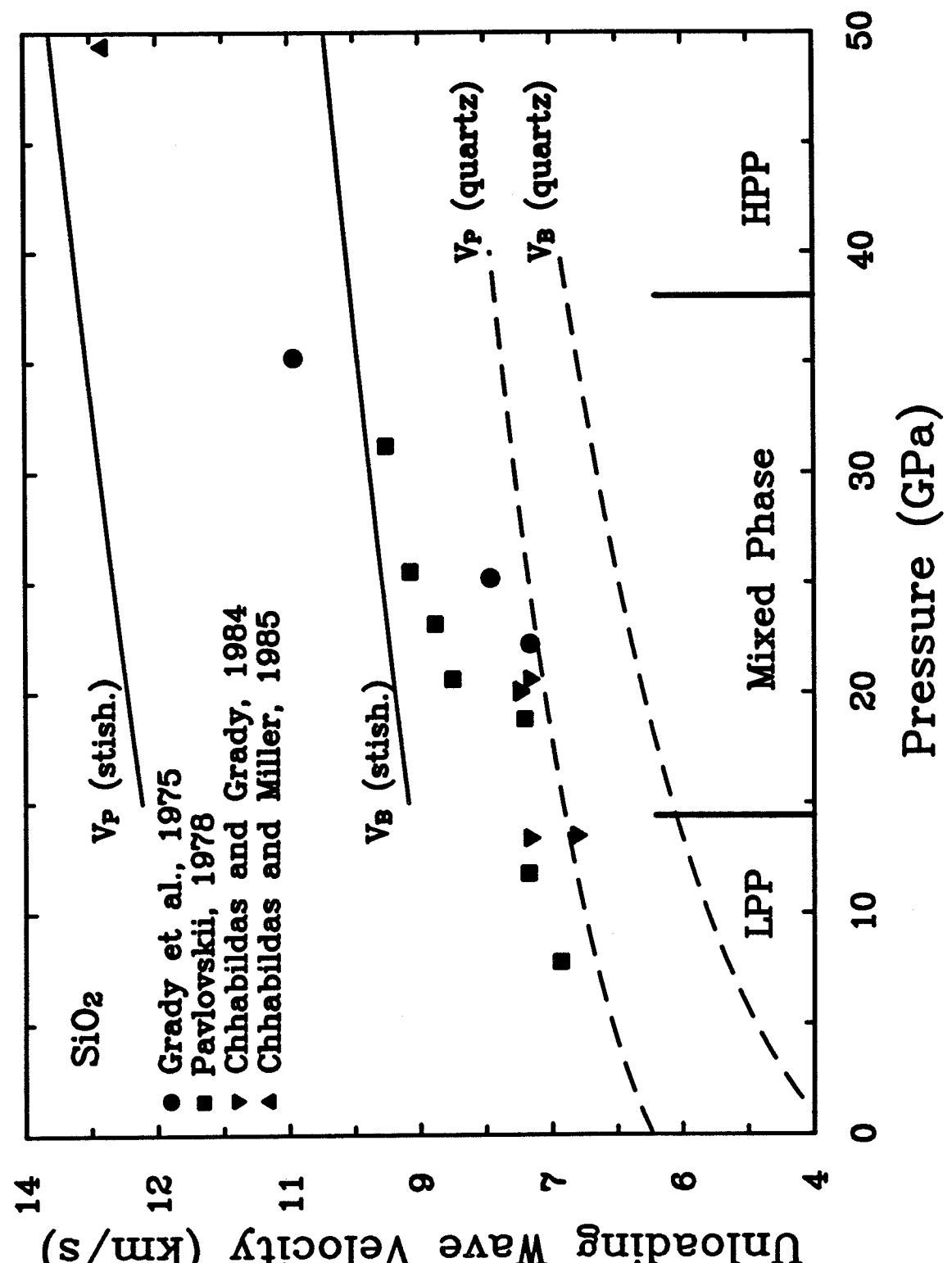
Unloading Wave Velocity (km/s)
Pressure (GPa)
SiO2
VP (stish.)
VB (stish.)
VP (quartz)
VB (quartz)
Grady et al., 1975
Pavlovskii, 1978
Chhabildas and Grady, 1984
Chhabildas and Miller, 1985
LPP
Mixed Phase
HPP
14
12
11
9
7
6
4
0
10
20
30
40
50

Figure 3.15: Initial unloading wave velocities in $Al_2O_3$ from Hugoniot data on single and polycrystals. The solid curves are estimated 300 K compressional velocities based on ultrasonic data [*Sumino and Anderson,* 1984]. The HEL for alumina is indicated by the vertical bar [*Munson and Lawrence,* 1979]. Hugoniot pressures have been converted to mean pressures using the method discussed in the text.

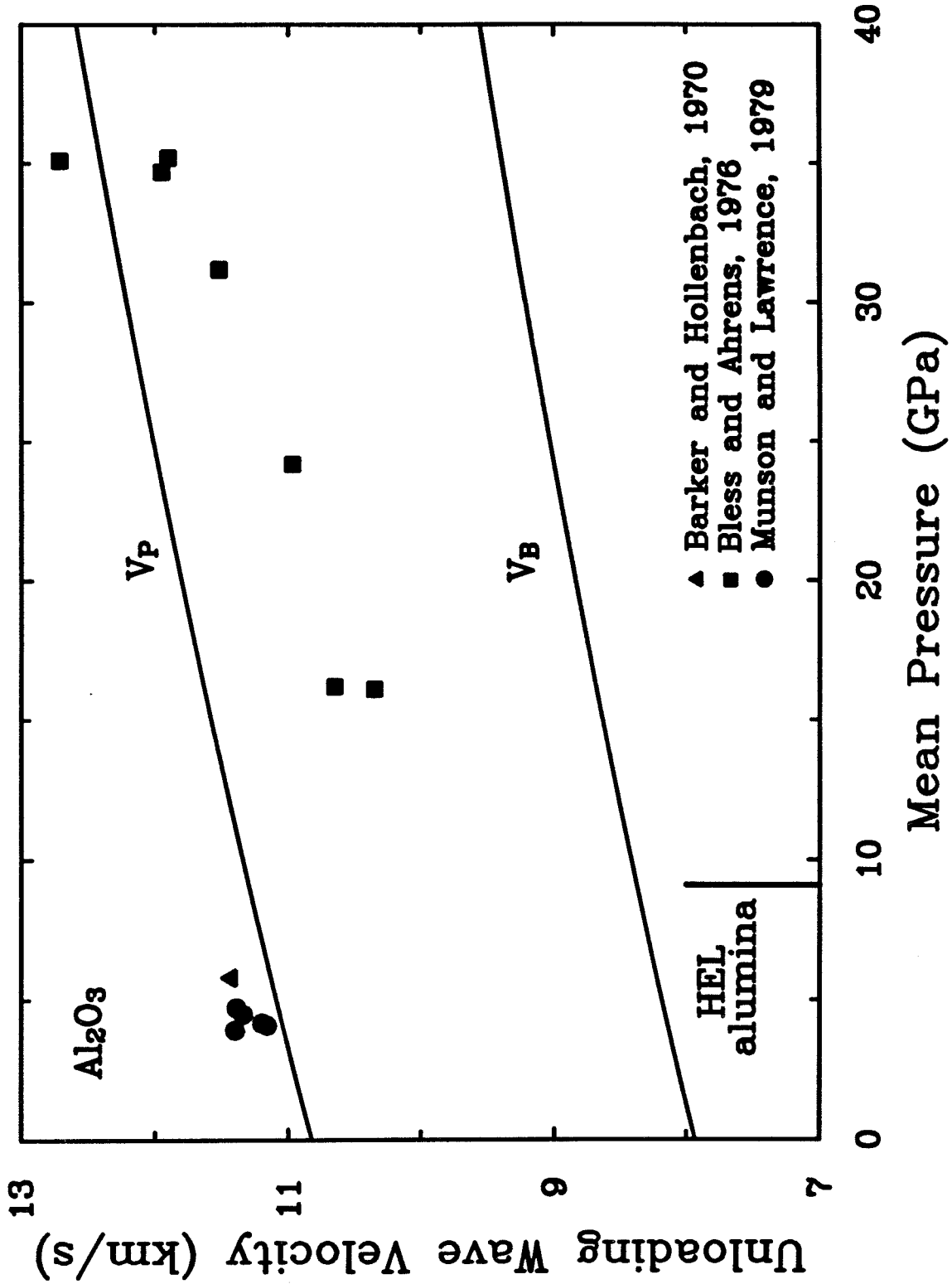
Unloading Wave Velocity (km/s)
13
11
9
7
0
10
20
30
40
Mean Pressure (GPa)
$Al_2O_3$
$V_P$
$V_B$
HEL
alumina
Barker and Hollenbach, 1970
Bless and Ahrens, 1976
Munson and Lawrence, 1979

observed features. Large, local temperature gradients can be created and persist in materials such as $CaCO_3$ and $SiO_2$ because of phase transitions which add significant amounts of thermal energy and their low thermal diffusivities. Local temperatures that are a significant fraction of or in excess of the melt temperature can be maintained, and these regions apparently dominate the dynamic response of the material. Dynamic yielding of strong solids such as alumina ($\sigma_{HEL}$ = 9.1 GPa) and single-crystal MgO ($\sigma_{HEL}$ = 2.5 GPa) also cause a loss of strength which partially recovers before passage of the unloading wave [*Bless and Ahrens,* 1976; *Grady,* 1977]. The recovery may be related to the larger thermal diffusivities in these materials which lead to faster thermal equilibration [*Grady* 1980]. Polycrystalline MgO, on the other hand, appears to unload in an almost purely elastic fashion. This may be controlled in part by the low initial yield strength (1.25 $\pm$ 0.25 GPa) which is more characteristic of a metal. More evidence for elastic-plastic behavior in MgO will be presented in the detailed analysis of the wave profiles in the next section. The distinction between the dynamic response of polycrystalline and single-crystal MgO was also apparent in the comparison of the Hugoniot relations discussed above.

### 3.4.3 Constitutive Behavior

Numerical simulations of the particle velocity histories were carried out using the one-dimensional finite difference wavecode WONDY [*Kipp and Lawrence,* 1982]. This program solves finite difference analogs for the equations of conservation of mass, momentum, and energy together with an appropriate constitutive law. For simulating plate-impact experiments, a rectilinear geometry with free boundary conditions is used. Descriptions of each material layer are entered into the code. These include the thickness, velocity, and the mesh dimension as well as material parameters such as the density, Hugoniot relation, Grüneisen parameter, and any constants required by the constitutive law. Criteria for fracture of layers and boundaries are also in-

cluded. Discontinuities in presure, velocity, and density associated with shock fronts are treated by the method of artificial viscosity. In general, the stress, $\sigma$, consists of a pressure (volumetric) term and a deviatoric term, $\sigma'$:

$$\sigma = P + \sigma', \tag{3.15}$$

where both stresses and pressures are taken to be positive in compression. The volumetric portion is described by the Mie-Gruneisen equation:

$$P = P_H + \frac{\gamma}{V}(E - E_H), \tag{3.16}$$

where V is the volume, E is the energy, $\gamma$ is the Grüneisen parameter, and the subscript H refers to the reference state. The reference state is taken to be the Hugoniot:

$$P_H = \frac{\rho_o c_o^2 \eta}{(1 - s\eta)^2}, \tag{3.17}$$

$$E_H = \frac{P_H \eta}{2\rho_o}, \tag{3.18}$$

where $\eta$ is given by:

$$\eta = 1 - \rho_o/\rho. \tag{3.19}$$

The Grüneisen parameter is modeled in the following way:

$$\rho\gamma = \rho_o\gamma_o. \tag{3.20}$$

The bulk sound velocity is given by:

$$V_B^2 = \left(\frac{\partial P}{\partial \rho}\right)_S, \tag{3.21}$$

and the compressional sound velocity is:

$$V_P^2 = 3\left(\frac{1-\nu}{1+\nu}\right) V_B^2, \tag{3.22}$$

where Poisson's ratio, $\nu$, is user-supplied, and in conjunction with $V_B$, also determines the shear modulus, $G$.

The stress deviators are obtained from a relation of the form:

$$\partial\sigma'/\partial t = 2G(\partial\epsilon/\partial t - g), \tag{3.23}$$

where $\epsilon$ is the engineering strain, t is time, and g is a relaxation function, which is zero for rate-independent behavior. The von Mises yield condition is used to determine whether plastic flow occurs. The yield stress can be zero, infinite, constant, or variable.

A simple description for solids with strength is the elastic-perfectly plastic model in which the yield strength is held constant (see Figure 3.19). Such a material behaves elastically until its yield point, after which it deforms plastically parallel to the Hugoniot, maintaining a constant offset of $2/3Y_o$ from the hydrostat. Upon unloading, the material again behaves elastically until it reaches a state of stress of $2/3Y_o$ below the hydrostat, after which it decompresses irreversibly to zero stress.

The yield strength, $Y_o$, of a material can be determined from the amplitude of the Hugoniot elastic limit (HEL) wave (assuming a von Mises yield condition):

$$Y_o = 2V_S^2\sigma_{HEL}/V_P^2. \tag{3.24}$$

The HEL amplitude of polycrystalline MgO was not directly measured in these experiments, but the compressive-wave structure was recorded at the buffer-window interface in the forward-impact experiments. The measured HELs were not entirely consistent for the four shots fired (Figure 3.10). For the two lower stress experiments (857 and 861), the HEL consisted of a relatively sharp jump to a velocity of 30-40 m/s, followed by a slower ramp to ~80 m/s before arrival of the main shock. The apparent elastic precursor velocity based on the time separation of the precursor and main shock arrivals was 9.5-9.6 km/s for these two experiments, although the velocity was not well resolved because of wave interactions generated at the buffer-sample interface. For the higher-stress experiments (859 and 864), the elastic precursor does not exhibit a jump but a long ramp increase in velocity. The toe of this ramp implies

a precursor velocity of ~12 km/s well above the longitudinal sound velocity of 9.81 km/s. Nonetheless, the amplitudes of the precursors are quite similar in all four wave profiles.

We modeled the amplitudes of the elastic precursor waves using WONDY simulations and an elastic-perfectly plastic material model for both MgO and Al 6061. The model parameters are listed in Table 3.4. The results of simulations for two of the four forward-impact experiments are shown in Figure 3.16. The yield strength of Al 6061 was fixed at 0.3 GPa [*Asay and Lipkin,* 1978]. The yield strength of polycrystalline MgO was varied between 0.5 and 2.5 GPa and the predicted compressive waveforms are shown in the figure. For yield stresses above about 1.5 GPa, significant secondary structure is evident as a consequence of the onset of plastic deformation in the Al buffer. That is, the elastic wave stress transmitted from MgO to the buffer exceeds its ability to support elastic stresses, and a two-wave structure with both elastic and plastic components propagates through the buffer. No such secondary structure is observed in the measured wave profiles. For yield stresses in MgO below 1.0 GPa, the predicted amplitude of the HEL waves lies well below the experimentally observed value. Yield stresses in the range of 1.0-1.5 GPa yield HEL amplitudes that are reasonably consistent ($\pm$10 m/s) with the experimentally measured values. We therefore adopt $Y_o = 1.25 \pm 0.25$ GPa as representing the possible range of compressive yield strengths of polycrystalline MgO. This implies a Hugoniot elastic limit of $1.6 \pm 0.3$ GPa. The HEL of single crystal MgO shocked along [100] was found to be 2.5 GPa for 3.3 mm-thick samples at peak stresses between 4.8 and 11.2 GPa [*Grady,* 1977]. *Ahrens* [1966] observed elastic wave amplitudes of 3.5-8.9 GPa in [001] MgO shocked to peak stresses between 16.6 and 42.3 GPa. *Ahrens* [1966] further noted that precursor amplitude decreases with propagation distance. This, together with the peak-stress dependence of the HEL, and *Grady's* [1977] observation of a decrease in particle velocity behind the precursor, are all evidence of

stress-relaxation phenomena taking place. There is no clear evidence of stress relaxation in the polycrystalline MgO wave profiles, but any such effects could be masked during passage through the buffer. The precursor amplitude in the polycrystalline material is significantly less than single crystal values. This has been observed before in other materials, notably $Al_2O_3$ [*Graham and Brooks,* 1971; *Mashimo et al.,* 1988] and is a reflection of different yielding processes in single and polycrystals.

The dynamic response of ceramics has long been of interest because of the engineering and geological importance of these materials. Alumina has received the most extensive study. EOS and stress history measurements [*Ahrens et al.,* 1968; *Mashimo et al.,* 1988] generally support an elastic-plastic model for this material with partial loss of shear strength. Specular velocity interferometer wave profile measurements in the elastic regime can be modeled using Maxwellian stress relaxation with a yield strength of 5.8 GPa and a relaxation time constant of 70 ns [*Munson and Lawrence,* 1979]. VISAR wave profile measurements have been reported in other high-strength ceramics (SiC, $B_4C$, $TiO_2$, $ZrO_2$) by *Kipp and Grady* [1989]. Of these, only SiC can be modeled with a relatively simple material model. This was a modified elastic-plastic model that incorporates anisotropic strain hardening (Bauschinger effect). The other materials all exhibit anomalous dispersion upon both loading and unloading that implies significant deviation from elastic-plastic behavior.

In order to assess whether an elastic-plastic model is an appropriate description of the dynamic response of magnesia, numerical simulations of the experiments were undertaken, utilizing an elastic-perfectly plastic (EPP) model for MgO. Al 6061 and LiF were also modeled as EPP with the parameters listed in Table 3.4. The foam model of *Grady and Furnish* [1988] was used to describe the flyer-backing material. The predicted particle velocity histories are compared to measured values for a representative reverse-impact experiment in Figures 3.17 and 3.18. The yield strength of MgO was assumed to be 1.25 GPa in the first simulation and 2.5 GPa

Figure 3.16: Comparison of compressive-wave structure transmitted through the aluminum buffer with wavecode simulations for two of the forward-impact experiments. The dotted curves are the experimental data with shot numbers listed to the left of each record. The solid lines show WONDY simulations using different values for the yield strength of polycrystalline MgO. Starting from the lowest amplitude profile, the computed profiles correspond to yield strengths of 0.5, 1.25, and 2.5 GPa as indicated next to each curve.

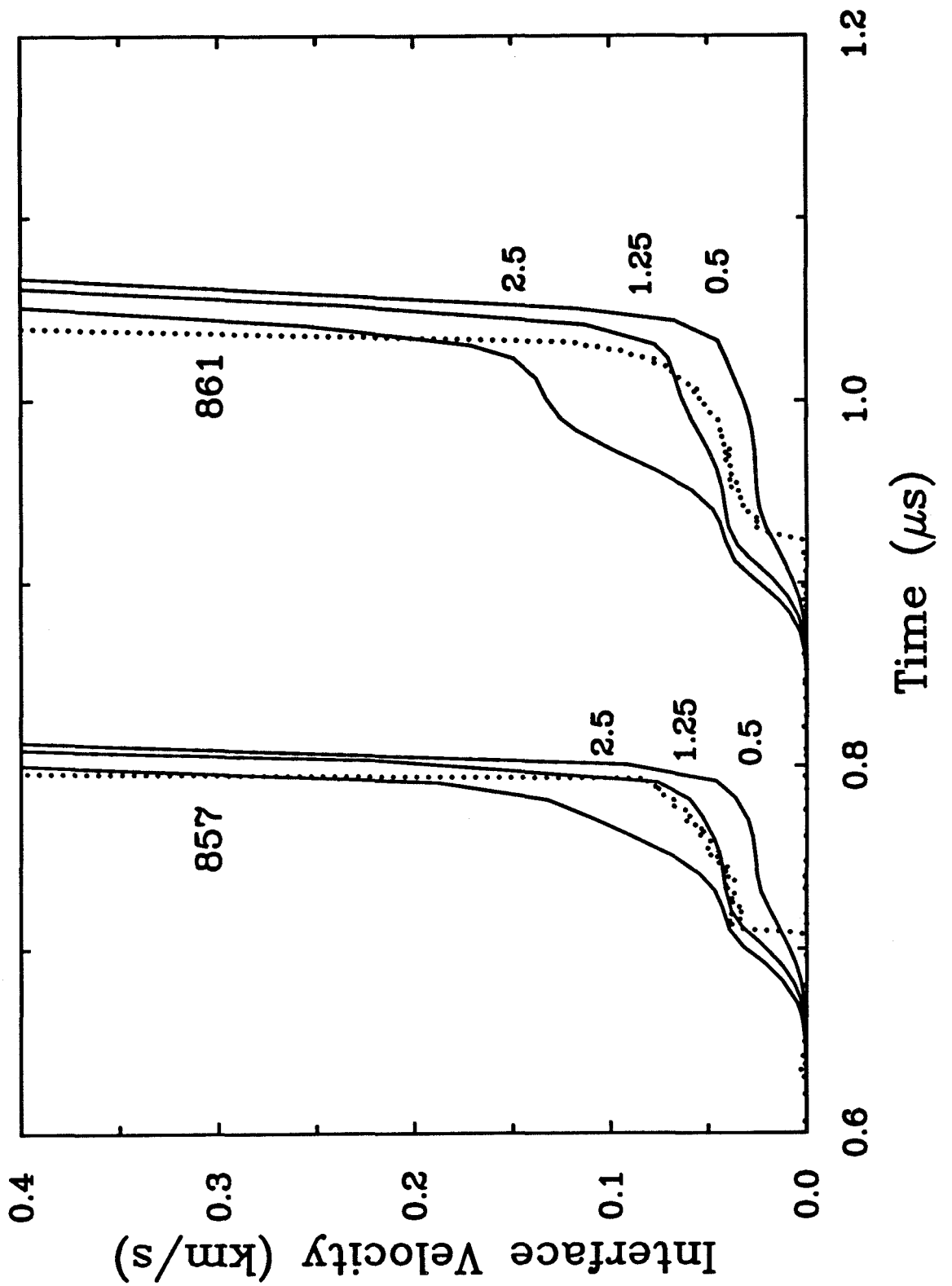
Interface Velocity (km/s)
0.0
0.1
0.2
0.3
0.4
Time (μs)
0.6
0.8
1.0
1.2
857
861
2.5
1.25
0.5
2.5
1.25
0.5

in the second simulation. The EPP model with $Y_o$ =1.25 GPa does a poor job of matching the observed wave profile. While the initial elastic release is well modeled, the bulk of the unloading history arrives much too late in the simulation. This indicates that the unloading behavior of MgO is not significantly dispersive.

Much better agreement between calculation and experiment is obtained when the initial yield strength is 2.5 GPa (Figure 3.18). This figure shows that the EPP model is generally appropriate for describing the dynamic response of MgO. A detailed comparison of measured and calculated wave profiles indicates that these are some important deviation from the model, however. The initial yield strength is a factor of 2 larger than that inferred from the HEL amplitudes. This implies that MgO undergoes significant strain hardening.

The EPP model also predicts four distinct wave arrivals. The first arrival is due to the reflection of the MgO elastic precursor from the foam backing which propagates back through MgO and the aluminum buffer as an elastic wave. This arrival (time $t_3$ in Figure 3.3) is in good agreement with the measured initial unloading which is very sharp (elastic). The second wave arrival also originates from the MgO precursor, but upon encountering the Al buffer, the elastic wave splits into elastic and bulk components, creating the second distinct arrival. In the experimental profile, only a single arrival is evident. This is due to the well-known Bauschinger effect in aluminum that blurs the distinction between elastic and plastic unloading waves in this material (*Lawrence and Asay,* 1979). The latter two predicted arrivals are due to reflection of the shock wave from the foam backing, which breaks into separate elastic and plastic components in traversing the MgO flyer and then propagates with a plastic wave velocity through the buffer. The experimental data instead show diffuse unloading here with no clear wave separation. There is no distinct arrival of the bulk wave in MgO at the buffer-window interface.

We attempted to improve our dynamic-response model by incorporating modifi-

Figure 3.17: Comparison of calculated and measured particle velocity histories at the aluminum-LiF interface for experiment 848. The dotted curve is the experimental profile, and the solid line is the numerical simulation. MgO, Al, and LiF are treated as elastic-perfectly plastic. The yield strength of MgO is 1.25 GPa. The experimental profile was shifted in time to line up with the calculation.

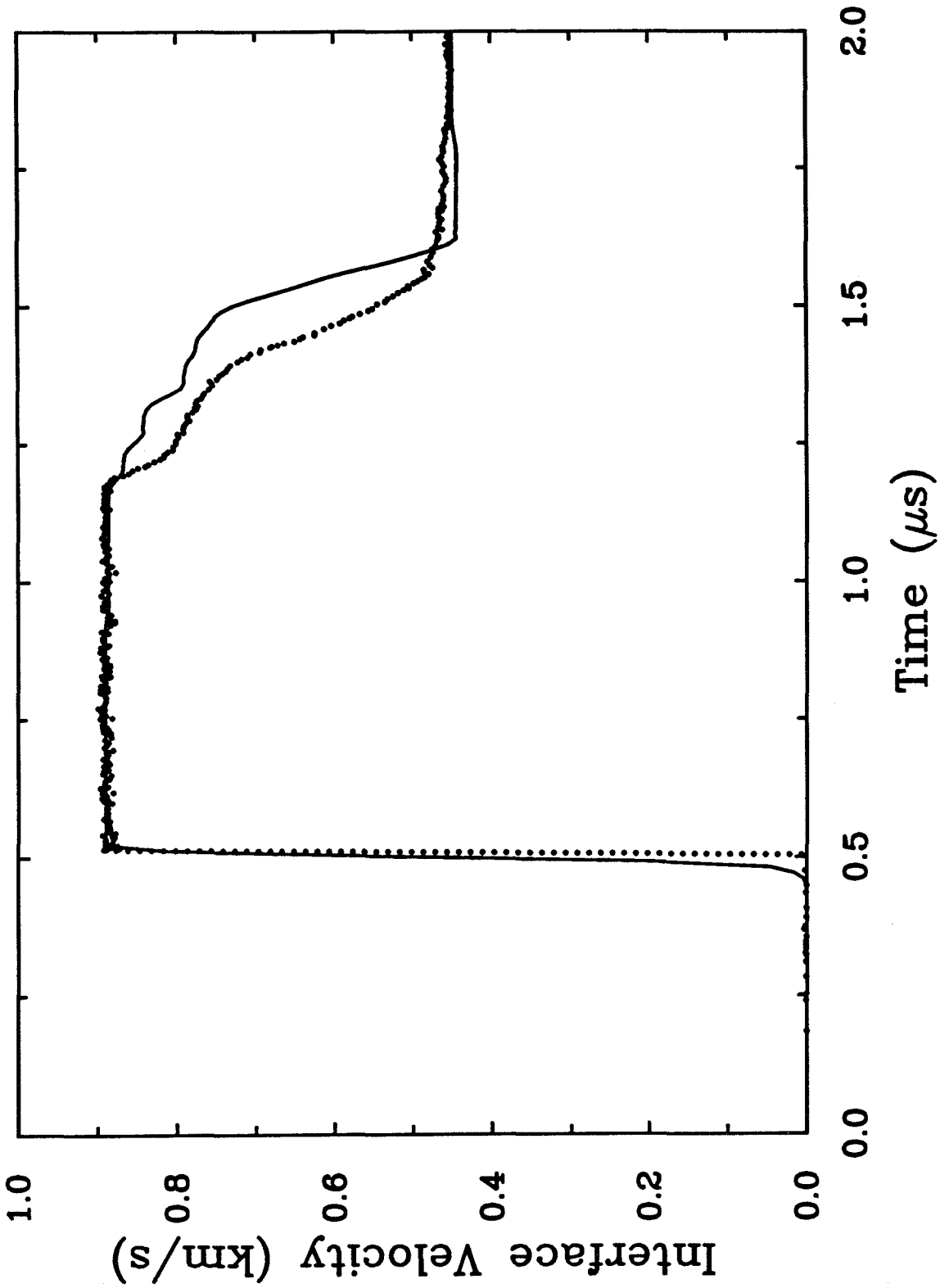
Interface Velocity (km/s)
0.0
0.2
0.4
0.6
0.8
1.0
0.0
0.5
1.0
1.5
2.0
Time (μs)

Figure 3.18: Comparison of calculated and measured particle velocity histories at the aluminum-LiF interface for experiment 848. An elastic-perfectly plastic constitutive model has been assumed for MgO with $Y_o = 2.5$ GPa.

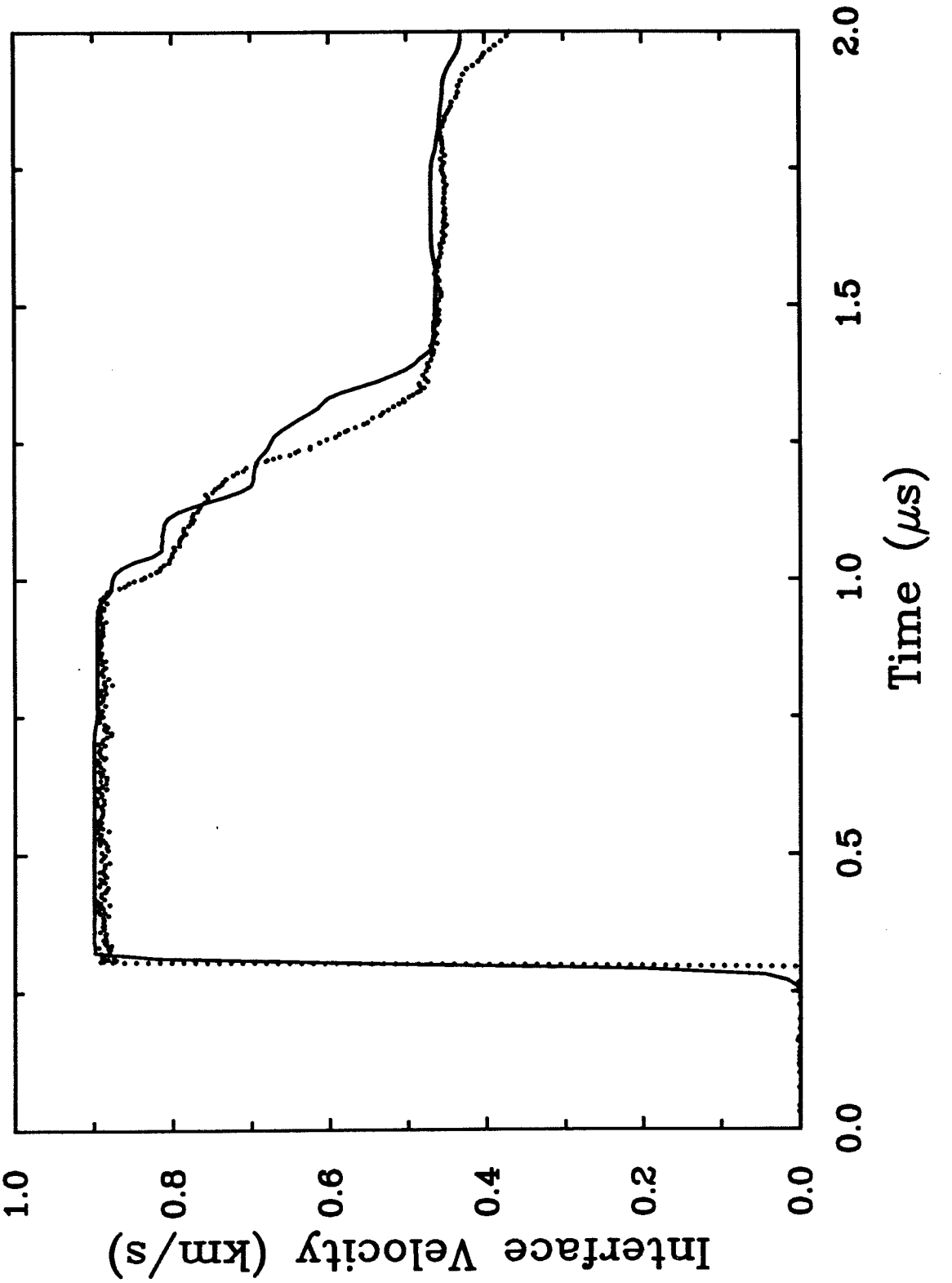
Interface Velocity (km/s)
0.0
0.2
0.4
0.6
0.8
1.0
Time (μs)
0.0
0.5
1.0
1.5
2.0

cations to the elastic-perfectly plastic model that have been successfully applied to metals. In particular, we included the possibility for a Bauschinger effect and strain-rate-dependent stress relaxation. In the Bauschinger effect, the yield stresses upon loading and unloading differ. In addition, significant non-linearity in the unloading path is introduced such that the distinction between elastic and plastic unloading becomes blurred [*Moss and Glenn*, 1984]. This behavior can be a consequence of micromechanical aspects of deformation, including dislocation interaction, slip bands, and twinning. Flow-stress anisotropy is implemented into the wavecode using a multielement kinematical model [*Herrmann,* 1974] in which the equilibrium stress deviator, $\sigma'_e$, is given by:

$$\sigma'_e = \sum a_i \sigma'_i, \tag{3.25}$$

where the $a_i$ are normalized weighting factors. Each elemental stress deviator, $\sigma'_i$, is subject to a von Mises yield condition:

$$\sigma'^2_i \leq (2/3Y_i)^2 \tag{3.26}$$

A representative stress-strain path for a material exhibiting the Bauschinger effect is compared to the ideal response in Figure 3.19.

Strain-rate dependence is also treated through the deviatoric stress. The stress deviator is obtained by relaxation from some instantaneous value to an equilibrium value, using the relaxation function in Eqn. 3.23. The relaxation function has the form:

$$g = \frac{\sigma' - \sigma'_e}{Gt_r}, \tag{3.27}$$

where $t_r$ is a characteristic material relaxation time. A schematic stress-strain diagram for a stress-relaxing solid is also shown in Figure 3.19.

The unloading wave profiles measured at the buffer-window interface are strongly affected by the properties of the buffer material and only indirectly represent the properties of MgO. The model that describes the buffer material is therefore of

Figure 3.19: Idealized stress-strain diagrams illustrating elastic-perfectly plastic response, strain-rate-dependent stress relaxation, and the Bauschinger effect. The dotted curve in each panel is the hydrostat. In the bottom two panels, the elastic-perfectly plastic response is shown as a dashed curve.

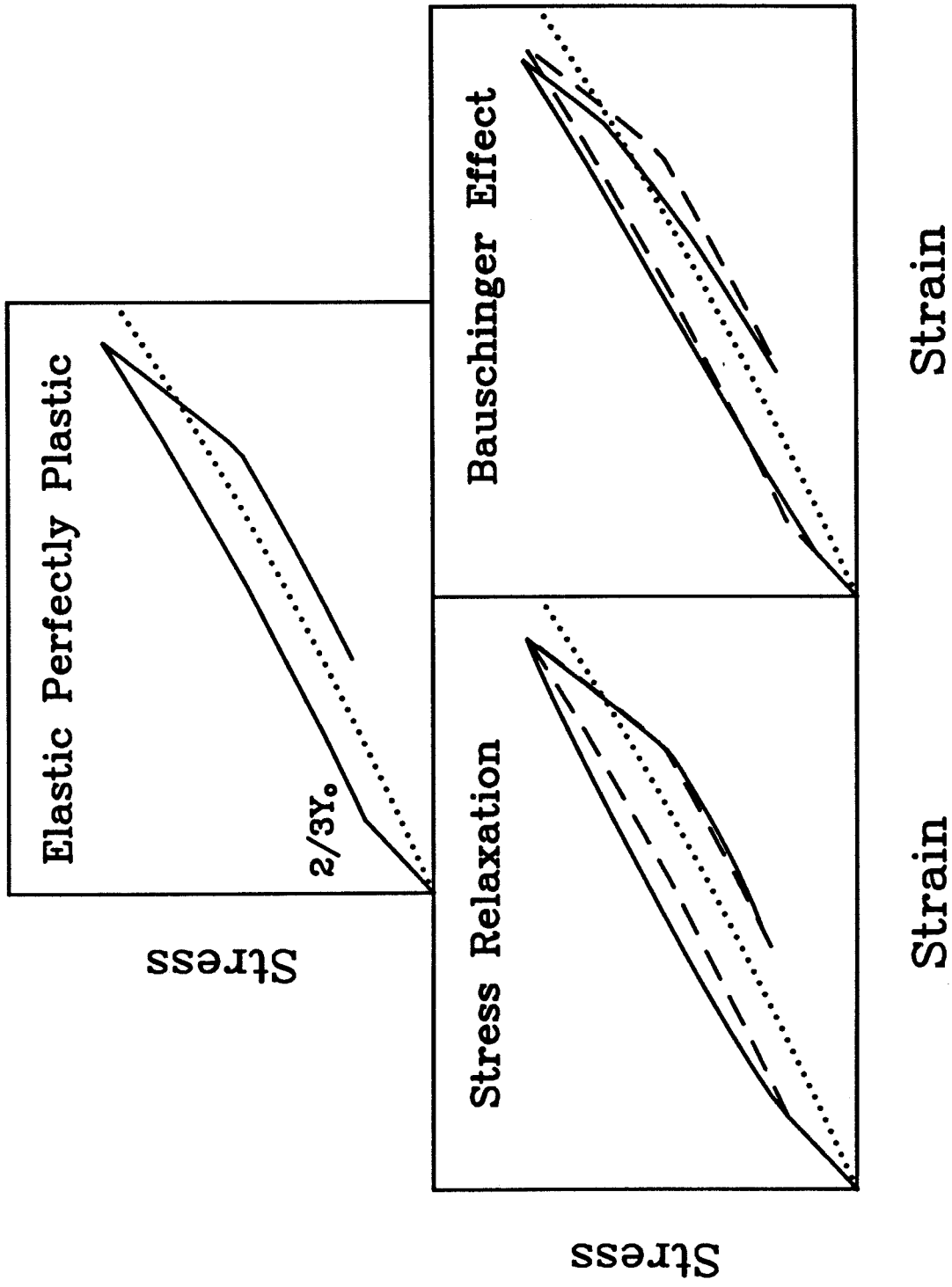
Elastic Perfectly Plastic
2/3Y₀
Bauschinger Effect
Stress Relaxation
Stress
Strain
Stress
Strain

| MgO | | | | Al 6061 | |
|---|---|---|---|---|---|
| Model 1 | | Model 2 | | | |
| $a_i$ | $Y_i$ (GPa) | $a_i$ | $Y_i$ (GPa) | $a_i$ | $Y_i$ (GPa) |
| 0.10 | 2.95 | 0.7 | 1.5 | 0.581 | 0.169 |
| 0.20 | 3.0 | 0.12 | 4.0 | 0.190 | 0.350 |
| 0.20 | 3.1 | 0.10 | 8.0 | 0.078 | 0.472 |
| 0.35 | 3.2 | 0.08 | 12.0 | 0.052 | 0.977 |
| 0.09 | 3.5 | - | - | 0.063 | 1.649 |
| 0.06 | 4.1 | - | - | 0.036 | 2.589 |

Table 3.8: Parameters of Bauschinger models for MgO and Al 6061.

great importance. We adopted an elastic-plastic model for Al 6061 which included a Bauschinger effect. The required parameters were adapted from the work of *Lawrence and Asay* [1979] and are listed in Table 3.8.

Starting with the elastic-perfectly plastic model, the wave profiles were fit in an iterative fashion by adjusting the parameters of the Bauschinger model and the relaxation time constant. The parameters derived are therefore particular to these wave profiles only. The first point to note is that very little rate dependence is required in fitting the profiles. A time constant of 5 ns was found to improve the fit slightly for approximately the final 20% of the unloading history. The Bauschinger effect, on the other hand, is very significant in MgO.

We were unable to fit all of the data with a single model. The reason for this can be seen with reference to Figures 3.10 and 3.8. The reverse-impact experiments exhibit significantly stronger and sharper initial release behavior that the forward experiments. The forward-impact experiments involved a propagation distance through

MgO of about 7 mm, while in the reverse experiments the MgO propagation distance was 3-4 mm. This may indicate that the wave profiles are not steady. There is further indication of non-steady wave propagation in comparing reverse-impact experiments at similar stresses in nominally 3-4 mm thick targets (cf: 853 and 848; 851 and 856). The unloading profiles appear to be diffusing with increasing propagation distance. Two other factors should be noted. First, the lowest-amplitude reverse-impact experiments (854) differs from the other reverse experiments in that it has a weak and diffuse elastic release. It is more similar to the forward-impact wave profiles. In the forward-impact experiments, the two highest-stress experiments (859 and 864) show nearly featureless unloading, particularly shot 864. These points illustrate that the shape of the profile in MgO is dependent both on peak stress and propagation distance.

Our modeling procedure converged on two models for MgO. Model 1 fits the forward-impact experiments and the lowest-amplitude reverse experiment. The Bauschinger parameters for this model are listed in Table 3.8 and the model predictions are compared to representative experimental data in Figure 3.20. The agreement between data and calculation is good for the unloading portions of the waveform. The rise time of the shock front is longer in the model calculations than in the experimental data because of the necessity of smearing the shock front over several zones in the calculations arising from the use of artificial viscosity.

The reverse-impact experiments were fit using model 2 (Table 3.8) and are displayed in Figure 3.21. This model reproduces the strong elastic release observed in these experiments. The primary difference between the model and the experimental records is that the model predicts a second elastic release originating from the reflection of the shock wave at the foam-flyer interface. In fact, the release at this point is quasi-elastic and highly dispersive.

Together, these two models show that the unloading response of polycrystalline

Figure 3.20: Comparison of numerical simulations of forward-impact experiments using model 1 with experimental data. The solid symbols are the experimental data, and the light solid line is the computed interface particle velocity history. Shot numbers are listed next to each profile. The timing is arbitrary and has been selected to offset the profiles. The experimental profile for shot 859 has been scaled by a factor of 1.05 to bring its amplitude into agreement with the calculated profile.

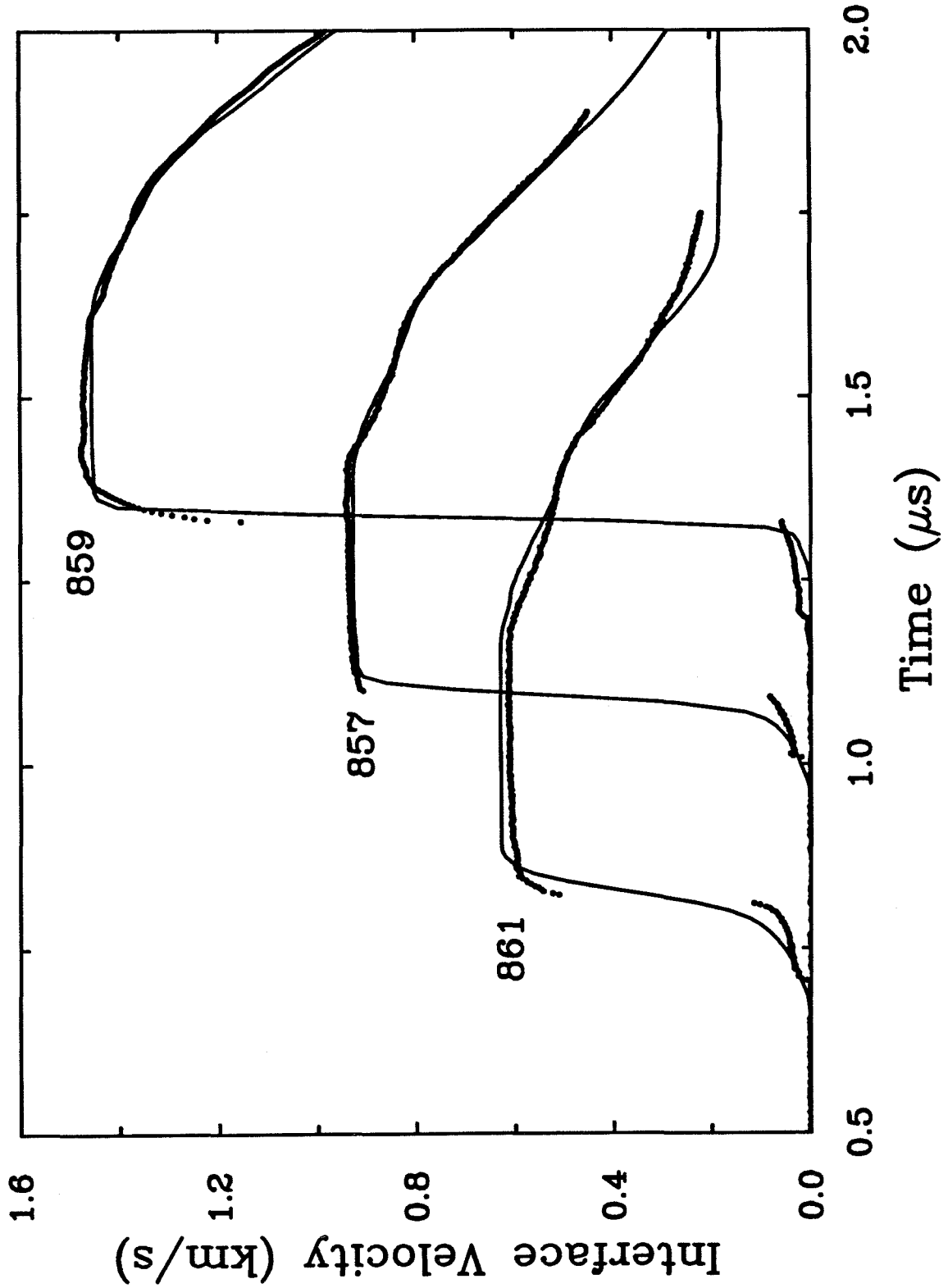
Interface Velocity (km/s)
1.6
1.2
0.8
0.4
0.0
0.5
1.0
1.5
2.0
Time (μs)
859
857
861

Figure 3.21: Comparison of numerical simulations of reverse-impact experiments with experimental data. The solid symbols are the experimental data, and the light solid line is the computed interface particle velocity history. Shot numbers are listed next to each profile. Shot 854 was simulated using model 1 and the remaining two profiles were simulated using model 2. The timing is arbitrary and has been selected to offset the profiles.

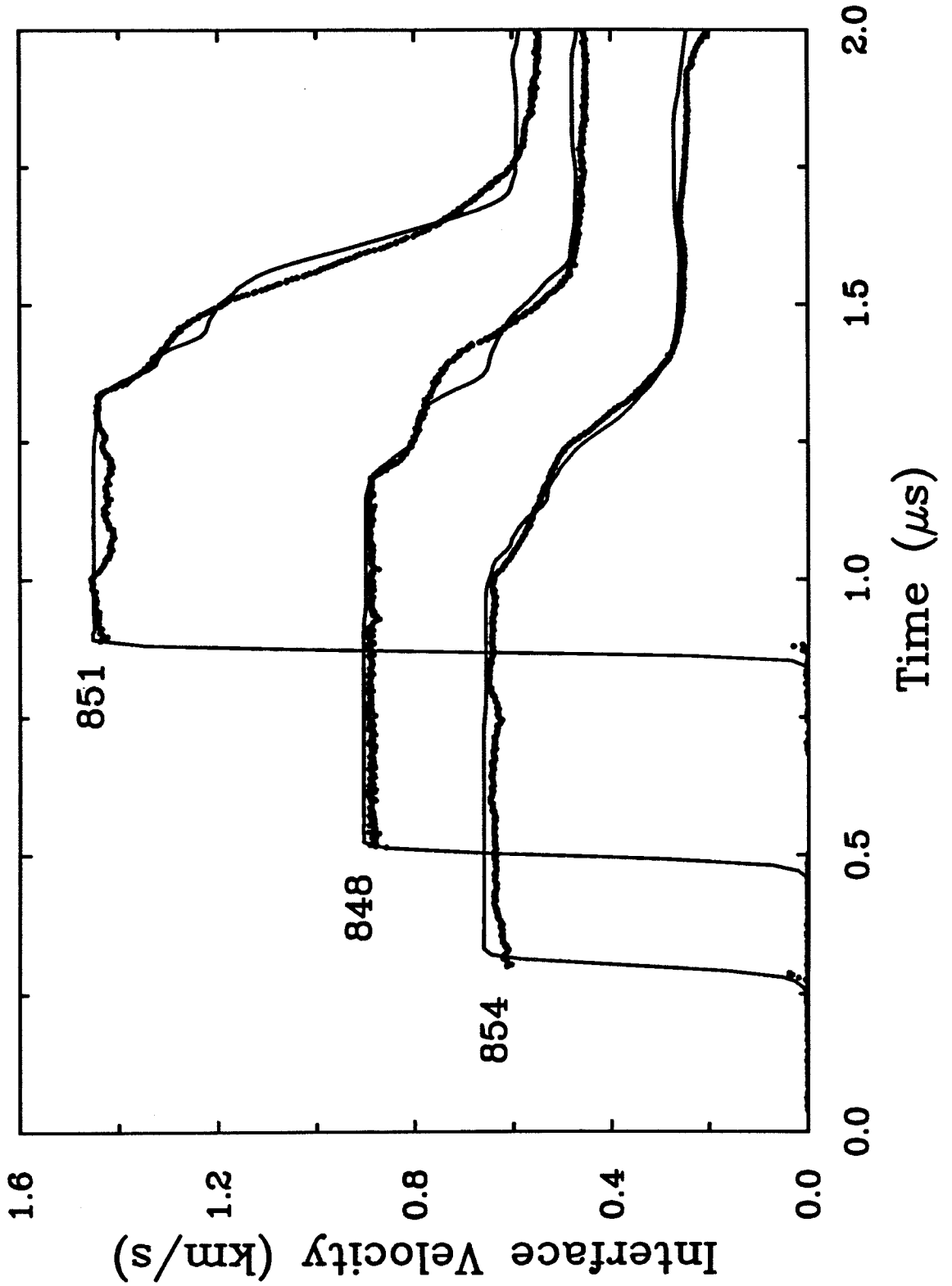
Interface Velocity (km/s)
1.6
1.2
0.8
0.4
0.0
0.0
0.5
1.0
1.5
2.0
Time (μs)
851
848
854

MgO can be accurately described using a modified elastic-plastic model that utilizes concepts that have been successfully applied to metals. Previously *Kipp and Grady* [1989] demonstrated that measured wave profiles in SiC could be fit by an elastic-plastic model incorporating the Bauschinger effect, but other materials ($B_4C$, $ZrO_2$, $TiBr_2$) were too dispersive to be fit with the elastic-plastic model. Alumina also appears to exhibit elastic-plastic behavior [*Ahrens et al.*, 1968], but this has not yet been confirmed on the basis of detailed wave profile measurements above the elastic limit.

The wavecode computes the velocity, density, energy, and axial stress at each time step for each zone in the problem. Once the interface velocity histories are successfully modeled, the behavior of other variables of interest can be extracted from the simulations. Figures 3.22 and 3.23 show representative stress-strain histories at the center of the MgO samples for the forward- and reverse-impact experiments. Here the strain is defined as:

$$\eta = 1 - \rho_o/\rho. \tag{3.28}$$

The Bauschinger effect is responsible for the smoothing of the transition from elastic to plastic strain upon both loading and unloading. This effect is much more pronounced in the forward-impact model (model 1). The higher-stress reverse-impact experiments (848 and 851) retain a clear transition from elastic to plastic unloading. The densities determined by the wavecode are about 1% less than those determined by impedance matching. The stresses computed by WONDY are consistent with the impedance-match determinations within their uncertainties. However, the WONDY determinations are greater by 0.4-0.8 GPa because of the inclusion of the deviatoric stresses.

There are several lines of evidence which suggest that polycrystalline MgO retains its strength when shock-compressed in the 10-37 GPa range. First, the pressure-volume states measured in the EOS experiments lie 0.5-1.5 GPa above the hydrostat

Figure 3.22: Stress-strain histories derived from numerical simulations of forward-impact particle velocity histories in Figure 3.20. The dashed curve is the static isotherm derived from the data of Table 3.7.

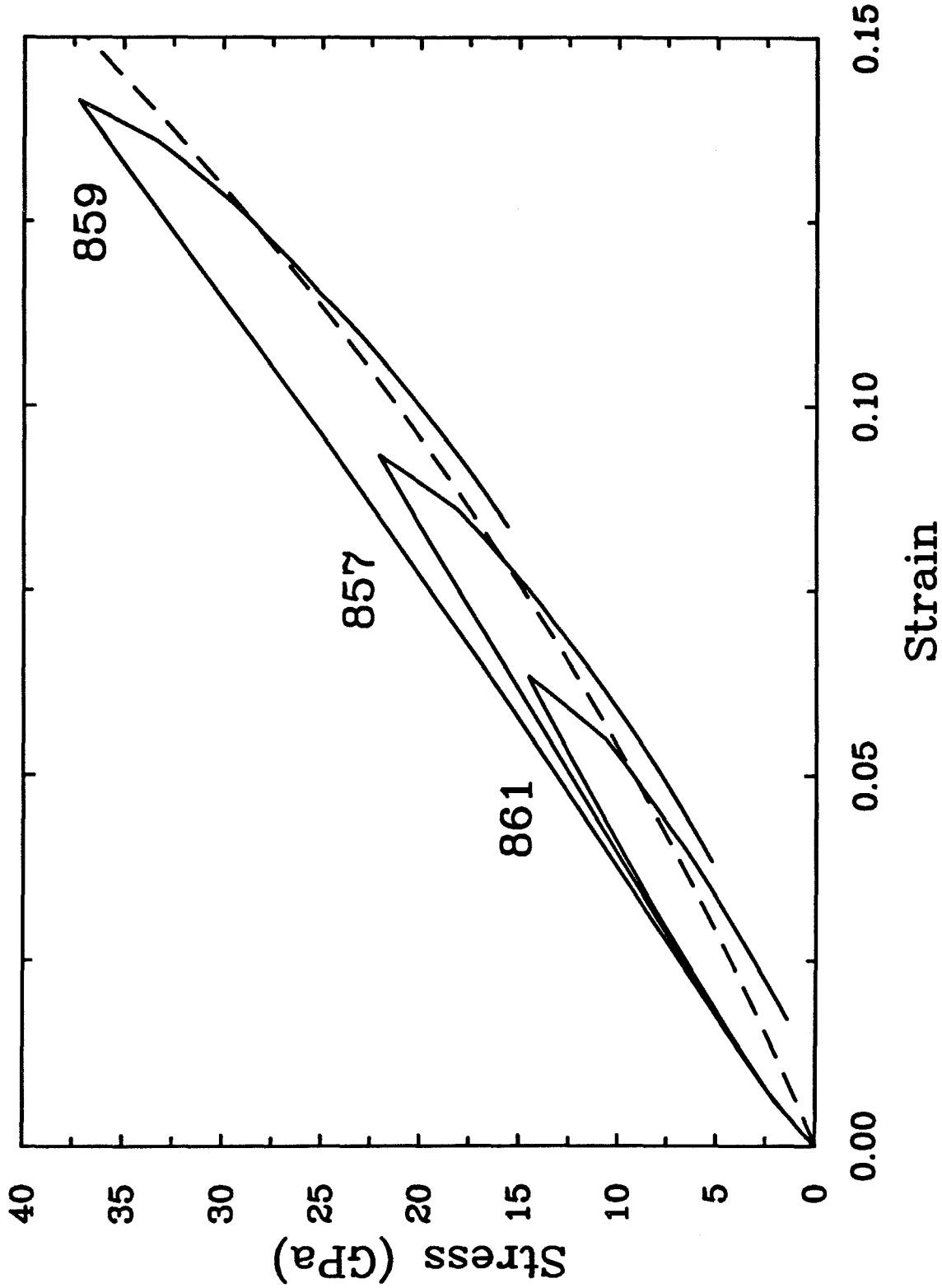
859
857
861
Stress (GPa)
Strain
0
5
10
15
20
25
30
35
40
0.00
0.05
0.10
0.15

Figure 3.23: Stress-strain histories derived from numerical simulations of reverse-impact particle velocity histories in Figure 3.21. The dashed curve is the static isotherm derived from the data of Table 3.7.

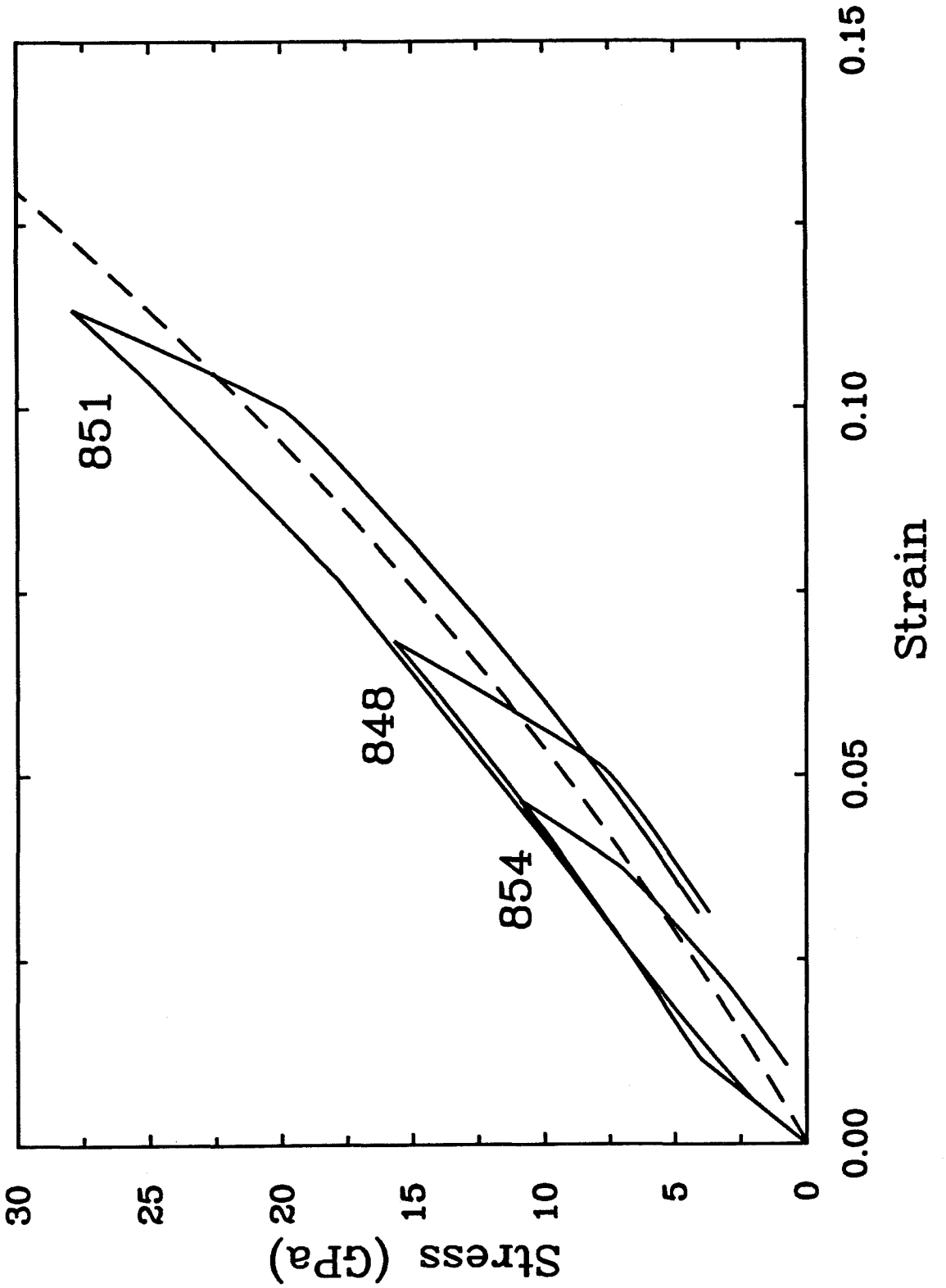
851
848
854
Stress (GPa)
Strain
0
5
10
15
20
25
30
0.00
0.05
0.10
0.15

(Figure 3.7). The numerical simulations of the unloading wave profiles yields stress-strain states that lie 2.5-3.7 GPa above the hydrostat for both models. In addition, the initial unloading is sharp and agrees well with the expected compressional sound velocity from ultrasonic data.

According to the model of *Grady* [1977], single-crystal periclase collapses to the hydrostat and exhibits a loss of shear strength when shock-compressed. The later unloading wave structure implies that material strength has recovered nearly completely. In contrast, polycrystalline MgO maintains significant ($1.0 \pm 0.5$) strength when shock-compressed. Upon unloading, material strength has apparently further increased to $3.1 \pm 0.6$ GPa. Significant differences in the strength properties of single crystals and polycrystals have also been observed in $Al_2O_3$ [*Graham and Brooks,* 1971].

### 3.4.4 Thermal Expansivity of MgO

As discussed previously, the single-crystal Hugoniot for MgO is coincident with the static isotherm derived from ultrasonic data at low pressure, supporting the notion of at least partial loss of strength for the single-crystal material under dynamic compression. At higher pressures, the Hugoniot and static isotherm diverge (Figure 3.24) because of thermal effects as material strength becomes small at high temperature (*Asay,* 1985 and Chapter 4). This interpretation for MgO is strongly supported by the work of *Jackson and Niesler* [1982] who demonstrated that Hugoniot data to 120 GPa are consistent with ultrasonic elasticity measurements to 3 GPa when the ultrasonic data is extrapolated using the Birch-Murnaghan equation, and thermal corrections are applied to the shock data using Mie-Grüneisen theory. In contrast, diamond anvil cell static-compression data for MgO [*Mao and Bell,* 1979] to 94 GPa show significant discrepancies with an isotherm derived from shock data. These static-compression data are also inconsistent with the ultrasonic data and may be biased

because of non-hydrostatic stresses in the diamond anvil cell. *Vassiliou and Ahrens* [1981] extended Hugoniot equation of state measurements on single-crystal MgO to 200 GPa and demonstrated that when reduced to isothermal conditions, these data are consistent with the ultrasonic parameters of *Jackson and Niesler* [1982]. Furthermore, these data show no evidence for a phase transition in MgO along its Hugoniot to these pressures.

More recently, *Svendsen and Ahrens* [1987] reported the results of four temperature measurements on shocked single-crystal MgO between 174 and 203 GPa. These data support the earlier conclusion of *Vassiliou and Ahrens* regarding the absence of phase changes up to this pressure as the measured temperatures are consistent with continuum calculations that do not include a phase-transition energy term. Furthermore, comparison of measured temperature trends with an inferred melting curve for MgO based on a Lindemann melting criterion indicates that the equilibrium melting boundary for MgO occurs at a Hugoniot pressure of 265 GPa, significantly above the range of the temperature measurements [*Svendsen and Ahrens,* 1987]. The partial release states measured by *Vassiliou and Ahrens* [1981] as well as that obtained from a Hugoniot pressure of 133 GPa in this study further support the absence of a phase change in that the release points imply unloading adiabats which are less steep than the Hugoniot (Figure 3.24). The consistency of the 133 GPa Hugoniot datum and its release point for polycrystalline MgO with single-crystal data suggest that differences between the single-crystal and polycrystal Hugoniot may become very small at high pressure.

Shock and static data are normally compared by inferring a thermal-pressure offset to be applied to the shock data at constant density using Mie-Grüneisen theory and by making an assumption about the volume dependence of the Grüneisen parameter. One could also apply a thermal correction at constant pressure. This approach is not usually adopted because the temperatures and thermal expansivities are not

Figure 3.24: Pressure-density Hugoniot data for magnesium oxide. The solid circles are the data of this study for low-porosity polycrystalline MgO. Open symbols show single-crystal and higher-porosity polycrystalline data [*Al'tshuler et al.,* 1965; *Marsh,* 1980; *Vassiliou and Ahrens,* 1981]. Partial release points are indicated by crosses and are tied to the corresponding Hugoniot point with straight lines. The solid curve is the single-crystal Hugoniot, and the dashed line is the static isotherm derived from ultrasonic data [*Jackson and Niesler,* 1982]. The boxed region shows the range of pressures for which temperatures have been measured in shock-compressed single-crystal MgO [*Svendsen and Ahrens,* 1987].. This is the range of pressures over which the thermal expansivity has been determined.

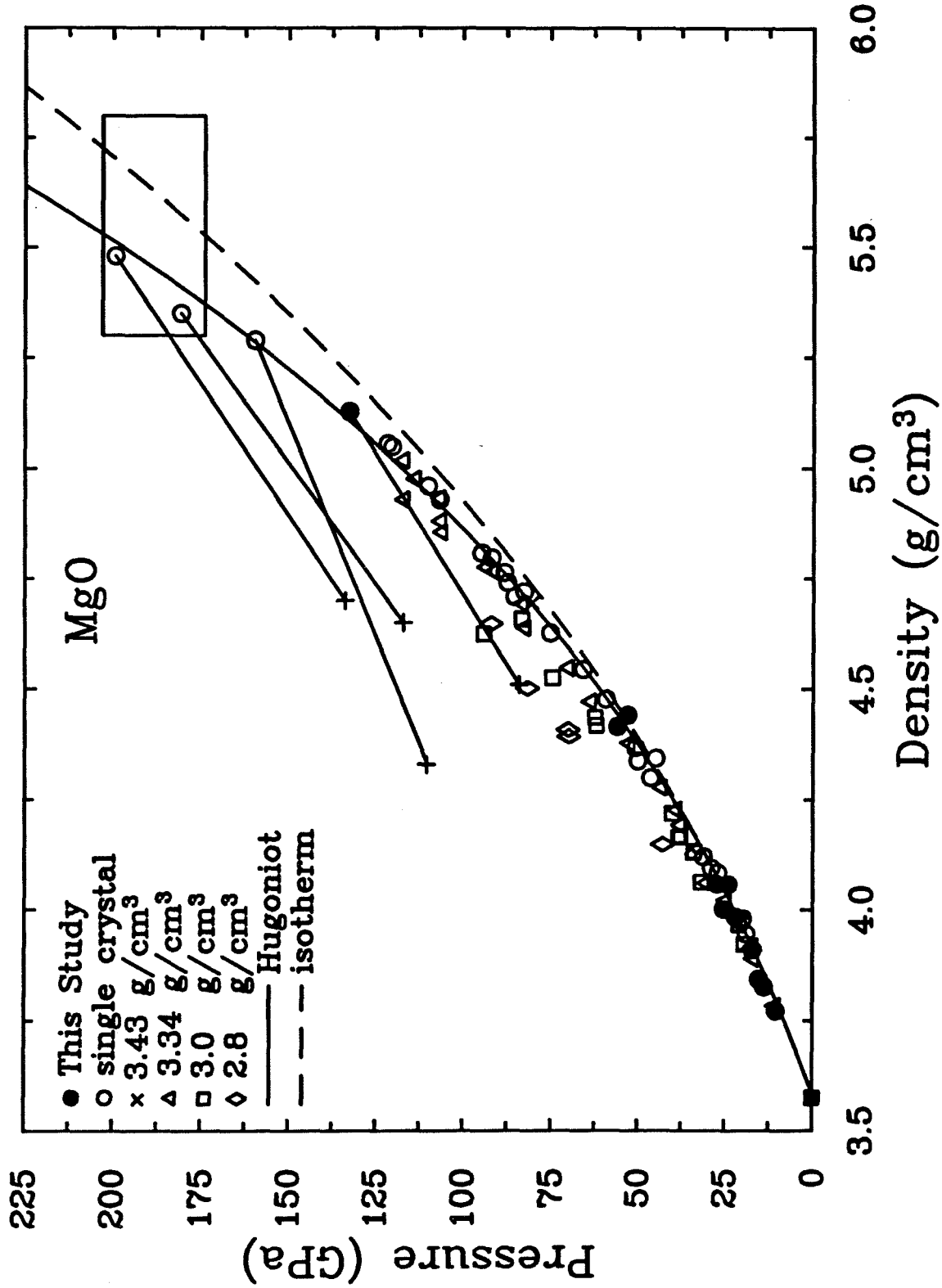
MgO
● This Study
○ single crystal
× 3.43 g/cm³
▲ 3.34 g/cm³
□ 3.0 g/cm³
◇ 2.8 g/cm³
Hugoniot
isotherm
Pressure (GPa)
Density (g/cm³)
225
200
175
150
125
100
75
50
25
0
3.5
4.0
4.5
5.0
5.5
6.0

| Pressure (GPa) | $\rho_H$ (g/cm$^3$) | $\rho_{iso}$ (g/cm$^3$) | $T_H$ K | $\alpha$ $10^6 K^{-1}$ |
|---|---|---|---|---|
| 174.0 ± 2.5 | 5.371 ± 0.047 | 5.542 ± 0.032 | 3081 ± 120 | 11.3 ± 3.8 |
| 181.1 ± 2.7 | 5.412 ± 0.048 | 5.592 ± 0.033 | 3071 ± 130 | 11.8 ± 3.9 |
| 187.9 ± 2.8 | 5.450 ± 0.049 | 5.640 ± 0.034 | 3281 ± 375 | 11.5 ± 3.9 |
| 203.1 ± 3.0 | 5.530 ± 0.052 | 5.743 ± 0.037 | 3663 ± 395 | 11.2 ± 3.6 |

Table 3.9: Thermal expansion coefficient of MgO at high pressure from comparison of the Hugoniot and static-compression curves.

independently known. In the case of MgO, however, knowledge of the Hugoniot and the ultrasonically derived 300 K isotherm together with the measured shock temperatures allows the thermal expansivity to be constrained between 174 and 203 GPa. As before, the static isotherm is constructed from the data of *Jackson and Niesler* [1982] using the Birch-Murnaghan equation. This approach is supported both by Mie-Grüneisen theory to 200 GPa and by the compressional sound velocities to 27 GPa presented earlier. Average thermal expansivities, $\bar{\alpha}$ were calculated using:

$$\bar{\alpha} = \frac{\ln(\rho_I/\rho_H)}{T_H - 300}, \tag{3.29}$$

where $\rho_I$ is the 300 K density at a given pressure, and $\rho_H$ and $T_H$ are the corresponding density and temperature along the Hugoniot. The calculated thermal expansivities for MgO are listed in Table 3.9.

The value of thermal expansivity under lower mantle conditions is important in assessing whether the lower mantle differs in composition from the upper mantle [*Jackson*, 1983; *Knittle et al.*, 1986; *Chopelas and Boehler*, 1989] and hence has implications for theories of the formation and evolution of the Earth. *Anderson et al.* [1990] have proposed the following relationship for the density dependence of the

thermal expansivity:

$$\alpha/\alpha_o = (\rho/\rho_o)^{-\delta_T}, \tag{3.30}$$

where the subscript o refers to ambient-pressure quantities and $\delta_T$ is given by:

$$\delta_T = -\frac{1}{\alpha K_T}\left(\frac{\partial K_T}{\partial T}\right)_P. \tag{3.31}$$

The basis for this relation is a data set of measured and calculated thermal expansivities compiled by *Chopelas and Boehler* [1989] for which $\delta_T$ was found to vary between 5 and 7. These values are broadly consistent with $\delta_T$ values from elasticity measurements [*Anderson et al.*, 1990].

The present data represent the highest pressures and temperatures for which the thermal expansivity has been yet determined and therefore offers a sensitive test for models of thermal expansion. Using a high-T value of $\alpha_o$ = 53.5 x $10^{-6}$ $K^{-1}$ for MgO [*Anderson and Suzuki,* 1983], these data can be fit to Equation 3.30 using $\delta_T$ = 3.7 $\pm$ 0.8 [Figure 3.25]. Also shown in the figure is the range of $\delta_T$ values for MgO inferred by *Chopelas* [1990] from spectroscopic measurements to 20 GPa at 300 K for which $\delta_T$ = 6.5 $\pm$ 0.5 was obtained. The significantly lower slope found here implies that $\delta_T$ has a temperature dependence and possibly a pressure dependence as well. The value of $\delta_T$ from high-T elasticity measurements (4.7 to 5.1) [*Isaak et al.*, 1989] lies just outside the uncertainty range of the present data. As discussed by *Anderson and Chopelas* [1992], the common assumption used in shock wave analysis that $\rho\gamma$ = const requires that $\delta_T = K'_T$. *Svendsen and Ahrens* [1987] have shown that $\rho\gamma$ = const is in fact consistent with their shock temperature measurements. Since $K'_T$ decreases with pressure, then a pressure dependence is implied for $\delta_T$ as well. *Anderson and Chopelas* [1992] determined the pressure dependence of $\delta_T$ for MgO at 2000 K largely from a theoretical analysis and have proposed that $\delta_T$ decreases from 4.5 to about 3 at pressures corresponding to the top and bottom of the mantle. They find that the average value of $\delta_T$ is slightly less than four over this range, which is in excellent agreement with the shock-compression results reported here.

Figure 3.25: Plot of $\ln(\alpha/\alpha_o)$ versus $\ln(\rho/\rho_o)$ for MgO. The solid symbols represent the present data and are fit by the solid curve with slope -3.7. The dashed curves show the room-temperature results of *Chopelas* [1990] to 10% compression which defines a slope of -6.5 $\pm$ 0.5. The dotted curve shows the slope expected on the basis of high-temperature elasticity measurements.

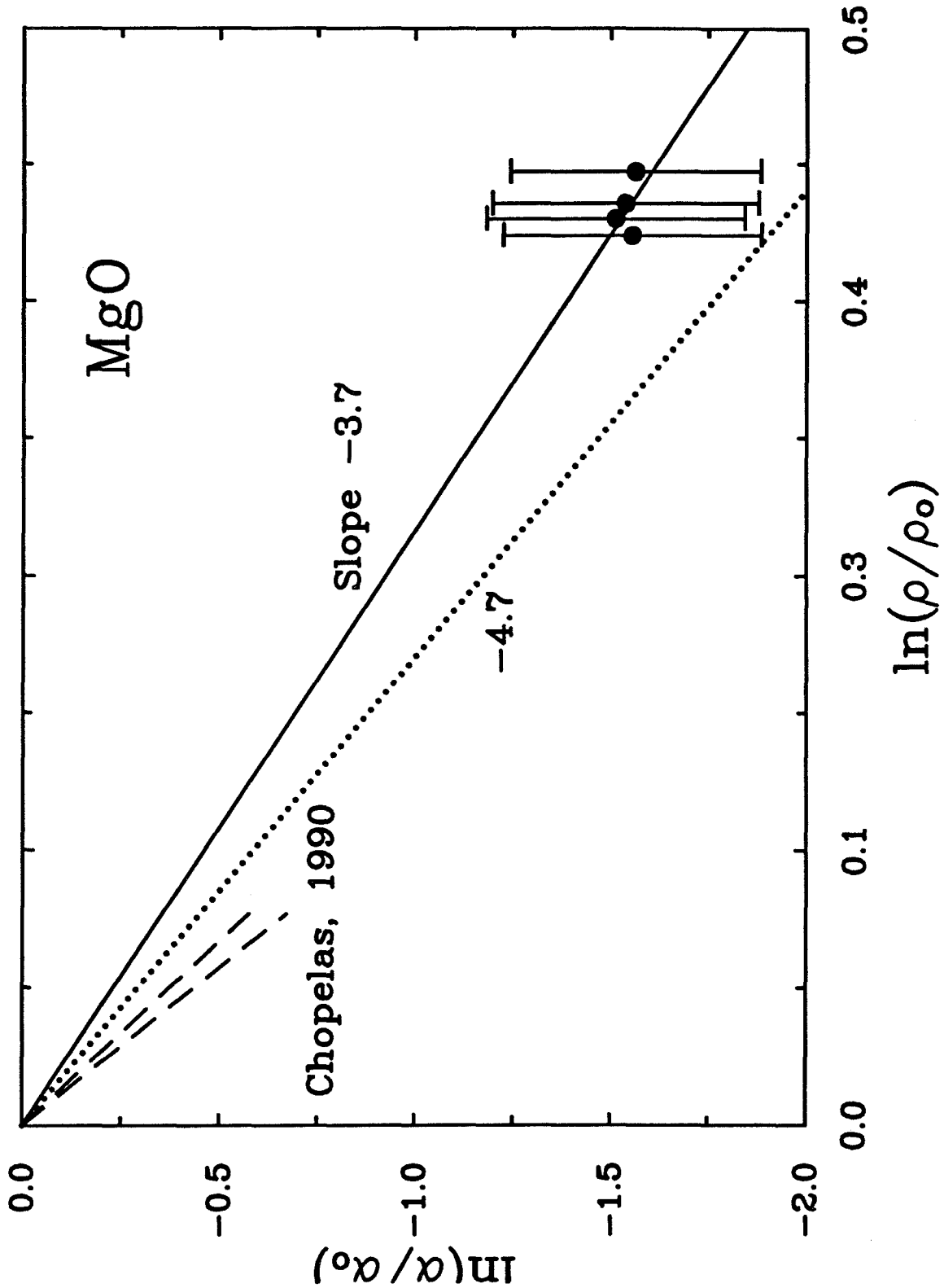
MgO
Slope −3.7
−4.7
Chopelas, 1990
ln(α/α₀)
ln(ρ/ρ₀)
0.0
−0.5
−1.0
−1.5
−2.0
0.0
0.1
0.3
0.4
0.5

In Figure 3.26, several estimates for the pressure dependence of the thermal expansivity in the Earth's mantle are compared with the shock wave determinations. The results of *Stacey* [1977] and *Anderson* [1987] are derived from a combination of seismological data and estimated thermodynamic properties under lower mantle conditions through closure of the identity:

$$\alpha = \frac{\rho C_P K_S}{\gamma}. \tag{3.32}$$

*Anderson* [1987] also estimated that $(\partial \ln \alpha / \partial \ln \rho)_T$ = -2.6 ± 0.5 locally in the lower mantle. This is lower than any of the estimates shown in Figure 3.25 and is consistent with a pressure dependence of $\delta_T$. The result of *Chopelas and Boehler* [1989] was derived from expansivity systematics discussed above. The expansivity data for MgO lie at higher pressure and temperature than found in the lower mantle. Nevertheless the data are consistent with trends defined by the Earth models in the deep lower mantle. Together these results imply thermal expansivities above ~10 x $10^{-6}$ $K^{-1}$ at the base of the lower mantle.

We now turn to a discussion of the implications of our thermal expansion results for the composition and possible layering of the Earth's mantle. Magnesium silicate perovskite $(Mg, Fe)SiO_3$ and magnesiowustite (Mg,Fe)O are taken to represent the bulk of lower mantle material. Pressure-density relations for these materials were calculated along a 300 K adiabat using the Birch-Murnaghan equation and the parameters listed in Table 3.10. An iron fraction of 12 mol.% was used, but the effect of Fe on the bulk modulus and its pressure derivative were assumed to be negligible. Next, thermal effects along an adiabat initially at 2000 K were calculated using thermal expansivities from Eqn. 3.30 with $\delta_T$ = 3.8. Thus, we are assuming that the $\alpha$-$\rho$ relation for perovskite is the same as for magnesiowustite. The results are compared with the P-$\rho$ relation of the lower mantle from Earth model PREM [*Dziewonski and Anderson,* 1981] in Figure 3.27. It is clear from the figure that the properties of silicate perovskite alone are consistent with lower mantle densities.

Figure 3.26: Estimated thermal expansivities for the Earth's lower mantle. The shock data for MgO are indicated by the solid symbols. The solid and chained curves are estimated lower mantle expansivities from seismological data and estimated thermodynamic properties of the lower mantle from *Stacey* [1977] and *Anderson* [1987]. The dashed curve is the estimate of *Chopelas and Boehler* [1989] from thermal expansion systematics. The present data are in accord with extrapolated trends from the Earth models.

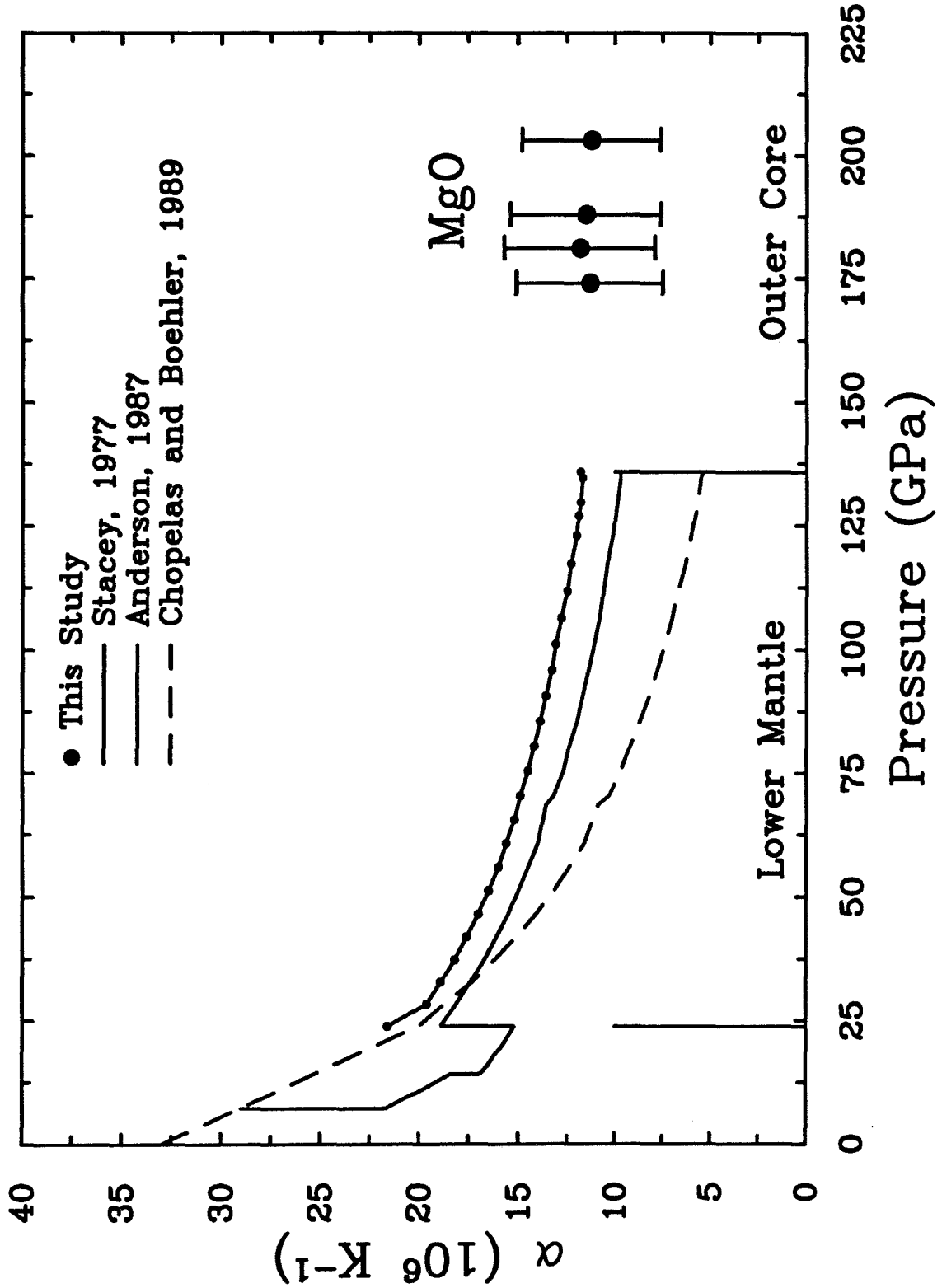
MgO
This Study
Stacey, 1977
Anderson, 1987
Chopelas and Boehler, 1989
Lower Mantle
Outer Core
α (10⁶ K⁻¹)
Pressure (GPa)
0
5
10
15
20
25
30
35
40
0
25
50
75
100
125
150
175
200
225

| Property | (Mg,Fe)O | $(Mg,Fe)SiO_3$ |
|---|---|---|
| $\rho_o$ (g/cm$^3$) | 3.878[a] | 4.238[a] |
| $K_{oT}$ (GPa) | 160.1[b] | 246.4[c] |
| $K'_{oT}$ | 4.13[b] | 3.9[d] |
| $\alpha$ (K$^{-1}$) | 53.5 x $10^{-6}$[e] | 40 x $10^{-6}$[f] |
| $\delta_T$ | 3.8[g] | 3.8[h] |

Table 3.10: Parameters used in constructing high-temperature P-$\rho$ curves for perovskite and magnesiowustite. The difference between the adiabatic and isothermal bulk moduli is neglected for perovskite. The references are: a, $x_{Fe} = 0.12$ *Jeanloz and Knittle* [1989]; b, *Jackson and Niesler* [1982]; c, *Yeganeh-Haeri et al.* [1989]; d,*Knittle and Jeanloz* [1987]; e, *Suzuki* [1975]; f, *Knittle et al.* [1986]; g, This study; h, assumed.

This implies that the lower mantle is enriched in Si relative to upper mantle compositions. An Mg/Si ratio close to upper mantle values would be allowed if the Fe content of the lower mantle were greater than 0.12. Since upper mantle samples have iron contents of 0.12 or less, this also implies a difference in average composition between the upper and lower mantle. Upper and lower mantle composition can be reconciled if the temperature in the lower mantle is less than 2000 K, but this is inconsistent with most temperature estimates for the region [*Jeanloz and Morris,* 1986]. Varying $\delta_T$ within the range allowed by the shock data does not significantly affect this conclusion (Figure 3.27).

That the upper and lower mantle must differ in bulk composition is the same conclusion reached by *Jeanloz and Knittle* [1989] in a parallel analysis which used anharmonic theory to account for thermal effects at elevated pressures. The present

Figure 3.27: Pressure-density relations for perovskite and magnesiowustite compared with Earth model PREM [*Dziewonski and Anderson,* 1981]. The solid and dashed curves are P-$\rho$ relations for perovskite and magnesiowustite, respectively, for a 2000 K adiabat. The iron content for both materials is 0.12 mole fraction. Error bars at selected points for magnesiowustite illustrate the effect of varying $\delta_T$ within the range determined from MgO shock data. Earth model PREM is shown by the chained curve.

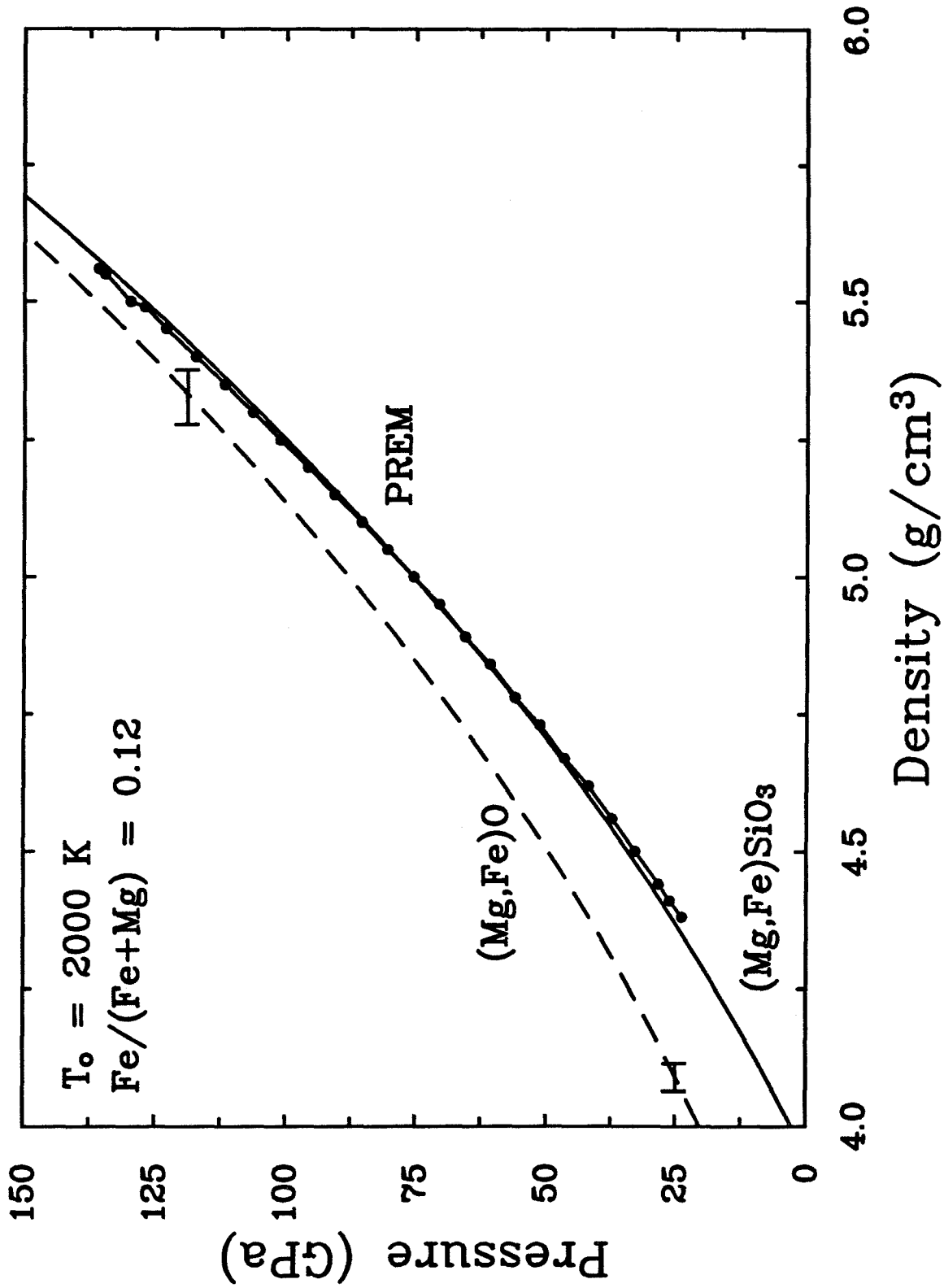
Pressure (GPa)
Density (g/cm$^3$)
150
125
100
75
50
25
0
4.0
4.5
5.0
5.5
6.0
$T_o$ = 2000 K
Fe/(Fe+Mg) = 0.12
PREM
(Mg,Fe)O
(Mg,Fe)SiO$_3$

results provide empirical support at high pressure for the anharmonic corrections used by those authors. *Chopelas and Boehler* [1989] reached the opposite conclusion – that the upper and lower mantle are uniform in composition – also on the basis of a similar analysis. The difference is entirely related to the density dependence of the thermal expansivity for which they used $\delta_T = 5.5 \pm 0.5$. As discussed above, this appears to underestimate thermal expansivities at high pressure by a factor of 2 because of the neglect of the pressure and/or temperature dependence of $\delta_T$ which is apparent in the Hugoniot data.

A number of potentially important factors have been neglected in the foregoing discussion including the effects of element partitioning and other possible lower mantle constituents. The potential significance of these and other factors has been discussed recently by both *Jeanloz and Knittle* [1989] and *Chopelas and Boehler* [1989]. Two issues deserve special mention. If the zero-pressure, high-temperature thermal expansion coefficient for silicate perovskite is significantly less ($< 30 \times 10^{-6}$ K$^{-1}$)than what we have used (Table 3.10), then an upper mantle composition might still be reconciled with lower mantle data for $\delta_T = 3.8$. Second, the thermal expansion data presented here apply only to MgO. It is possible that the $\alpha$-$\rho$ relationship for perovskite could be much different. It has been shown, however, that the expansivities calculated using this relationship are consistent with lower mantle values.

## 3.5 Summary

Equation of state and wave profile measurements (VISAR) have been performed on low-porosity (<1%) polycrystalline MgO for the first time. The equation of state has been determined over the range 10-133 GPa and is given by the relation:

$$U_S = 6.77(0.08) + 1.27(0.04)u_p$$

This equation yields $K_{oS} = 163 \pm 3$ GPa and $K'_{oS} = 4.1 \pm 0.2$, which are in excellent agreement with ultrasonic values of $K_{os} = 162.5 \pm 0.1$ GPa and $K'_{oS} = 4.13 \pm 0.09$. This equation of state is similar to that of single-crystal MgO and slight differences can be related to different levels of material-strength retention in single-crystal and polycrystalline material. The high-precision streak camera EOS data for polycrystalline MgO at $\rho < 4.0$ g/cm$^3$ lie ~1 GPa above the MgO static isotherm.

Compressional sound velocities were measured between 10 and 27 GPa using the VISAR technique and a reverse-impact experimental arrangement. The sound velocities were measured to 2-3% precision and are in good agreement with third-order finite-strain extrapolation of *Jackson and Niesler's* ultrasonic data to 3 GPa. Thermal differences between the Hugoniot and a 300 K adiabat are negligible at these pressures. These results support the use of finite-strain extrapolations for $V_P$ at upper mantle pressures, at least for close-packed solids such as MgO. It is also consistent with shock EOS data for MgO to 220 GPa, which agree with the static isotherm of *Jackson and Niesler* [1982] when reduced to an isotherm. The longitudinal modulus and pressure derivative derived from a combination of shock data and the zero-pressure compressional sound velocity are: $C_{Lo} = K_{oS} + 4/3G = 335 \pm 1$ GPa and $C_{Lo}\prime = 7.0 \pm 0.4$, which are also in good agreement with ultrasonic determinations.

Unloading wave velocities in MgO stand in contrast to those recorded for other minerals ($SiO_2$, $Al_2O_3$, and single-crystal MgO) which indicate a bulk or quasi-elastic response at stresses equal to a few times the Hugoniot elastic limit. The non-elastic response of these materials is related to phase transitions or heterogeneous dynamic yielding, neither of which occurs in polycrystalline MgO.

The unloading wave profiles recorded in reverse-impact experiments generally show a very sharp, elastic release that extends over ~0.2 km/s. The forward-impact

experiments exhibit a more dispersive and weaker elastic response. This is thought to be a consequence of the longer propagation distance in the forward experiments and is evidence for non-steady wave propagation. The HEL stress was determined by modeling the observed particle velocity histories using an elastic-perfectly plastic model and the WONDY wavecode. The HEL of polycrystalline MgO was found to 1.6 $\pm$ 0.3 GPa, and the compressive strength is 1.25 $\pm$ 0.25 GPa. For comparison, single-crystal MgO possesses an HEL amplitude of 2.5-8.9 GPa.

Wavecode simulations of the particle velocity histories were performed to assess whether a modified elastic-plastic model could accurately describe the dynamic unloading of MgO. Elastic-perfectly plastic models were found to satisfy the reverse-impact profiles approximately, but required a yield strength of 2.5 GPa, significantly greater than determined from the HEL amplitude. Models incorporating a Bauschinger effect and strain-rate-dependent stress relaxation with a time constant of 5 ns agreed well with the measured particle velocity histories. Separate Bauschinger models were arrived at for the forward- and reverse-impact experiments because of the different nature of the waveforms observed under these two conditions. Overall, MgO can be described by elastic-plastic material models which employ concepts originally derived to describe the dynamic response of metals. In this sense, MgO is similar to $Al_2O_3$ [*Ahrens et al.,* 1968] and SiC [*Kipp and Grady,* 1989] but differs from $B_4C$, $TiBr_2$, and $ZrO_2$ [*Kipp and Grady,* 1989].

There are several lines of evidence suggesting polycrystalline MgO maintains its strength under shock compression. First, the EOS data tend to lie above the static isotherm, as discussed previously. Second, the initial unloading wave velocity corresponds to extrapolations of ultrasonically measured compressional wave speeds. Third, the initial portion of the unloading wave, particularly for the reverse experiments, is very sharp and non-dispersive, and can be fit by wavecode models having a yield strength of 2.5 GPa. Finally, stress-volume trajectories inferred from successful

wavecode models yield unloading adiabat slopes that are significantly steeper than the Hugoniot for both the forward and reverse-impact experiments.

It has been shown that ultrasonic and Hugoniot density and compressional sound velocity data are entirely consistent for MgO. Comparison of shock and static data together with Hugoniot temperatures measured by *Svendsen and Ahrens* [1987] can be used to constrain the volumetric thermal expansivity of MgO at $P$ = 174-203 GPa and $T$ = 3100-3600 K. It was found that $\alpha = 12 \pm 4$ x $10^{-6}$ $K^{-1}$ under these conditions and can be fit by: $(\alpha/\alpha_o) = (\rho_o/\rho)^{\delta_T}$ with $\delta_T = 3.7 \pm 0.8$. This is much less than the 300 K value of $\delta_T = 6.5 \pm 0.5$ for MgO [*Chopelas,* 1990]. It is also less than the high-temperature value of $\delta_T$=4.7 from 1800 K elasticity data [*Isaak et al.,* 1989]. These results imply that $\alpha$ ranges from 10-30 x $10^{-6}$ $K^{-1}$ for lower mantle materials under lower mantle conditions and favor mantle models in which the lower mantle is enriched in Si and/or Fe relative to the upper mantle.

# Chapter 4

# Sound Velocity, Equation of State, and Constitutive Behavior of Shock-Compressed Molybdenum at 1400°C

## 4.1 Introduction

The effects of pressure and temperature on the elastic properties of metals and minerals must be understood in order to interpret the observed seismic structure of the Earth properly. Elastic wave velocities are the best-resolved properties of the deep interior and therefore offer the best hope for constraining the composition and state of interior regions. Shock-compression methods are uniquely capable of producing high-pressure and high-temperature states through which elastic wave velocities can be measured. Two limitations of shock techniques are that pressure and temperature cannot be varied independently (for non-porous samples) and that direct measurement of temperature is difficult and currently controversial for metals. These

difficulties are circumvented in the present study by heating samples to a precisely known high temperature prior to impact.

In this study, we report new wave profile measurements on molybdenum shock-compressed to between 12 and 81 GPa from a 1400°C initial state. The results provide insight into the effects of temperature on the elastic, constitutive, and equation of state (EOS) properties of this material under shock compression. Optical velocity interferometric techniques were pioneered by Barker and coworkers [*Barker and Hollenbach,* 1965; *Barker,* 1968; *Barker and Hollenbach,* 1972] and can be used to probe the detailed response of metals and minerals to shock wave compression. In this study, for the first time, we have extended the range of such measurements to materials at significantly high initial temperatures.

Molybdenum (Mo) was chosen as the material for study for a number reasons. The EOS of this material at 1400°C has been studied previously [*Miller et al.,* 1988]. Molybdenum is used as a containment material in EOS studies of molten silicates [*Rigden et al.,* 1984], and therefore it is desirable to characterize its high-pressure dynamic behavior as completely as possible. Mo is also a candidate high-pressure standard for static diamond anvil experiments and has been shown to remain stable to 272 GPa at 300 K [*Vohra and Ruoff,* 1990]. Detailed understanding of thermal effects is required in order to relate shock and static data properly. Finally, sound velocities measured on shock-compressed Mo from room temperature reveal interesting and complex behavior at pressures at and above 150 GPa which appear to reflect changes in bonding character [*Hixson et al.,*1989; *Godwal and Jeanloz,* 1990].

Data obtained in this study also address questions concerning material strength which are important issues when comparing shock and static data. Material strength has been observed to decrease at high-pressure and high-temperature in aluminum [*Asay and Kerley,* 1987], and many constitutive models include a thermal softening effect [*Steinberg et al.,* 1980]. However, there is little quantitative knowledge about

the effect of temperature upon material strength and other constitutive properties. The potential effects of material strength upon EOS measurements for Mo is also addressed by the present data.

## 4.2 Experimental Technique

Dynamic compression of molybdenum was carried out by high-velocity plate impact. Impactor or flyer plates were mounted in lexan projectiles and accelerated to high velocities using a single-stage propellant gun with a 40-mm bore [*Ahrens et al.*, 1971]. The flyer plates were made from aluminum 6061 or tantalum and were backed by a layer of low-density polyurethane foam. The attainable range of projectile velocities for this gun, with chemical propellant, is 0.9-2.5 km/s and is measured to $\pm 1\%$ by recording two x-ray shadowgraphs of the projectile in flight (10-50 $\mu$sec apart) on a single piece of film just prior to impact. A He-Ne laser-intervalometer system provided a back-up velocity measurement.

Molybdenum samples were machined from rods of polycrystalline stock of better than 99.95% purity (Climax Performance Materials Co.). The samples were cut into a stepped or top-hat shape as shown in Figure 4.1 with an outer diameter of 44.5 mm and an inner diameter of 25.4 mm. The total thickness was about 5.55 mm. The rear surface of the smaller disk was lapped to a diffusely reflecting finish using 5 $\mu$m alumina powder. Crystal densities were measured by the Archimedean method and are consistent with the standard density of molybdenum (Table 4.1).

The sample was positioned in the vacuum chamber of the gun tank by attaching it to a fibrous ceramic holder. A water-cooled copper coil was positioned around the inner disk and connected to a 10-kW radio-frequency source which acted as an induction heater. Temperatures were measured using a Pt-Pt10%Rh thermocouple attached to the sample. Details of the sample heating procedure are contained in *Rigden et al.* [1988] and *Miller et al.* [1988]. Important experimental parameters

Figure 4.1: Experimental arrangement for high-temperature molybdenum experiments. The molybdenum sample (a) is held by a fibrous ceramic target plate (b) and radiatively heated to ~1400°C using copper coils (c) attached to a 10-kW radio-frequency source acting as an induction heater. Temperature is measured using the thermocouple (d). The impactor assembly consists of an aluminum flyer plate (e) with foam backing (f) mounted in a lexan projectile body (g). The free surface of the hot Mo sample is monitored with single-frequency light from a 3 W $Ar^+$ laser which is focused using the lens (j) and directed onto the target using the expendable mirror (i). The returned diffuse light (h) is returned to the VISAR along a path parallel to the incident beam.

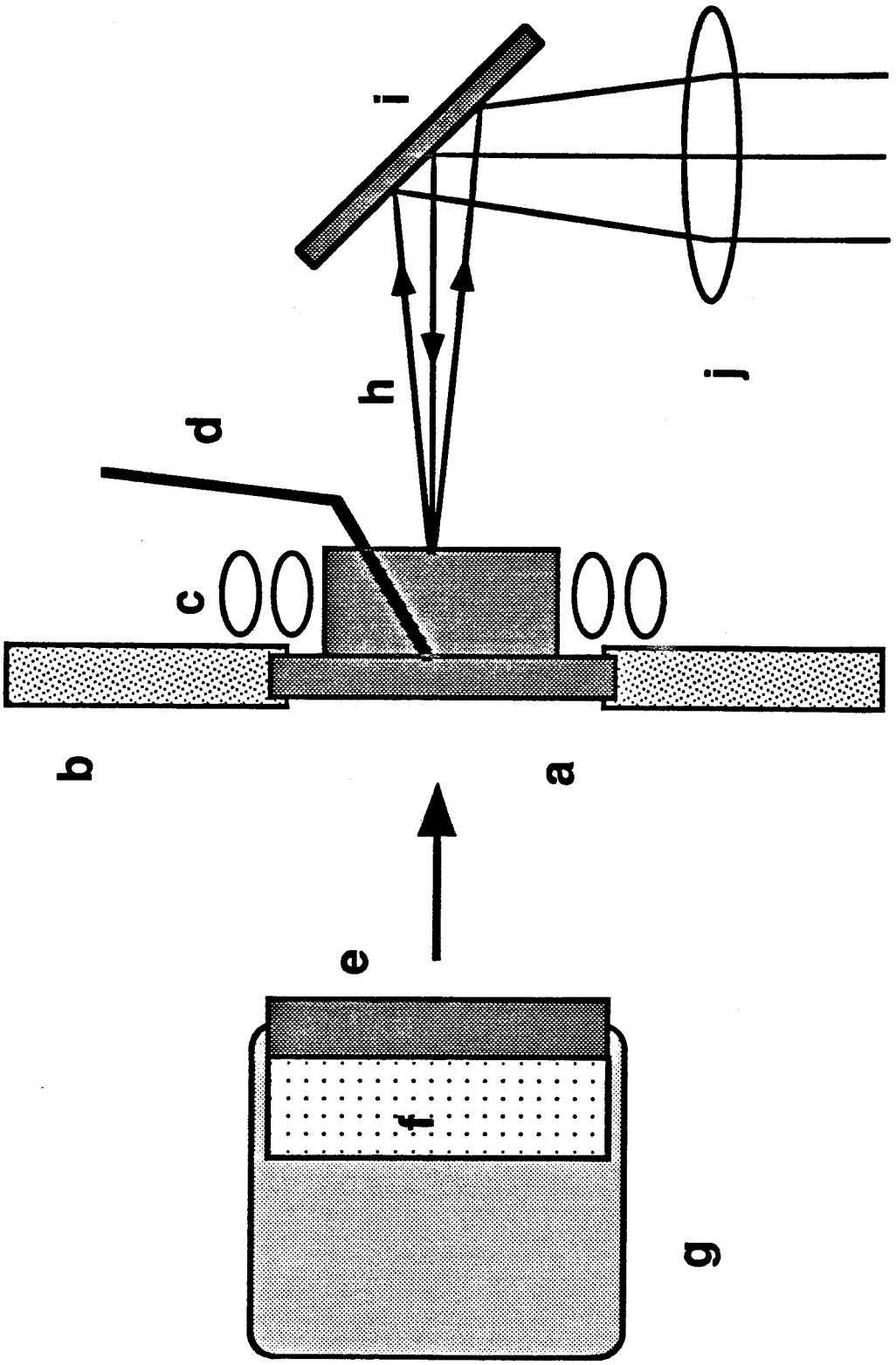
i
h
j
d
c
b
a
e
f
g

| Shot | Flyer material | Flyer $\rho_o$ ($g/cm^3$) | Flyer thickness (mm) | Sample $\rho_o$ (300 K) ($g/cm^3$) | Sample thickness (mm) | $T_o$ (K) | $U_{fp}$ (km/s) |
|---|---|---|---|---|---|---|---|
| 865 | Al6061 | 2.688 | 1.525 | 10.210 | 5.538 | 1676 | 0.95 |
| | | 0.012 | 0.005 | 0.006 | 0.003 | | 0.01 |
| 866 | Al6061 | 2.692 | 1.464 | 10.204 | 5.535 | 1686 | 1.57 |
| | | 0.008 | 0.005 | 0.006 | 0.005 | | 0.01 |
| 867 | Al6061 | 2.699 | 1.984 | 10.197 | 5.565 | 1691 | 2.16 |
| | | 0.007 | 0.005 | 0.005 | 0.005 | | 0.02 |
| 868 | Ta | 16.58 | 1.103 | 10.208 | 5.553 | 1684 | 2.28 |
| | | 0.07 | 0.004 | 0.006 | 0.006 | | 0.02 |

Table 4.1: Initial conditions for high-temperature molybdenum experiments. $\rho_o$ is the initial density, $T_o$ is the initial temperature, and $U_{fp}$ is the impact velocity.

are listed in Table 4.1.

The motion of the molybdenum free surface was monitored using a laser velocity interferometer system (VISAR) [*Barker and Hollenbach,* 1972]. Light from an $Ar^+$ laser is focused on the molybdenum back surface using a lens and turning mirror which was mounted on a ceramic pedestal inside the tank (Figure 4.1). The turning mirror is protected from the high-temperature environment by a ceramic shutter which is pneumatically retracted immediately prior to firing the gun. Alignment techniques insure that the laser beam is centered on and normal to the Mo surface. The diffusely reflected light, which is Doppler-shifted because of sample motion, is collected and transformed into time-dependent light-intensity fluctuations (interference fringes) in a wide-angle Michelson interferometer. The signals are recorded

using photomultipliers and digital oscilloscopes. An example of a typical experimental record, and the wave profile derived from it, is shown in Chapter 3. The VISAR we have constructed is similar to that originally described by *Barker and Hollenbach* [1972], but we have incorporated the push-pull modification of *Hemsing* [1979]. The surface velocity, $u_{fs}$, is related to the number of interference fringes recorded through:

$$u_{fs}(t - \tau/2) = kF(t), \tag{4.1}$$

where $t$ is the time, $\tau$ is the 1-2 ns delay time of the interferometer, $F(t)$ is the total number of fringes recorded up to that time, and $k$ is the velocity-per-fringe constant, which is controllable in part by varying the delay time of the interferometer. A fringe constant of 225 m/s/fringe (7.5" of fused silica etalon) was used for all of the present experiments. The relationship that determines the fringe constant is discussed in detail in the appendix. Fringe records were converted to velocity histories using an interactive data-reduction procedure which incorporates the velocity algorithm of *Hemsing* [1983a]. A complete discussion of VISAR experimental techniques is contained in the appendix.

Because of the high-temperature sample environment, electrical shorting pins could not be used for triggering and tilt diagnostics. Instead, a trigger signal was generated by the intersection of the oncoming projectile with a cw laser beam positioned 5 cm in front of the target. Because of the long time window between triggering and data acquisition, oscilloscope sampling rates between 250-500 MS/s were used rather than the normal sampling rate of 1 GS/s for VISAR experiments, resulting in somewhat reduced time resolution. The sample reflectivity did not change significantly when heated to 1400°C for ~15 minutes in the < 100-$\mu$m Hg air pressure of the impact tank. Thermal radiation from the hot sample produced an ~30 mV offset in the fringe records which was subtracted in the data-reduction process.

## 4.3 Experimental Results

### 4.3.1 Wave Profiles

A total of four experiments were conducted on Mo samples, three of which yielded free surface velocity profiles. In the fourth experiment, data recording failures prevented a wave profile from being obtained but the arrival times of the shock front and the initial unloading wave could be read directly from the partial fringe records. The velocity profiles are shown in Figure 4.2.

The distance-time diagram of Figure 4.3 illustrates the essential features of the observed wave profiles. Impact (t=0) generates a shock wave in the flyer and a two-wave structure consisting of an elastic precursor followed by a slower plastic shock in the sample. These reach the free surface and are recorded by the interferometer at times $t_1$ and $t_2$. The shock wave in the flyer reflects from the low-impedance foam backing as a rarefaction fan. The reflection of the elastic precursor from the free surface at time $t_1$ has been neglected. Similarly, the shock arrival at the Mo free surface produces an unloading fan. For an elastic-plastic material, the velocity of the head of the rarefaction fan corresponds to the compressional sound velocity at high pressure [*Zel'dovich and Razier,* 1967]. This reaches the free surface at time $t_3$. An unloading wave traveling with the bulk velocity, $V_B$, is also propagated. The interaction of the unloading waves takes the material into tension, eventually leading to spall fracture near the free surface. This produces the characteristic increase or pull-back in free surface velocity shown in Figure 4.2 (time $t_4$).

### 4.3.2 Elastic Precursor

The structure of the elastic precursor is generally consistent for the three wave profiles. The precursor manifests itself as a sharp jump in velocity which then relaxes by about 25%. Under a steady-wave assumption, the stress amplitude of the Hugoniot

Figure 4.2: Free surface profiles measured on 1400°C molybdenum samples. The times are arbitrary. The wave profile is characterized by an elastic precursor, a plastic shock front, and a spall signal upon unloading. The peak shock pressures attained in each experiment are listed to the left of the profiles. The times $t_1$-$t_4$ correspond to the arrival times shown on the distance-time diagram of Figure 4.3.

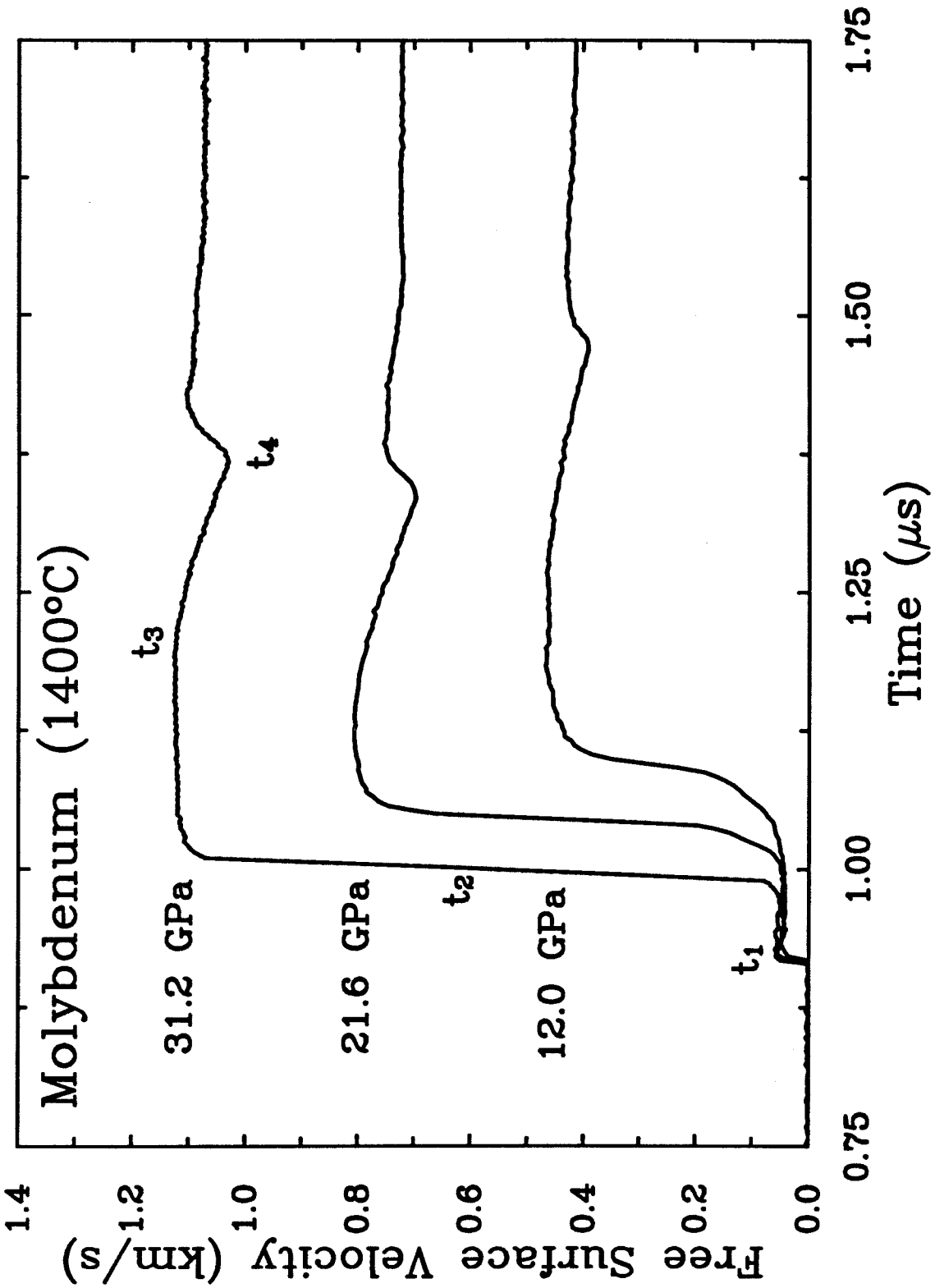
Molybdenum (1400°C)
31.2 GPa
21.6 GPa
12.0 GPa
$t_1$
$t_2$
$t_3$
$t_4$
Free Surface Velocity (km/s)
Time ($\mu$s)
0.0
0.2
0.4
0.6
0.8
1.0
1.2
1.4
0.75
1.00
1.25
1.50
1.75

Figure 4.3: Lagrangian distance-time diagram for the 21.6 GPa experiment of the previous figure. Impact at $t$=0 produces an elastic precursor and shock which propagate through the sample and reach the free surface at times $t_1$ and $t_2$. The reflection of the shock at the free surface produces a rarefaction fan propagating back to the left. In the meantime, a shock travels through the thin flyer and reflects off the low-impedance backing layer, producing a forward-propagating rarefaction fan. The lead characteristics of these two fans intersect at a distance $h^*$, near the free surface. The forward-propagating unloading wave then reaches the free surface at $t_3$. The interaction of the two unloading waves generates a state of tension in the sample, eventually leading to spall at the spall plane and producing the velocity pull-back seen in Figure 4.2.

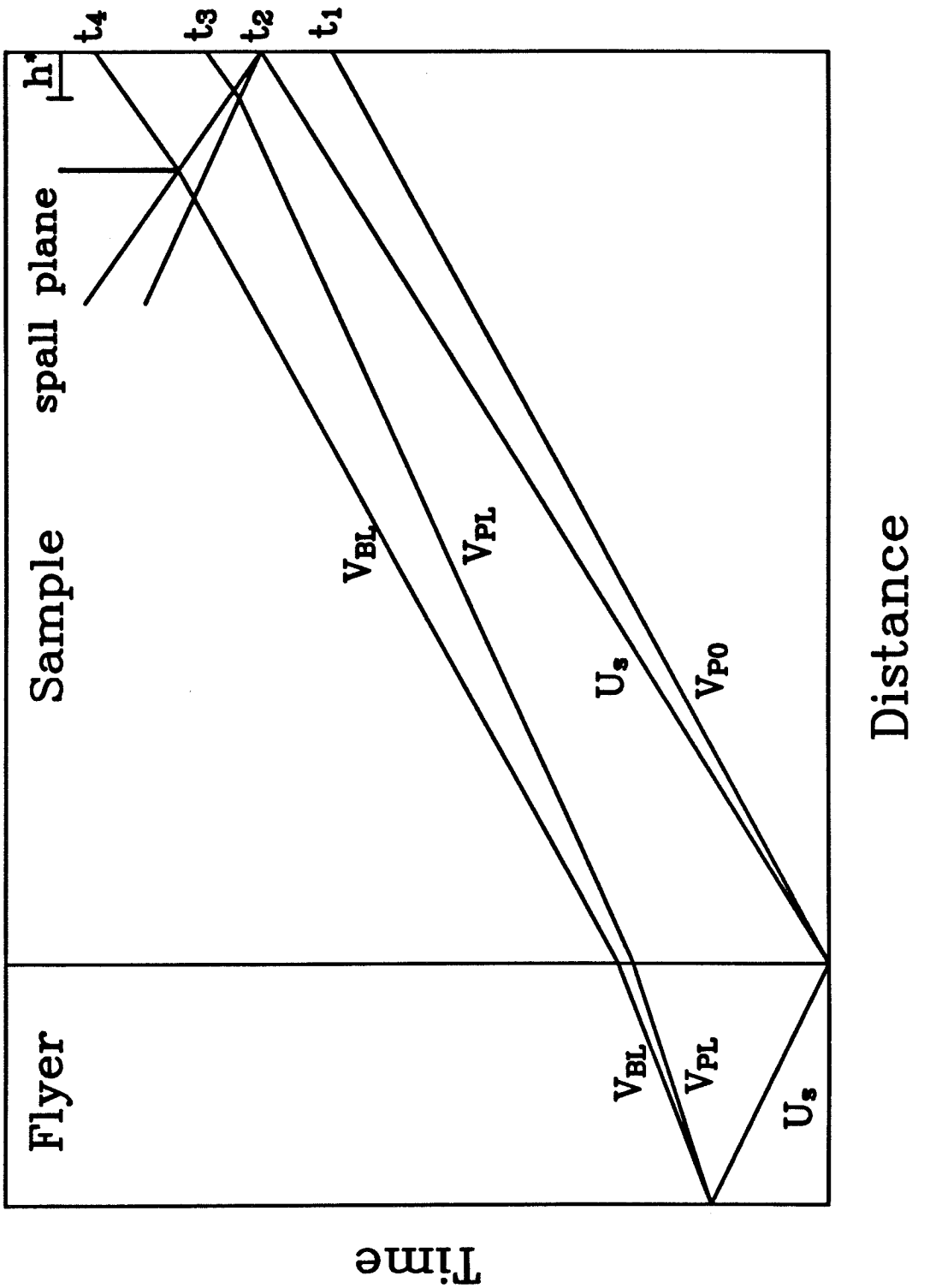
Time
Distance
Flyer
Sample
spall plane
h'
t4
t3
t2
t1
VBL
VPL
Us
VPO
VBL
VPL
Us

elastic limit (HEL) can be obtained from

$$\sigma_{HEL} = \frac{\rho_o V_{Po} u_{fs}}{2}, \tag{4.2}$$

where $\sigma_{HEL}$ is the HEL stress, $\rho_o$ is the initial density, $V_{Po}$ is the elastic precursor velocity, $u_{fs}$ is the peak free surface velocity, and the factor-of-two relationship between the free surface and particle velocity has been assumed [*Walsh et al.,* 1957]. Values for the parameters in Equation 4.2 and the HEL stresses are listed in Table 4.2. Ambient-pressure high-temperature densities were computed using the temperature dependence of the volume given by *Miller et al.* [1988]. The elastic precursor velocity, $V_{Po}$, is assumed to be the ambient-pressure longitudinal sound velocity at high temperature. Good agreement between the elastic precursor velocity and the ambient-pressure compressional wave velocity is commonly observed in metals that have relatively low elastic limits. Stress dependence of the elastic precursor velocity has been demonstrated in high-strength materials such as quartz and sapphire [*Davison and Graham,* 1979]. For Mo, the expected compressional velocity at 1.5 GPa is within 1% of the zero-pressure velocity. $V_{Po}$ was estimated by extrapolating to 1676 K the linear velocity-temperature trend observed over the range 73-973 K in the ultrasonic measurements of *Dickinson and Armstrong* [1967]. This yields $V_{Po} = 6.11 \pm 0.03$ km/s at 1400°C.

The HEL amplitudes range between 1.5 and 1.7 GPa and are shown as a function of peak stress in Figure 4.4. No clear stress dependence of the HEL magnitude can be resolved over the 12-31 GPa pressure range. It is of interest to compare the elastic precursor structure at 1673 K with the observed structure at 300 K. *Chhabildas et al.* [1990] reported a single free surface profile for Mo shocked to 12 GPa, which yielded $\sigma_{HEL} = 3.1$ GPa. Thus, at 1673 K, the HEL amplitude of Mo is about 50% of its room-T value. This contrasts with the observations of *Asay* [1974], who found that precursor amplitude was independent of temperature up to 523 K in bismuth, which is near the melting temperature for that material. No temperature dependence of

| Shot | $T_o$ (K) | $\rho_o$ (g/cm$^3$) | $V_{Po}$ (km/s) | $u_{fs}$ (km/s) | $\sigma_{HEL}$ (GPa) | $Y_o$ (GPa) |
|---|---|---|---|---|---|---|
| | 300 | 10.206 | 6.46 | 0.094 | 3.10 | 1.80 |
| 865 | 1676 | 9.950 | 6.11 | 0.057 | 1.73 | 0.94 |
| 866 | 1686 | 9.942 | 6.10 | 0.048 | 1.46 | 0.79 |
| 867 | 1691 | 9.934 | 6.10 | 0.057 | 1.73 | 0.94 |
| 868 | 1684 | 9.947 | 6.10 | - | - | - |

Table 4.2: Properties of the elastic precursor in molybdenum at 300 K and at 1400 K. The 300 K properties are from *Chhabildas et al.* [1990].

$\sigma_{HEL}$ was found for iron between 76 and 573 K [*Rohde,* 1969]. These differences may reflect differences in the dislocation processes that are operative under dynamic loading for different materials. There is some ambiguity in the 300 K elastic precursor amplitude in Mo, as *McQueen et al.* [1970] reported $\sigma_{HEL} = 1.6$ GPa for a 5-mm thick sample and further noted measurable precursor decay over a 1 cm distance. This value for $\sigma_{HEL}$ and the apparent precursor decay are quite comparable to the present high-temperature measurements.

Assuming a von Mises yield condition, the compressive yield strength, $Y_o$, is related to the HEL amplitude through:

$$Y_o = \frac{(1-2\nu)}{(1-\nu)}\sigma_{HEL}, \tag{4.3}$$

where $\nu$ is Poisson's ratio. At 1400°C, Poisson's ratio is estimated to be 0.313, again from extrapolation of ultrasonic elasticity data to 700°C [*Dickinson and Armstrong,* 1967]. The resulting yield strengths are listed in Table 4.2 and are also about 50% of the 300 K value at 12.6 GPa [*Chhabildas et al.,* 1990].

Another interesting feature of the the elastic precursor structure is the decrease

Figure 4.4: The Hugoniot elastic limit stress as a function of peak stress in Mo. The solid symbols are from the present study at initial temperatures near 1400°C. The open symbol is at 300 K initial temperature and is from *Chhabildas et al.* [1990].

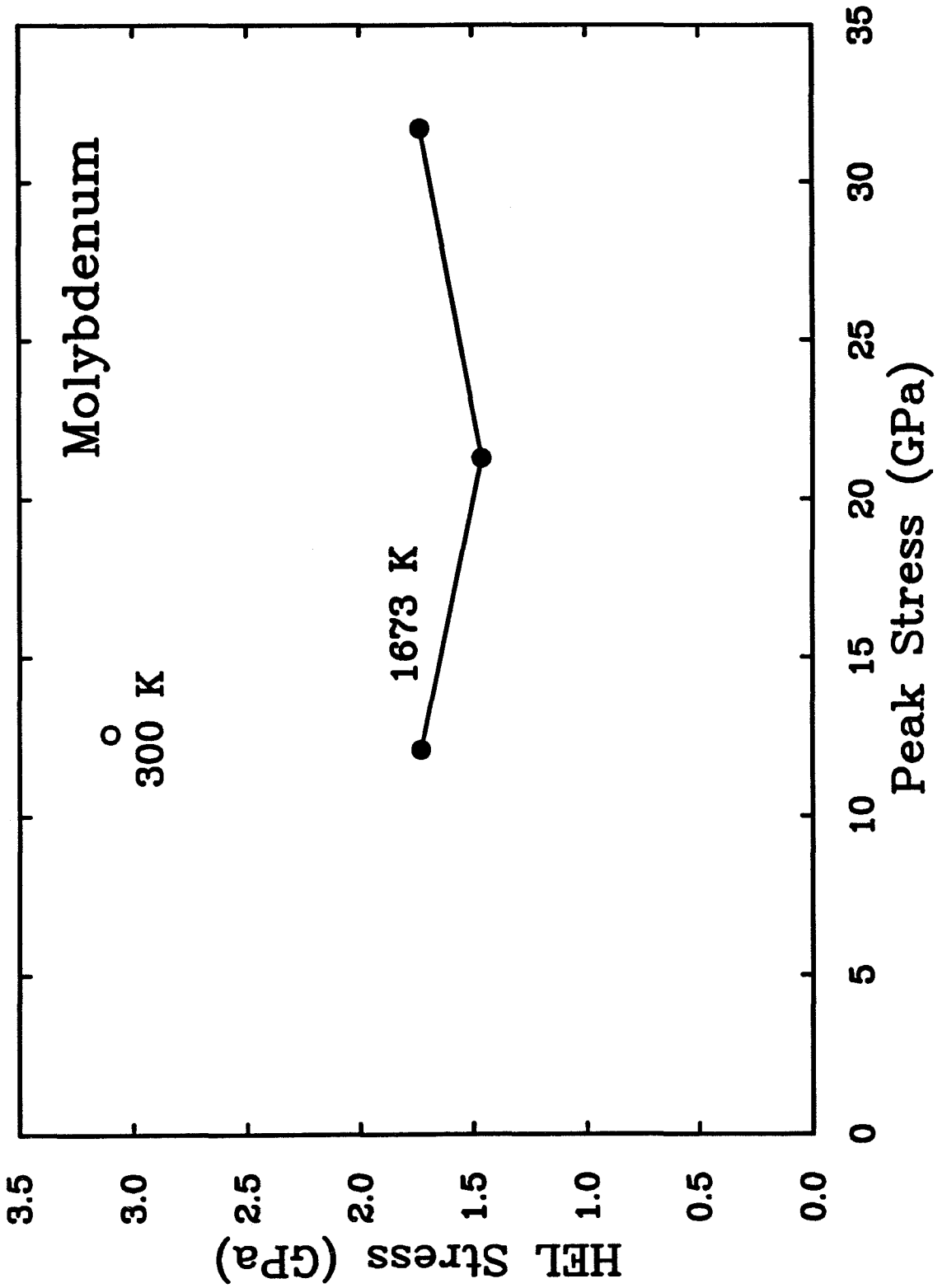
Molybdenum
300 K
1673 K
HEL Stress (GPa)
Peak Stress (GPa)
0.0
0.5
1.0
1.5
2.0
2.5
3.0
3.5
0
5
10
15
20
25
30
35

in free surface velocity observed behind the precursor. The minimum free surface velocity behind the precursor is 74-88% of the peak precursor velocity and ranges between 42-44 m/s. Elastic wave overshoot has been previously identified in other materials such as iron [*Barker and Hollenbach* [1974] and is interpreted as a consequence of stress relaxation behind the precursor. The 300 K free surface profile in Mo shows no stress relaxation behind the precursor. Therefore, the effect of high initial temperature on the compressive-wave structure of Mo is both to decrease the magnitude of the HEL and to promote stress relaxation behind the precursor. The results for Mo are somewhat anomalous in that reduction of velocity behind the HEL is observed, but no dependence of HEL amplitude on the peak-driving stress can be resolved. Both of these phenomena are generally associated with stress relaxation in solids [*Ahrens and Duvall,* 1966; *Graham and Brooks,* 1971]. It may be that the present data are insufficient to resolve the peak-stress dependence of the HEL.

### 4.3.3 Hugoniot States

The VISAR measurements allow only relative time measurements since the impact time is not recorded. An absolute time reference was therefore established from the measured arrival time of the elastic precursor, which is assumed to travel with the ambient-pressure, high-temperature longitudinal sound velocity in the sample. The longitudinal sound velocity was extrapolated from the linear velocity-temperature trend of the ultrasonic data as discussed above (Table 4.2). The absolute arrival time of the elastic precursor wave could then be calculated using the known sample thickness. The shock wave arrival time was taken to be the arrival time of the midpoint of the wave between the peak HEL velocity and the peak free surface velocity. The shock velocity, $U_S$, was then calculated from the sample thickness and is listed in Table 4.3. The particle velocity, $u_p$, was calculated from the measured free surface velocity, $u_{fs}$, by accounting for the elastic-plastic interaction at the free

surface [*Grady*, 1977]:

$$u_p = \frac{1}{2}\left[u_{fs} + \frac{(V_{Po} - V_{Bo})\sigma_{HEL}}{\rho_o V_{Po} V_{Bo}}\right], \tag{4.4}$$

where $V_{Po}$ and $V_{Bo}$ are the longitudinal and bulk sound velocities, and $\rho_o$ is the initial density. The subscript $o$ indicates ambient-pressure quantities. The resultant particle velocities are listed in Table 4.3, and the shock states are plotted in Figure 4.5. The present results are in excellent agreement with the Hugoniot states determined from the streak camera experiments of *Miller et al.* [1988]. The combined Hugoniot data for 1400°C Mo can be fit with the following linear shock wave equation of state:

$$U_S = 4.78(0.02) + 1.42(0.02)u_p, \tag{4.5}$$

where the numbers in parentheses are one standard deviation uncertainties. This EOS is only slightly different from that reported by *Miller et al.* [1988] but has the advantage that the formal uncertainties are decreased by more than a factor of two and extends the EOS to particle velocities as low as 0.236 km/s (and Hugoniot pressures as low as 12 GPa).

### 4.3.4 Compressional Sound Velocities

A primary goal of the present experiments was to measure sound velocities at high pressure from an initial high-temperature state. The method for doing this is similar to that presented in Chapters 1 and 2. For each experiment, the time difference, $\Delta t$, between the arrival of the unloading wave and the arrival of either the shock or elastic precursor at the free surface is measured from the wave profile or from the fringe records. The measured time separations are listed in Table 4.4. For experiments 865-867, the time separation listed is between the elastic precursor and the initial release. For experiment 868, the elastic precursor is overdriven and the time separation is between the shock and release. With reference to Figure 4.3, it can be shown that

| Shot | $u_p$ | $U_S$ | $P$ | $\rho$ |
|---|---|---|---|---|
| | (km/s) | (km/s) | (GPa) | (g/cm$^3$) |
| 865 | 0.236 | 5.118 | 12.0 | 10.431 |
| | 0.003 | 0.024 | 0.2 | 0.009 |
| 866 | 0.405 | 5.358 | 21.6 | 10.755 |
| | 0.005 | 0.037 | 0.3 | 0.013 |
| 867 | 0.563 | 5.582 | 31.2 | 11.048 |
| | 0.007 | 0.062 | 0.5 | 0.021 |
| 868 | 1.238 | 6.549 | 80.7 | 12.270 |
| | 0.014 | 0.035 | 1.2 | 0.030 |

Table 4.3: Hugoniot states achieved in molybdenum. Results are from measured wave profiles except for experiment 868, in which case the measured flyer velocity and impedance matching were used to calculate the Hugoniot state. $u_p$ is the particle velocity, $U_s$ is the shock velocity, $P$ is the Hugoniot pressure, and $\rho$ is the Hugoniot density.

Figure 4.5: Shock velocity - particle velocity data for Mo shocked from STP and preheated to 1400°C. The error bars are smaller than the symbols where not shown. The solid curve shows a weighted least-squares fit to the data at a 1400°C initial state. The dashed curve shows the Hugoniot relationship from a 25°C initial state [*Marsh*, 1980].

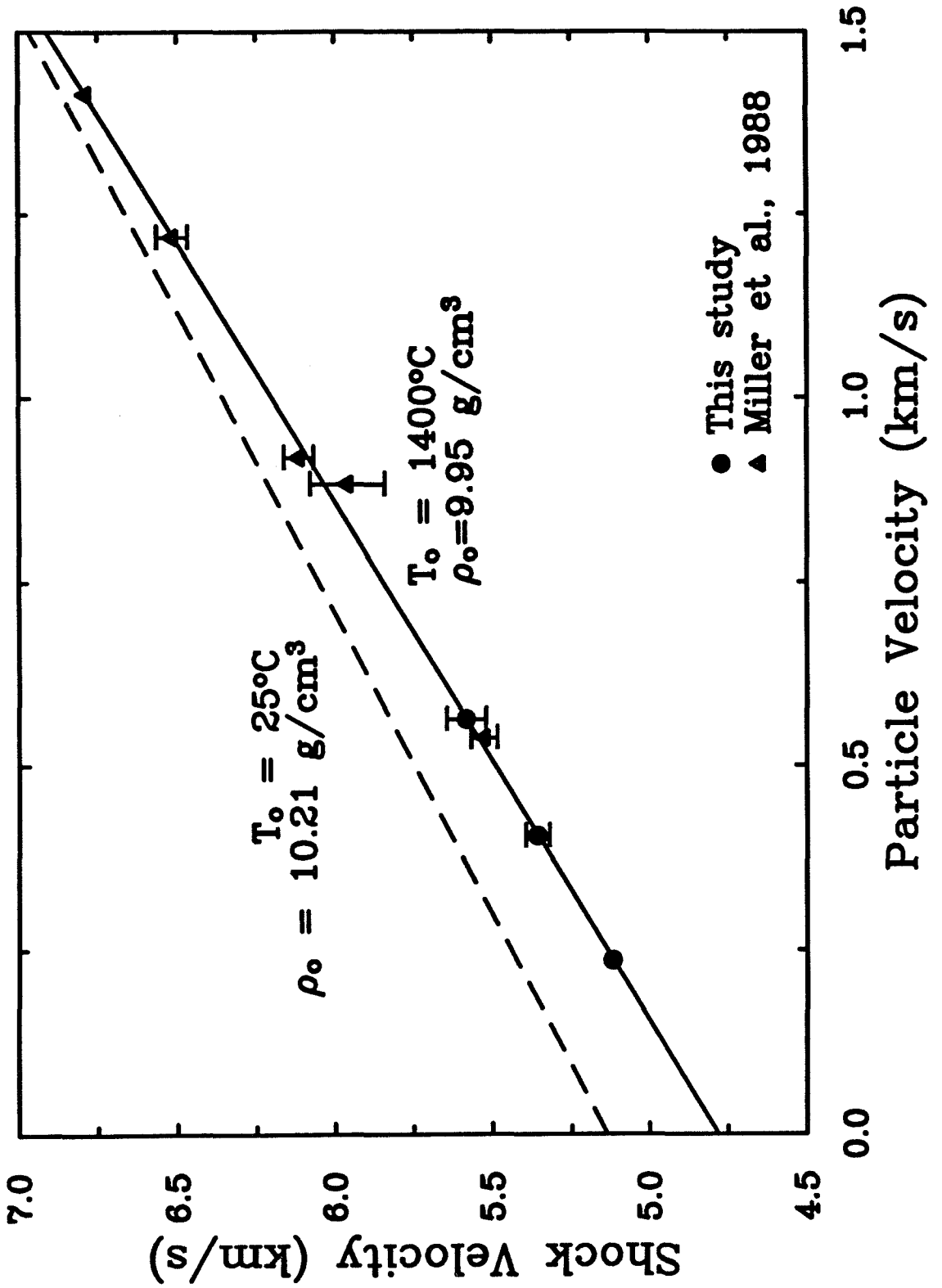
Shock Velocity (km/s)
Particle Velocity (km/s)
7.0
6.5
6.0
5.5
5.0
4.5
0.0
0.5
1.0
1.5
This study
Miller et al., 1988
$T_o$ = 25°C
$\rho_o$ = 10.21 g/cm³
$T_o$ = 1400°C
$\rho_o$=9.95 g/cm³

the initial Lagrangian unloading velocity, $V_{PL}$, in the sample is given by:

$$V_{PL} = \frac{x_s - h^*}{\Delta t + x_s/U_1 - x_f(1/U_{Sf} + 1/V_{PLf}) - h^*/V^*}, \tag{4.6}$$

where $x_s$ and $x_f$ are the sample and flyer thicknesses, $U_{Sf}$ and $V_{PLf}$ are the shock velocity and the Lagrangian unloading velocity in the flyer, $U_1$ is either the shock or precursor velocity in the sample depending on how $\Delta t$ is measured, and $V^*$ is the average velocity in the perturbed region, $h^*$, which is defined by the intersection of the unloading wave from the back of the flyer and the unloading wave from the free surface, both of which travel with velocity $V_{PL}$ through the sample:

$$h^* = \frac{V_{PL}}{2}\left[x_f(1/V_{PLf} + 1/U_{Sf}) + x_s(1/V_{PL} - 1/U_S)\right], \tag{4.7}$$

where $U_S$ is the shock wave velocity through the sample. Behind the interaction region, the oncoming unloading wave travels through a non-simple region of near zero stress. Therefore, the initial bulk sound velocity, $V_{Bo}$, was used as an estimate of the average velocity, $V^*$, in the interaction region. The intercept of the shock velocity-particle velocity relationship (Equation 4.5) was used as the initial bulk sound speed. Because of the large stress change in the interaction region, it could have a potentially large effect on the measured sound velocity. The interaction region was therefore kept as small as possible to minimize any such effects. The interaction regions were 5-11% of the total sample thicknesses for the four shots fired (Table 4.4). The large stress drop in the interaction region could be minimized if a window were attached to the free surface (Chapter 1). We have not developed a window-attachment method that can easily withstand the high-temperature environment of the present experiments.

Equations 4.6 and 4.7 form a coupled set of equations that are solved iteratively for $V_{PL}$. Hugoniot states in the flyer materials were determined through impedance matching [*Ahrens,* 1987]. The relevant EOS parameters are listed in Table 4.5. Unloading wave velocities in Al 6061 have been determined in previous work and are

discussed in Chapter 3. For experiment 868, the Hugoniot stress (80.7 GPa) is close to the 83.1 GPa experiment of *Asay et al.* [1986] for which a Ta unloading velocity of 5.5 ± 0.2 km/s was measured. This value was therefore used for $V_{PLf}$ in Equations 4.6 and 4.7 for this experiment. The velocities $V_{PL}$ are based on a Lagrangian or material reference frame rather than on a laboratory (Eulerian) coordinate system. The Lagrangian sound velocities were converted to Eulerian velocities, $V_P$, using:

$$V_P = \frac{\rho_o}{\rho} V_{PL}, \tag{4.8}$$

where $\rho$ is the density in the Hugoniot state. The resultant Eulerian sound velocities are listed in Table 4.4 and are plotted as a function of Hugoniot pressure in Figure 4.6.

For solids in the absence of dispersion, the initial unloading wave velocity corresponds to the compressional sound velocity, $V_P$, while for liquids it corresponds to the bulk sound velocity, $V_B$. If the Grüneisen parameter, $\gamma$, is known, the local slope of the Hugoniot curve can be used to estimate the high-pressure bulk sound velocity [*McQueen et al.*, 1967; Chapter 1]. This is shown in Figure 4.6 using the previously determined EOS for hot Mo and a constant product of density and Grüneisen parameter. An estimate of the compressional sound velocity can then be made by assuming that Poisson's ratio, $\nu$, is constant with pressure (Figure 4.6). The measured Hugoniot velocities are reasonably consistent with the latter estimate at low P, indicating that Mo remains in the solid state over the pressure range investigated, consistent with the inference of *Miller et al.* [1988]. The measured velocities lie significantly below trends based on third-order finite-strain extrapolations of 300 K ultrasonic data (solid lines in Figure 4.6), which can be attributed to the effects of temperature.

| Shot | $P$ | $\Delta t$ | $h^*$ | $V_P$ | $T_H$ | $\lvert(\partial V_P/\partial T)_P\rvert$ | $\nu$ |
|---|---|---|---|---|---|---|---|
| | (GPa) | ($\mu$sec) | mm | (km/s) | (K) | (m/s/K) | |
| 865 | 12.0 | 0.373 | 0.55 | 6.30 | 1805 | 0.35 | 0.34 |
| | 0.2 | 0.008 | 0.05 | 0.22 | 22 | 0.13 | 0.03 |
| 866 | 21.6 | 0.229 | 0.30 | 6.72 | 1915 | 0.24 | 0.33 |
| | 0.3 | 0.003 | 0.03 | 0.12 | 37 | 0.09 | 0.02 |
| 867 | 31.2 | 0.285 | 0.59 | 7.07 | 2026 | 0.16 | 0.33 |
| | 0.5 | 0.004 | 0.05 | 0.21 | 57 | 0.13 | 0.03 |
| 868 | 80.7 | 0.170 | 0.54 | 7.91 | 2721 | 0.18 | 0.38 |
| | 1.2 | 0.005 | 0.04 | 0.24 | 186 | 0.11 | 0.03 |

Table 4.4: Properties of molybdenum along the ~1400°C Hugoniot. Numbers below each quantity represent one standard deviation uncertainties. $P$ is the Hugoniot pressure, $\Delta t$ is the measured time between arrival of the loading and unloading waves, $h^*$ is the thickness of the interaction region, $V_P$ is the compressional velocity, $T_H$ is the Hugoniot temperature, $|(\partial V_P/\partial T)_P|$ is the magnitude of the temperature coefficient of velocity, and $\nu$ is Poisson's ratio.

| Material | $\rho_o$ | $c_o$ | $s$ | $\gamma_o$ | $\nu_o$ | $Y_o$ | Refs. |
|---|---|---|---|---|---|---|---|
| | (g/cm$^3$) | (km/s) | | | | (GPa) | |
| Mo (300 K) | 10.21 | 5.136 | 1.220 | 1.52 | 0.293 | 1.8 | a |
| | 0.01 | 0.016 | 0.010 | | | | |
| Mo (1400 K) | 9.95 | 4.78 | 1.42 | 1.52 | 0.313 | 0.8 | b,c |
| | 0.01 | 0.02 | 0.02 | | | | |
| Al6061 | 2.69 | 5.349 | 1.338 | 2.1 | 0.34 | 0.2 | a |
| | 0.01 | 0.056 | 0.020 | | | | |
| Ta | 16.58 | 3.293 | 1.307 | 1.6 | 0.34 | 0.8 | d |
| | 0.07 | 0.005 | 0.025 | | | | |

Table 4.5: Equation of state and constitutive properties of materials used in molybdenum experiments. Numbers below each line represent one standard deviation uncertainties. $c_o$ and $s$ are the Hugoniot EOS constants, $\gamma$ is the Grüneisen parameter, and the subscript o refers to ambient-pressure quantities. The references are: a, *Marsh* [1980]; b, *Miller et al.* [1988]; c, This Study; d, *Mitchell and Nellis* [1981a].

Figure 4.6: Compressional sound velocity in 1400°C Mo as a function of Hugoniot pressure. Solid circles are the present experimental results. The squares and triangles are the ambient-pressure compressional and bulk sound speeds at 25°C and 1400°C, respectively. The solid curves are third-order Eulerian finite-strain extrapolations of compressional and bulk sound velocities at 25°C, using parameters from the ultrasonic data of *Katahara et al.* [1979]. The dashed curves are calculated sound velocities based on the local slope of the Hugoniot and the assumptions that $\rho\gamma$ and $\nu$ are constant.

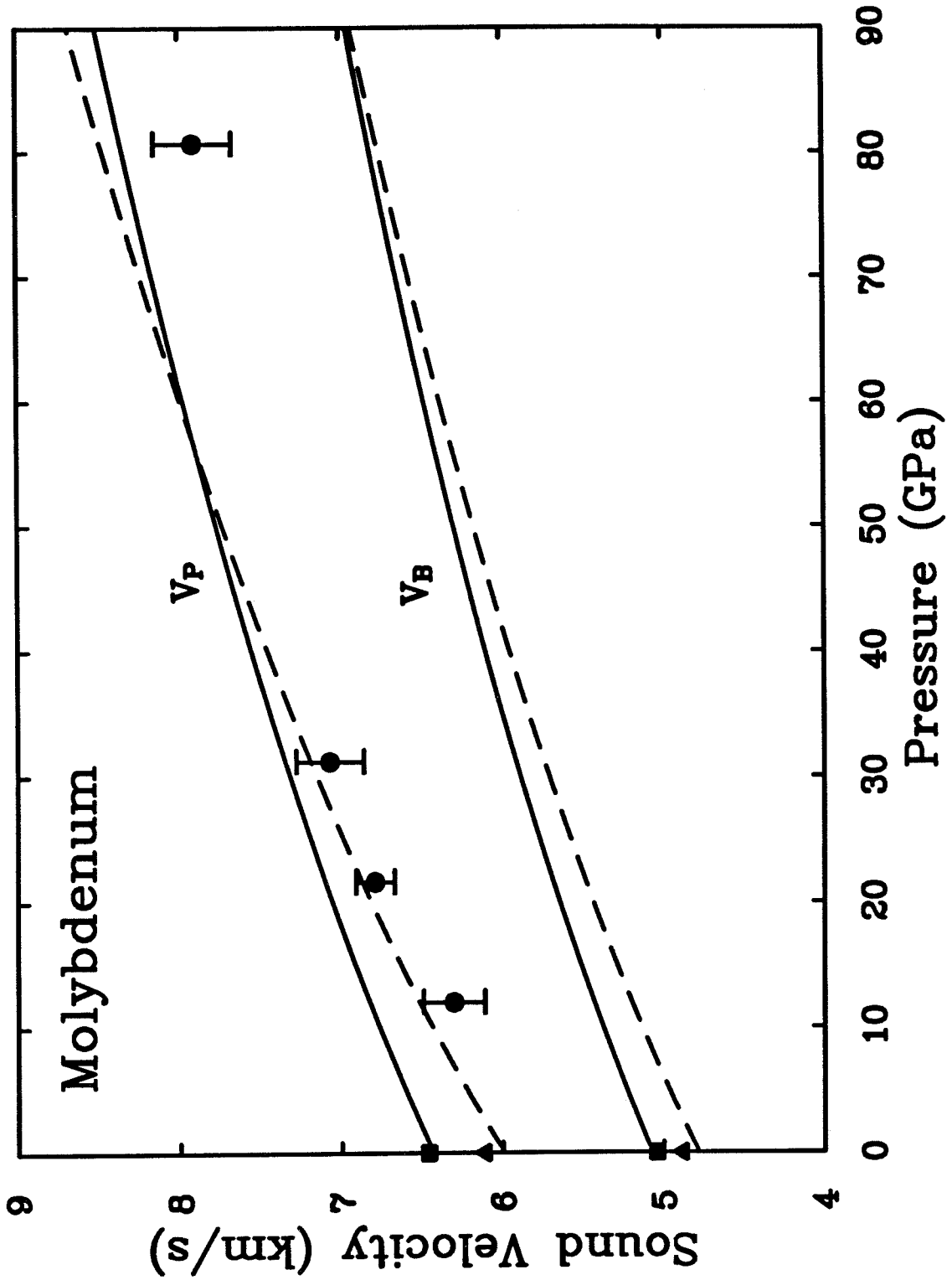
Molybdenum
$V_P$
$V_B$
Sound Velocity (km/s)
Pressure (GPa)
9
8
7
6
5
4
0
10
20
30
40
50
60
70
80
90

### 4.3.5 $(\partial V_P/\partial T)_P$ at High Pressure and Temperature

The primary objective of this study was to constrain the temperature coefficient of compressional velocity at high pressure. The approach for accomplishing this using Hugoniot data has been discussed by *Duffy and Ahrens* [1992a]. Sound velocities along the Hugoniot and a reference isotherm are compared, and temperature differences between the two curves are taken into account. The temperature coefficient of velocity, $(\partial V_P/\partial T)_P$, can be approximated as:

$$(\partial V_P/\partial T)_P \approx \frac{V_{PH} - V_{PI}}{T_H - T_I}, \tag{4.9}$$

where $T$ is the temperature, and the subscripts $H$ and $I$ represent conditions on the Hugoniot and isotherm, respectively. Sound velocities along the reference 300 K isotherm were computed using third-order Eulerian finite-strain theory [*Sammis et al.*, 1970 and Chapter 1] and the elastic moduli and pressure derivatives of Mo given by *Katahara et al.* [1979]. The measured Hugoniot velocities and calculated isotherm velocities are shown in Figure 4.6.

Hugoniot temperatures were calculated from the $\sim 1400°C$ initial state by solving the following differential equation which holds under Hugoniot conditions [*McQueen et al.*, 1970]:

$$V\frac{dT}{dV} = -\gamma T + \left(\frac{V}{2C_V}\right)\left[\frac{dP}{dV}(V_o - V) + P\right], \tag{4.10}$$

where $V$ is the specific volume and $C_V$ is the constant volume specific heat. Values of the Grüneisen parameter and specific heat for Mo at 1400°C were taken from *Miller et al.* [1988], and the difference between the isobaric and isochoric specific heats has been neglected. Both the specific heat and the product $\rho\gamma$ are assumed constant along the Hugoniot. The resulting Hugoniot temperatures are listed in Table 4.4.

The temperature coefficients of $V_P$ calculated using Equation 4.9 are shown in Figure 4.7. Within their uncertainties, the high-pressure values are consistent with

the ambient-pressure value of $(\partial V_P/\partial T)_P$ = -0.247 m/s/K from the ultrasonic data of *Dickinson and Armstrong* [1967]. An expression for the temperature dependence of $V_P$ can be obtained by differentiating the expression

$$V_P^2 = C_L/\rho, \tag{4.11}$$

where $C_L$ is the longitudinal modulus given by $C_L = K_S + 4/3G$, and $K_S$ is the adiabatic bulk modulus to obtain:

$$\left(\frac{\partial V_P}{\partial T}\right)_P = \frac{V_P}{2}\left[\frac{(\partial C_L/\partial T)_P}{C_L} + \alpha\right], \tag{4.12}$$

where $\alpha$ is the volume thermal expansivity. An estimate of the pressure dependence of $(\partial V_P/\partial T)_P$ can be made by assuming that $\alpha K_S$ and $(\partial C_L/\partial T)_P$ are constant functions of pressure. This has been shown to provide an upper bound on measured temperature derivatives under Hugoniot conditions for Al, Cu, Ta, and the high-pressure phases of forsterite [*Duffy and Ahrens,* 1992a]. The present experimental results are consistent with the trend defined by Equation 4.12 as shown in the figure. The parameters for Mo used to solve Eqn. 4.12 are listed in Table 4.6. Although significant experimental uncertainties prevent an unequivocal conclusion from being drawn, the trend of the present results suggests a decrease in the magnitude of $(\partial V_P/\partial T)_P$ with pressure, as has been determined from similar data for several other materials that were shocked to sufficiently high pressures from room temperature so that deviation of the P-wave velocity due to shock heating became apparent [*Duffy and Ahrens,* 1992a]. A weighted least-squares fit to the data of Figure 4.9 yields a value for the pressure-temperature cross derivative of $\partial^2 V_P/\partial T \partial P$ = 0.8 x $10^{-6}$ km/s/GPa/K. This value is comparable to values obtained for other incompressible metals such as W and Ta [*Duffy and Ahrens,* 1992a]. The Mo data are consistent with the trend observed by *Duffy and Ahrens* [1992a] that $\partial^2 V_P/\partial T \partial P$ is a decreasing function of the longitudinal modulus for some six materials investigated to date. The dimensionless pressure-temperature cross derivative satisfies the

| Property | value | Ref. |
|---|---|---|
| $K_S$ | 262.6 GPa | a |
| $G$ | 119.6 GPa | a |
| $K'_S$ | 4.44 | a |
| $G'$ | 1.42 | a |
| $\partial K_S/\partial T$ | -0.016 GPa/K | b |
| $\partial G/\partial T$ | -0.018 GPa/K | b |
| $\alpha$ | 15.0 x $10^{-6}$ $K^{-1}$ | a |

Table 4.6: Thermoelastic parameters for Mo used in the solution of Eqn. 4.12. All quantities are at ambient-pressure conditions. The primes indicate first pressure derivatives. The references are: a, *Katahara et al.* [1979]; b, *Dickinson and Armstrong* [1967].

following relationship for Mo, Al, Cu, Ta, W, and $Mg_2SiO_4$:

$$\frac{K_S}{\alpha V_P}\left(\frac{\partial^2 V_P}{\partial P \partial T}\right)_{P=0} = 1.5 \pm 0.7, \tag{4.13}$$

where all quantities are evaluated at ambient conditions. Values for the individual materials are listed in Table 4.7.

Figure 4.8 compares values of $(\partial V_P/\partial T)_P$ for Mo with values for other materials determined by the analysis of *Duffy and Ahrens* [1992a]. The results of *Duffy and Ahrens* [1992a] were obtained by comparing isotherm and Hugoniot velocities at pressures for which the shock-induced temperature rise was sufficiently high that the temperature coefficients could be resolved. All the materials show decreases in the magnitude of the temperature coefficient of velocity with increasing pressure. Temperature coefficients for the more incompressible metals (Ta, W, Mo) decrease at a slower rate than those for the less incompressible metals (Al, Cu) and the forsterite

Figure 4.7: Magnitude of the temperature coefficient of compressional velocity for Mo along the 1400°C Hugoniot. The results of this study are shown as solid circles. The solid curve is the predicted magnitude of $(\partial V_P/\partial T)_P$ from Eqn. 4.12 using the assumptions discussed in the text. The solid squares show room-pressure values for molybdenum, aluminum, stainless steel 304, copper, tungsten, and tantalum determined from high-temperature ultrasonic data [*Duffy and Ahrens* 1992a].

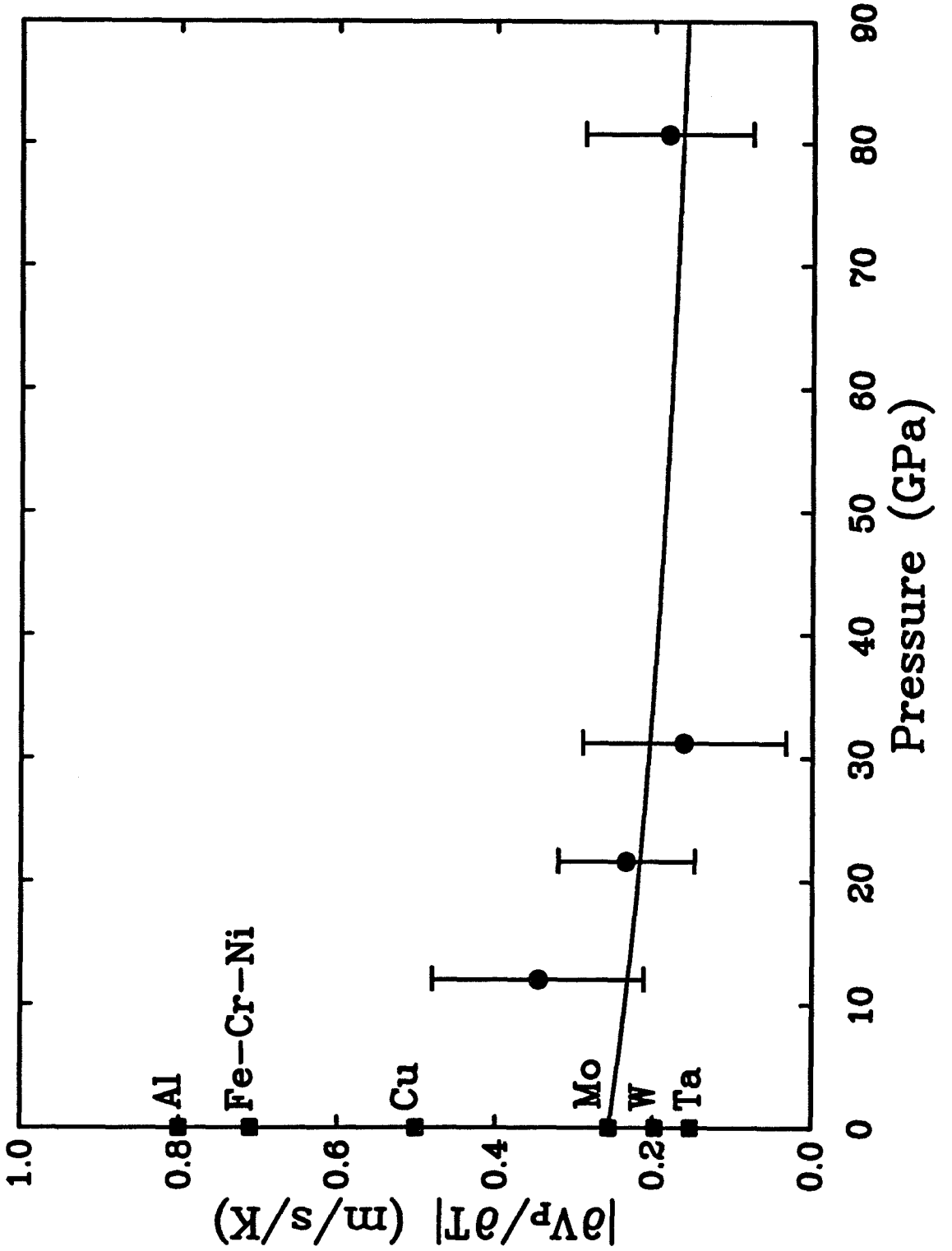
Al
Fe–Cr–Ni
Cu
Mo
W
Ta
1.0
0.8
0.6
0.4
0.2
0.0
0
10
20
30
40
50
60
70
80
90
Pressure (GPa)
|∂Vp/∂T| (m/s/K)

| Material | $(\partial^2 V_P/\partial P \partial T)$ ($10^6$ km/s/GPa/K) | $(K_S/\alpha V_P)(\partial^2 V_P/\partial P \partial T)$ |
|---|---|---|
| Al | 6.1 | 1.0 |
| Cu | 3.6 | 2.1 |
| $Mg_2SiO_4$ | 3.3 | 1.9 |
| Mo | 0.8 | 2.2 |
| Ta | 0.4 | 1.0 |
| W | 0.2 | 0.9 |

Table 4.7: The mixed pressure-temperature derivative of compressional velocity in both dimensional and dimensionless forms. The data for Mo are from this study, and other data are from *Duffy and Ahrens* [1992a].

high-pressure phases (Table 4.7). In Figure 4.9, the product of the ambient-pressure bulk modulus and the temperature coefficient of velocity, $K_o\,(\partial V_P/\partial T)_P$, is plotted as a function of $P/K$, the pressure divided by the bulk modulus. At ambient pressure, this collapses much of the observed variation in $(\partial V_P/\partial T)_P$. The only exception is Ta which differs from the other materials by a factor of two. At high pressure, the data vary in a similar manner when plotted in this way, implying that a universal relationship is approximately represented here.

While the present results are consistent with the previous analysis of *Duffy and Ahrens* [1992a], the method used here offers significant advantages for constraining temperature derivatives. In these experiments, the shock temperature rise is relatively small compared with the precisely known initial temperature. For example, at 12.0 GPa, the shock temperature rise accounts for only 7% of the total temperature, and at 80.7 GPa, the shock temperature component has risen to 38% of the

Figure 4.8: Magnitude of the temperature coefficient of compressional velocity along the Hugoniot for various metals and the high-pressure phases of forsterite. Solid circles are results of this study. Other results are from *Duffy and Ahrens* [1992a].

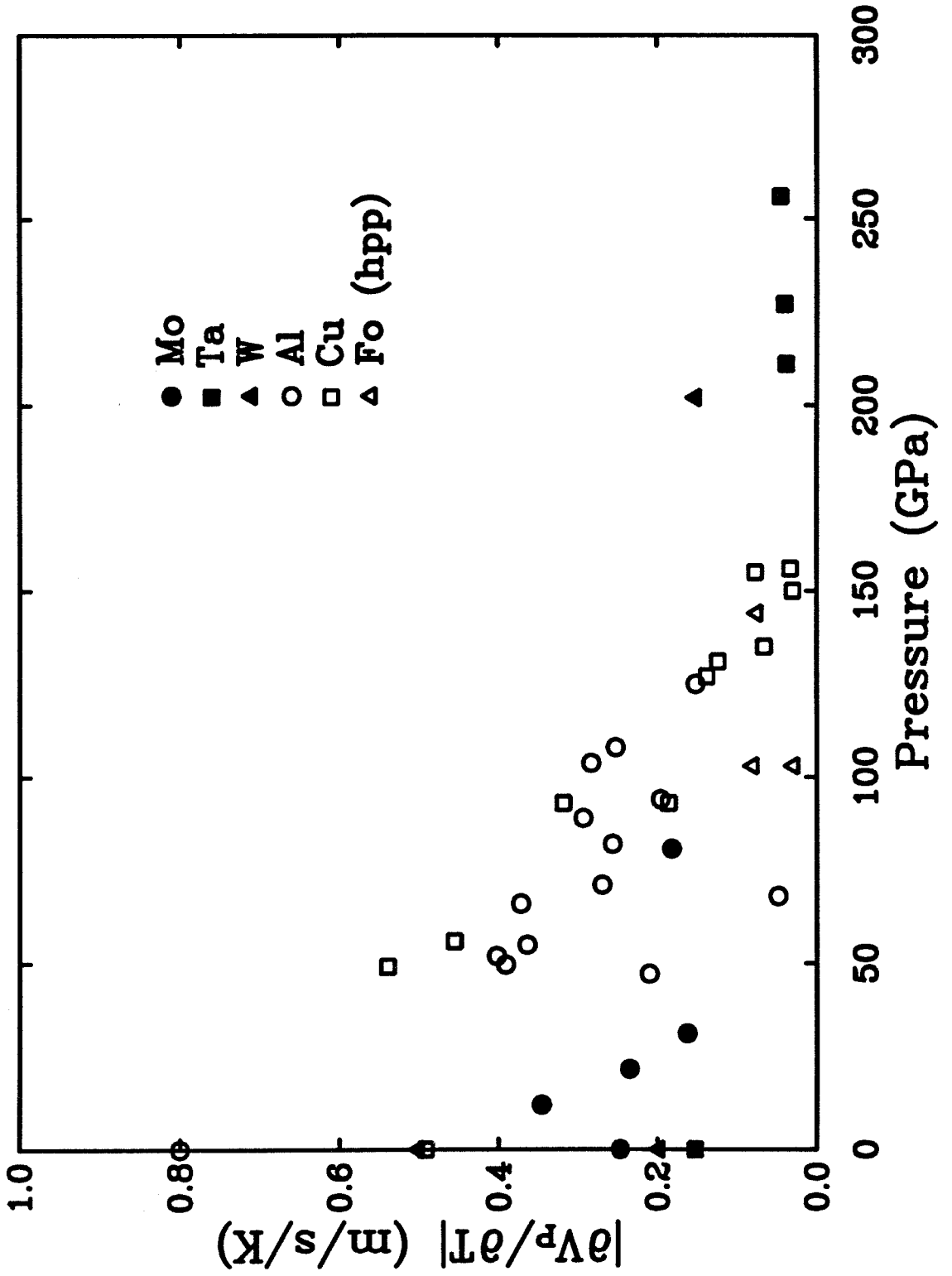
Mo
Ta
W
Al
Cu
Fo (hpp)
|∂Vp/∂T| (m/s/K)
Pressure (GPa)
0.0
0.2
0.4
0.6
0.8
1.0
0
50
100
150
200
250
300

Figure 4.9: The product of the bulk modulus at ambient conditions and $(\partial V_P/\partial T)_P$ plotted as a function of $P/K$, where $K$ is the bulk modulus. The bulk modulus at high pressure was determined from the local slope of the Hugoniot and the assumption that the product $\rho\gamma$ is constant. The Mo data are from the present study, and other data are from *Duffy and Ahrens* [1992a]. The solid line is a quadratic fit using all the data shown in the Figure.

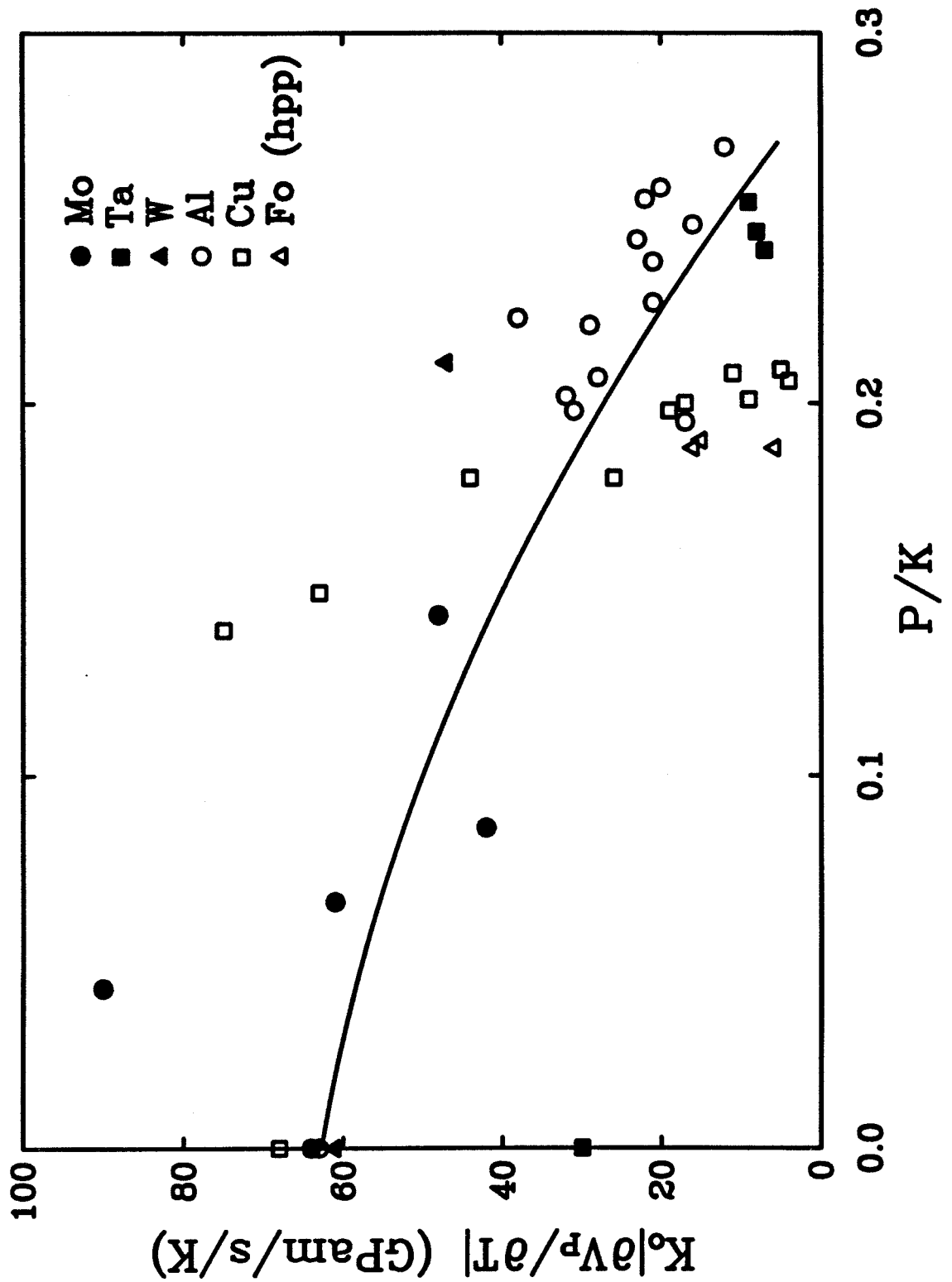
Mo
Ta
W
Al
Cu
Fo (hpp)
100
80
60
40
20
0
0.0
0.1
0.2
0.3
P/K
$K_o|\partial V_p/\partial T|$ (GPam/s/K)

total temperature. Therefore, the uncertainty associated with the calculated shock temperatures is much reduced when compared with experiments in which shock compression accounts for the entire temperature rise. It should be noted, however, that the uncertainties in the velocities themselves are the major contributor to the uncertainty in the temperature derivatives. Secondly, the high initial temperature allows comparison of shock and ultrasonic data at relatively low pressure (~10 GPa). This significantly reduces uncertainty associated with finite-strain extrapolations of ultrasonic data to very high pressure. For these reasons it is felt that the present results are much less likely to suffer from systematic biases than the previous analysis.

*Hixson et al.* [1989] measured sound velocities in Mo shock compressed to between 150 and 441 GPa from a 300 K initial state. They identified a solid-solid transition at about 210 GPa and melting at about 390 GPa. On the basis of theoretical calculations, the solid-solid transformation is interpreted as a bcc to hcp transition caused by $s \rightarrow d$ electronic transfer. The sound velocities of *Hixson et al.* are compared with our high initial-temperature results in Figure 4.10. The data between 150 and 210 GPa are somewhat anomalous in that they imply large values of Poisson's ratio which decrease across this pressure interval whereas Poisson's ratio generally increases with both pressure and temperature. This, together with a softening of the EOS, has also been interpreted as a consequence of the $s \rightarrow d$ electronic transfer which begins approximately above 1 Mbar [*Godwal and Jeanloz,* 1990].

We see no evidence of anomalous behavior in $V_P$ up to 81 GPa from our high-temperature initial state. The increase in Poisson's ratio over this pressure range is normal and will be discussed below further. The Hugoniot velocities are subparallel to but define a shallower slope than the ultrasonic extrapolations. This is consistent with trends observed in shock data for several other metals [*Duffy and Ahrens,* 1992a] and can be attributed to thermal effects. In contrast, between 150-210 GPa, the slope of the Hugoniot velocities is steeper than the ultrasonic trend. We also note that $V_P$

Figure 4.10: Sound velocities in Mo from Hugoniot experiments of *Hixson et al.* [1989] and the present study. Solid lines are third-order finite-strain extrapolations of compressional and bulk velocity using low-pressure ultrasonic parameters. Solid squares are ambient-pressure sound velocities at 300 K and solid triangle shows extrapolated ambient-pressure compressional sound velocity at 1400°C.

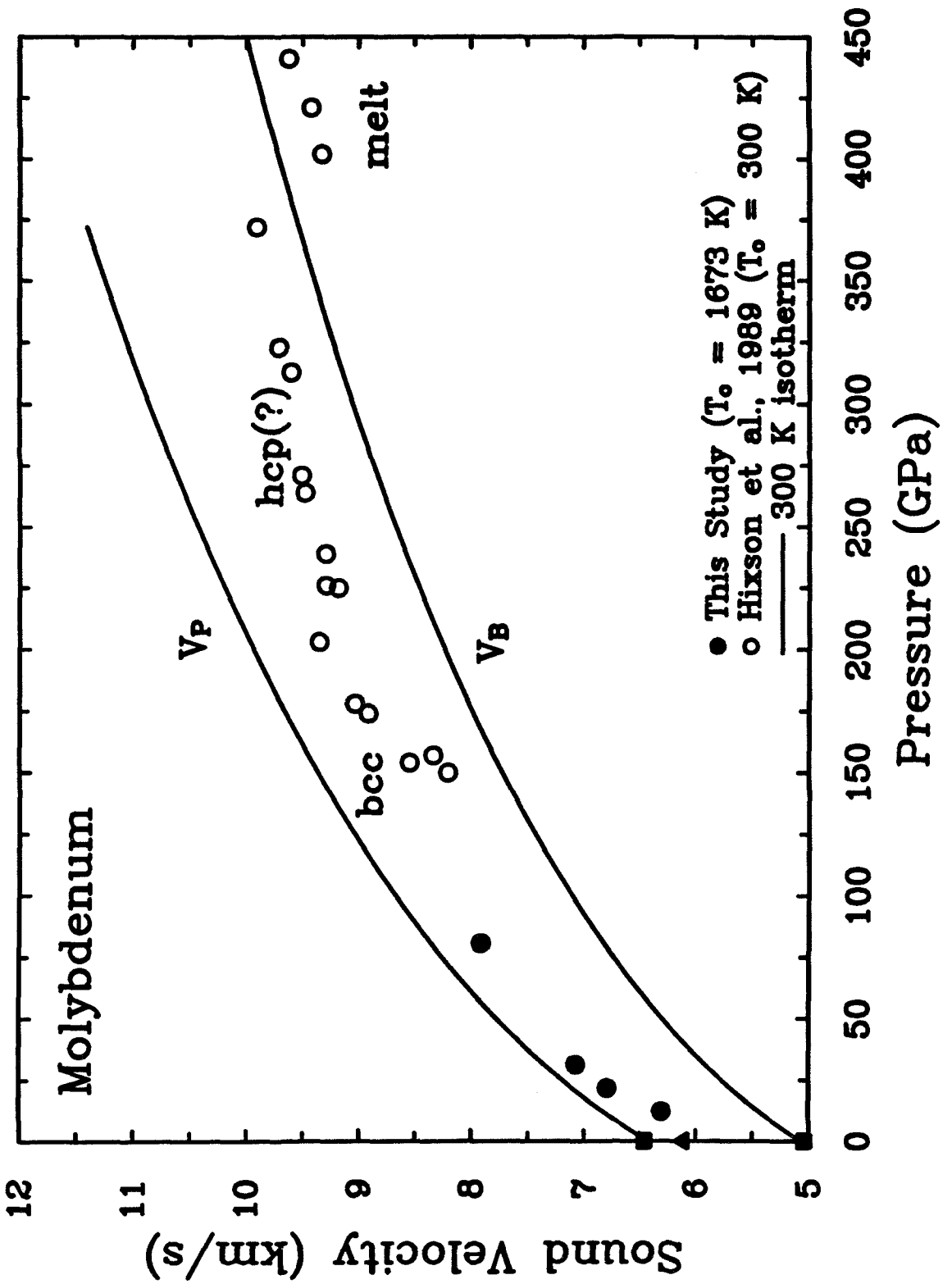
Molybdenum
$V_P$
$V_B$
bcc
hcp(?)
melt
● This Study ($T_o$ = 1673 K)
o Hixson et al., 1989 ($T_o$ = 300 K)
—— 300 K isotherm
Sound Velocity (km/s)
Pressure (GPa)
12
11
10
9
8
7
6
5
0
50
100
150
200
250
300
350
400
450

= 7.91 km/s at 81 GPa and 2721 K, and that at 150 GPa and approximately 2300 K, $V_P$ is only 4% greater (8.20 km/s). This compares with an increase in $V_P$ of 30% between ambient pressure and 81 GPa. There thus appears to be no simple way to join the present data smoothly with the ~150 GPa data of *Hixson et al.* [1989]. The sound velocities measured by *Hixson et al.* may be strongly influenced by the effect of the electronic transfer. On the basis of theoretical calculations, *Godwal and Jeanloz* [1990] concluded that pressure-induced shifts in electronic structure begin around 100 GPa. The possibility of a second solid-solid phase change at pressures between 81 and 150 GPa must also be considered. It should be noted that under room-temperature static compression no solid-solid phase change is observed in Mo to at least 272 GPa [*Vohra and Ruoff,* 1990].

Temperature derivatives derived from the data of *Hixson et al.* are compared with the present results in Figure 4.11. These were obtained by comparing the measured velocities with extrapolations of ultrasonic data (Figure 4.10) and using temperatures calculated by *McQueen et al.* [1970]. The data from a 300 K initial state yield temperature derivatives that are large compared with the trend of the present data and decrease rapidly over the 150-210 GPa range. For the three data points between 150 and 157 GPa, the inferred T derivatives are also large relative to the ambient-pressure temperature coefficient of Mo. If structural changes at high pressure due to electronic transfers are occurring, this would potentially bias any comparison of Hugoniot and ultrasonic data.

The anomalous nature of the Mo sound velocities above 150 GPa is also illustrated when plotted as a function of density (Figure 4.12). *Duffy and Ahrens* [1992b] have shown that compressional sound velocity data for a variety of metals approximately satisfy Birch's Law over broad pressure intervals. That is, velocity is a linear function of density with a slope that depends upon the material's atomic weight. As noted by *Duffy and Ahrens* [1992b], in contrast to the other materials examined, velocities

Figure 4.11: Temperature coefficients of compressional velocity determined from the present study and from the 300 K initial state data of *Hixson et al.* [1989]. The solid square shows the ambient-pressure value from ultrasonic data. The solid curve shows the expected trend based on Equation 4.12 and the assumptions discussed previously.

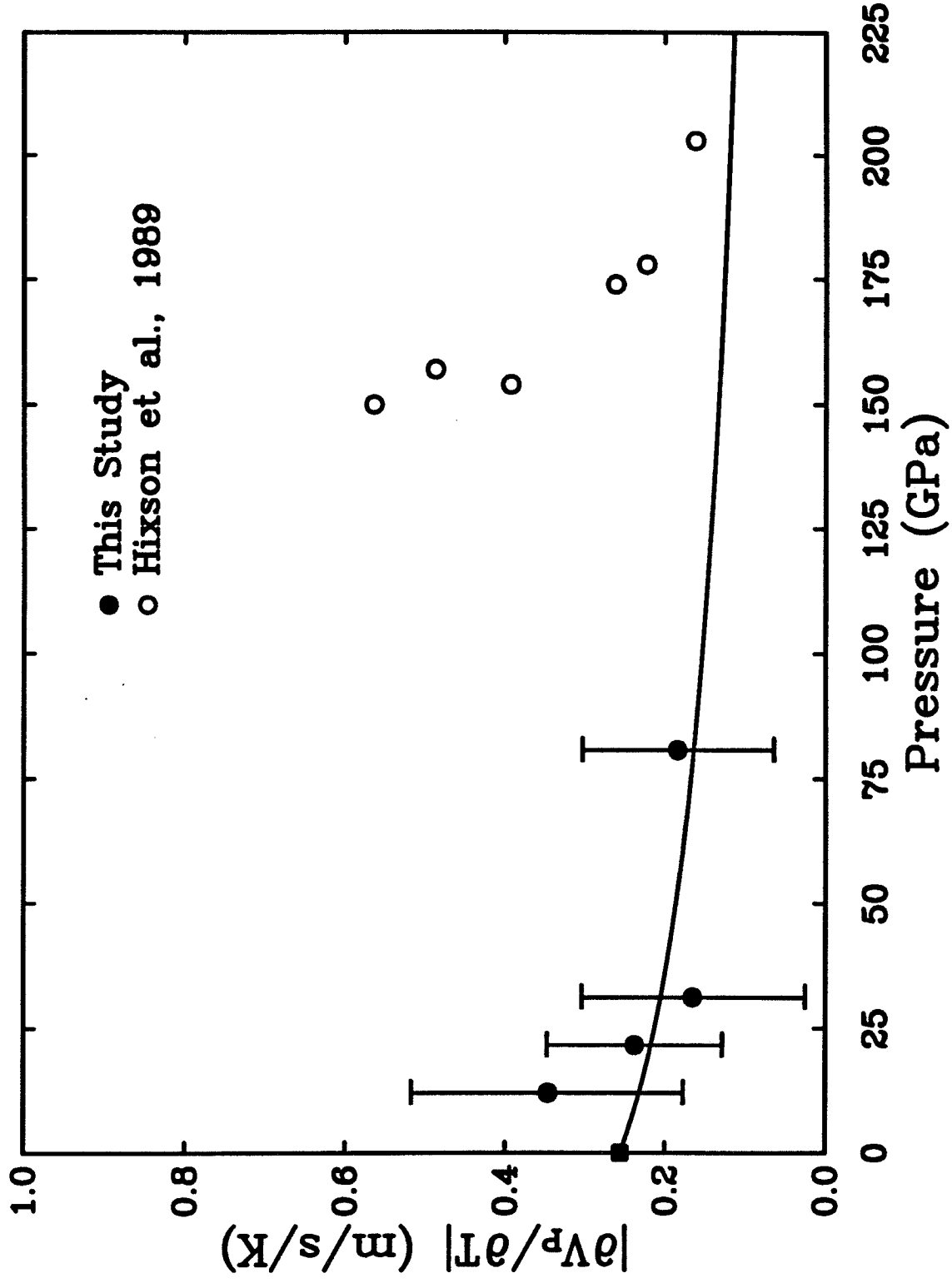
● This Study
o Hixson et al., 1989
|∂Vp/∂T| (m/s/K)
Pressure (GPa)
0.0
0.2
0.4
0.6
0.8
1.0
0
25
50
75
100
125
150
175
200
225

in Mo between 150-210 GPa are linear in $\rho$ but do not extrapolate to the ambient-pressure compressional velocity. In contrast, the high-temperature sound velocities between 0 and 81 GPa define an approximately linear trend which is consistent with the ambient-pressure velocity and with the trend of the ultrasonic data. This serves to further emphasize the apparent importance of structural changes in Mo at pressures above 81 GPa but below the 210 GPa phase-transition pressure.

Poisson's ratio, $\nu$, can be computed by combining measured compressional velocities with bulk velocities constrained by the Hugoniot slope and the assumption that $\rho\gamma = \text{const}$ [*McQueen et al.,* 1967; *Ahrens,* 1987; see also Chapter 1]. Poisson's ratio values for Mo are listed in Table 4.6. The ambient-pressure 1400°C value of $\nu$ from extrapolation of ultrasonic data is 0.313, as discussed previously. These data suggest that Poisson's ratio increases along the Hugoniot over this pressure range. Similar increases in $\nu$ have been observed for other metals under Hugoniot conditions [*Duffy and Ahrens,* 1992b].

### 4.3.6 Spall Strength

The interaction of unloading waves depicted in Figure 4.3 leads to the development of tensile stresses within the specimen which can be sufficiently strong to lead to dynamic fracture or spall. The characteristic signature of spall is an increase or "pull-back" in free surface velocity as seen in Figure 4.2. From the amplitude of the pull-back signal, an estimate of the spall strength, the maximum tensile stress the material can support, can be obtained. For an elastic-plastic material, the spall strength, S, can be obtained from [*Romanchenko and Stepanov,* 1980]:

$$S = S_{fs} + \Delta S, \tag{4.14}$$

where $S_{fs}$ is the amplitude of the tensile-stress pulse recorded at the free surface:

$$S_{fs} = \rho_o V_P \Delta u_{pb}, \tag{4.15}$$

Figure 4.12: Compressional velocities in Mo as a function of density. The solid square shows compressional and bulk sound velocities under ambient conditions [*Dickinson and Armstrong,* 1967]. The solid triangle shows the 1400°C, ambient-pressure compressional velocity. Solid line shows finite-strain extrapolations of low-P ultrasonic data. Dashed lines are linear fits to data between 0-81 GPa, 150-210 GPa, and 210-390 GPa. The data between 150-210 GPa show a distinctly different slope from the finite-strain trend and from the 0-81 GPa data.

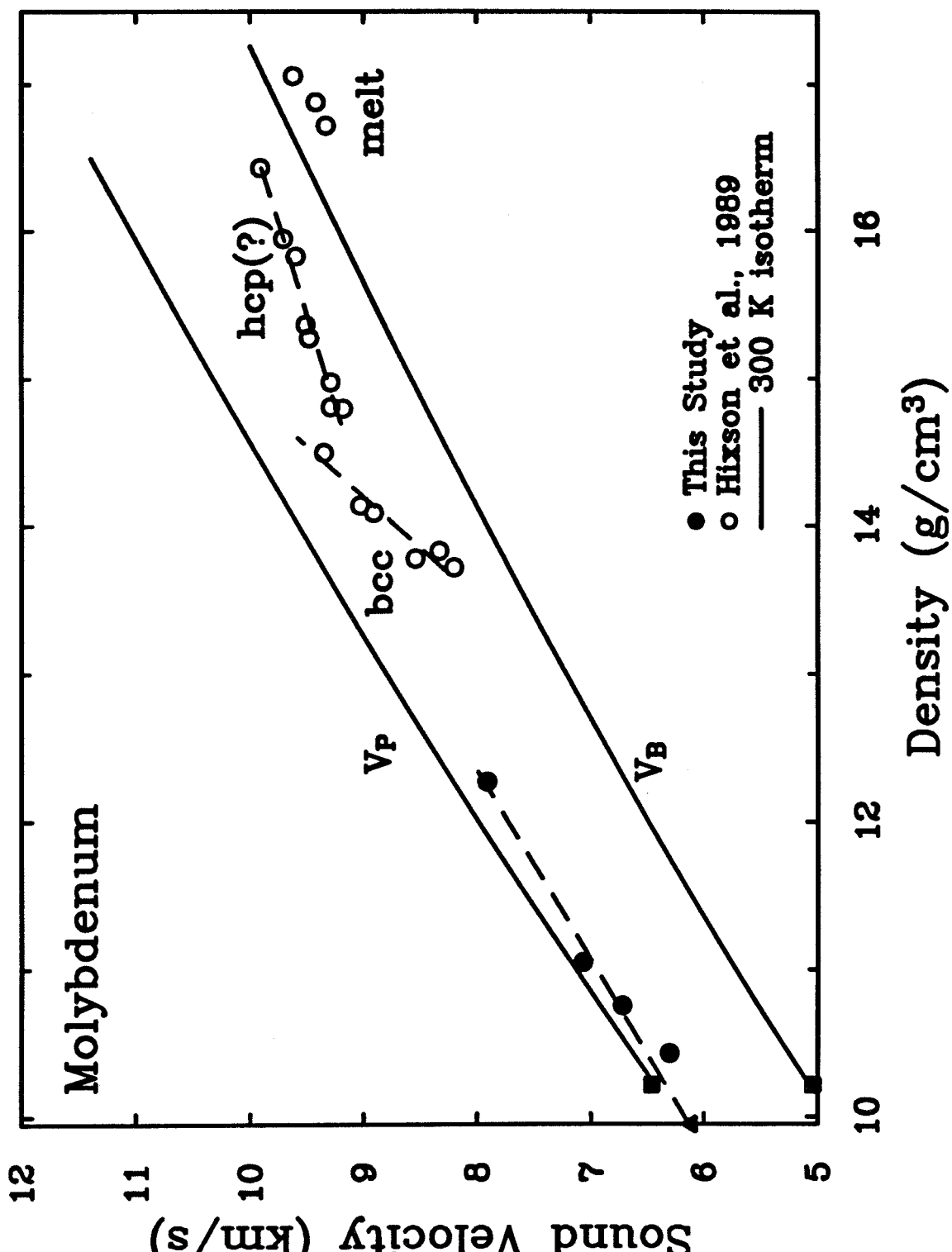
Molybdenum
$V_P$
$V_B$
bcc
hcp(?)
melt
● This Study
○ Hixson et al., 1989
—— 300 K isotherm
Sound Velocity (km/s)
Density (g/cm³)
12
11
10
9
8
7
6
5
10
12
14
16

where $\Delta u_{pb}$ is the pull-back amplitude measured from the peak free surface velocity to the velocity minimum. The term $\Delta S$ accounts for the attenuation of the spall signal in propagating from the spall plane:

$$\Delta S = \frac{S_{fs}\delta}{\tau}\left(\frac{1}{V_B} - \frac{1}{V_P}\right), \tag{4.16}$$

where $\tau$ is the pull-back pulse duration, and $\delta$ is the distance to the spall plane which we have assumed is close to $h^*$. The resulting spall strengths for Mo between 12 and 31 GPa are shown in Figure 4.13. Near 12 GPa, the spall strength of high-temperature Mo is 2.4 GPa, only slightly different from the value of 2.31 GPa reported for room-temperature Mo [*Chhabildas et al.,* 1990]. Thus, in contrast to the compressive yield strength, the spall or tensile strength appears to be only weakly dependent on temperature for this material. The room-temperature and high-temperature experiments differ in the location of the spall plane, however. In the present experiments, the spall plane was maintained near the free surface whereas the spall plane was in the middle of the sample for the room-T experiment of *Chhabildas et al.* [1990]. The spall strengths shown in Figure 4.13 tend to increase with increasing peak stress. This has also been observed in other materials such as uranium [*Grady,* 1986].

### 4.3.7 Additional Compressive-Wave Features

The compressive waveforms for the three free surface profiles are displayed in Figure 4.14. In order to better understand the waveforms, computer simulations of the experiments were undertaken using the one-dimensional finite-difference wavecode WONDY [*Kipp and Lawrence* 1982] which is described in Chapter 1. Both Mo and Al6061 are modeled as elastic-perfectly plastic materials with the parameters listed in Table 4.5. The results of the simulations are shown in Figure 4.14 and are in very good agreement with the experimental profiles. The elastic precursors in the simulations are highly dispersive because of the artificial viscosity term included for

Figure 4.13: Spall strength of Mo as a function of peak stress. Solid symbols are present high-temperature results. Open symbol is room-temperature result of *Chhabildas et al.* [1990].

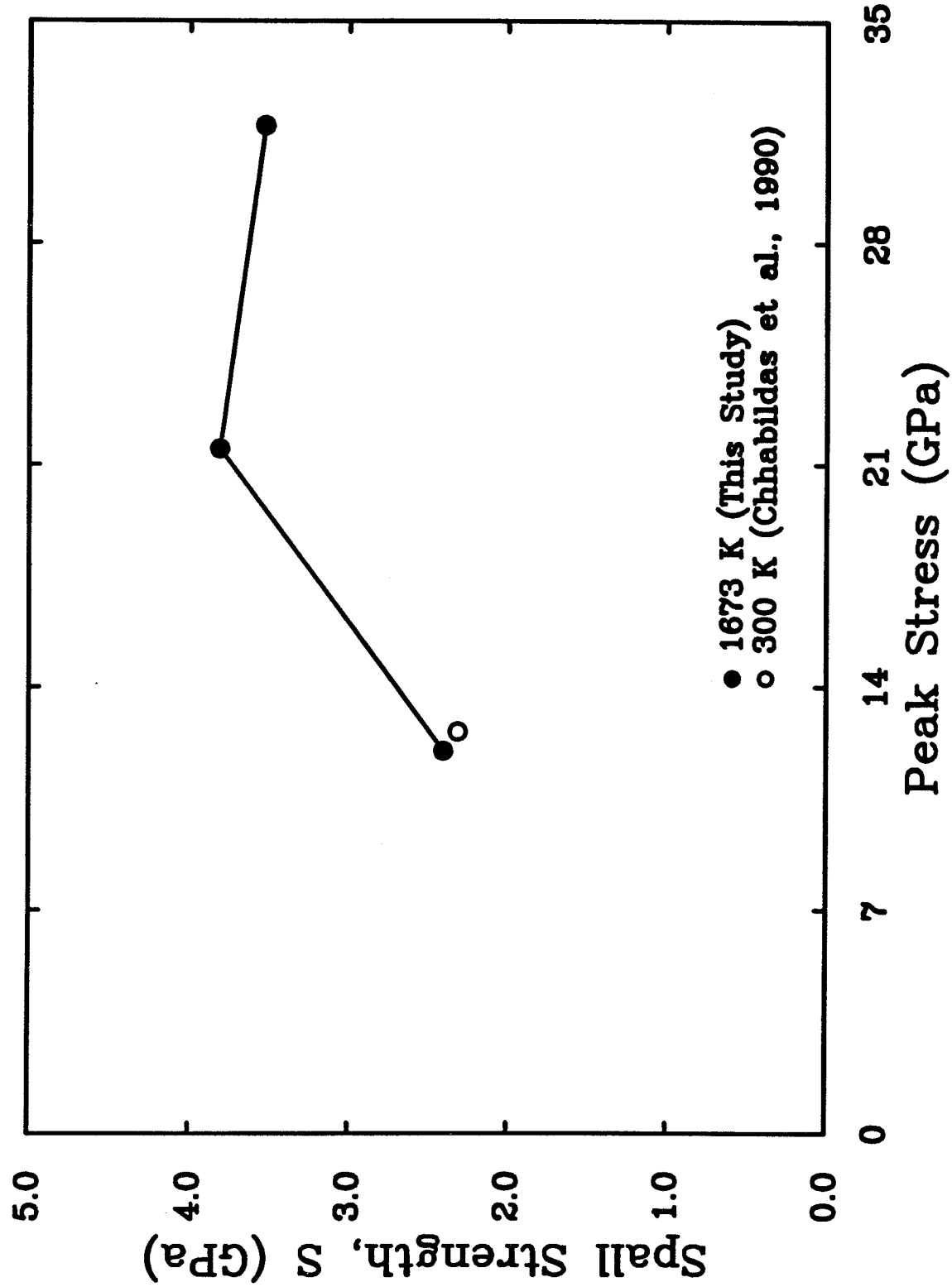
Spall Strength, S (GPa)
5.0
4.0
3.0
2.0
1.0
0.0
0
7
14
21
28
35
Peak Stress (GPa)
● 1673 K (This Study)
o 300 K (Chhabildas et al., 1990)

numerical stability. The main feature to note is that the rise time of the plastic shock front is significantly greater at low pressure and is on the order of 50 ns for the 12 GPa experiment.

The agreement obtained in Figure 4.14 suggests that wavecode calculations can reasonably simulate the shock structure observed in such experiments. EOS experiments on high-temperature molten silicates encapsulated in Mo have yielded important insights into magma petrogenesis [*Rigden et al.*, 1988; *Miller et al.*, 1991]. We have performed additional wavecode simulations in order to investigate the expected shock structure in such experiments. The computer simulations consisted of Al impactors traveling at 1 and 2.5 km/s impacting a 0.76-mm Mo driver plate behind which was a 3.3-mm thick layer of molten komatiite followed by a 2.0-mm thick Mo cap. The lateral dimensions were assumed to be sufficiently large that they could be safely neglected over the time scale of the experiment. Molten komatiite was treated as a hydrodynamic fluid with the EOS parameters determined by *Miller et al.* [1991].

The compressive waveforms from the simulations are shown in Figure 4.15 as well as waveforms from identical simulations in which the Mo-silicate sandwich is replaced by a single layer of Mo of equal thickness. For the 2.5 km/s simulation, the compressive waveforms with and without the komatiite layer are similar. At 1 km/s, significant additional structure is introduced into the waveform because of reflections at the silicate/Mo interface which significantly broaden the shock front. These results suggest that EOS experiments on molten silicates using streak camera detection may be ambiguous at low shock pressures ($\sim$10 GPa) because of the long rise time of the plastic wave front and the additional structure that arises due to wave interactions. This may in part explain inconsistencies observed in streak camera records from low-pressure molten-silicate experiments [*Miller et al.*, 1991].

Comparison of shock- and static-compression data is useful for a variety of purposes, including establishing a reliable pressure scale for diamond anvil cell experi-

Figure 4.14: Comparison of measured compressive waveforms with finite-difference simulations. The solid lines show the measured waveforms and the dashed lines are computer simulations using the WONDY code. The timing is arbitrary.

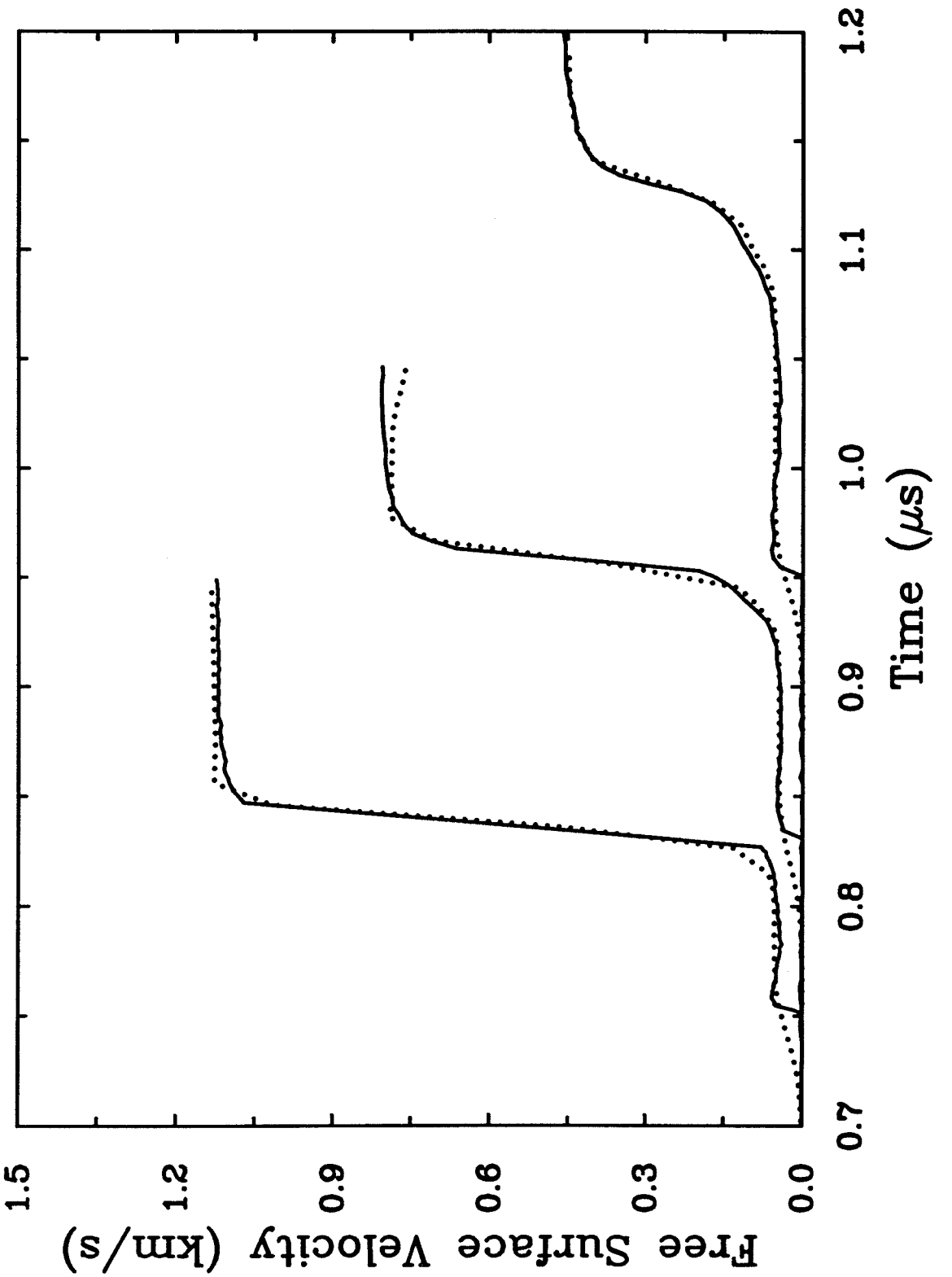
Free Surface Velocity (km/s)
1.5
1.2
0.9
0.6
0.3
0.0
0.7
0.8
0.9
1.0
1.1
1.2
Time (μs)

Figure 4.15: Calculated free surface velocity profiles for molten-silicate experiments based on computer simulations. The solid curves show calculated compressive-wave structure for a komatiite sample encapsulated by Mo and impacted with an Al 6061 flyer at 2.5 km/s (left) and 1.0 km/s (right). The dashed curves show the same simulations except that the komatiite layer has been replaced by a single thickness of Mo. At low impact velocities, the komatiite experiments show significant additional structure that is due to wave interactions in the Mo cap.

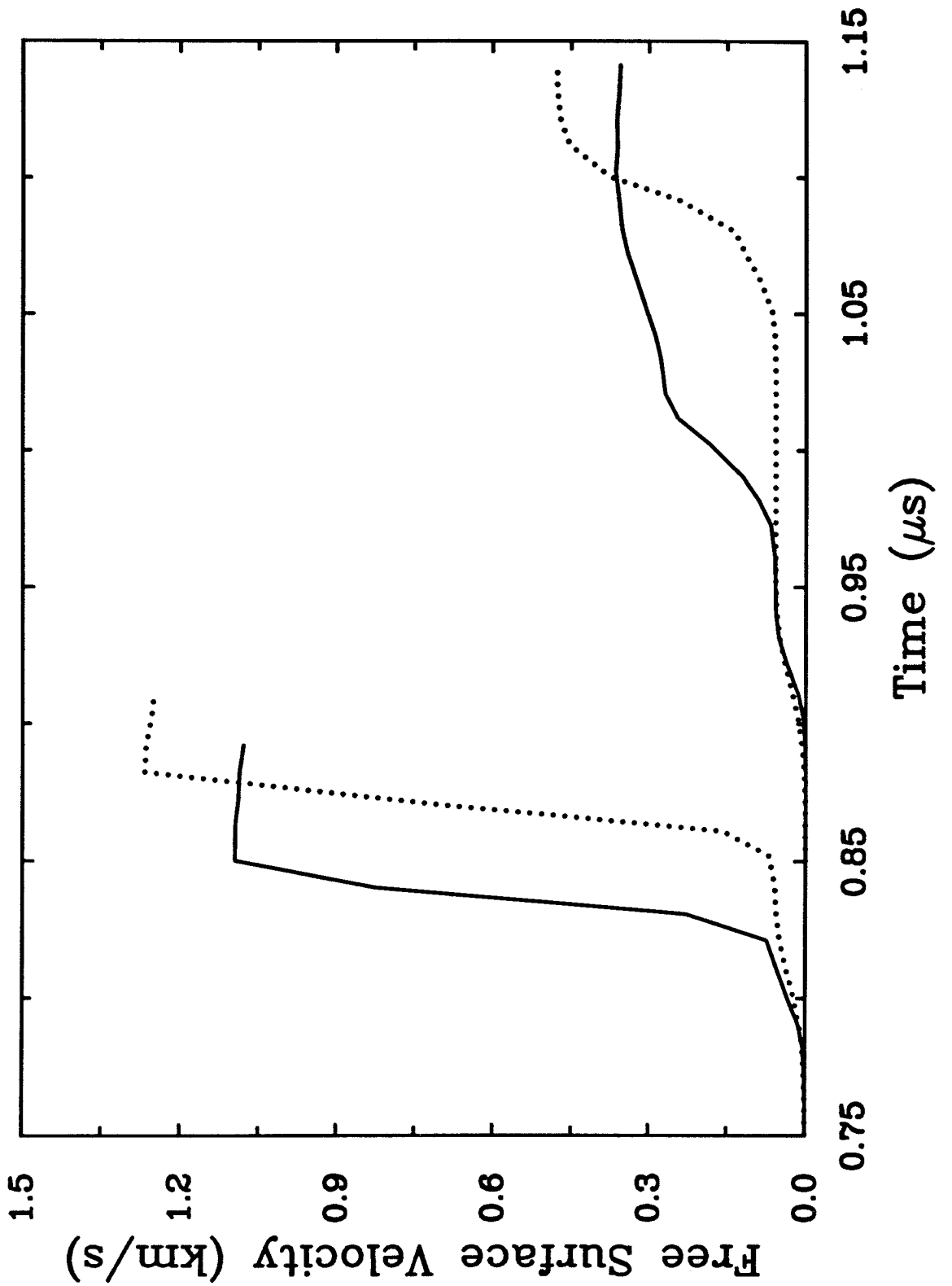
Free Surface Velocity (km/s)
1.5
1.2
0.9
0.6
0.3
0.0
0.75
0.85
0.95
1.05
1.15
Time (μs)

ments. Such comparisons may be hampered by the effects of material strength. Material strength has been observed to decrease at high shock pressure in aluminum, presumably because of thermal effects [*Asay and Kerley,* 1987]. However, there is little quantitative information on thermal softening of material strength under dynamic compression. The yield strengths determined previously (Table 4.2) are plotted as a function of initial temperature in Figure 4.16. In the constitutive model of *Steinberg et al.* [1980], thermal effects are approximated by assuming that the ratio Y/G is constant, where G is the shear modulus. In fact, according to Figure 4.16, the yield strength of Mo decreases at a faster rate than the shear modulus. A better representation is that the yield strength is the following linear function of homologous temperature:

$$Y_o = 2.016(1 - T/T_m), \tag{4.17}$$

where $T_m$ is the melting temperature. This is similar to the relationship of *Hageman and Walsh* [1970] in which the yield strength depends on the ratio of internal energy to the melt energy. The above relationship was obtained by using the 300 K yield strength at 12.6 GPa and requiring that $Y_o = 0$ at the 2890 K melting point [*Robie et al.,* 1978]. This relationship predicts a yield strength at 1676 K within about 10% of the measured value for a 12 GPa peak stress.

## 4.4 Summary

Wave profile measurements have been carried out on molybdenum preheated to ~1400°C in order to investigate its high-temperature constitutive, equation of state, and elastic properties under shock compression. We are able to quantify the thermal softening of Mo due to the effects of temperature for the first time. The Hugoniot elastic limit stress ranges from 1.5-1.7 GPa between 12 and 31 GPa at 1400°C, which is significantly below the 25°C value of 3.1 GPa. The high initial temperatures also induce stress relaxation behind the elastic precursor which manifests itself as a 14-

Figure 4.16: Yield strength of molybdenum as a function of initial temperature. 300 K value is from *[Chhabildas et al.* [1990].

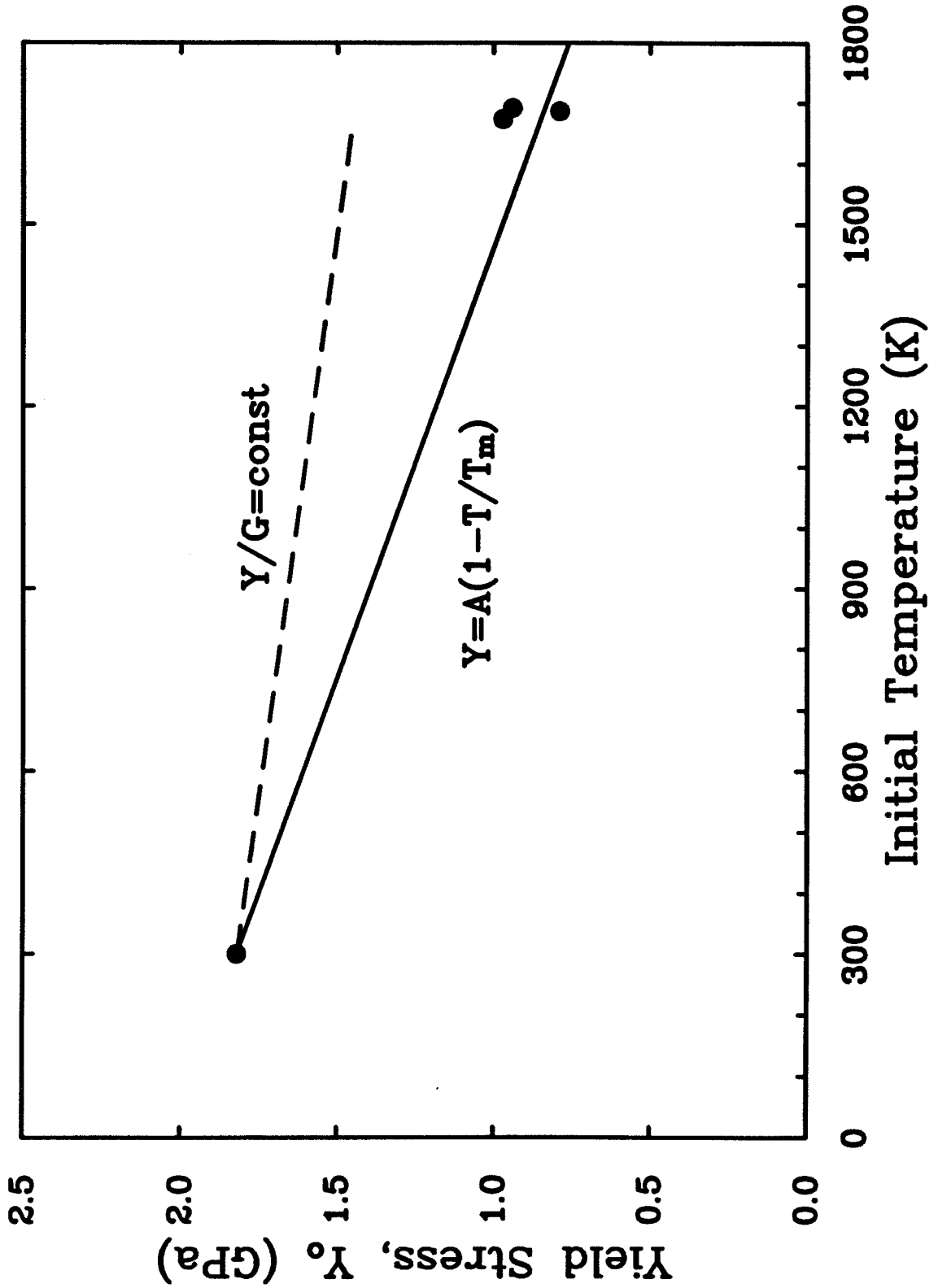
Yield Stress, $Y_o$ (GPa)
2.5
2.0
1.5
1.0
0.5
0.0
0
300
600
900
1200
1500
1800
Initial Temperature (K)
Y/G=const
$Y=A(1-T/T_m)$

36% reduction in free surface velocity behind the precursor. The compressive yield strength is also strongly temperature-sensitive, decreasing from its room-T value of 1.8 GPa to values between 0.79-0.94 GPa at ~1400°C. The yield strength decreases approximately linearly with the homologous temperature. In contrast, spall-strength measurements near 12 GPa suggest that this quantity is only weakly temperature-sensitive in Mo. The 12 GPa spall strength of Mo at 1400°C is 2.4 GPa which differs only slightly from the room-temperature value of 2.3 GPa at a similar pressure.

Equation of state measurements on 1400°C Mo (initial density, 9.95 g/cm$^3$) are in excellent agreement with the results of earlier streak camera experiments [*Miller et al.,* 1988]. The shock wave equation of state obtained from a combination of all data is:

$$U_s = 4.78(0.02) + 1.42(0.02)u_p,$$

which covers a range in pressure from 12-96 GPa.

Measured compressive waveforms in Mo are in good agreement with one-dimensional finite-difference wavecode (WONDY) simulations of the experiments. Simulations of high-temperature experiments on molten silicates contained in Mo capsules were also carried out. The principal conclusion regarding molten-silicate experiments is that at low pressures (~10 GPa), the shock front transmitted through the Mo cap has a long rise time (> 50 ns) and contains significant secondary structure due to internal wave interactions. This suggests that EOS measurements on molten silicates at low shock pressures ($\leq$ 10 GPa) using streak camera methods may not be reliable.

Compressional sound velocities were measured over the range 12-81 GPa. In combination with 300 K isotherm velocities from ultrasonic data and the calculated temperature rise due to shock compression, these data constrain the temperature coefficient of compressional velocity. Resultant values of $(\partial V_P/\partial T)_P$ are consistent with ambient-pressure values of this quantity from ultrasonic data and also suggest

that $(\partial V_P/\partial T)_P$ decreases in magnitude with pressure. The pressure dependence of $(\partial V_P/\partial T)_P$ is comparable to the previously determined behavior of Al, Cu, W, Ta, and $Mg_2SiO_4$. However, the present values of $(\partial V_P/\partial T)_P$ are believed to be more reliable because the ultrasonic data are extrapolated over a smaller range and the temperatures are more precisely known. Velocity trends to 81 GPa are inconsistent with measured velocities between 150 and 190 GPa from a 300 K initial state reported by *Hixson et al.* [1989]. This is interpreted as a consequence of high-pressure structural changes in Mo caused by electronic transfers. No evidence of anomalous structural effects are observed up to 81 GPa in the high-temperature data.

# Appendix A

# Shock Wave Interferometry

Two types of velocity-sensitive interferometers were used in the present work: the specular velocity interferometer (SVI) and the velocity interferometer system for any reflector (VISAR). These two devices, although related, are useful under different experimental situations and have different experimental requirements. In this section, a description of the theory, construction, and operation of these interferometers for shock wave studies is given.

Interferometers for use in shock wave studies have undergone several modifications. The original interferometer (known as the normal displacement interferometer or NDI) was a displacement interferometer in which a specularly reflecting target served as one leg of a Michelson interferometer [*Barker and Hollenbach,* 1965]. A subsequent modification turned this device into a differential displacement or velocity-sensitive interferometer known as the specular velocity interferometer (SVI) [*Barker,* 1968]. Finally, development of the VISAR extended the applicability of interferometry to diffuse reflectors (that is, spatially incoherent sources) as well as provided increased precision [*Barker and Hollenbach,* 1972]. The VISAR has subsequently been used widely in shock wave studies with relatively minor modifications to the original design [*Barker,* 1983].

Optical interferometry provides a means to record the time-resolved motion of a position on a sample surface by recording the Doppler shift induced in reflected laser light by that surface's motion. Measurements can be made either at a free surface or through a transparent window epoxied to the test specimen. frequently wishes to measure a wave profile that is as close as possible to that propagating through the interior of the sample. In such cases, it is desirable to view the surface through a window that matches the shock impedance of the sample as closely as possible. This produces a waveform that is minimally perturbed by wave interactions arising at the sample-window interface. In contrast, free-surface velocity measurements of necessity record waveforms that are simultaneously affected by the compressive and release characteristics of the material being studied. The use of a window necessitates changes in the optical set-up (discussed below) and the stress-induced change in the window's refractive index must be accounted for in the data-reduction process. *Wise and Chhabildas* [1986] discuss various window materials and the stress ranges over which they are calibrated and have been successfully used in shock interferometry.

## A.1 Specular Velocity Interferometer

A number of preliminary experiments were conducted using a specular velocity interferometer (SVI) modeled after the device of *Barker* [1968]. This is a modified Michelson interferometer which records the Doppler shift induced in laser light reflected from a specular-reflecting target surface. A schematic diagram of the SVI is shown in Figure A.1. In a normal Michelson interferometer, interference is produced by recombining light that has been split and reflected from two separate mirrors. In the SVI, however, the target reflecting surface acts as both mirrors of a Michelson interferometer, but the mirrors are separated in time rather than space [*Barker,* 1968]. This is accomplished by dividing the light with a beam splitter and routing a portion

of it around a delay leg that delays it by 1-2 nsec. Therefore, at any given time, the SVI combines light reflected from the target with a reference beam which consists of light reflected a short time earlier from the target. During periods of constant velocity, both beams will have the same Doppler shift, and signal intensity will not vary. However, during periods of acceleration, the two recombined beams will have different Doppler shifts and signal intensity will vary. It can be shown that the fringe count is proportional to surface velocity through the following relationship [*Barker,* 1968]:

$$u(t - \tau/2) = \lambda_o F(t)/(2\tau), \tag{A.1}$$

where $u$ is the surface velocity, $t$ is the time, $\tau$ is the delay time of the interferometer, $\lambda_o$ is the laser wavelength (612.3 nm).

Figure A.1 shows how the SVI is incorporated into a plate-impact experiment. The details of the sample assembly are shown in Figure 1.3. The target is polished to a specular finish, and a window is epoxied to it. The purpose of the window is to provide a wave profile that is only minimally affected by unloading (or reloading) at the material interface. The sample-window assembly is then impacted by a high-speed flyer plate as shown in the Figures A.1 and 1.3. The rear-surface motion of the target is monitored by illuminating it with a long coherence length 1.5 mW He-Ne laser (Spectra-Physics 117A). The light is focused onto the target using an expendable 30-mm diameter, 75-mm focal length lens mounted inside the tank. An expendable mirror directs the laser light onto the back of the target. The reflected light is returned at a slight angle to the incident beam and separated by a mirror. A portion of the light is split away by a beam splitter and directed to a beam-intensity-monitoring photomultiplier tube (Burle 7764). The rest of the light is split again by a second beam splitter. A portion of this light is delayed by 1-2 nsec by passing it around a delay leg using a 60-mm right-angle prism (Rolyn Optics Co.). Upon recombination at the third beam splitter, interference fringes are generated and

Figure A.1: Schematic illustration of the specular velocity interferometer (SVI). The abbreviations are: M, mirror (25.4-mm diameter, laser line coating); L, lens (plano-convex, 30-mm diameter, 75-mm f.l.); BS, beam splitter (10-mm cube with broadband dielectric coating); F, neutral-density filter (0.001-0.1% transmission); PMT, photomultiplier tube (Burle 7764).

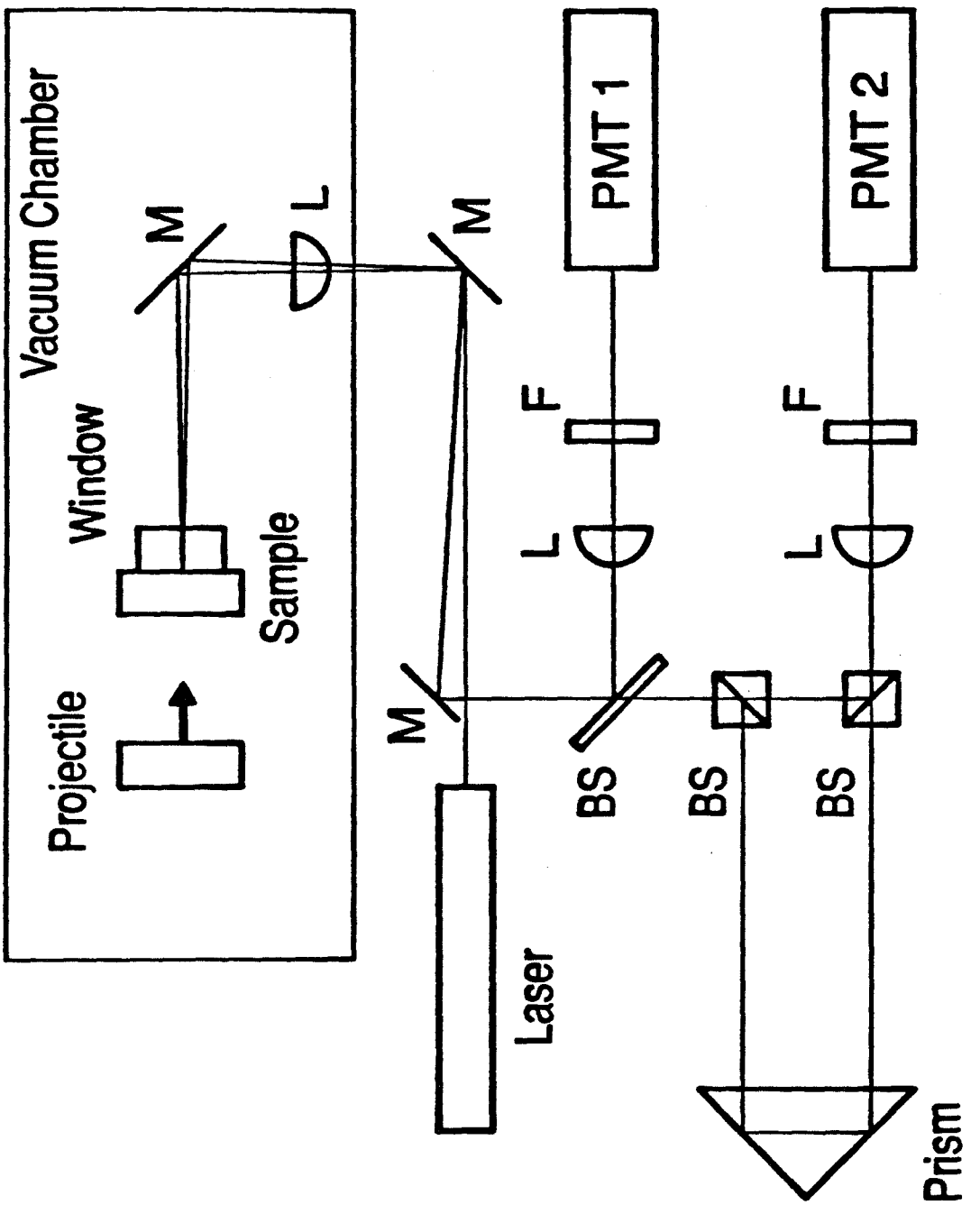
Vacuum Chamber
Window
Sample
Projectile
M
L
M
M
PMT 1
PMT 2
F
F
L
L
BS
BS
BS
Laser
Prism

detected using a second photomultiplier tube. The data is recorded photographically on Tektronix 485 analog oscilloscopes as well as with a LeCroy (model 8081) 100 MHz transient digitizer.

The primary limitation of the SVI is that the sample must retain a mirror finish throughout the duration of the experiment. This is because in a long path difference interferometer the spatial coherence of the reflected light must be maintained. However, strong shocks have a tendency to destroy a mirror finish, resulting in a catastrophic loss of returned signal intensity and fringe contrast. In the present work, this interferometer was used with stainless steel 304 targets to pressures between 6.5 and 11.3 GPa. This is comparable to the maximum pressures achieved by other workers using this device [*Barker,* 1968; *Barker and Hollenbach,* 1970; *Munson and Lawrence,* 1979]. In order to obtain wave profiles at higher pressures, it is necessary to make use of an interferometer for diffuse reflectors. The VISAR, described below, is one such interferometer. The SVI is also strongly sensitive to misalignment due to impact-induced tilt.

## A.2 VISAR

### A.2.1 Theory

In order to extend the useful range of interferometry, *Barker and Hollenbach* [1972] developed the VISAR which can be used with diffuse reflectors and has several advantages over the SVI device. The VISAR works by introducing a ~1-2 ns delay between the two beams of the interferometer through the use of fused silica delay bars in one leg. At the same time, the mirror positions are adjusted so that the two end mirrors appear to be coincident from the point of view of the detector. This technique, known as field-widening, extends the use of interferometry to spatially incoherent sources while at the same time maintaining the time delay which is necessary to record velocity information. Since the VISAR collects only a small portion

of the diffusely scattered light from the specimen, it is largely insensitive to tilting of the reflector.

A schematic of the VISAR set-up is shown in Figure A.2. A brief summary of the essential features is given here, and a description of the details of the optical components and their arrangement is contained in Section A.2.2. The VISAR constructed for the present work is similar to that originally described by *Barker and Hollenbach* [1972]. We have, in addition, incorporated the push-pull modification of *Hemsing* [1979]. As shown in the figure, incident laser light is focused on the sample, and the returned light is recollimated by the collection lens L1. The telescope is used to reduce the beam diameter to a more workable size. Next, the light travels through a depolarizer, immediately followed by a polarizing prism that insures proper orientation of the polarization components of the light. Specifically, the effect of any rotation of the polarization vector of the reflected light that is due to optical activity in the window is removed by randomizing the polarization of the light before it reaches the polarizer. The polarizing prism is oriented such that the p- and s-components (parallel and perpendicular to the plane of incidence, respectively) of the beam are equal. The beam splitter, together with mirrors m3 and m4 are the place where the essential splitting, delay, and recombination tasks are performed. The amount of fused silica etalon (up to 7.5" for our VISAR) necessary to introduce the desired delay ($< 2$ ns) is placed in the right-hand leg. Mirror m3 is then translated so that the apparent distance to each mirror from the perspective of the detector is the same. Upon recombination of the beams at the beam splitter, interference fringes are generated and directed toward the four photomultipliers.

The $\lambda/8$ plate in the delay leg introduces a $90^o$ phase shift between the s- and p-polarized components of the returned light. Separate recording of the p- and s-components has several advantages. First, it can be shown that ambiguities in the sign of the acceleration are removed by this process [*Barker and Hollenbach,*

Figure A.2: Schematic illustration of the velocity interferometer system for any reflector (VISAR). The abbreviations are: M, mirror; L, lens; S, polarization scrambler; P, Glan-Thomson polarizing prism; BS, beam splitter; PZT, piezoelectric translator; PBS, polarizing beam splitter cube; F, laser-line filter; PMT, photomultiplier tube. The sample and mirror M1 are contained within the evacuated impact chamber. Light enters and exits the chamber through a 3/4"-thick plexiglass port (not shown) between L1 and M1.

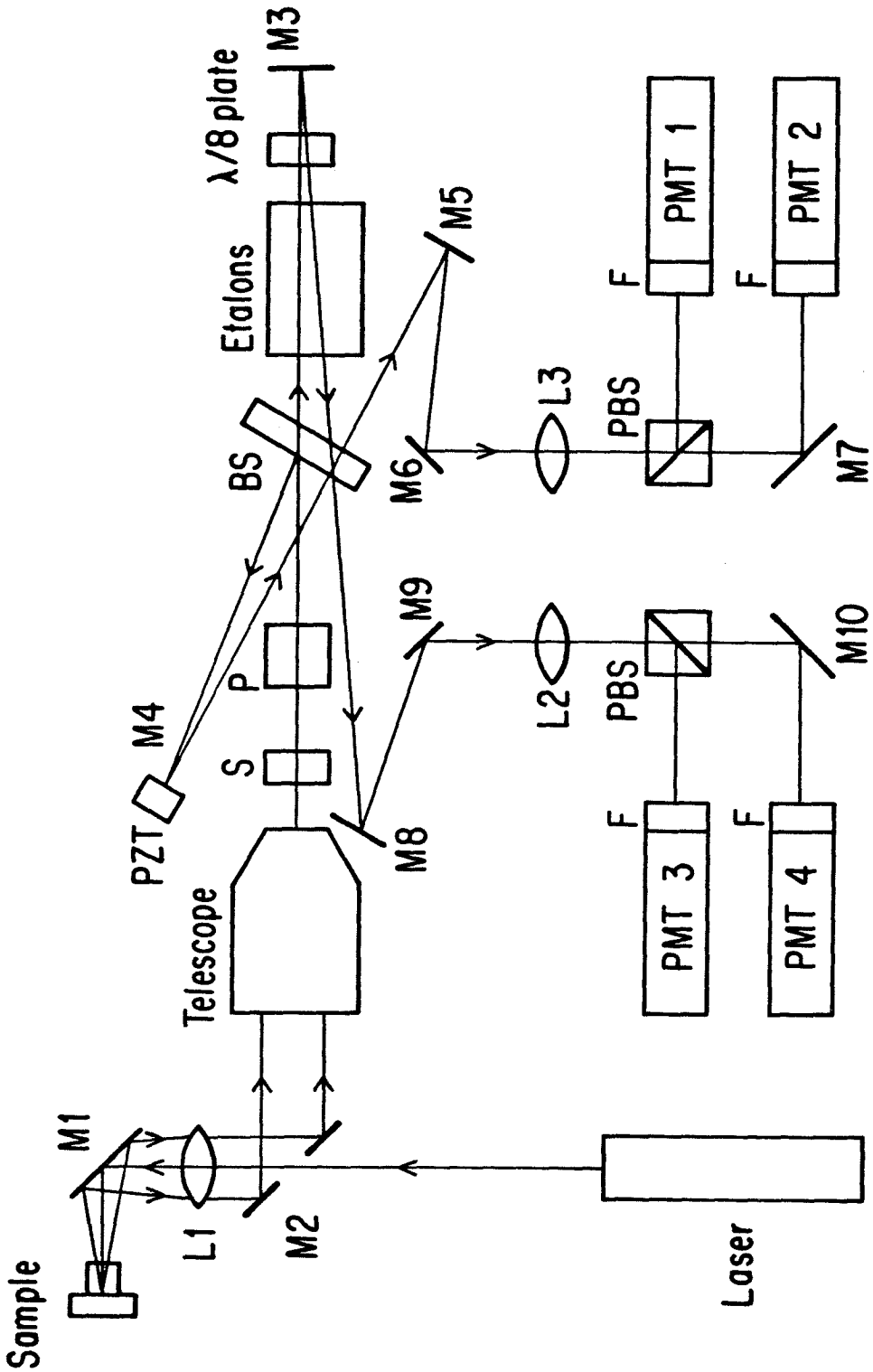
Sample
M1
L1
M2
Telescope
PZT
M4
S
P
M8
BS
λ/8 plate
M3
Etalons
M5
M6
M9
L2
L3
PBS
PBS
F
F
F
F
PMT 1
PMT 2
PMT 3
PMT 4
M7
M10
Laser

1972]. When the sign of the acceleration reverses, the leading polarization component reverses as well. Furthermore, the loss of velocity resolution near fringe peaks and troughs is eliminated since when one component is near an inflection point, the other is near its midpoint, where velocity resolution is maximized. These features are taken into account in the arctangent velocity algorithm discussed below. The interference patterns traveling to the left and right of the beam splitter are $180^o$ out-of-phase because of phase shifts upon reflection. These are recorded separately and subtracted from each other to cancel non-interfering stray light and to double the signal levels. This is known as the push-pull VISAR modification [*Hemsing,* 1979].

The relationship between the reflector velocity, $u$, and the fringe count, $F$, is given by [*Barker and Hollenbach,* 1972]:

$$u(t - \tau/2) = kF(t), \tag{A.2}$$

where $k$ is the fringe constant, which is given by [*Barker and Schuler,* 1974]:

$$k = \frac{\lambda_o}{2\tau(1 + \Delta\nu/\nu_o)(1 + \delta)}, \tag{A.3}$$

where the incident laser wavelength, $\lambda_o = 514.5$ nm, $(1 + \delta)$ is a correction term related to dispersion in the fused silica etalons, and $(1 + \Delta\nu/\nu_o)$ is a correction term that accounts for the change in the refractive index of the shock-compressed window material [*Barker and Hollenbach,* 1970]. For the latter term, $\nu_o$ is the frequency shift the scattered light would have if no window were present, and $\Delta\nu$ represents the correction for strain-induced changes in the window refractive index. For LiF, the correction term is $1.281 \pm 0.009$ and has been calibrated up to 115 GPa [*Wise and Chhabildas,* 1986]. The correction was determined by comparing particle velocities measured using the VISAR with calculated values using the EOS of LiF and the impactor material and the independently measured impact velocity. The EOS for LiF used by *Wise and Chhabildas* for this calculation is the same as that given in Table 1.2. The correction term can be used to compute the stress

dependence of the window refractive index using:

$$n = \frac{\rho}{\rho_o} n_o - \left(\frac{\rho}{\rho_o} - 1\right)\left(1 + \frac{\Delta\nu}{\nu_o}\right), \tag{A.4}$$

where n is the refractive index, $\rho$ is the density, and the subscript o refers to ambient-pressure quantities. In the case of a free-surface velocity measurement, the correction term is, of course, zero. The dispersion term has been determined by *Barker and Schuler* [1974] to be 1.0339 at $\lambda$=514.5 nm.

The delay time $\tau$ is determined from:

$$\tau = \frac{2h}{c}\left(n - \frac{1}{n}\right), \tag{A.5}$$

where $h$ is the etalon thickness, $n$ is the etalon refractive index, and $c$ is the speed of light. The effect of the fused silica beam splitter and crystal quartz $\lambda/8$ plate must be accounted for in computing the delay time, but the effect of non-normal incidence through the components is neglected. The refractive index of fused silica was measured differentially by measuring the required back-off distances using different thicknesses of etalon. It was found that $n = 1.468 \pm 0.003$ for our etalon material which is 0.4 % greater than the value reported by *Malitson* [1965] at this wavelength. The relationship between etalon refractive index and back-off distance is [*Zwick and Shepard,* 1971]:

$$x = h(1 - 1/n), \tag{A.6}$$

where $x$ is the back-off distance or the distance the mirror must be translated in order to equalize the two legs of the interferometer. The back-off distances were determined by satisfying the zero defocusing condition [*Zwick and Shepard,* 1971] and the resulting refractive index values are listed in Table A.1.

The error in the fringe constant from the errors in all the above quantities is estimated to be $\pm 1\%$ when the maximum amount of fused silica is used. This is comparable to the uncertainty level in other VISARs [*Barker,* 1988b]. The present

| Etalon Length (mm) | Back-off Distance (mm) | $n$ |
|---|---|---|
| 189.92 | 60.50 | 1.467 |
| 177.09 | 56.49 | 1.468 |
| 164.87 | 52.48 | 1.467 |
| 152.04 | 48.46 | 1.468 |
| 139.70 | 44.45 | 1.467 |
| 126.54 | 40.46 | 1.470 |
| 114.30 | 36.37 | 1.467 |
| 101.50 | 32.39 | 1.468 |
| 88.42 | 28.19 | 1.468 |
| 75.59 | 24.21 | 1.471 |
| 63.37 | 20.14 | 1.466 |

Table A.1: Refractive index of fused silica etalon determined from measuring back-off distance required for various lengths of fused silica.

interferometer can accommodate between 0 and 7.5" of fused silica etalon material. When these thicknesses are inserted in Eqn. A.5 and the resulting $\tau$ value is used in A.3, the resulting fringe constants range between 0.176 and 1.796 km/s/fringe when an LiF window is used. For free-surface measurements, the limits on the range of possible fringe constants are larger by a factor of 1.281. Since the fringe count can be determined to about $\pm 0.02$ [*Barker,* 1988b], the minimum velocity that can be resolved by our VISAR is $\sim$4 m/s.

### A.2.2 Optical Layout

In this section a discussion of the VISAR optical system is presented. All VISAR optical surfaces are flat to $\lambda/20$ except for the critical interferometer mirrors (m3 and m4) which are flat to $\lambda/40$. Multilayer antireflection coatings are applied to all lenses, beam splitters, and etalons.

The VISAR components (with the exception of the laser and associated beam-steering optics) are mounted on a 2' x 6' optical table next to the Caltech 40-mm propellant gun. The table is decoupled from floor vibrations by placing it upon vibration-damping pads. A 3 Watt $Ar^+$ ion laser (Lexel 5000-3) is the input light source. A temperature-controlled etalon assembly provides single-frequency output of greater than 1 Watt at 514.5 nm. Typical VISAR experiments using steel or aluminum reflectors required 100-300 mW of laser power. The laser is mounted on a vibration-isolated steel H-beam next to the VISAR. A polarization rotator attached to the laser output allows the polarization vector of the laser beam to be rotated through 360°.

Laser light enters the vacuum tank of the 40-mm gun through a series of three mirrors (not shown is Fig. 1.2) and passes through a 1/4" hole drilled at 45° through mirror m2. Collimating lens L1 focuses the incident light on the back of the target and recollimates the return beam. This lens is mounted on a translation stage which

is rigidly attached to the 40-mm gun tank. The lens itself is a 51-mm diameter achromatic doublet with a focal length of 245 mm. An expendable mirror (m1) inside the tank directs the incident beam onto the target. Alignment techniques insure that the beam strikes the center of the target at near-normal incidence. The spot size of the focused laser beam at the sample-window interface is about 0.1 mm. The returned diffuse light is directed out of the tank by m1 and recollimated using L1. A 3-inch diameter mirror (m2) with a 3-mm hole separates the returned light from the incident beam. A reversed laser beam expander (Special Optics 50-71SP-8.4-514.5, 71-mm input aperture, 10-mm output aperture, expansion factor 0.119) reduces the diameter of the beam to about 1 cm. The light entering the telescope must be well collimated or a constant diameter reduced beam is not achievable. It has been observed that optical activity in shock-compressed window materials can cause rotation of the polarization vector of returned light [*Asay and Barker,* 1974]. Since this light must be passed through a polarizer for proper orientation of VISAR signals, this can result in rapid random beam intensity fluctuations. To overcome this, a cemented quartz polarization scrambler (Karl Lambrecht Corp. SQWC25, 1.5° angle) is inserted after the telescope. The light then passes through a Glan-Thompson prism polarizer (Karl Lambrecht Corp. MGT25A12, 12-mm aperture) which equalizes the p- and s-components of the scattered light.

The beam then impinges on a beam splitter (Newport Corp, 51-mm diameter) mounted at an angle of about 5° to the incident beam. The dielectric coating of the beam splitter is chosen to give approximately 50% reflection and 50% transmission for both the s- and p-components at near-normal incidence. Half the light is directed toward mirror m4 which is mounted on an adjustable mirror mount (Lansing Corp. AOD 10.253) with sensitive micrometer threads for fine adjustment of the interference pattern. The remainder of the light passes through the beam splitter and strikes mirror m3, which has coarse angular adjustment and is mounted on a translation

stage (Unislide Corp.). A zero-order $\lambda/8$ plate (Continental Optical Corp., 25.4-mm diameter) is mounted immediately in front of m3 and a 45° phase shift between the s- and p-components upon both incidence and reflection, resulting in a 90° total phase shift. Up to 7.5" of fused silica etalon material (Continental Optical Corp, 1.5" diameter, lengths of 4", 2", 1", and 0.5") can be inserted in this leg of the interferometer to provide variable delay time. Upon insertion of the etalon material, m3 is translated by the required amount as discussed in the previous section. The light is recombined at a different portion of the beam splitter, and interference fringes are generated. Angular adjustments on the mirrors and beam splitter allow the two beams to be exactly superimposed. A piezoelectric translator (Lansing Research 21.937) is attached to m4, and when driven at high voltage continuously changes the path between the beam splitter and m4, resulting in a slowly ($\sim$ 1 khz) varying fringe pattern which is of use during alignment.

180° out-of-phase interference patterns are generated to the left and right of the beam splitter. These are directed towards the photomultiplier tubes (pmts) by beam-folding mirrors. Lenses L2 and L3 are used to focus the light onto the pmt photocathodes. The pmts are carefully positioned so as to be equidistant from the lenses on equal optical axes so that intensity changes affect all tubes in an identical manner. The tubes are mounted in isolated housings to protect them from stray electromagnetic fields. Ground-glass diffusing plates are used to insure that the pmt photocathodes are uniformly illuminated. Polarizing beam splitter cubes (Karl Lambrecht Corp.) separate the p- and s-components of the beam, sending them to separate photomultipliers. Narrow-bandwidth (1 nm) interference filters (Janos Technology F3611-514) are mounted in front of each photomultiplier to filter out extraneous light generated during the experiment. This has the additional benefit of allowing operation of the system with the room lights on.

### A.2.3 VISAR Electronics

A diagram of the VISAR system electronics components is shown in Figure A.3. Velocity-induced intensity fluctuations are detected by photomultiplier tubes (Burle 7764) and then amplified (Comlinear CLC-100, 500 MHz bandwidth, gain of 10 ) before being stored using digitizing oscilloscopes. While in principle the VISAR frequency response is limited only by the delay time, $\tau$, in practice the response of the detectors limits the overall frequency response. We used a photomultiplier tube circuit design with an estimated frequency response of 500 MHz [*Crump and Stanton,* 1988]. The arrival of the shock wave at the reflecting surface frequently produces a burst of fringes at a frequency too high to be detected. When this occurs, the velocity profile becomes ambiguous by an integral number of fringes. However, the number of fringes lost can usually be estimated from the measured impact velocity, and an accurate wave profile is obtained by adding this to the fringe fraction necessitated by the intensity levels before and after the jump. The necessity of adding velocity jumps at the shock arrival could be avoided only at low-stress levels ($\sim$10 GPa) in dispersive materials (e.g., granite).

Measurement of the tilt between the flyer and sample at impact is important for timing and diagnostics in VISAR experiments. Tilt is typically measured by recording the closure time of electrical shorting pins (Dynasen Corp. ca-1038). The pins are small electrical switches in which two conductors are separated by a small air gap (0.635 $\pm$ 0.012 mm) which is closed mechanically by impact of the flyer plate onto the electrically conducting front surface or cap (0.051 $\pm$ 0.003 mm thick) of the pin. In order to take advantage of faster digital-storage oscilloscopes, construction was undertaken of a new high-speed pulse circuit for recording shorting pin closure with nanosecond precision. Four pins were set into small holes drilled 90° apart on a 1.125"-diameter circle. The target diameter is 1.25". The pins are set flush with the impact surface, and equal-thickness ($\sim$ 0.01") steel shims are epoxied to each

Figure A.3: Block diagram showing principal VISAR electronics components. The abbreviations are the following: PZT, piezoelectric translator; PMTs, photomultiplier tubes; P.S., power supply.

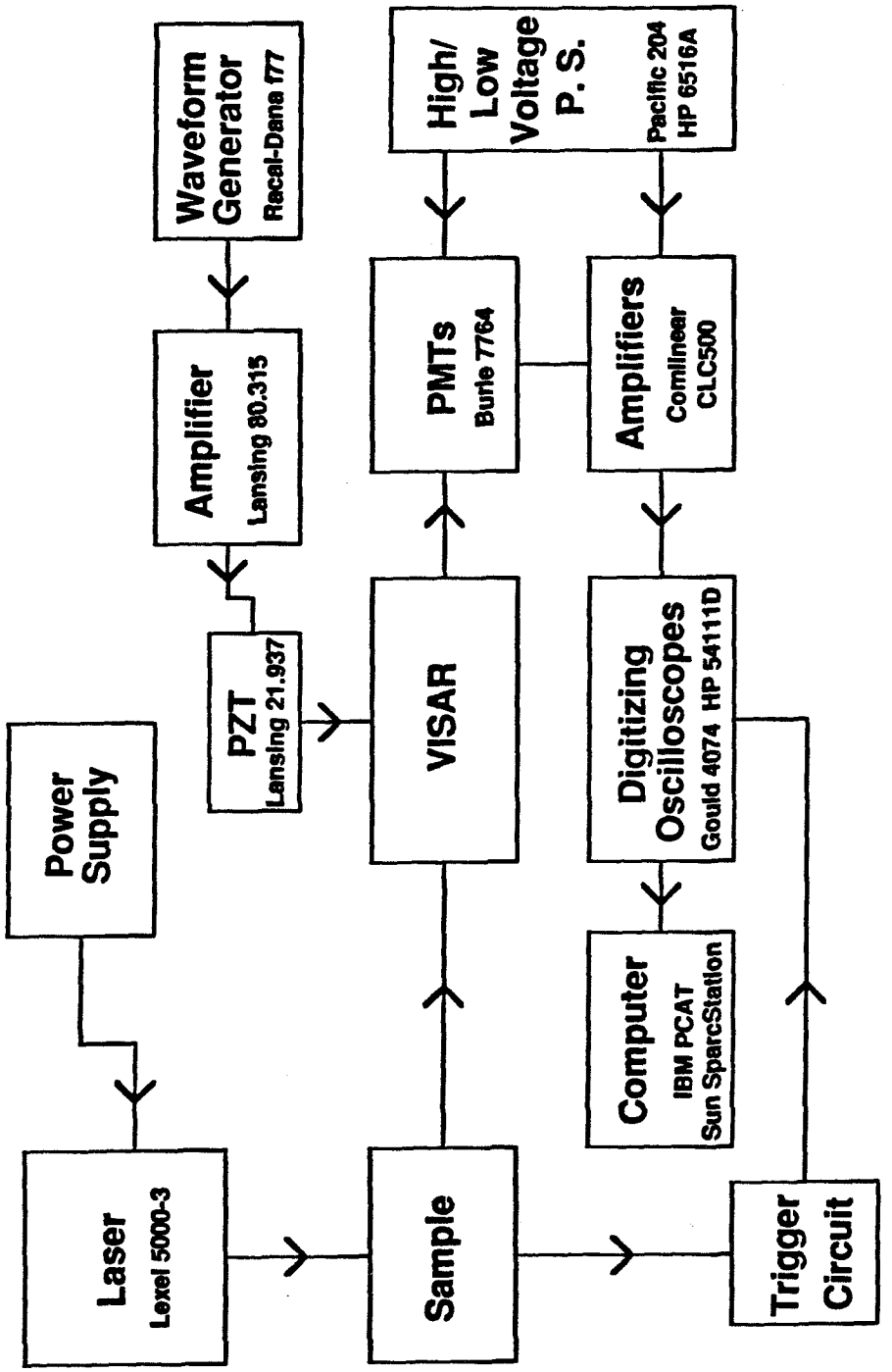
Waveform Generator
Recal-Dana f77
High/ Low Voltage P. S.
Pacific 204
HP 6516A
Amplifier
Lansing 80.315
PMTs
Burle 7764
Amplifiers
Comlinear
CLC500
Power Supply
PZT
Lansing 21.937
VISAR
Digitizing Oscilloscopes
Gould 4074 HP 54111D
Computer
IBM PCAT
Sun SparcStation
Laser
Lexel 5000-3
Sample
Trigger Circuit

pin. The purpose of the shims is to protect the pins from pretriggering. A schematic diagram of the circuit used for recording pin-closure times is shown in Figure A.4. The closure of each pin produces a different-sized voltage step because of the different resistor values in each branch of the circuit. A 50-Ω resistor connected in series with each pin suppresses reflections in the coaxial line between the pin and the circuit. This allows the circuit to be placed outside the impact chamber without significant deterioration of the frequency response and greatly simplifies target fabrication while preventing damage to the circuit from repeated impacts. The pulse rise time for this circuit is typically 3-5 ns and the time between successive pin closures can be determined routinely to ± 2 ns.

A pin-closure record from a typical experiment is shown in Figure A.5. The calculated center-impact time is indicated by the arrow in the figure. From these data, the tilt angle at impact was calculated to be 4.3 milliradians using the analysis of [*Mitchell and Nellis,* 1981b] and assuming no distortion of the impactor.

A limitation of VISAR experiments is that it is difficult to establish absolute timing for the experiment. For experiments in which the elastic precursor is not overdriven, the arrival time of the elastic precursor together with the known ambient-pressure compressional sound velocity can be used to establish absolute times (see Chapter 4). In principle, however, shock wave velocities could be directly measured by recording both the impact time and the arrival time of the shock front at the interface being monitored by the VISAR. Preliminary attempts to do this were carried out, but the precision of the resulting shock velocities was somewhat poor (±5%). The difficulty lies in accurately relating the shorting pin and VISAR signals. For the VISAR, the quantities that must be measured are: the optical transit time from the reflecting surface to the pmt photocathode, the electron transit time through the pmt, the rise time of the pmt and amplifier circuits, and all cable delays. For the shorting-pin circuit, the required parameters are the wave transit times through

Figure A.4: Circuit diagram of high-speed switch-closure circuit for impact tilt measurement. The circuit is a simple capacitor-discharge circuit utilizing a 90 V battery. The tilt pins are shown as open switches that are connected to the remotely located circuit with coaxial lines.

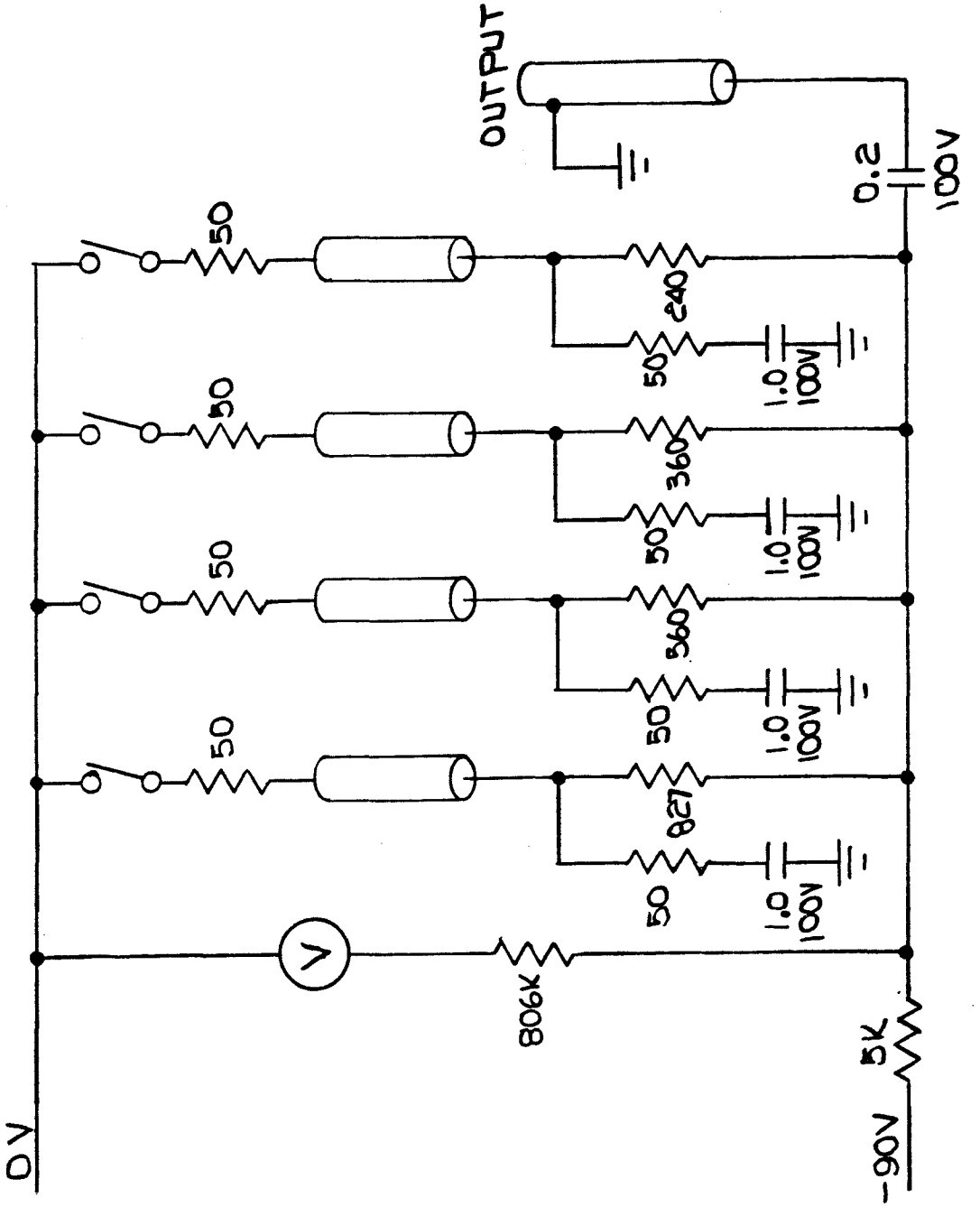
OUTPUT
0.2
100V
50
240
50
1.0
100V
50
360
50
1.0
100V
50
560
50
1.0
100V
50
827
50
1.0
100V
V
806K
5K
0V
-90V

Figure A.5: Example of a typical experimental tilt pin closure record. Closure times of the 4 pins, each of which produces a different voltage step, are indicated. The arrow labeled CI shows the calculated center-impact time. The time scale is arbitrary. The data sampling rate for this experiment was 500 MS/s.

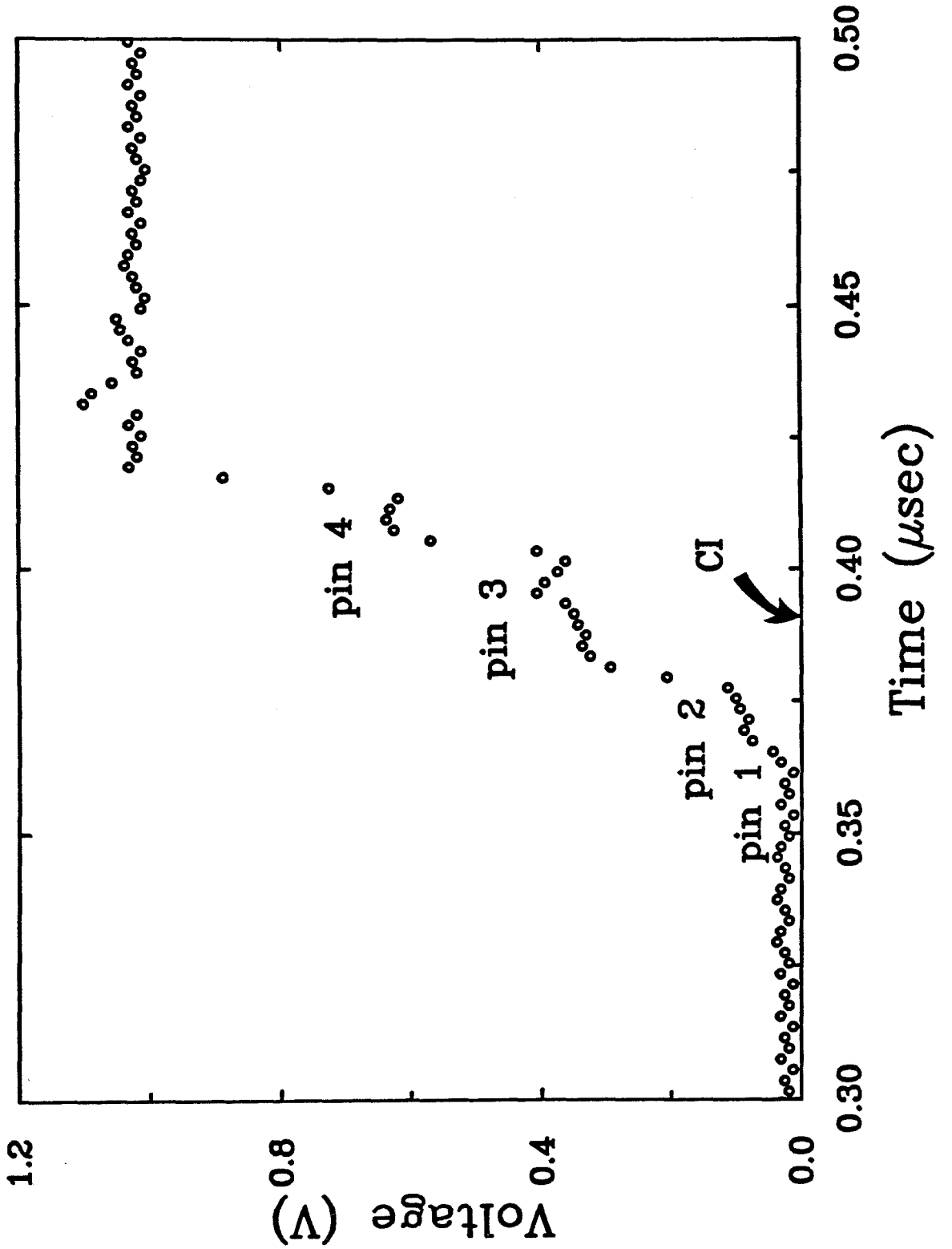
Voltage (V)
1.2
0.8
0.4
0.0
0.30
0.35
0.40
0.45
0.50
Time (μsec)
pin 4
pin 3
pin 2
pin 1
CI

the shim, cap, and air gap of the pins, the rise time of the tilt circuit, cable delays, and the correction of measured times at the periphery of the sample to the sample center. In practice, most of these quantities can be determined to within a few ns. Uncertainties in the wave transit times through the pin components can introduce uncertainties of 10s of ns which limit the precision of the shock velocity measurement. Improvements to this system could be achieved by the use of higher-quality shorting pins or more precise measurement of their dimensions before each experiment. Some improvement could also be made by using the impact pin signal to generate an optical signal that could be recorded by the photomultiplier tubes. This would guarantee that the impact and VISAR signals travel along identical paths from the pmts onward and would eliminate the tedious necessity of measuring rise times, cable lengths, etc. A fast optical fiducial would also simplify the process of properly aligning fringe records recorded on different oscilloscopes. At present, sharp waveform features such as the shock or elastic precursor arrival are used to determine time shifts for the traces. Some discussion of optical fiducial systems is contained in *Hemsing* [1983b] and *Crump and Stanton* [1988].

### A.2.4 Data Reduction

Photomultiplier tube voltages are amplified and then recorded using digital oscilloscopes (see Figure A.3). Two types of digitizing oscilloscopes were used: 2 channel HP54111D oscilloscopes with a maximum sampling rate of 1 GS/s and a 4-channel Gould 4074 with a sampling rate of 250 MS/s. The four PMT outputs are recorded on both types of oscilloscopes but at different vertical sensitivities. The reason for this is that sample reflectivity can change abruptly when the shock front reaches the reflector, resulting either in much larger or much smaller ( by up to a factor of 5) signal amplitudes than expected. The stored oscilloscope records are transferred to a computer for further analysis. Some of the oscilloscopes record for 8 $\mu$sec or

more, although the region of interest lasts only 2-3 $\mu$sec. The next step in the data-reduction process, therefore, is to window the data using the FORTRAN program SHRINK [*Barker,* 1988a]. This reduces the experimental data to about 1000-3000 digitized points. Velocity histories are then extracted from the interferometer records using a modified version of the program VISAR88 [*Barker,* 1988b]. This program was modified in several ways for use with a four-detector VISAR. Most importantly, the algorithm of *Hemsing* [1983b] was substituted for the velocity calculation. The velocity is determined using the equation:

$$V(t) = k\left(\arctan\left(\frac{d2(t) - d1(t)\cos\phi}{d1(t)\sin\phi}\right) - \psi_o\right), \tag{A.7}$$

where $d1(t)$ and $d2(t)$ are the signal intensities of the two data channels, $\phi$ is the phase angle between the two channels, about $90^o$, $\psi_o$ is the initial random phase at $t$ = 0, and $k$ is the fringe constant in velocity per degree. This data reduction method is insensitive to signal-intensity fluctuations and is therefore more appropriate for a push-pull VISAR for which the beam intensity is not explicitly monitored. Other modifications allow for software subtraction of two $180^o$ out-of-phase oscilloscope traces and plotting of a Lissajous figure, which simplifies correction of data defects and determination of the actual phase angle of the experiment.

## A.3 Impactor and Sample Preparation

Preparation of specular targets for the SVI was a tedious and time-consuming process, requiring many hours of labor for each target. The stainless steel 304 targets used in these experiments were initially lapped by hand on glass plates using a series of successively finer alumina powders. The smallest grit size used was 5 $\mu$. The target was then polished using a polishing cloth mounted on a glass plate and 3 and 1 $\mu$ alumina powders. Cleanliness must be carefully maintained as the introduction of only a few large particles is sufficient to cause deep scratches that require relapping

to remove. Samples must be carefully cleaned before changing powder size. It is also important to maintain target flatness at each stage in the operation, or it will not be possible to obtain a final specular surface. The quality of the final specular surface is judged by reflecting a laser beam off the surface and verifying that there is no significant degradation of the reflected beam. A few specular targets were purchased commercially (Spawr Optical Co, Corona, CA) and these performed quite satisfactorily.

Diffuse reflectors for use in VISAR experiments are much simpler to prepare. Steel, molybdenum, and aluminum reflectors were prepared by lapping on glass plates with alumina powder. The finest grit size used was 3 or 5 $\mu$. The targets were lapped at a particular grit until all large scratches are removed, and a uniform surface was obtained across the entire specimen. Care must be taken to insure that both the part and the glass plate below are lapped uniformly. Thin (1-2 mm) aluminum buffer plates must be lapped with particular care, as it is challenging to maintain flatness tolerances on such pieces. The quality of the diffuse surface is checked by observing reflected laser light and insuring that the reflected beam is of uniform intensity with no central bright region. Windows were epoxied to the reflecting surface with 910 adhesive and epoxy-layer thicknesses of 10-20 $\mu$ were achieved. Epoxy thicknesses were determined by comparing the total thickness of the epoxied composite with the previously measured thicknesses of the individual components. Thicknesses were measured to $\pm$0.00005" at 12-16 locations on each material using a standard micrometer.

Other techniques for obtaining diffuse reflectors were also attempted with varying degrees of success. In one experiment, a small piece of aluminum foil was sandwiched between 2 layers of NaCl and impacted. Although the shock arrival was well recorded in this experiment, a subsequent loss of intensity caused the unloading history to be lost. This may have been due either to loss of reflectivity of the Al foil or to loss of

transparency in the NaCl window.

A few reflectors were prepared by lapping LiF windows and vapor-depositing aluminum on the lapped surface. The windows were lapped using 17.5 $\mu$ alumina powder in a mineral oil slurry. Care must be taken as LiF is easily scratched. The quality of the lapped surface before coating is most easily observed by passing a laser beam through the diffuse surface in a darkened room and verifying that there is no central bright spot. A double thickness of aluminum coating is then applied to a nominal thickness of 0.25 - 0.5 $\mu$. In practice, these windows turned out to be very good reflectors, requiring laser power of only 10-20 mW for sufficient signal. However, the reflectivity generally deteriorates strongly after shock arrival, resulting in weak fringe amplitudes.

In order to generate controlled unloading, the flyer plates used in VISAR experiments are frequently backed by a low-impedance material. Backing the flyer directly with the lexan projectile material produces a partial unloading whose magnitude depends on the impedance contrast between the flyer and lexan. More complete unloading is attained by backing the flyer with 40 lb/ft$^3$ polyurethane foam (General Plastics Manufacturing Co.). This foam is light, rigid, and easily machined and thus both supports the flyer plate during its acceleration and also allows for more complete unloading of the sample to be recorded. The thickness of the foam layer is typically 3 mm and is chosen such that reflection from the foam-lexan interface arrive well after the experimental time of interest.

# Bibliography


Ahrens, T. J., High-pressure electrical behavior and equation of state of magnesium oxide from shock wave measurements, *J. Appl. Phys., 37,* 2532-2541, 1966.

Ahrens, T. J., Shock wave techniques for geophysics and planetary physics, in *Methods of Experimental Physics,* vol. 24, edited by C. G. Sammis and T. L. Henyey, pp. 185-235, Academic, San Diego, Calif., 1987.

Ahrens, T. J., and G. E. Duvall, Stress relaxation behind elastic shock waves in rocks, *J. Geophys. Res., 71,* 4349-4360, 1966.

Ahrens, T. J., and V. G. Gregson, Shock compression of crustal rocks: data for quartz, calcite, and plagioclase rocks, *J. Geophys. Res., 69,* 4839-4874, 1964.

Ahrens, T. J., and R. Jeanloz, Pyrite: shock compression, isentropic release, and composition of the Earth's core, *J. Geophys. Res, 92,* 10363-10375, 1987.

Ahrens, T. J., J. H. Lower, and P. L. Lagus, Equation of state of forsterite, *J. Geophys. Res., 76,* 514-528, 1971.

Ahrens, T. J., W. H. Gust, and E. B. Royce, Material strength effects in shock compression of alumina, *J. Appl. Phys., 39,* 4610-4616, 1968.

Al'tshuler, L. V., S. B. Kormer, M. I. Brazhnik, L. A. Vladimirov, M. P. Speranskaya, and A. I. Funtikov, The isentropic compressibility of aluminum, copper, lead, and iron at high pressures, *Sov. Phys. JETP,* Engl. Transl., *11,* 761-775, 1960.

Al'tshuler, L. V., R. F. Trunin, and G. V. Simakov, Shock-wave compression of periclase and quartz and the composition of the Earth's lower mantle, *Izv. Earth Phys., 10,* 657-660, 1965.

Al'tshuler, L. V., M. I. Brazhnik, and G. S. Telegin, Strength and elasticity of iron and copper at high shock-wave compression pressures, *J. Appl. Mech. Tech. Phys.,* Engl. Transl., *12,* 921-926, 1971.

Anderson, D. L., A seismic equation of state, II, Shear properties and thermodynamics of the lower mantle, *Phys. Earth Planet. Inter., 45,* 307-323, 1987.

Anderson, O. L., Properties of iron at the Earth's core conditions, *Geophys. J. R. Astron. Soc., 84,* 561-579, 1986.

Anderson, O. L., and A. Chopelas, A thermodynamic theory for the Grüneisen ratio at extreme conditions: MgO as an example, submitted to *Phys. Chem. Minerals,* 1992.

Anderson, O. L., and I. Suzuki, Anharmonicity of three minerals at high temperature: forsterite, fayalite, and periclase, *J. Geophys. Res., 88,* 3549-3556, 1983.

Anderson, O. L., A. Chopelas, and R. Boehler, Thermal expansion versus pressure at constant temperature: A re-examination, *Geophys. Res. Lett., 17,* 685-688, 1990.

Anderson, W. W., High-pressure states in condensed matter, Ph.D. thesis, 235 pp., *California Institute of Technology,* Pasadena, 1990.

Asay, J. R., Shock-induced melting in bismuth, *J. Appl. Phys., 45,* 4441-4452, 1974.

Asay, J. R., Measurement of material properties to Mbar pressures using time-resolved shock wave techniques, *Sandia Natl. Lab., Rep. SAND84-2657,* Albuquerque, NM, 1985.

Asay, J. R., and L. M. Barker, Interferometric measurement of shock-induced particle velocity and spatial variations of particle velocity, *J. Appl. Phys., 45,* 2540-2546, 1974.

Asay, J. R., and L. C. Chhabildas, Determination of the shear strength of shock-compressed 6061-T6 aluminum, in *Shock Waves and High Strain-Rate Phenomena in Metals,* edited by M. A. Meyers, and L. E. Murr, pp. 417-431, Plenum, New York, 1981.

Asay, J. R., and G. I. Kerley, The response of materials to dynamic loading, *Int. J. Impact Eng., 5,* 69-99, 1987.

Asay, J. R., and J. Lipkin, A self-consistent technique for estimating the dynamic yield strength of a shock-loaded material, *J. Appl. Phys., 49,* 4242-4247, 1978.

Asay, J. R., L. C. Chhabildas, and D. P. Dandekar, Shear strength of shock-loaded polycrystalline tungsten *J. Appl. Phys., 51,* 4774-4783, 1980.

Asay, J. R., L. C. Chhabildas, G. I. Kerley, and T. G. Trucano, High-pressure strength of shocked aluminum, in *Shock Waves in Condensed Matter – 1985,* edited by Y. M. Gupta, pp. 145-149, Plenum, New York, 1986.

Badding, J. V., R. J. Hemley, and H. K. Mao, High-pressure chemistry of hydrogen in metals - *in situ* study of iron hydride, *Science, 253,* 421-424, 1991.

Barker, L. M., Fine structure of compressive and release wave shapes in aluminum measured by the velocity interferometer technique, in *Behavior of Dense Media under High Dynamic Pressure,* Gordon and Breach, New York, pp. 483-504, 1968.

Barker, L. M., Velocity interferometry for time-resolved, high-velocity measurements, in *High Speed Photography, Videography, and Photonics, 427,* edited by D. L. Paisley, SPIE, San Diego, 116-126, 1983.

Barker, L. M., SHRINK - a program for reducing the size of digitizing oscilloscope records, *Sandia Natl. Lab., Rep. SAND88-2787,* Albuquerque, NM, 1988a.

Barker, L. M., VISAR88 - a new data-reduction program for VISARs, *Sandia Natl. Lab., Rep. SAND88-2788,* Albuquerque, NM, 1988b.

Barker, L. M., and R. E. Hollenbach, Interferometer technique for measuring the dynamic mechanical properties of materials, *Rev. Sci. Instrum., 36,* 1617-1620, 1965.

Barker, L. M., and R. E. Hollenbach, Shock-wave studies of PMMA, fused silica, and sapphire, *J. Appl. Phys., 41,* 4208-4226, 1970.

Barker, L. M., and R. E. Hollenbach, Laser interferometer for measuring high velocities of any reflecting surface, *J. Appl. Phys., 43,* 4669-4675, 1972.

Barker, L. M., and R. E. Hollenbach, Shock wave study of the $\alpha \rightleftharpoons \epsilon$ phase transition in iron, *J. Appl. Phys., 45,* 4872-4887, 1974.

Barker, L. M., and K. W. Schuler, Correction to the velocity-per-fringe relationship for the VISAR interferometer, *J. Appl. Phys., 45,* 3692-3693, 1974.

Bass, J. D., T. J. Ahrens, J. R. Abelson, and T. Hua, Shock temperature measurements in metals: new results for an Fe alloy, *J. Geophys. Res., 95,* 21,767-21,776, 1990.

Birch, F., The velocity of compressional waves in rocks to 10 kilobars 2, *J. Geophys. Res., 66,* 2199-2224, 1961.

Birch, F., Finite-strain isotherm and velocities for singe-crystal and polycrystalline NaCl at high pressures and 300 K, *J. Geophys. Res., 83,* 1257-1268, 1978.

Bless, S. J., and T. J. Ahrens, Measurement of release wave speed in shock-compressed polycrystalline alumina and aluminum, *J. Geophys. Res., 81,* 1935-1942, 1976.

Boness, D. A., and J. M. Brown, Time-resolved optical spectroscopy of shock-compressed fluid alkali halides, in *Shock Waves in Condensed Matter – 1989*, edited by S. C. Schmidt, J. N. Johnson, and L. W. Davison, pp. 863-866, North-Holland, New York, 1990a.

Boness, D. A., and J. M. Brown, The electronic-band structure of iron, sulfur, and oxygen at high pressures and the Earth's core, *J. Geophys. Res., 95,* 21721-21730, 1990b.

Brett, R., The current status of speculations on the composition of the core of the Earth, *Rev. Geophys. Space Phys., 14,* 375-383, 1976.

Brown J. M., and R. G. McQueen, Phase transitions, Grüneisen parameter, and elasticity for shocked iron between 77 GPa and 400 GPa, *J. Geophys. Res., 91,* 7485-7494, 1986.

Brown, J. M., and J. W. Shaner, Rarefaction velocities in shocked tantalum and the high-pressure melting point, in *Shock Waves in Condensed Matter – 1983*, edited by J. R. Asay, R. A. Graham, and G. K. Straub, pp. 91-94, Elsevier, New York, 1984.

Brown, J. M., and T. J. Shankland, Thermodynamic parameters in the Earth as determined by seismic profiles, *Geophys. J. R. astr. Soc., 66,* 579-596, 1981.

Chhabildas, L. C., and J. R. Asay, Time-resolved wave profile measurements in copper to megabar pressures, in *High Pressure in Research and Industry,* 8th AIRAPT Conf., edited by C. M. Backman, T. Johannisson, and L. Tegman, pp. 183-189, 1982.

Chhabildas, L. C., and D. E. Grady, Shock-loading behavior of fused quartz, in *Shock Waves in Condensed Matter – 1983*, edited by J. R. Asay, R. A. Graham, and G. K. Straub, pp. 175-178, Elsevier, New York, 1984.

Chhabildas, L. C., and J. M. Miller, Release-adiabat measurements in crystalline quartz, Sandia Natl. Lab., *Rep. SAND85-1092*, Albuquerque, N. M., 1985.

Chhabildas, L. C., J. R. Asay, and L. M. Barker, Shear strength of tungsten under shock- and quasi-isentropic loading to 250 GPa, Sandia Natl. Lab., *Rep. SAND88-0306*, Albuquerque, N. M., 1988.

Chhabildas, L. C., L. M. Barker, and T. G. Trucano, Spall-strength measurements on shock-loaded refractory metals, in *Shock Compression of Condensed Matter - 1989,* edited by S. C. Schmidt, J. N. Johnson, and L. W. Davison, Elsevier, New York, 429-432, 1990.

Chopelas, A., and R. Boehler, Thermal expansion measurements at very high pressure, systematics, and a case for a chemically homogeneous mantle, *Geophys. Res. Lett., 16,* 1347-1350, 1989.

Chopelas, A., Thermal expansion, heat capacity, and entropy of MgO at mantle pressures, *Phys. Chem. Min., 17,* 142-148, 1990.

Crump, O. B., and P. L. Stanton, Push-pull, double-delay-leg or dual VISAR, *Sandia Natl. Lab., Report SAND87-1974,* Albuquerque, NM, 1988.

Davison, L., and R. A. Graham, Shock compression of solids, *Phys. Rep., 55,* 255-379, 1979.

Dickinson, J. M., and P. E. Armstrong, Temperature dependence of the elastic constants of molybdenum, *J. Appl. Phys., 38,* 602-606, 1967.

Duffy, T. S., and T. J. Ahrens, Sound velocities at high pressure and temperature and their geophysical implications, in press, *J. Geophys. Res.* 1992a.

Duffy, T. S., and T. J. Ahrens, Hugoniot sound velocities in metals with applications to the Earth's inner core, *High-Pressure Research in Mineral Physics: Applications to Earth and Planetary Sciences,* in press, 1992b.

Duffy, T. S., and D. L. Anderson, Seismic velocities in mantle minerals and the mineralogy of the upper mantle, *J. Geophys. Res., 94,* 1895-1912, 1989.

Dziewonski, A. D., and D. L. Anderson, Preliminary reference Earth model, *Phys. Earth Planet. Inter., 25,* 297-356, 1981.

Falzone, A. J., and F. D. Stacey, Second-order elasticity theory: explanation for the high Poisson's ratio of the inner core, *Phys. Earth Planet. Inter., 21,* 371-377, 1980.

Gerlich, D., and S. Hart, Pressure dependence of the elastic moduli of three austenitic stainless steels, *J. Appl. Phys., 55,* 880-884, 1984.

Godwal, B. K., and R. Jeanloz, Pressure-induced s→d transfer and the equation of state of molybdenum, *Phys. Rev. B, 41,* 7440-7445, 1990.

Grady, D. E., Processes occurring in shock wave compression of rocks and minerals, in *High-Pressure Research: Applications to Geophysics,* ed. by M. H. Manghnani and S. Akimoto, 389-438, Academic, New York, 1977.

Grady, D. E., Shock deformation of brittle solids, *J. Geophys. Res., 85,* 913-924, 1980.

Grady, D. E., Steady-wave risetime and spall measurements on uranium (3-15 GPa), in *Metallurgical Applications of Shock-Wave and High Strain-Rate Phenomena,* edited by L. E. Murr, K. P. Staudhammer, and M. A. Meyers, Marcel Dekker, New York, 763-780, 1986.

Grady, D. E., and M. D. Furnish, Shock- and release-wave properties of MJ-2 grout, Sandia Natl. Lab., *Rep. SAND88-1642,* Albuquerque, N. M., 1988.

Grady, D. E., W. J. Murri, and P. S. De Carli, Hugoniot sound velocities and phase transformations in two silicates, J. Geophys. Res., 80, 4857-4861, 1975.

Grady, D. E., R. E. Hollenbach, and K. W. Schuler, Compression wave studies on calcite rock, J. Geophys. Res., 83, 2839-2849, 1978.

Graham, R. A., and W. P. Brooks, Shock-wave compression of sapphire from 15 to 420 kbar. The effects of large anisotropic compressions, *J. Phys. Chem Solids, 32,* 2311-2330, 1971.

Guinan, M. W., and D. J. Steinberg, Pressure and temperature derivatives of the isotropic polycrystalline shear modulus for 65 elements, *J. Phys. Chem. Solids, 35,* 1501-1512, 1974.

Hageman, L. J., and J. M. Walsh, HELP, a multimaterial Eulerian program for compressible fluid and elastic-plastic flows in two space dimensions and time, *Systems, Science, and Software, Report 3SR-350,* La Jolla, Ca., 1970.

Hemsing, W. F., Velocity-sensing interferometer (VISAR) modification, *Rev. Sci. Instrum., 50,* 73-78, 1979.

Hemsing, W., VISAR: Some things you should know, in *High-Speed Photography, Videography, and Photonics,* Proc. *SPIE, 427,* 144-148, 1983a.

Hemsing, W., VISAR: $2\frac{1}{2}$ minutes for data reduction, in *High-Speed Photography, Videography, and Photonics,* Proc. *SPIE, 427,* 199-202, 1983b.

Herrmann, W., Development of a high-strain-rate constitutive equation for 6061-T6 aluminum, *Sandia Natl. Lab., Rep. SLA-730897,* Albuquerque, NM, 1974.

Hixson, R. S., D. A. Boness, J. W. Shaner, and J. A. Moriarty, Acoustic velocities and phase transitions in molybdenum under shock compression, *Phys. Rev. Lett., 62,* 637-640, 1989.

Isaak, D. G., O. L. Anderson, and T. Goto, Measured elastic moduli of single-crystal MgO measured to 1800 K, *Phys. Chem. Miner., 16,* 704-713, 1989.

Jackson, I., and H. Niesler, The elasticity of periclase to 3 GPa and some geophysical implications, in *High Pressure Research in Geophysics,* edited by S. Akimoto and M. H. Manghnani, pp. 93-133, Center for Academic Publishing, Tokyo, 1982.

Jackson, I., Some geophysical constraints on the chemical composition of the Earth's lower mantle, *Earth Planet. Sci. Lett., 62,* 91-103, 1983.

Jeanloz, R., Shock-wave equation of state and finite-strain theory, *J. Geophys. Res., 94,* 5873-5886, 1989a.

Jeanloz, R., The nature of the Earth's core, *Ann. Rev. Earth and Planet. Sci., 18,* 357-386, 1990.

Jeanloz, R., and T. J. Ahrens, Equations of state of FeO and CaO, *Geophys. J. R. Astron. Soc., 62,* 505-528, 1980.

Jeanloz, R., and E. Knittle, Density and composition of the lower mantle, *Phil. Trans. Royal Astron. Soc., 328,* 377-389, 1989.

Jeanloz, R., and S. Morris, Temperature distribution in the crust and mantle, *Ann. Rev. Earth Planet. Sci, 14,* 377-415, 1986.

Jeanloz, R., and H. R. Wenk, Convection and anisotropy of the inner core, *Geophys. Res. Lett., 15,* 72-75, 1988.

Jephcoat, A., and P. Olson, Is the inner core of the Earth pure iron? *Nature, 325,* 332-335, 1987.

Jones, A. H., W. M. Isbell, and C. J. Maiden, Measurement of the very high-pressure properties of materials using a light-gas gun, *J. Appl. Phys., 37,* 3493-3499, 1966.

Jones, O. E., and R. A. Graham, Shear strength effects on phase-transition pressures determined from shock-compression measurements, in *Accurate Characterization of the High-Pressure Environment,* edited by E. C. Boyd, pp. 229-242, NBS special pub. 326, Washington, D.C., 1971.

Katahara, K. W., M. H. Manghnani, and E. S. Fisher, Pressure derivatives of the elastic moduli of BCC Ti-V-Cr, Nb-Mo, and Ta-W alloys, *J. Phys. F: Metal Phys., 9,* 773-790, 1979.

Kipp, M. E., and R. J. Lawrence, WONDY V - A one-dimensional finite-difference wave-propagation code, *Sandia Natl. Lab., Rep. SAND81-0930,* Albuquerque, NM, 1982.

Kipp, M. E., and D. E. Grady, Shock compression and release in high-strength ceramics, *Sandia Natl. Lab., Rep. SAND89-1461,* Albuquerque, NM, 1989.

Knittle, E., R. Jeanloz, and G. L. Smith, Thermal expansion of silicate perovskite and stratification of the Earth's mantle, *Nature, 319,* 214-216, 1986.

Knittle, E., and R. Jeanloz, Synthesis and equation of state of $(Mg, Fe)SiO_3$ perovskite to over 100 Gigapascals, *Science, 235,* 668-670, 1987.

Lawrence, R. J., and J. R. Asay, High-pressure multiple-shock response of aluminum, in *High-Pressure Science and Technology,* vol. 1, edited by K. D. Timmerhaus and M. S. Barber, Plenum, New York, 1979.

Lay, T., T. J. Ahrens, P. Olsen, J. Smyth, and D. Loper, Studies of the Earth's deep interior: goals and trends, *Phys. Today,* 44-52, October, 1990.

Ledbetter, H. M., W. F. Weston, and E. R. Naimon, Low-temperature elastic properties of four austenitic stainless steels, *J. Appl. Phys., 46,* 3855-3860, 1975.

Ledbetter, H. M., N. V. Frederick, and M. W. Austin, Elastic-constant variability in stainless-steel 304, *J. Appl. Phys., 51,* 305-309, 1980.

Leese, J., and A. E. Lord, Elastic stiffness coefficients of single-crystal iron from room temperature to 500°C, *J. Appl. Phys., 39,* 3986-3988, 1968.

Lipkin, J., and J. R. Asay, Reshock and release of shock-compressed 6061-T6 aluminum, *J. Appl. Phys., 48,* 182-189, 1977.

Loper, D. E., and D. R. Fearn, A seismic model of a partially molten inner core, *J. Geophys. Res., 88,* 1235-1242, 1983.

Malitson, I. H., Interspecimen comparison of the refractive index of fused silica, *J. Opt. Soc. Am., 55,* 1205-1209, 1965.

Mao, H. K., and P. M. Bell, Equations of state of MgO and $\epsilon$ Fe under static-pressure conditions, *J. Geophys. Res., 84,* 4533-4536, 1979.

Mao, H. K., Y. Wu, L. C. Chen, and J. F. Shu, Static compression of iron to 300 GPa and $Fe_{0.8}Ni_{0.2}$ alloy to 260 GPa: Implications for composition of the core, *J. Geophys. Res., 95,* 21737-21742, 1990.

Marsh, S. P., *LASL Shock Hugoniot Data,* 658 pp., U. of California Press, Berkeley, 1980.

Mashimo, T., Y. Hanaoka, and K. Nagayama, Elastoplastic properties under shock compression of $Al_2O_3$ single crystal and polycrystal, *J. Appl. Phys., 63,* 327-336, 1988.

Masters, T . G., and P. M. Shearer, Summary of seismological constraints on the structure of the Earth's core, *J. Geophys. Res., 95,* 21691-21695, 1990.

McQueen, R. G., J. W. Hopson, and J. N. Fritz, Optical technique for determining rarefaction wave velocities at very high pressures, *Rev. Scien. Instr., 53,* 245-250, 1982.

McQueen, R. G., and S. P. Marsh, Shock-wave compression of iron-nickel alloys and the Earth's core, *J. Geophys. Res., 71,* 1751-1756, 1966.

McQueen, R. G., S. P. Marsh, and J. N. Fritz, Hugoniot equation of state of twelve rocks, *J. Geophys. Res., 72,* 4999-5035, 1967.

McQueen, R. G., S. P. Marsh, J. W. Taylor, J. N. Fritz, and W. J. Carter, The equation of state of solids from shock wave studies, in *High-Velocity Impact Phenomena,* edited by R. Kinslow, pp. 294-419, Academic Press, New York, 1970.

Miller, G. H., T. J. Ahrens, and E. M. Stolper, The equation of state of molybdenum at 1400°C, *J. Appl. Phys., 63,* 4469-4475, 1988.

Miller, G. H., E. M. Stolper, and T. J. Ahrens, The equation of state of a molten komatiite 1. Shock-wave compression to 36 GPa, *J. Geophys. Res., 96,* 1831-1848, 1991.

Mitchell, A. C., and W. J. Nellis, Shock compression of aluminum, copper, and tantalum, *J. Appl. Phys., 52,* 3363-3374, 1981a.

Mitchell, A. C., and W. J. Nellis, Diagnostic system of the Lawrence Livermore National Laboratory two-stage light-gas gun, *Rev. Sci. Instrum., 52,* 347-359, 1981b.

Morris, C. E., *Los Alamos Shock Wave Profile Data*, University of CA Press, Berkeley, 488 pp., 1982.

Moss, W. C., and L. A. Glenn, A Bauschinger-effect model suitable for use in large computer codes, in *Shock Waves in Condensed Matter – 1983*, edited by J. R. Asay, R. A. Graham, and G. K. Straub, pp. 133-136, Elsevier, New York, 1984.

Munson, D. E., and R. J. Lawrence, Dynamic deformation of polycrystalline alumina, *J. Appl. Phys., 50,* 6272-6282, 1979.

Murr, L. E., Effects of peak pressure, pulse duration, and repeated loading on the residual structure and properties of shock-deformed metals and alloys, in *Shock Waves and High-Strain-Rate Phenomena in Metals,* edited by M. A. Meyers, and L. E. Murr, Plenum, New York, 753-777, 1981.

Murr, L. E., Examination of microstructural development by shock waves in condensed matter: theoretical and practical consequences, in *Shock Waves in Condensed Matter 1987,* edited by S. C. Schmidt and N. C. Holmes, North-Holland, New York, 315-320, 1988.

Pavlovskii, M. N., Measurements of the velocity of sound in shock-compressed dolomite, anhydrite, sodium chloride, paraffin, lexiglass, polyethylene and fluoroplast-4, *Z. Prik. Mek. Tek., 17,* 136-139, 1976.

Rigden, S. M., T. J. Ahrens, and E. M. Stolper, Densities of liquid silicates at high pressures, *Science, 226,* 1071-1074, 1984.

Rigden, S. M., T. J. Ahrens, E. M. Stolper, Shock compression of molten silicate: Results for a model basaltic composition, *J. Geophys. Res., 93,* 367-382, 1988.

Robie, R. A., B. S. Hemingway, and J. R. Fischer, Thermodynamic properties of minerals and related substances at 298.15 K and 1 bar ($10^5$ Pascals) pressure and at higher temperatures, *U.S. Geol. Surv. Bull., 1452,* 456 pp., 1978.

Rohde, R. W., Dynamic yield behavior of shock-loaded iron from 76 to 573 K, *Acta Metall., 17,* 353-363, 1969.

Romanchenko, V. I., and G. V. Stepanov, Dependence of the critical stresses on the loading-time parameters during spall in copper, aluminum, and steel, *J. Appl. Mech. Tech. Phys., 21,* 555-561, 1980.

Ross, M., D. A. Young, and R. Grover, Theory of the iron phase diagram at Earth core conditions, *J. Geophys. Res., 95,* 21713-21716, 1990.

Sammis, C., D. Anderson, and T. Jordan, Application of isotropic finite-strain theory to ultrasonic and seismological data, *J. Geophys. Res., 75,* 4478-4480, 1970.

Schuler, K. W., and J. W. Nunziato, The dynamic mechanical behavior of polymethyl methacrylate, *Rheol. Acta, 13,* 265-273, 1974.

Shaner, J. W., R. S. Hixson, M. A. Winkler, D. A. Boness, and J. M. Brown, Birch's law for fluid metals, in *Shock Waves in Condensed Matter – 1987,* edited by S. C. Schmidt and N. C. Holmes, pp. 135-138, North-Holland, New York, 1988.

Simmons, G., and H. Wang, *Single-Crystal Elastic Constants and Calculated Aggregate Properties: A Handbook,* 370 pp., MIT Press, Cambridge, Mass., 1971.

Stacey, F. D., A thermal model of the Earth, *Phys. Earth Planet. Inter., 15,* 341-348, 1977.

Stark, P. B., P. L. Parker, G. Masters, and J. A. Orcutt, Strict bounds on seismic velocity in the spherical Earth, *J. Geophys. Res., 91,* 13,892-13,902, 1986.

Steinberg, D. J., S. G. Cochran, and M. W. Guinan, A constitutive model for metals applicable at high-strain rate, *J. Appl. Phys., 51,* 1498-1504, 1980.

Sumino, Y., and O. L. Anderson, Elastic constants of minerals, in *Handbook of Physical Properties of Rocks,* vol. III, edited by R. S. Carmichael, pp. 39-137, CRC Press, Boca Raton, Fla., 1984.

Suzuki, I., Thermal expansion of periclase and olivine and their anharmonic properties, *J. Phys. Earth, 23,* 145-159, 1975.

Svendsen, B., and T. J. Ahrens, Shock-induced temperatures of MgO, *Geophys. J. I., 91,* 667-691, 1987.

Thomas, J. F., Third-order elastic constants of aluminum, *Phys. Rev., 175,* 955-962, 1968.

Vassiliou, M. S., and T. J. Ahrens, Hugoniot equation of state of periclase to 200 GPa, *Geophys. Res. Lett., 8,* 229-232, 1981.

Vohra, Y. K., and A. L. Ruoff, Static compression of metals Mo, Pb, and Pt to 272 GPa: Comparison with shock data, *Phys. Rev. B, 42,* 8651-8654, 1990.

Walsh, J. M., M. H. Rice, R. G. McQueen, and F. L. Yarger, Shock-wave compression of twenty-seven metals: Equation of state of metals, *Phys. Rev., 108,* 196-216, 1957.

Wang, G., An empirical expression of elastic sound speed of materials at high pressure, *Chinese J. High Pressure Phys., 2,* 92-95, 1988.

Williams, Q., R. Jeanloz, J. D. Bass, B. Svendsen, and T. J. Ahrens, The melting curve of iron to 2.5 Mbar: first experimental constraint on the temperature at the Earth's core, *Science, 236,* 181-182, 1987.

Williams, Q., Molten $(Mg_{0.88}Fe_{0.12})_2SiO_4$ at lower mantle conditions: melting products and structure of quenched glasses, *Geophys. Res. Lett., 17,* 635-638, 1990.

Wise, J. L., and L. C. Chhabildas, Laser-interferometer measurements of refractive index in shock-compressed materials, in *Shock Waves in Condensed Matter - 1985,* edited by Y. M. Gupta, 441-454, Plenum, New York, 1986.

Yeganeh-Haeri, A., D. J. Weidner, and E. Ito, Elasticity of $MgSiO_3$ in the perovskite structure, *Science, 243,* 787-789, 1989.

Zel'dovich, Ya. B., and Y. P. Razier, *Physics of Shock Waves and High-Temperature Hydrodynamic Phenomena,* 916 pp., Academic, New York, 1967.

Zwick, H. H., and G. G. Shepard, Defocusing a wide-angle Michelsen interferometer, *Appl. Opt., 10,* 2569-2571, 1971.